Versatile Microscopy Platforms for Imaging in vivo and in Cleared Tissue

Dissertation

zur

Erlangung der naturwissenschaftlichen Doktorwürde
(Dr. sc. nat.)

vorgelegt der

Mathematisch-naturwissenschaftlichen Fakultät

der

Universität Zürich

von

Fabian Friedrich Voigt

aus

Deutschland

Promotionskommission

Prof. Dr. Fritjof Helmchen (Vorsitz)
Prof. Dr. Stefan Neuhauss
Prof. Dr. Bruno Weber

Zürich, 2019

Doktorvater: Professor Fritjof Helmchen Fabian F. Voigt

Vielseitige Mikroskopieplattformen für die Bildgebung in vivo und in gecleartem Gewebe

Zusammenfassung

Kombiniert mit Techniken zum Erzeugen optischer Schnitte gehört die Fluoreszenzmikroskopie zu den am häufigsten verwendeten bildgebenden Verfahren in der modernen Biologie. Sie liefert qualitativ hochwertige dreidimensionale Bilder aus lebendem oder fixiertem Gewebe, um Anatomie und Morphologie zu rekonstruieren sowie funktionelle Experimente durchzuführen – letzteres zum Beispiel mittels der optischen Messung neuronaler Aktivität. Optische Schnitte werden erzeugt, indem entweder ausserhalb der Fokalebene emittiertes Fluoreszenzlicht nicht detektiert wird oder durch Beschränkung des Anregungsvolumens auf eine Zone um den Objektivfokus. Zwei Mikroskopieverfahren, die den zweiten Ansatz verwenden, sind die Multiphotonenmikroskopie und die Lichtblattmikroskopie. In der Multiphotonenmikroskopie wird das Anregungsvolumen mittels eines nichtlinearen Prozesses eingeschränkt, wohingegen die Lichtblattmikroskopie dafür einen Beleuchtungsstrahlengang senkrecht zum Detektionsstrahlengang verwendet. Die Multiphotonenmikroskopie eignet sich besonders gut für tiefe Bildgebung in streuendem Gewebe wie beispielsweise dem lebenden Gehirn der Maus und erfordert Femtosekundenlaser mit hoher Spitzenleistung und guter Strahlqualität. Die Lichtblattmikroskopie ist hingegen insbesondere für die Bildgebung in transparenten Proben optimal, eignet sich jedoch weniger für stark streuendes oder absorbierendes Gewebe. In diesem Fall erlauben es Clearingverfahren, die Probe durch Homogenisierung der optischen Eigenschaften durchsichtig zu machen, was die Mikroskopie mit Lichtblättern ermöglicht.

In dieser Dissertation werden zwei Projekte vorgestellt, die darauf abzielen, Mikroskopie mit optischen Schnitten weiter zu verbessern und kostengünstiger zu gestalten. Im ersten Teil wird die Anwendung eines neuartigen Femtosekunden-Halbleiterscheibenlasers für die Multiphotonenmikroskopie *in vivo* demonstriert. Der zweite Teil stellt die "mesoscale selective plane illumation microscopy" (mesoSPIM)-Initiative vor, ein open-source Hardwareprojekt, welches beabsichtigt, der Imaging-Community vielseitige Instrumente für die Bildgebung in gecleartem Gewebe zur Verfügung zu stellen.

Das erste Kapitel bietet eine allgemeine Einführung in die Geschichte der Gewebeschnitte und dem Streben nach verbesserten anatomischen Rekonstruktionen und führt eine Reihe von Verfahren zum Erzeugen optischer Schnitte ein, insbesondere Konfokal-, Multiphotonen- und Lichtblattmikroskopie.

Das zweite Kapitel enthält ein veröffentlichtes Manuskript zu den Versuchen mit dem Halbleiterscheibenlaser. Der in dieser Studie verwendete Laser erzeugt im Mikroskopfokus 170 fs-Pulse bei einer Wellenlänge von 1027 nm mit einer Repetitionsrate von 1,63 GHz und verfügt

über ein sehr einfaches und kompaktes Design der Laserkavität. Ich demonstriere die Eignung dieses Lasers für die Zweiphotonenmikroskopie *in vivo* in Drosophila-Larven und Mäusen für eine Vielzahl von Fluorophoren (einschließlich mKate2, tdTomato und Texas Red) und für die Mikroskopie mit Frequenzverdopplung in Muskeln. Darüber hinaus werden Messungen neuronaler Aktivität mit den Calciumindikatoren OGB-1 und R-CaMP1.07 im Cortex von Mäusen vorgestellt. Femtosekunden- Halbleiterscheibenlaser stellen daher eine vielversprechende und kostengünstige alternative Laserquelle für die Multiphotonenmikroskopie dar.

Das dritte Kapitel dient als Einführung in das Gewebe-Clearing und in die Lichtblattmikroskopie. Der erste Teil enthält eine Übersicht über eine Vielzahl von Clearingverfahren. Dazu gehören sowohl Verfahren, die auf organischen Lösungsmitteln basieren als auch hydrophile Methoden. Im zweiten Teil gebe ich einen Überblick über die Grundlagen und Anwendungen der Lichtblattmikroskopie und stelle Designoptionen für Instrumente für gecleartes Gewebe vor.

Das vierte Kapitel enthält ein unveröffentlichtes Manuskript zum mesoSPIM-Instrument. Dieses Mikroskop erlaubt es, Übersichtsdaten eines geclearten Mäusegehirns innerhalb weniger Minuten zu gewinnen. Um dies zu erreichen, wird eine Technik verwendet, die als "Axially scanned light-sheet microscopy" (ASLM) bezeichnet wird und eine gleichmäßige axiale Auflösung über das gesamte Gesichtsfeld ermöglicht. Das mesoSPIM ist mit allen gängigen Clearing-Methoden kompatibel und ist in der Lage, das intakte, durchsichtige und vollständige Zentralnervensystem einer Maus aufzunehmen.

Im letzten Kapitel wird beschrieben, wie die in den vorherigen Kapiteln vorgestellten Mikroskopieverfahren für biologische Projekte verwendet werden. Zudem gibt das Kapitel einen Ausblick auf mögliche Erweiterungen und Verbesserungen des mesoSPIM.

Thesis advisor: Professor Fritjof Helmchen Fabian F. Voigt

Versatile Microscopy Platforms for Imaging in vivo and in Cleared Tissue

Abstract

Fluorescence microscopy with optical sectioning is among the most common imaging methods in modern biology. It provides high quality three-dimensional data from living or fixed specimens to reconstruct anatomy, morphology and to conduct functional studies, for example by visualization of neuronal activity. Optical sectioning is achieved by either rejecting light generated outside of the focal plane or by restricting the excitation volume to a region around the microscope focus. Two imaging modalities using the latter approach are multiphoton microscopy, which achieves this confinement by nonlinear excitation, and light-sheet microscopy, which utilizes excitation orthogonal to the detection path. Multiphoton imaging is especially well suited for deep imaging in scattering tissue such as the living mouse brain and requires femtosecond laser sources with high peak power and good beam quality. Light-sheet microscopy excels at imaging transparent samples with high throughput, but is less well suited for strongly scattering or absorbing tissue. To address this problem, it can be combined with tissue clearing methods that homogenize the optical properties of the specimen which in turn reduces scattering. To allow light-sheet imaging of large fixed samples, they can be processed using tissue clearing methods which reduce scattering by homogenizing the optical properties of the specimen.

This thesis presents two projects aimed at making microscopy with optical sectioning more accessible and cost-efficient. The first project demonstrates the utility of a femtosecond semiconductor disk laser (SDL) for multiphoton microscopy for *in vivo* imaging. The second project introduces the mesoscale selective plane illumination microscopy (mesoSPIM) initative, an open hardware project aimed at providing the imaging community with versatile light-sheet microscopes for imaging cleared tissue.

The first chapter provides a general introduction to the history of tissue sectioning in the pursuit of the creation of better anatomical reconstructions of tissue and introduces a variety of optical sectioning methods, including confocal, multiphoton, and light-sheet microscopy.

The second chapter contains a published manuscript on my demonstration experiments with the femtosecond semiconductor disk laser (SDL). The laser utilized in this study generates 170-fs pulses in the microscope focus at a center wavelength of 1027 nm with a repetition rate of 1.63 GHz and features a very compact and simple cavity design. I demonstrate the suitability of this laser for *in vivo* multiphoton imaging in both Drosophila larvae and mice for a variety of fluorophores (including mKate2, tdTomato, and Texas Red) and for endogenous second-harmonic generation in muscle cell sarcomeres. In addition, recordings of neuronal activity using the calcium indicators OGB-1 and R-CaMP1.07 in the neocortex of mice are presented. Taken together, these results

establish femtosecond semiconductor disk lasers as promising and cost-efficient alternative laser sources for multiphoton microscopy.

The third chapter acts as an introduction to tissue clearing and light-sheet microscopy. It contains an overview of a wide variety of tissue clearing methods ranging from techniques based on organic solvents to methods utilizing hydrophilic reagents. In addition, I provide an overview of the fundamentals and applications of light-sheet microscopy and introduce design options to construct instruments for cleared samples.

The fourth chapter contains an unpublished manuscript on the mesoSPIM instrument. The microscope is designed to allow low-resolution overview imaging of whole cleared mouse brains within minutes. To achieve this, it utilizes a technique called axially scanned light-sheet microscopy (ASLM) which allows uniform axial resolution across a whole-brain field-of-view. Here, I demonstrate the compatibility of the mesoSPIM with all major types of clearing techniques and show that it allows imaging of a whole cleared mouse central nervous system without remounting or cutting the sample.

The last chapter discusses how the imaging capabilities presented in the previous chapters are being transitioned into biological applications and provides an outlook of possible extensions and improvements of the mesoSPIM.

Contents

List of figures

List of tables

The next generation of "scientific zoologists" will only know cross sections and stained tissues, but neither the animal nor its mode of life!

Ernst Haeckel to Theodor von Siebold: *Letter, March 5th, 1881*

1

Introduction

In the second half of the 19th century, microscopy and sample preparation had progressed considerably from their roots in the 17th century when Anthony van Leeuwenhoek and Robert Hooke made their discoveries (Leeuwenhoek, 1677; Hooke, 1665). High-quality compound microscopes were becoming available and in 1848, the first microtome for animal tissue was designed (Bracegirdle, 1981). In the same period, staining techniques evolved substantially – in 1863, the first hematoxylin stain was reported (Waldeyer, 1863) which was later developed into the hematoxylin and eosin (H&E) stain (Wissozky, 1877) still used in modern histopathology. Camillo Golgi discovered his silver nitrate method in 1873 (Golgi, 1873) and by the 1880s, tissue sectioning methods were commonplace (Bracegirdle, 1991). Sectioning and staining rendered previously indiscernible anatomical features accessible to light microscopy and allowed to place their structure and morphology into the context of the surrounding tissue. Before, light scattering and absorption limited observations to small or highly transparent specimens.

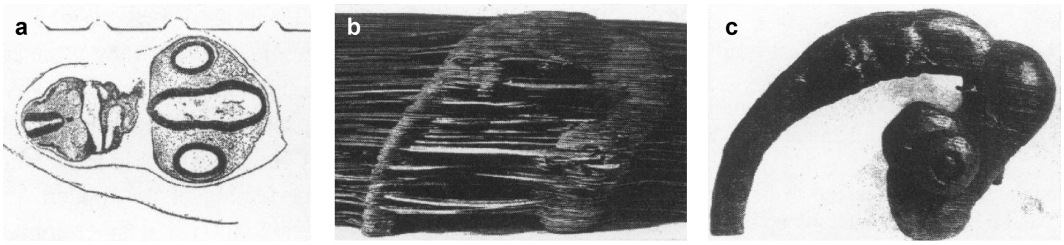

Figure 1.1: From cross sections to wax models. By transferring the outline of hand-drawn cross-sections (a) onto thin wax plates (b), an accurate magnified model of a lizard embryo can be assembled (c). The four indentations visible in the cross section serve as guides to align the wax plates relative to each other. After assembly and smoothing the model was painted. Figure adapted from Peter (1906) and Hopwood (1999).

The rise of the microtome also marked a change in how research in zoology, physiology, and embryology was conducted: Experimenters shifted away from observing the animal in its environment and started to perform extensive histological studies. This lead to older zoologists lamenting (like Haeckel in the quotation above) that their students were alienating themselves from their subject by mindless sectioning and could no longer visualize the animal as a whole (Russell, 1916). One of Haeckels main scientific adversaries, Wilhelm His* envisioned tissue slicing as the way forward towards a better understanding of anatomy and eventually physiology (Hopwood, 1999): His contrasted Haeckels phylogenetics with a mechanistic view of embryology and saw the major advantage of the microtome he designed in that it made serial sectioning possible (His, 1870). From the sections he proceded to assemble detailed wax models of chicken and human embryos (Hossfeld et al., 2012). He also designed an "embryograph" (His, 1880), a combination of a macroscope and a camera lucida, which allowed him to speed up the drawing of embryo cross-sections for later transfer onto wax plates (Figure 1.1). Ideally, the same embryo would provide both transversal and longitudinal sections for this procedure – however, no embryo could be sliced twice. His worked around this problem by inventing a method for "projective construction" which allowed him to painstakingly reconstruct the orthogonal view from a set of sections. The models created with this method were not just three-dimensional illustrations, His considered the very process of crafting models as an aid in understanding the biomechanics

*His famously disputed the truthfulness of the embryo drawings Haeckel used to underline his theory of phylogenetics.

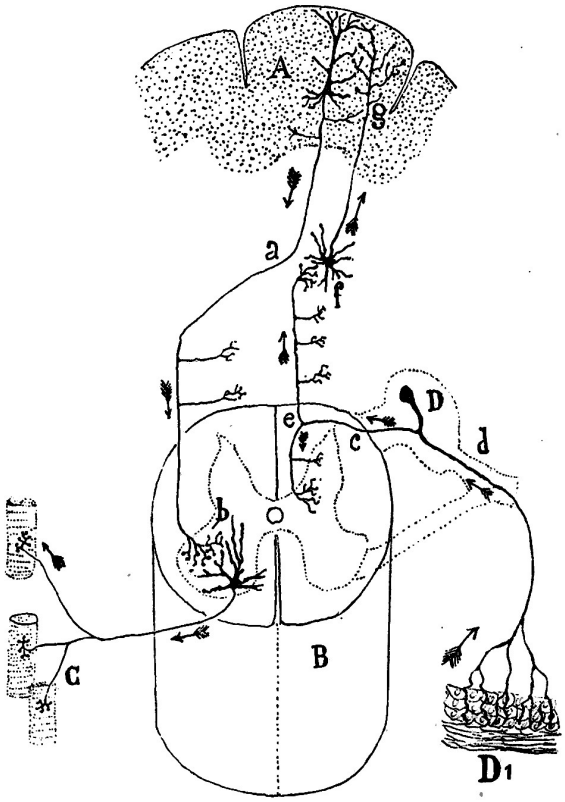

Figure 1.2: The sensorymotor loop as drawn by Cajal in 1893. The sensorymotor loop as drawn by Cajal in 1893: Sensory inputs from the skin (D1) are sent to the cortex (A) via the spinal cord (B) and motor commands are relayed to muscles (C) via descending pathways (a) (Cajal, 1893).

of development (Hopwood, 1999). With improvements in fixation techniques, such modelling techniques became more widespread and by the end of the 19th century, were a common teaching tool in universities to illustrate the stages of development (de Chadarevian and Hopwood, 2004).

Beyond creating physical artifacts, the process of modelling also involves the creation of a mental picture to distill observations into a common framework. This was the approach Ramon y Cajal took when he worked out the neuron doctrine in the late 19th century – with the word "neuron" coined by von Waldeyer (Waldeyer, 1863). Importantly, when creating summary diagrams such as the one in Figure 1.2, Cajal had to piece together observations gained from hundreds of tissue slices to arrive at a model (Cajal, 1893) – but he never had access to a technique that allowed him to visualize the morphology of a neuron throughout the whole body of an animal.

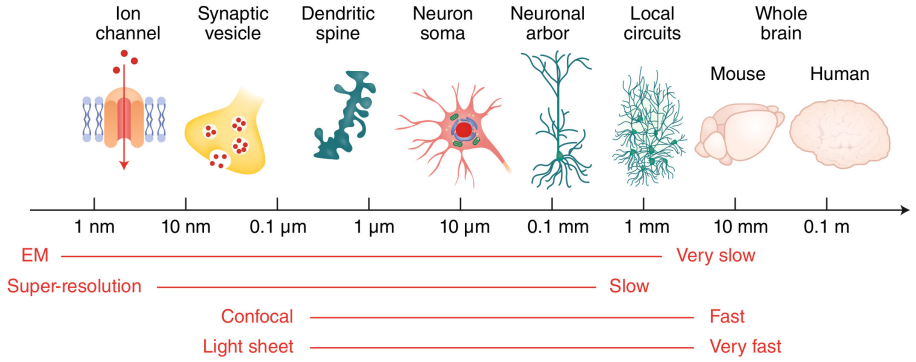

Figure 1.3: Spatial scales in brain mapping. The spatial levels of investigation in neuroscience span 9 orders of magnitude. Electron microscopy (EM) and superresolution methods are capable of resolving very fine details, but suffer from low throughput on a whole-brain level. Optical imaging techniques such as confocal and light-sheet microscopy are faster, but are limited in resolution. Figure adapted from Yang and Yuste (2019).

In fact, it took almost a century after Cajal's work for the first comprehensive wiring diagram of an animal to be published (White et al., 1986) – in the form of the connectome of the flatworm *Caenorhabditis elegans* (Emmons, 2015) by the group of Sydney Brenner. For this undertaking, a serial sectioning approach combined with electron microscopy (EM) had to be used – which to this day is the only technique capable of "dense" reconstructions that cover all cells in a volume (Kleinfeld et al., 2011). The reason lies in the intricate way structure and function in nervous systems are linked across scales (Yang and Yuste, 2019) (Figure 1.3). As synaptic transmission happens on nm-scales and as axons have lengths of up to many centimeters in mice and up to a meter in humans, only electron microscopy has the necessary resolution and spatial coverage to unequivocally identify synaptic connections and trace their morphology. If, however, only a subset of neurons or subcellular structures is of interest, optical methods such as superresolution microscopy can be used (Sigal et al., 2018). Some optical microscopy methods are also capable of "optical sectioning" – instead of mechanically slicing the sample, the microscope is able to create such sections with optical methods which speeds up volume acquisitions. When the worm connectome project of Sydney Brenner reached its conclusion in the late 1980s, one of the key team members, John G. White, also had a pioneering role in bringing the first widely known imaging technique with optical sectioning into biological research: Confocal microscopy (Amos and White, 2003).

1.1 Fluorescence microscopy with optical sectioning

In modern biology, the most common microscopy modality uses fluorescent molecules to tag and observe cellular structures of interest. Fluorescence is a form of luminescence involving the absorption and subsequent emission of light by a molecule. After absorption of a photon, the molecule is excited to a higher-order vibrational state, but quickly gives off excess energy as heat to reach the lowest excited state (Figure 1.4). When transitioning back to the electronic ground state, the molecule emits a photon with lower energy than the excitation photon which shifts the emission spectrum towards the red – an effect known as Stokes shift. A normal absorption and emission cycle involves singlet states and happens on timescales of nanoseconds. Out of the excited singlet state, the fluorophore can also make a transition to a low triplet state via inter-system crossing. As radiative triplet-singlet transitions are forbidden, this state can have a very long lifetime. Triplet states form a major photobleaching pathway, which describes the loss of active fluorophores over time. To use fluorescence as a modality for microscopy, the excitation and emission light have to be separated by filters or dichroic mirrors. In the best case, this approach allows single fluorescent molecules to be detected (Ha and Tinnefeld, 2012), a feat only possible because the Stokes shift allows the weak emission light to be spectrally separated from the strong illumination radiation.

As PHOTOBLEACHING involves the production of reactive oxygen species that can damage living cells and the degradation of the fluorophore, fluorescence imaging can affect sample health. There is a trade-off in fluorescence microscopy between the signal-to-noise-ratio (SNR) of the acquired images, temporal resolution, spatial resolution, and the well-being of the specimen (Scherf and Huisken, 2015): The more fluorescence photons are emitted, the more photobleaching events take place and – as each fluorophore can only undergo a limited number of absorption/emission cycles – the sooner the available photon budget is depleted. Ideally, in vivo imaging techniques should be minimally invasive to reduce the impact of photobleaching and phototoxicity in general (Laissue et al., 2017).

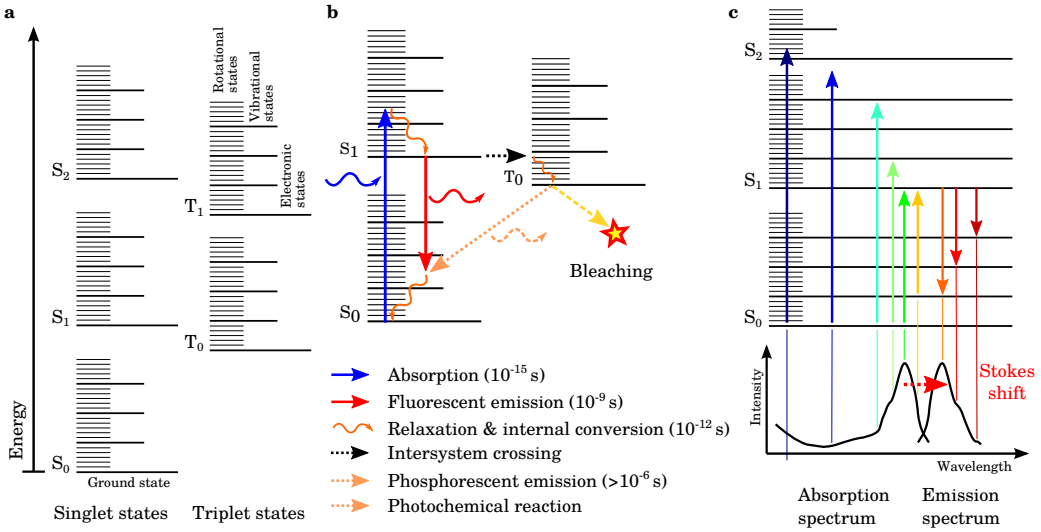

Figure 1.4: Jablonski diagram of a typical fluorophore. a) Arrangement of different energy levels, each having distinct electronic, vibrational, and rotational states. b) Electronic transitions involved in fluorescence with typical timescales. c) Composition of the absorption and emission spectrum out of a superposition of the elementary transitions involved in fluorescence. Figure adapted from (Voigt, 2014).

The most basic form of a fluorescence microscope broadly illuminates the sample through a microscope objective and detects the emitted and filtered light using a camera through the same objective. As this widefield microscope excites fluorophores in- and outside of the focal plane, the resulting images suffer from out-of-focus background (Figure 1.5).

The confocal microscope solves this problem by confining the detection volume: Instead of widefield excitation, the sample is illuminated by a laser beam focused to a single spot and a pinhole positioned in a conjugate focal plane to the sample rejects emission photons not originating from a small volume around the excitation focus (Minsky, 1988). By reducing the size of the pinhole, the thickness of the optical section can be lowered to diffraction-limited conditions at the expense of SNR. The pinhole also rejects photons which originate from the excitation focus, but get scattered on the way out of the sample. This allows a confocal microscope to image deeper than a widefield instrument. To acquire an image, the excitation beam can be raster-scanned across the sample. However, to create a single image, a confocal microscope has to illuminate the whole sample which leads to photobleaching both of in-focus and out-of-focus regions of the sample.

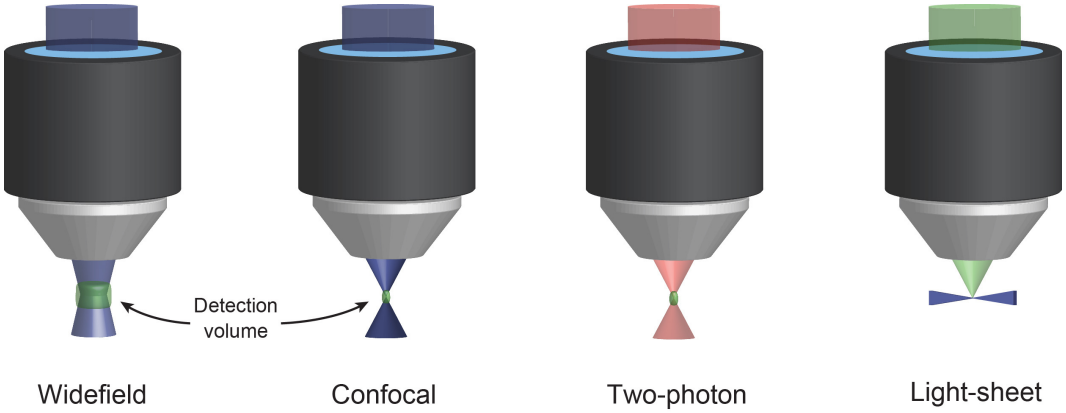

Figure 1.5: Microscopy techniques with optical sectioning A widefield fluorescence microscope does not have optical sectioning, the resulting images contain out-of-focus background. In a confocal microscope, the out-of-focus signal is rejected using a pinhole acting as a spatial filter which shrinks the detection volume. In two-photon microscopy, out-of-focus background is not generated as only in the focus near-infrared laser intensities are sufficiently high to excite fluorophores. In light-sheet microscopy, the sample is illuminated from the side which avoids the generation of out-of-focus background signal.

If the sample needs to be scanned faster than feasible with a single beam (shorter signal collection or "dwell" times for each pixel lead to lower SNR), scanning can be done with many excitation spots in parallel, for example in a spinning-disk confocal microscope (Egger and Petráń, 1967).

A different method to achieve optical sectioning is to use a nonlinear excitation process, for example two-photon absorption (2PA): If a fluorophore is irradiated with near-infrared light with twice the wavelength of standard single-photon illumination, there is a vanishingly small probability that two photons will be absorbed at the same time and drive the fluorophore into the excited state. To increase the probability of this process, high illumination intensities are necessary which are typically reached by concentrating the excitation photons both in time by femtosecond laser pulses and in space by using a high numerical aperture (NA) objective. As two photons need to take part for a 2PA-event to happen, the intensity of the emitted fluorescence depends on the square of the illumination intensity. This nonlinearity confines the excitation volume both laterally and axially to a small spot and leads to intrinsic optical sectioning. Two-photon microscopy was first demonstrated in 1990 by Denk and colleagues (Denk et al., 1990) and has been widely

adoped for deep imaging *in vivo* (Helmchen and Denk, 2005). Two-photon microscopy is able to image deeper in scattering tissue as the near-infrared excitation light is scattered and absorbed less. In addition, the confinement of the excitation spot to a small volume means that even when emission photons are scattered on their way out of sample, they can still be attributed to their point of origin. To create an image with a two-photon microscope, the illumination beam is raster-scanned as in a confocal microscope, but no detection pinhole is required: Instead, a photodetector can collect as many scattered photons as possible from each scanned spot. As the selection rules differ between single and two-photon absorption, two-photon absorption spectra can be substantially different than a scaled version of their single-photon counterpart (Drobizhev et al., 2011). Two-photon microscopy is part of a wide range of nonlinear microscopy methods, a selection of which is outlined in section 1.2.

Two-photon microscopy highlights the value of confining the excitation volume to achieve optical sectioning. Light-sheet fluorescence microscopy (LSFM, Voie et al. (1993); Huisken (2004)) is a technique that uses the same concept in single-photon microscopy: By illuminating the sample from the side with a thin sheet of light, minimal out-of-focus background fluorescence is excited. This method allows rapid acquisition speeds because the point-by-point scanning procedure of a confocal or two-photon microscope can be replaced with a widefield detection path using a camera. Light-sheet microscopy is especially well suited for imaging transparent developing embryos due to its speed and low phototoxicity: As only the focal plane is illuminated, no out-of-plane photobleaching can occur (Huisken and Stainier, 2009; Huisken, 2012). A more detailed overview of light-sheet imaging techniques is given in section 3.2.

All optical sectioning techniques allow the acquisition of three-dimensional datasets by sequentially imaging single planes along the z-axis and mechanically translating either the sample or the excitation focus. Given that no time-consuming mechanical slicing procedure has to be carried out, generating three-dimensional reconstructions with optical sectioning is faster than classical

histology and can be done *in vivo*. The major disadvantage is that all optical methods require a high degree of transparency in the case of single photon microscopes and sufficently low absorption and – to some extent – low scattering in the case of two-photon microscopy. Two-photon imaging can reach imaging depths of up to 1 mm (Theer and Denk, 2006), but for deeper and deeper imaging looses SNR due to increasing background from two-photon absorption at the surface. If imaging depths beyond a millimeter are desired in a fixed sample, tissue clearing methods can be employed (see section 3.1). An alternative is to use a combination of two-photon microscopy and serial sectioning (serial two-photon tomography or STP, Ragan et al. (2007, 2012)), which provided the basis for the mouse mesoscale connectome released by the Allen Institute (Oh et al., 2014). Serial sectioning can also be combined with tissue clearing which is a technique employed by the MouseLight project at Janelia Research Campus (Economo et al., 2016) to study long-range projections in the mouse brain (Winnubst et al., 2019).

1.2 Multiphoton microscopy

Apart from two-photon absorption, other nonlinear interactions of light with molecules exist. An overview is provided in Figure 1.6. These modalities can be grouped into incoherent and coherent processes: In the case of a coherent process, the emitted photon is in phase with the excitation radiaton. Just as in the case of two-photon microscopy, creation of a detectable number of emission photons by driving a nonlinear process in typical microscopy conditions requires very high laser intensities – typically in the MW/cm^2 to GW/cm^2 range. The corresponding average powers are far beyond the damage threshold of biological samples if continous wave (CW) lasers are used (Podgorski and Ranganathan, 2016). Therefore, biological multiphoton microscopy requires pulsed illumination with pico- and femtosecond light sources. During the laser pulse, the instantaneous high laser intensity leads to sufficient nonlinear signal levels and in the interval between pulses, the sample can recover from absorption-induced heating.

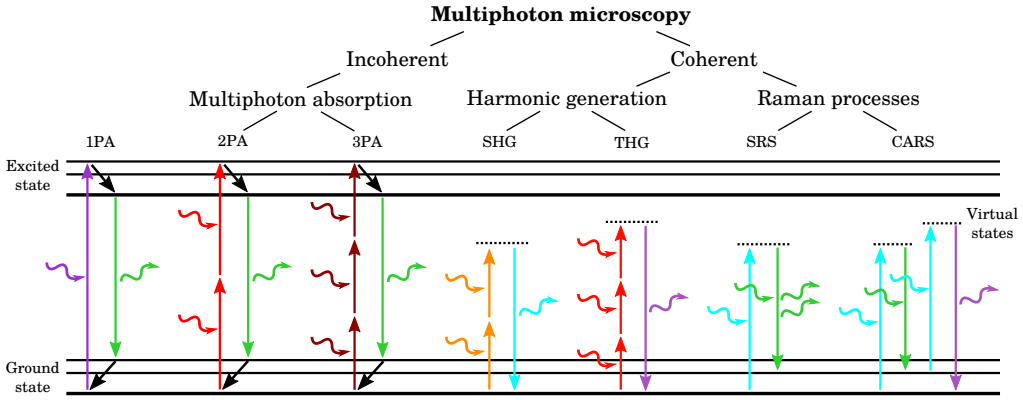

Figure 1.6: Energy diagrams of the most common multiphoton microscopy methods: For comparison, single-photon absorption (1PA) is shown as well. Two- and three-photon absorption (2PA and 3PA) are used to excite fluorescence, second and third harmonic generation (SHG and THG), stimulated Raman scattering (SRS) and coherent anti-Stokes Raman scattering (CARS) are examples of coherent processes. Figure adapted from (Voigt, 2014).

Three-photon microscopy (3PA) was first demonstrated in 1996 (Xu and Webb, 1996), but was not extensively adopted until now as excitation of visible fluorophores requires laser sources in the 1.2-1.6 µm region which were not widely available at the time. After the demonstration of ultra-deep (> 1 mm) structural imaging in the brain of living mice (Horton et al., 2013). 3PA gained more interest. Recently, 3PA was used for functional imaging of hippocampal neurons through the intact cortex (Ouzounov et al., 2017).

Second-harmonic generation (SHG): The focusing of laser pulses on biological non-centrosymmetric structures can lead to second-harmonic generation (Freund et al., 1986). This phenomenon can provide a contrast- forming mechanism without the need to apply exogenous labels. Strong SHG contrast is generated by collagen fibers, in muscle tissue, in the cornea, in cellulose and from microtubules which thus all form ideal samples. It is possible to label certain cellular structures (e.g. membranes) with compounds leading to increased SHG signal using nanoparticles or organic molecules known as harmonophores.

Third harmonic generation (THG): Contrary to SHG, third-harmonic generation (Barad et al., 1997) does not require a non-centrosymmetric structure for signal generation, which allows to image variations in the refractive index in the sample, thus visualizing interfaces like cell membranes. THG generated by typical ultrafast-laser sources in the 0.8-1.0 µm region is emitted in the UV, which is not transmitted very well by standard microscope objectives. Similar to 3PA, specialized sources such as optically parametric oscillators are necessary.

1.3 Design of a two-photon microscope

According to the first paper demonstrating two-photon microscopy (Denk et al., 1990), the two-photon absorption probability p per laser pulse in the focus of a microscope objective can be estimated as (if saturation is neglected):

$$p = \frac{\sigma P_{\text{avg}}^2}{\tau_p f_{\text{rep}}^2} \cdot \left(\frac{\pi \text{NA}^2}{hc\lambda} \right)^2 \tag{1.1}$$

Here, λ is the excitation wavelength, P_{avg} is the average illumination power. f_{rep} is the repetition rate and τ_p is the pulse length of the laser. σ is the two-photon cross-section which is usually expressed in Göppert-Mayer (GM) units in honor of Maria Göppert-Mayer, who provided the first quantum-mechanical description of two-photon excitation in the 1930s (Göppert-Mayer, 1931): 1 GM = $1 \cdot 10^{-50} \text{cm}^4$ s/Photon/Molecule.

The collected fluorescence signal S from a single pixel (measured as the number of detected photons) can then be estimated as:

$$S = p \cdot \eta_{\text{em}} \cdot \eta_{\text{det}} \cdot f_{\text{rep}} \cdot \tau_{\text{dwell}} \cdot N \tag{1.2}$$

Here, η_{em} is the emission efficiency from the fluorophore, η_{det} is the detection efficiency of the microscope, τ_{dwell} is the pixel dwell time and N is the number of fluorescent molecules in the focal volume. Taken together, this means that $S \propto \frac{P_{\text{avg}}^2}{f_{\text{rep}} \tau_p}$. The laser source thus forms the key

component of the microscope – and by achieving the shortest possible pulse length τ_p at high average power P_{avg}, the signal can be increased. The pulse energy and peak power of a pulsed laser are given by:

$$E_p = \frac{P_{\text{avg}}}{f_{\text{rep}}} \tag{1.3}$$

$$P_{\text{Peak}} = \begin{cases} 0.88\frac{E_p}{\tau_p} & \text{for Pulses with sech}^2\text{-profile} \\ 0.94\frac{E_p}{\tau_p} & \text{for Pulses with Gaussian profile} \end{cases} \tag{1.4}$$

Squared hyperbolic secant pulses (sech^2) are often produced by ultrafast lasers oscillators operating in the soliton modelocking regime (Mollenauer and Stolen, 1984). The process by which ultrashort laser pulses are created is known as modelocking (Saleh and Teich, 2007): In a laser cavity, a multitude of longitudinal modes can exist. If all modes are made to oscillate in phase, constructive interference results in a single laser pulse oscillating in the cavity. This can be achieved by introducing a loss mechanism that leads to higher losses for continuous wave (CW) operation than for laser pulses. Possible mechanisms are either active, for example by using an acousto-optic modulator (AOM) to induce a time-varying loss modulation or passive, for example by using a semiconductor saturable absorber mirror (SESAM). A SESAM introduces higher losses for CW radiation as an intense laser pulse is able to saturate the absorption transition which allows the bulk of the pulse to be reflected.

The time-bandwidth product is used to compare the spectral bandwidth[†] $\Delta\lambda$ (or $\Delta\nu_p$) and pulse duration τ_p of measured pulses to the physical limit (sech^2-pulses):

$$\Delta\nu_p \cdot \tau_p = \frac{c \cdot \Delta\lambda}{\lambda^2} \cdot \tau_p = 0.3148 \tag{1.5}$$

The corresponding value for Gaussian pulses is 0.44. A pulse with parameters close to the best possible values is said to be transform-limited. Standard two-photon microscopes utilize Titanium:Sapphire laser with pulse lengths of 100 fs.

[†]In laser engineering, both are usually defined as full-width at half-maximum (FWHM).

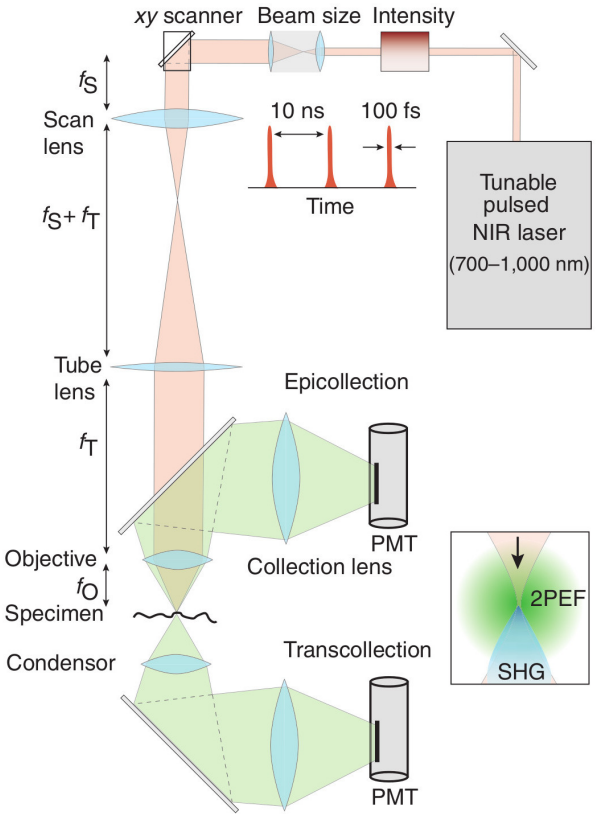

Figure 1.7: Layout of a two-photon microscope. Light from a ultrafast NIR laser source is regulated in its intensity and send to the scan mirrors of the laser scanning system. A scan lens and a tube lens act as a telescope and direct the laser beam to the objective. Two-photon excited fluorescence (2PEF) can be collected both from above and below the focal plane, depending on the accessibility of the sample. Light emitted from second harmonic generation (SHG) is predominantly detected in the forward direction. Figure adapted from (Helmchen and Denk, 2005).

To build a two-photon microscope, the laser needs to be combined with means for intensity adjustment (i.e. a Pockels cell), beam expansion optics and a laser scanning system (Figure 1.7). A combination of a scan- and tube lens then directs the beam into a microscope objective and onto the sample. By collecting all the emitted light with a photomultiplier, an image can be created.

The following chapter introduces semiconductor disk lasers as another type of femtosecond lasers and demonstrates their suitability for multiphoton imaging.

When God said "let there be light" he surely must
have meant perfectly coherent light.

(Lamb et al., 1999)

2

Multiphoton imaging with semiconductor disk lasers

2.1 Introduction

The first experiments demonstrating two-photon microscopy (Denk et al., 1990) used a dye laser based on colliding pulse mode-locking (CPM), a form of passive mode-locking which is rarely used today. In a CPM laser, a saturable absorber – which can be a dye cell or a semiconductor mirror (Keller et al., 1996) – is placed in the ring cavity in addition to the gain medium. Counter-propagating pulses arrive in the saturable absorber at the same time and drive the majority of molecules into an excited state due to the instantaneous high light intensities. In this state, the absorber material becomes transparent as there are less and less molecules in the ground state. This leads to a cavity in which intense pulses experience lower roundtrip losses than countinous-

wave (CW) emission which leads to mode-locked operation. While CPM lasers were the first laser sources to reach pulse lengths of less than 100 fs (Fork et al., 1981) and later <30 fs by intracavity dispersion control (Valdmanis et al., 1985), they were cumbersome to use due to the presence of two dye cells with circulating gain and absorber media.

After the discovery of self-mode-locked Titanium-Sapphire (Ti:Sapphire) lasers (Spence et al., 1991) – a principle of operation later understood to be based on Kerr lensing (Keller et al., 1991) – Ti:Sapphire quickly became the gain medium of choice for two-photon microscopy. It has a wide emission spectrum centered at 790 nm with a full width at half maximum (FWHM) gain bandwidth of 230 nm (Keller, 2007) which leads to a tuning range of 690-1040 nm. With the advent of high-power diode-pumped solid state (DPSS) lasers in the mid-1990s such as frequency-doubled Nd:Glass oscillators, femtosecond Ti:Sapphire lasers became low-maintenance sources for microscopy as the multi-watt argon lasers in use up to that point could be replaced with a solid state source. Typical modern Ti:Sapphire sources have an average power of 3.5W, pulse energies of 20-40 nJ, pulse durations of 100 fs and a repetition rate of 80 MHz. While in last decade, laser sources based on optical fibers saw widespread adoption (Fermann and Hartl, 2013; Xu and Wise, 2013), they do not offer the wavelength tuning range of Ti:Sapphire lasers but are instead limited to a single wavelength – most commonly in the 1040-1080 nm range. Only recently, turn-key optically parametric oscillators (OPOs) with tuning ranges from 680-1300 nm such as the Spectra-Physics "InSight" or the Coherent "Chameleon Discovery" became an additional option for nonlinear microscopy, albeit at very high costs.

To this day, the most expensive component of a two-photon microscope is still the laser source. While with fiber lasers, low power ($\approx$ 100 mW) sources in the range of 10.000-20.000 USD have become available, it would be highly beneficial to have a wider selection of wavelengths. One option is to use semiconductor disk lasers (SDL) (Giesen et al., 1994) which provide high beam quality directly from an oscillator and are based on a very simple cavity layout. Recently, such laser

sources have been demonstrated with pulse lengths of 100 fs (Waldburger et al., 2016). Owing to their high repetition frequency and low-noise performance, mode-locked SDLs are ideal for frequency combs (Zaugg et al., 2014).

To TEST THE SUITABILITY of the current generation of SDLs for multiphoton microscopy, we used a laser prototype created by Florian Emaury in the Ultrafast Laser Physics group of Ursula Keller at ETH Zurich. I was responsible for the conceptualization, experimental design, and data collection of the study. I wrote the first draft of the manuscript and refined it with input from my coauthors, prepared figures and was strongly involved in data analysis. The manuscript was published by Biomedical Optics Express in July 2017*.

*Biomedical Optics Express 8(7) 3213-3231 (2017), https://www.osapublishing.org/boe/abstract.cfm?uri=boe-8-7-3213

2.2 Multiphoton in vivo imaging with a femtosecond semiconductor disk laser

Fabian F. Voigt[*†], Florian Emaury*[*], Philipp Bethge, Dominik Waldburger, Sandro M. Link, Stefano Carta, Alexander van der Bourg, Fritjof Helmchen, and Ursula Keller*

2.2.1 Abstract

We use an ultrafast diode-pumped semiconductor disk laser (SDL) to demonstrate several applications in multiphoton microscopy. The ultrafast SDL is based on an optically pumped Vertical External Cavity Surface Emitting Laser (VECSEL) passively mode-locked with a semiconductor saturable absorber mirror (SESAM) and generates 170-fs pulses at a center wavelength of 1027 nm with a repetition rate of 1.63 GHz. We demonstrate the suitability of this laser for structural and functional multiphoton in vivo imaging in both Drosophila larvae and mice for a variety of fluorophores (including mKate2, tdTomato, Texas Red, OGB-1, and R-CaMP1.07) and for endogenous second-harmonic generation in muscle cell sarcomeres. We can demonstrate equivalent signal levels compared to a standard 80-MHz Ti:Sapphire laser when we increase the average power by a factor of 4.5 as predicted by theory. In addition, we compare the bleaching properties of both laser systems in fixed Drosophila larvae and find similar bleaching kinetics despite the large difference in pulse repetition rates. Our results highlight the great potential of ultrafast diode-pumped SDLs for creating a cost-efficient and compact alternative light source compared to standard Ti:Sapphire lasers for multiphoton imaging.

2.2.2 Introduction

Over the past decades, multiphoton microscopy (MPM) methods have been widely adopted in biomedical research owing to their combination of high spatial resolution, intrinsic optical sectioning and the ability to perform deep imaging in scattering samples (Helmchen and Denk,

[†]"*" indicates equal contributions.

2005; Zipfel et al., 2003). Nonlinear imaging techniques such as two-photon microscopy (Denk et al., 1990), second-harmonic generation (SHG, Freund et al. (1986)), and nonlinear Raman microscopy offer a wide variety of label-dependent and label-free contrast mechanisms to study fixed and living tissues. While imaging capabilities are constantly improving with the introduction of new labeling methods (Miyawaki and Niino, 2015) and novel scanning approaches (Wilt et al., 2009), the cost of such microscopes is still prohibitively high for many laboratories. A considerable fraction of the budget for a multiphoton system has to be allocated to acquire an expensive ultrafast laser source such as a tunable Ti:Sapphire laser. Typical commercial Ti:Sapphire lasers acquired for this application generate $\approx$ 1.5 to 3.5 W of average power at the gain maximum of around 800 nm. However, for most experiments, only a small fraction is used to illuminate a biological sample. For example, when imaging the superficial layers of the murine neocortex with a single scanned excitation spot, an average power between 10 mW (for superficial layer 2/3) and 100 mW (for deep layer 5) is sufficient for functional recordings with the calcium indicator GCaMP6 (Wang et al., 2014a). As the transmittance of the microscope's optical path can be optimized to >50%, considerable potential exists for less expensive laser sources with a few hundreds of mW output power and with a center wavelength close to the absorption peak of selected fluorophores (Figure 2.1).

An ideal ultrafast laser for MPM should be able to efficiently excite a variety of fluorophores, generate sufficiently short pulses, and provide good beam quality. In addition, a small footprint to ease integration into a microscope system, maintenance-free operation, and an affordable price are highly beneficial. The pulse duration τ needs to be optimized as there is a trade-off between the generated two-photon signal which scales theoretically as τ^{-1} (experimentally $\tau^{-0.85}$) (Tang et al., 2006), the pulse broadening which scales as τ^{-1} (Saleh and Teich, 2007), and the photodamage effects which scales as $\tau^{1.5}$ (Hopt and Neher, 2001). In practice, most imaging studies use a pulse duration in the range of 100-200 fs as a compromise. Recently, Ti:Sapphire laser technology was improved towards higher efficiency (Antal and Szipőcs, 2012) and by novel direct-diode pumping schemes using high-power visible semiconductor lasers (Durfee et al., 2012; Gürel et al.,

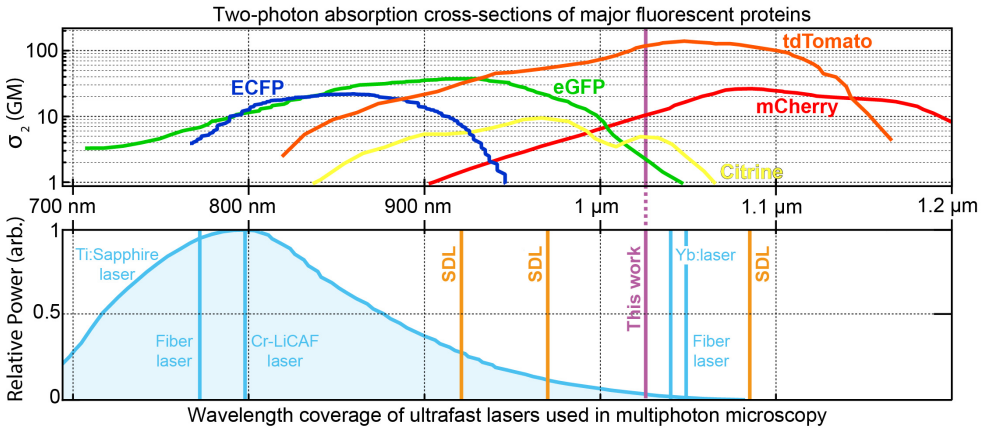

Figure 2.1: Overview of the two-photon absorption cross-sections of various fluorescent proteins used in two-photon microscopy combined with the spectral coverage of existing ultrafast lasers. Ti:Sapphire lasers have a large tuning range of >300 nm. In contrast, other commercial ultrafast lasers (blue lines) cannot be tuned to match the absorption peaks of dyes. Ultrafast semiconductor disk lasers (SDLs, orange lines) have the potential to become less expensive sources and can be designed with emission wavelengths between 650 and 2800 nm (typical lasers with a center wavelength at 920-nm, 970-nm and 1080-nm are shown here, but more options are possible). The SDL laser presented in this paper operates at 1027 nm (indicated as "This work")

2015). Such a Ti:Sapphire laser was demonstrated to be a suitable source for MPM (Young et al., 2013), but despite the lower cost and improvements in compactness, commercial impact is still limited. Fiber lasers (Tang et al., 2009; Perillo et al., 2016), Yb:KGd$(WO_4)_2$ (Sheetz et al., 2008), Cr:LiSrAlFl (Svoboda et al., 1996) or Cr:LiSAF (Robertson et al., 1997) crystals in a bulk configuration, or Cr:Forsterite lasers operating at 1230 nm (Chu et al., 2001; Liu et al., 2001) are interesting low-cost alternatives in MPM applications. However, the center wavelengths of these lasers limit their operation to only a few discrete spectral regions. Access to a wider spectrum can be obtained by spectral broadening with a tunable cavity (Resan et al., 2014), but at the expense of a significant increase in complexity for the laser source. Semiconductor lasers are attractive for biological applications as the center wavelength can be optimized towards desired values by bandgap engineering. In microscopy, this approach has already been commercialized successfully for continuous-wave (cw) lasers, with a wide available range of optically pumped semiconductor lasers at center wavelengths ranging from the UV to the mid-IR (Figure 1.12 in (Kuznetsov, 2010)). During the past decades various concepts for pulsed semiconductor lasers suitable for MPM were demonstrated,

such as gain-switched semiconductor lasers (Yokoyama et al., 2006), external cavity mode-locked laser diodes (Kuramoto et al., 2007; Wang et al., 2014b), or mode-locked laser diodes (Kusama et al., 2014). These pulsed lasers, however, all rely on transverse emitters and in most cases on an additional amplifier, producing rather long pulses in the 1-20 ps range with rather poor beam quality. This requires higher average power when used in nonlinear microscopy. In contrast, a surface emitting semiconductor laser provides an ideal Gaussian beam and optical pumping allows for power scaling. The interaction with the gain medium is perpendicular to the gain layers and much shorter than the cavity length which leads to excellent noise performance (Mangold et al., 2014). In analogy to solid-state thin-disk lasers, this type of laser is also referred to as semiconductor disk laser (SDL, Giesen et al. (1994)). Mode-locked SDLs combine simple cavity design, excellent beam quality, and scalability of the production process. The laser cavity can be embedded directly on the semiconductor chip creating a Vertical Cavity Surface Emitting Laser (VCSEL), which is employed in lighting and telecommunications (Michalzik, 2012). With electrical or optical pumping high output powers can be achieved directly from the oscillator.

A vertically emitting semiconductor chip with an external cavity leads to a Vertical External Cavity Surface Emitting Laser (VECSEL; Figure 2.2 (A)), yielding better beam quality ($M^2 < 1.05$ in both axes) and higher power compared to VCSELs. Moreover, this approach allows for an intracavity semiconductor saturable absorber mirror (SESAM) for passive pulse formation (Tilma et al., 2015; Hoogland et al., 2000; Keller and Tropper, 2006) (Figure 2.2(A)). Since the first demonstration of a SESAM-mode-locked VECSEL in 2000 (Hoogland et al., 2000), the laser performance has been drastically improved. Mode-locked VECSELs have been operated from 650 nm to 2800 nm (Tilma et al., 2015; Gaafar et al., 2016), with the best results achieved in the 900-1100 nm region due to lattice-matched materials for high-quality distributed Bragg reflectors (DBRs) and due to low-cost high-power pump diode arrays operating at 808 nm. Figure 2.2 (B) illustrates the evolution of the shortest pulse durations of fundamental SESAM-mode-locked VECSELs operating around 1000 nm during the last two decades (Hoogland et al., 2000; Haring et al., 2001; Garnache et al., 2002; Hoogland et al., 2005; Wilcox et al., 2010). While several other mode-

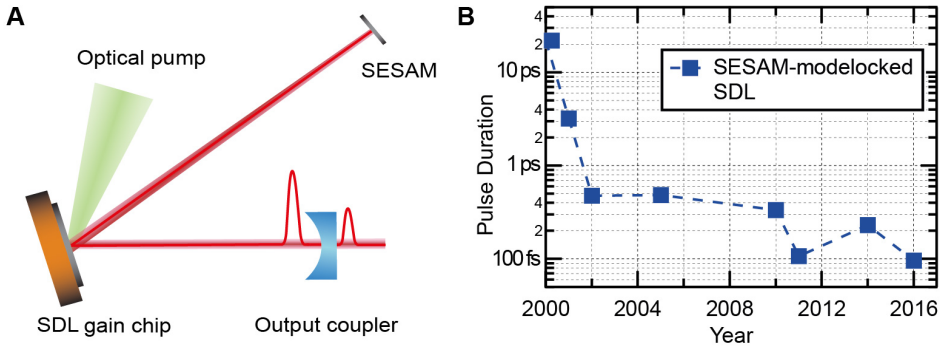

Figure 2.2: Overview of semiconductor disk lasers (SDL). A) Typical laser cavity of a pulsed Semiconductor Disk Laser (SDL) or Vertical External Cavity Surface Emitting Laser (VECSEL) consisting of an optically pumped gain chip, a SESAM to enable pulse formation with passive mode-locking and an output coupler. The cavity length is set to reach a pulse repetition rate of 1-2 GHz with an (unfolded) length of 10-15 cm. B) Overview of the evolution of pulse durations from SESAM-mode-locked SDLs around 1000 nm since the first demonstration in 2000, recently reaching sub-100 fs (Waldburger et al., 2016).

locking techniques were demonstrated, SESAM- mode-locked VECSELs are currently the most promising approach to reach shorter pulses with the important milestone of sub-100 fs achieved in 2016 (Waldburger et al., 2016). The use of a SDL for MPM was first proposed by Girkin and Wokosin in 2001 (Girkin and Wokosin, 2001), who also noted that an array of SDLs operating at different wavelengths might constitute a cost-efficient replacement of a tunable Ti:Sapphire source. In 2011, a pulsed SDL was used for MPM for the first time (Aviles-Espinosa et al., 2011). This laser operated at 500 MHz with 1.5-ps long pulses at a center wavelength of 965 nm and an average output power of 287 mW. It allowed imaging of neuronal processes and cell bodies in Caenorhabditis elegans (C. elegans) expressing Green Fluorescent Protein (GFP). While this first demonstration showed the potential of ultrafast SDLs, the long pulses limited the practical use of such a laser compared to existing technology. In 2013, a VECSEL with a peak power of 4.35 kW (Wilcox et al., 2013) and a pulse duration of 450 fs was developed and foreseen to be applicable for MPM (Mirkhanov et al., 2016). With the recent progress in the laser technology (Waldburger

et al., 2016), the pulse length of ultrafast SDLs has become more comparable with Ti:Sapphire lasers commonly used for MPM. In this paper, we demonstrate the use of the latest generation of mode-locked SDLs for a variety of MPM imaging applications. We describe the microscope setup and a novel ultrafast SDL that generated pulses as short as ≈100 fs and 145 mW of average power. At a center wavelength of 1027 nm, our laser delivers 72 mW of average power and 170 fs pulses below the objective. We compare the two-photon excited fluorescence signal and bleaching dynamics generated with the SDL to data recorded from the same samples with a standard Ti:Sapphire laser. We then proceed to present a number of in vivo imaging demonstrations, ranging from two-photon and SHG imaging in Drosophila larvae to structural and functional imaging in the living mouse brain using acute or chronic cranial window preparations. With this work, we demonstrate for the first time — to the best of our knowledge — that a state-of- the art femtosecond SDL is a compelling laser source for MPM applications in neuroscience and biology in general. Given the lower complexity and thus lower cost of SDLs compared to Ti:Sapphire lasers, we believe that SDLs will pave the way towards a wider adoption of MPM in research and medical applications.

2.2.3 Multiphoton imaging at high laser repetition rates

As noted by Girkin and Wokosin (Girkin and Wokosin, 2001), due to the short gain carrier lifetime in semiconductors passively mode-locked SDLs typically operate at repetition rates in the gigahertz domain compared to the approximately 80-MHz repetition rate provided by Ti:Sapphire lasers. As the two-photon fluorescence signal scales as $S \propto P_{avg}^2/(\tau \cdot f_{rep})$ (Denk et al., 1990), increasing the repetition rate f_{rep} n-fold requires scaling the average excitation power P_{avg} by $\sqrt{n}$ in order to keep the emitted fluorescence signal constant (see Figure 2.3).

High average power may lead to heating-induced damage of the sample, which has to be prevented for imaging in living tissue. Especially during functional imaging in the mouse brain (Podgorski and Ranganathan, 2016), power levels have to be closely monitored. In contrast to heating due to linear absorption, photodamage in two-photon microscopy has been reported to scale as

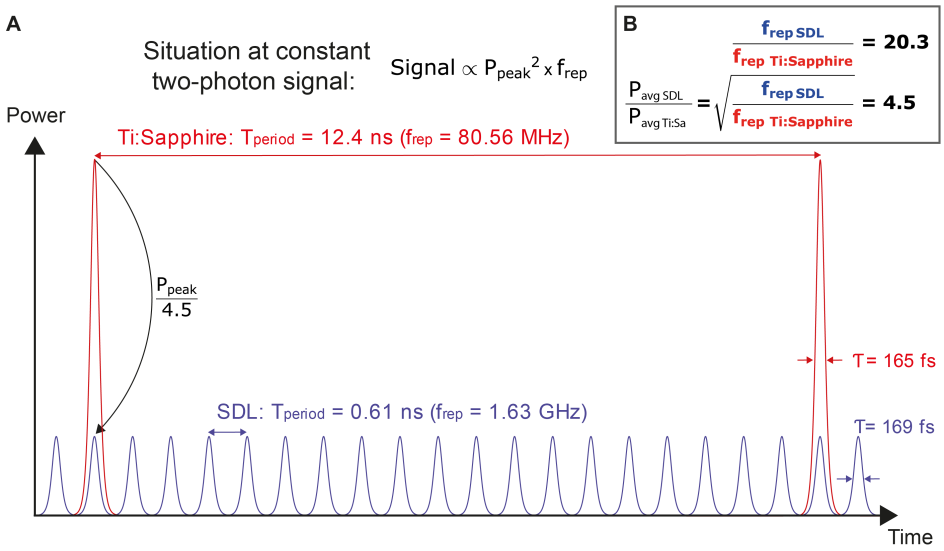

Figure 2.3: Multiphoton microscopy (MPM) imaging at high repetition rates. A) Overlay of the pulse trains from a Ti:Sapphire laser and a SDL set to generate the same two-photon excited fluorescence signal at comparable pulse duration, center wavelength, and optical resolution. We use the parameters of the two lasers compared in this study as examples. B) In order to achieve constant signal, the ratio of average powers has to be set to the square root of the ratio of repetition rates.

$D \propto P_{\text{avg}}^{\beta}$ with $\beta > 2$ (Hopt and Neher, 2001). This strong nonlinear dependence may reduce photobleaching rates at high repetition rates as demonstrated by Ji et al. (Ji et al., 2008) through the use of passive pulse-splitting. In this study, the authors divided pulses from a standard 80 MHz Ti:Sapphire laser into bursts of pulses of smaller peak power, adding, however, the complexity and cost of the custom beamsplitting setup to the one of the laser. The use of GHz sources based on Ti:Sapphire as a gain medium has been demonstrated in only a small number of studies for SHG microscopy and two-photon microscopy (Ehlers et al., 2007; Studier et al., 2010, 2011), likely due to the high complexity and cost of these lasers.

2.2.4 Experimental setup: lasers and microscope

This section describes the details of the microscope setup and the parameters of the SDL and Ti:Sapphire laser used in this study

The microscope setup

The multiphoton microscope used in this study is based on a multi-area two-photon microscope described previously (Figure 2.5) (Chen et al., 2016b; Voigt et al., 2015) Excitation light from either the SDL or a Ti:Sapphire laser (Spectra-Physics Mai Tai HP DS) was intensity-modulated with Pockels cells (Conoptics 350-105 for the SDL and Conoptics 350-80 for the Ti:Sapphire laser) and the laser beam expanded before being sent to the scan mirrors (6220H, d = 10 mm, Cambridge Technologies). The beam then passed a telescope formed by a f = 89 mm scan lens (S4LFT0089, Sill Optics) and a f = 200 mm tube lens (AC508-200B, Thorlabs) and was directed into the microscope objective (Olympus XLUMPlanFL 20x 0.95W or a Nikon CFI75 LWD 16xW NA 0.8). For detection, the emitted light was separated from the excitation light by an IR-VIS dichroic (HC705 MP Longpass, AHF AG) and directed towards hybrid photodetectors (HPD, R11322U-40 MOD, Hamamatsu). For small transparent samples a custom single-channel transmission detector, composed of a NA = 1.0 water immersion condenser (Zeiss) and including an additional HPD, could be placed below the sample. HPD signals were preamplified (C1077B, Hamamatsu) and digitized by an analog-to-digital converter (ADC, NI-5771, National Instruments) connected to a field-programmable array (FPGA, NI-7962R, National Instruments). Scanning and data acquisition were controlled using the two-photon microscope control software "Scope", (rkscope.sourceforge.net). For SHG imaging, a 514/30 BrightLine HC (AHF AG) emission filter was used both in the transmission and reflection path. In the epidetection path, a dichroic mirror with a cut-on wavelength of 552 nm (HC BS 552, AHF AG) was used to separate the SHG emission from longer-wavelength fluorescence. For parallel fluorescence imaging with a red and green channel (e.g. Figure 2.7), a filter set consisting of a Qioptic DC-Green dichroic and two emission filters (Semrock Brightline Basic 535/22 and Chroma ET605/70M) were used.

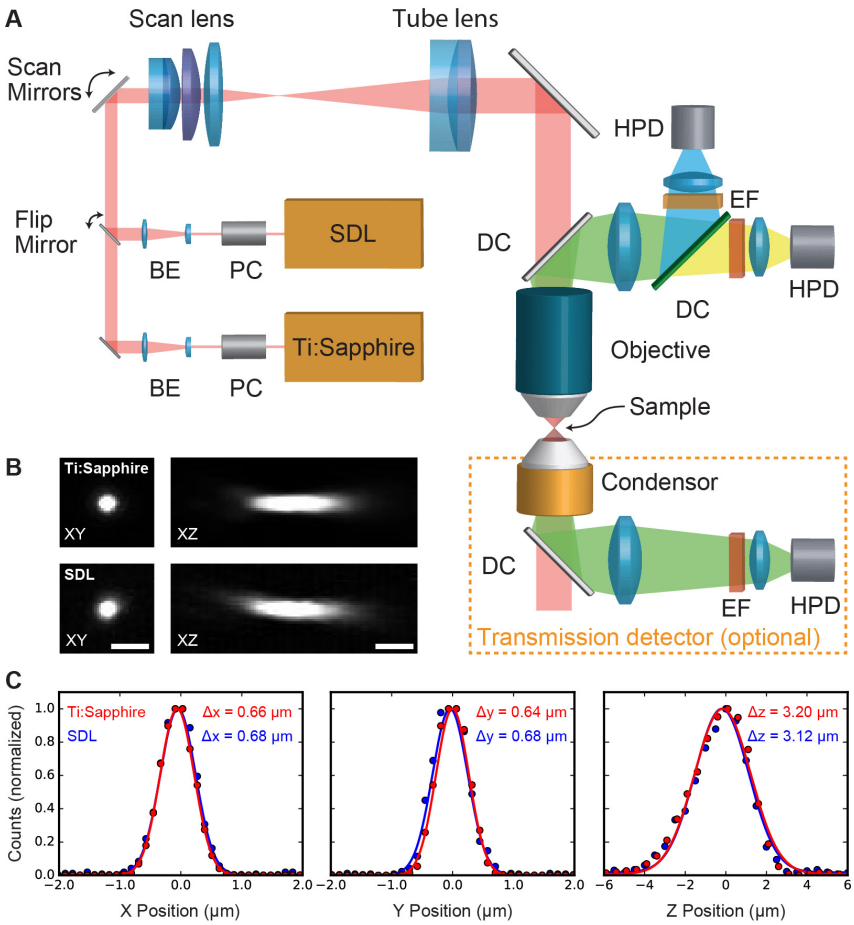

Figure 2.4: A) Overview of the microscope setup: Excitation light from either the SDL or a Ti:Sapphire laser (Spectra-Physics Mai Tai DeepSee) can be coupled into the microscope via a Pockels cell (PC) and a beam expander (BE). After the scan mirrors, the beam is directed into the objective by a scan and tube lens. The emission light is sent to a two-channel detection system via dichroic mirrors (DCs), emission filters (EF) and then collected by hybrid photodetectors (HPDs). For small, transparent samples, a transmission detector with a single HPD can be added. B) Maximum intensity projections of images of the same 200 nm bead taken with the Ti:Sapphire and SDL. C) Gaussian fit of the data in B) with full width at half maximum (FWHM) values for both lasers.

Matching of point spread functions between the SDL and the Ti:Sapphire laser

In order to ensure that both lasers were focused equally well for the comparison experiments, we matched the point spread functions (PSFs) of the microscope for the two lasers. For this, we adapted the beam expansion optics in front of both lasers to equalize the beam diameters at the 20x objective. To allow maximum power throughput, we underfilled the back aperture of the 20x objective, which means that the PSFs were not diffraction-limited for NA = 0.95 at

1027 nm (Figures 2.5 B and C). PSF measurements were done using Fluoresbrite Multifluorescent Microspheres (Polyscience, 0.2 µm). For the SDL, we measured a full width at half maximum of the PSF of $FWHM_x$ = 0.68 ± 0.01 µm, $FWHM_y$ = 0.68 ± 0.02 µm, and $FWHM_z$ = 3.14 ± 0.01 µm (± SEM, n = 3 beads), demonstrating in addition the good beam quality of the SDL. For the Ti:Sapphire laser, the corresponding values were $FWHM_x$ = 0.65 ± 0.02 µm, $FWHM_y$ = 0.63 ± 0.01 µm, and $FWHM_z$ = 3.13 ± 0.07 µm (SEM, n = 3 beads). Both laser beams thus resulted in comparable PSFs of approximately $(0.67\ \mu m)^2$ x 3.1 µm focal volume.

The mode-locked semiconductor disk laser

We designed a prototype mode-locked semiconductor disk laser based on recent improvements in the technology (Waldburger et al., 2016). We used the same gain chip and combined it with a quantum well (QW) SESAM similar to the one used in (Waldburger et al., 2016). A QW SESAM has the advantage of having a faster recovery time compared to quantum dot SESAMs used previously for a SDL developed for MPM (Aviles-Espinosa et al., 2011). We optimized the laser cavity (depicted in Figure 2.2 (A)) for long-term stability and ensured operation at room temperature by placing the whole cavity and pump optics in a laser head with a small footprint of 22 cm x 25 cm.

The SDL chip was cooled to 16°C and the SESAM was kept at a temperature of 20°C in order to avoid any water condensation in a laboratory environment. Turn-key operation with long- term stability was obtained with strain-compensated semiconductor growth (Mangold et al., 2015). As presented in Figure 2.5, the SDL generated stable and clean mode-locking at a center wavelength of 1027 nm with 9.5 nm of full width at half maximum (FWHM) spectrum supporting 118-fs pulses (measured with a HP-70952B Optical Spectrum Analyzer). The center wavelength was chosen as the recent development of <100 fs SDLs was achieved around 1 µm. Furthermore, this wavelength allows excitation of red fluorescent proteins. The radio frequency (RF) signal was measured with a fast photodiode (Newport 1454, 25 GHz bandwidth) and a radio-frequency spectrum analyzer (HP-8592L). The pulse duration of the laser was measured after the objective of the

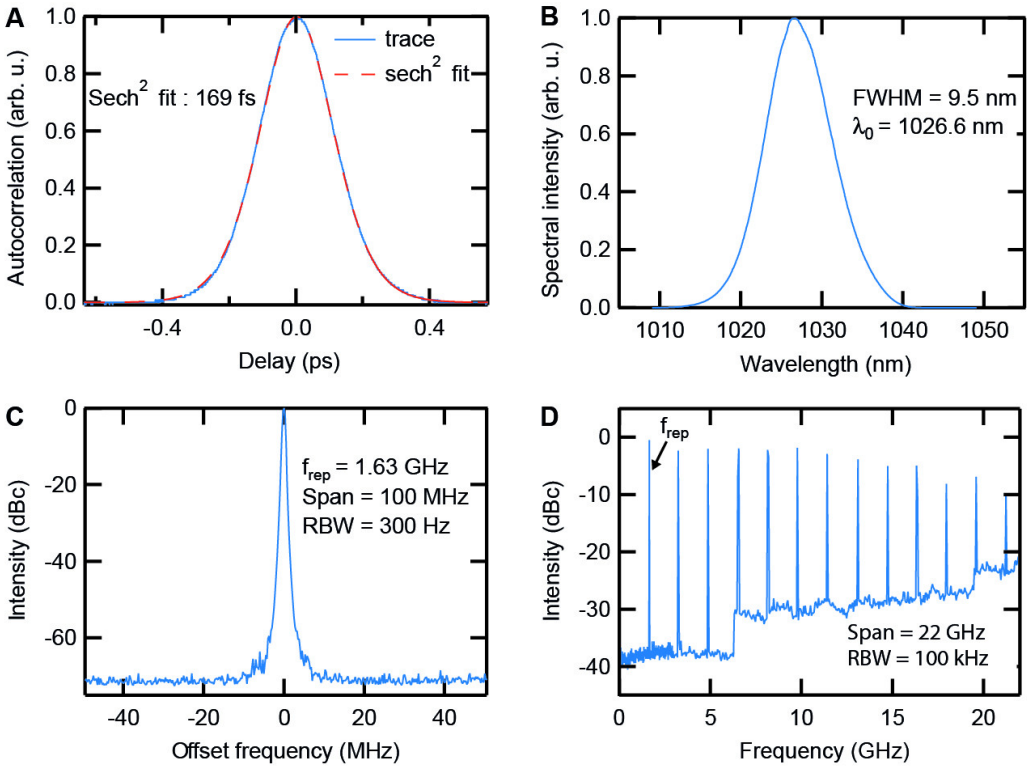

Figure 2.5: Pulse width measurements of the ultrafast SDL. A) SDL in combination with the 20x microscope objective. B) The SDL has a spectrum with 9.5 nm full width at half maximum (FWHM) (i.e the spectrum is supporting 118 fs pulses). C-D) Fundamental mode-locking is demonstrated with the Radio Frequency (RF) traces taken at the main laser frequency of 1.63 GHz and on its harmonics. The drop of the power in the harmonics is due to the limited bandwidth of the RF amplifier used to measure it. The resolution bandwidth (RBW) is the smallest frequency increment that can be resolved.

microscope system to take into account the dispersion and spectral filtering that could arise in the system. For this measurement we used a 15-mm focal lens (Thorlabs C260TMD-B) to capture the divergent beam exiting the 20x objective. Without additional dispersion compensation, pulses of around 169 fs FWHM (using a sech 2 fit) were measured with a Femtochrome Research FR-103MN second- harmonic autocorrelator (Figure 2.5(A)), which correspond to 1.44x the transform limit. The laser operates at a repetition rate of 1.63 GHz (Figure 2.5C and D) and could deliver up to 145 mW of average output power at a pump power of 15 W provided by a standard commercial 808 nm fiber coupled diode. With the 20x objective, up to 72 mW (i.e. ≈50% of transmission) were available for imaging, corresponding to 230 W of peak power. Using the fig-

ure of merit (FOM) defined in Resan et al. (2014); Aviles-Espinosa et al. (2011) we could achieve $\mathrm{FOM}_{2\mathrm{PM}} = P_{\mathrm{avg}} \cdot P_{\mathrm{peak}} = 16\mathrm{W}^2$ below the objective, which was sufficient for MPM imaging in a variety of applications (see section 2.2.6). As shown in Figure 2.2A), the laser cavity contains only three components in addition to the optical pump, which in combination with the GHz repetition rate leads to a highly compact, stable, and simple laser head. During the last decade we have observed significant industrial developments of III-V semiconductor foundries for applications in machining, telecommunication or distance ranging. Thus there are commercial suppliers for providing SDL components at high volume. This combination of simplicity and availability of affordable components will support the commercialization of ultrafast SDLs as compact and cost-efficient sources.

The Ti:Sapphire laser

In order to compare the SDL to a standard laser used in MPM imaging, we used a tunable Ti:Sapphire laser (Mai Tai HP Deep See, Spectra-Physics), which allowed the evaluation of imaging performance for different repetition rates while keeping the other parameters constant (Figure 2.6). With clean mode-locking at a repetition rate of 80.65 MHz, i.e. 20.3 times lower than the SDL, the Ti:Sapphire spectrum could be tuned to match the center wavelength of the SDL (Figure 2.6B), with an OceanOptics USB2000 spectrometer). With nearly 12 nm FWHM, the Ti:Sapphire laser spectrum could however support pulses as short as 104 fs at this wavelength. To equalize the pulse lengths, we used the prechirping unit inside the Ti:Sapphire laser. As shown in Figure 2.6A, the pulse duration of this Ti:Sapphire laser could be adjusted to 169 fs below the microscope objective measured with the autocorrelator. The RF traces, which were measured with a fast photodiode (Alphalas UPD-200-SP, 2 GHz bandwidth) and an RF spectrum analyser (Rohde & Schwarz FSH4), indicate fundamental mode-locking (Figures 2.6C and D). Hence, pulse duration, center wavelength and spatial resolution were matched for both lasers with only the repetition rate being different.

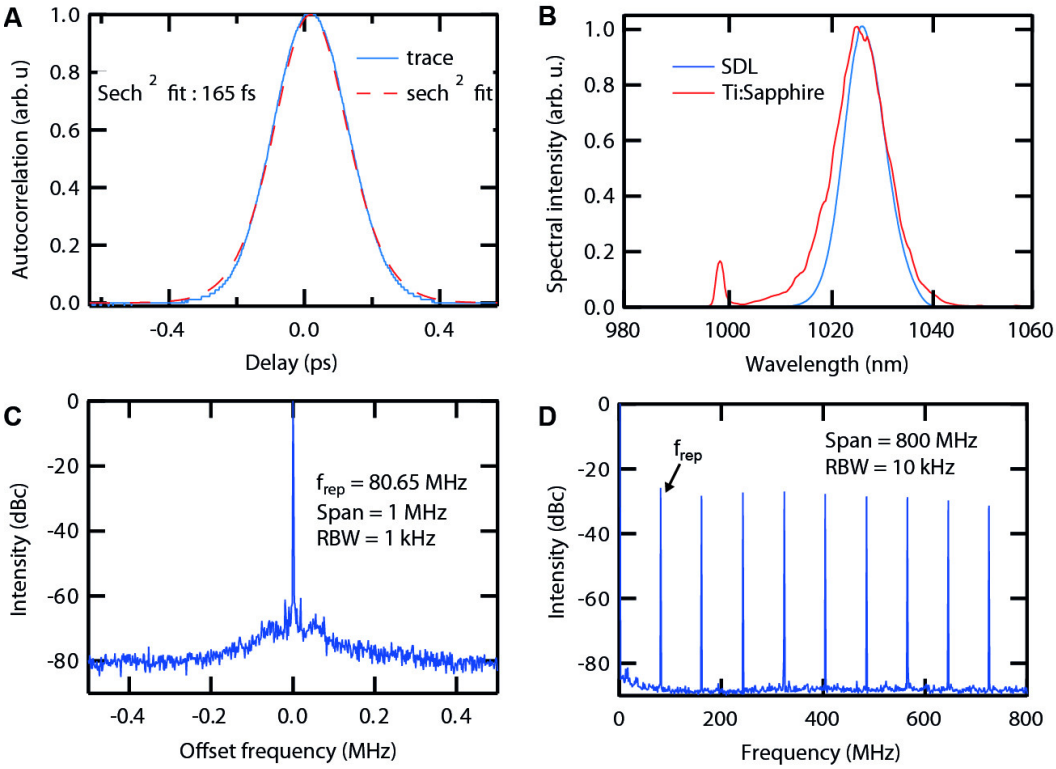

Figure 2.6: Pulse width measurements of the Ti:Sapphire laser. A Ti:Sapphire laser (Mai-Tai HP from Spectra-Physics) was used for comparison with the SDL. A) Using the prechirping unit in the Ti:Sapphire laser, the pulses were adjusted to a length of 165 fs after the objective (20x). B) The spectrum was centered at 1026 nm to overlap with the spectrum of the SDL. Both spectra were measured after the microscope objective. C-D) Fundamental mode-locking was confirmed by the Radio Frequency (RF) traces taken at the main laser frequency of 80.65 MHz and on its harmonics. The resolution bandwidth (RBW) is the smallest frequency increment that can be resolved.

2.2.5 Comparison of the SDL and a matched Ti:Sapphire laser

In this section, we evaluate the achievable multiphoton signal levels and bleaching properties of imaging using the SDL in comparison to a standard Ti:Sapphire laser with matched operation parameters except for the different repetition rate.

Comparison of the generated two-photon signal

To compare both laser systems we imaged a confocal test slide (FluoCells No. 2 Molecular Probes), which contains fixed bovine pulmonary artery endothelial cells (BPAEC). In this sample, Texas Red-X phalloidin is labeling F-actin and microtubules are labeled with antibodies conjugated to BODIPY FL. We set the Ti-Sapphire laser to an average power of 11 mW after the 20x objective and imaged the cells by taking a stack of 10 planes at 1 µm spacing (2048 x 2048 pixel images with 10 µs pixel dwell time, 42 s/image). We then set the SDL power to 49 mW, which corresponds to a power ratio of $4.5 \approx \sqrt{20.3} \approx \sqrt{f_{\text{rep, SDL}} / f_{\text{rep, Ti-sapphire}}}$, so that both lasers should produce similar signal levels (Denk et al., 1990). Figure 2.7 shows a comparison of both data sets in the form of a sum projection of all slices and line profiles. The signal levels and resolved features were indeed comparable (a 11-17% difference in generated fluorescence signal can be noted for the SDL), validating the theoretical predictions (Denk et al., 1990) and the matching of the two laser systems. The small difference is likely caused by slight inaccuracies in the matching parameters, for example in the pulse duration, or might be due to slight bleaching when sequentially imaging the same volume of the sample with both lasers.

Bleaching comparison

To investigate the bleaching properties when using the two matched laser systems in our microscope, we performed bleaching tests on a Drosophila larva generated by crossing the line UAS-palmKate2-K7 (attP2), driving palmitoylated mKate2 in muscle cells with c381Gal4w+ and 332.3Gal4w+ (Caviglia et al., 2016). The larva was embedded in Mowiol (Sigma-Aldrich) and regions sized 80.8 x 5.4 µm² at a depth of 60 µm were imaged at 256 x 16 pixel with 10 µs pixel dwell

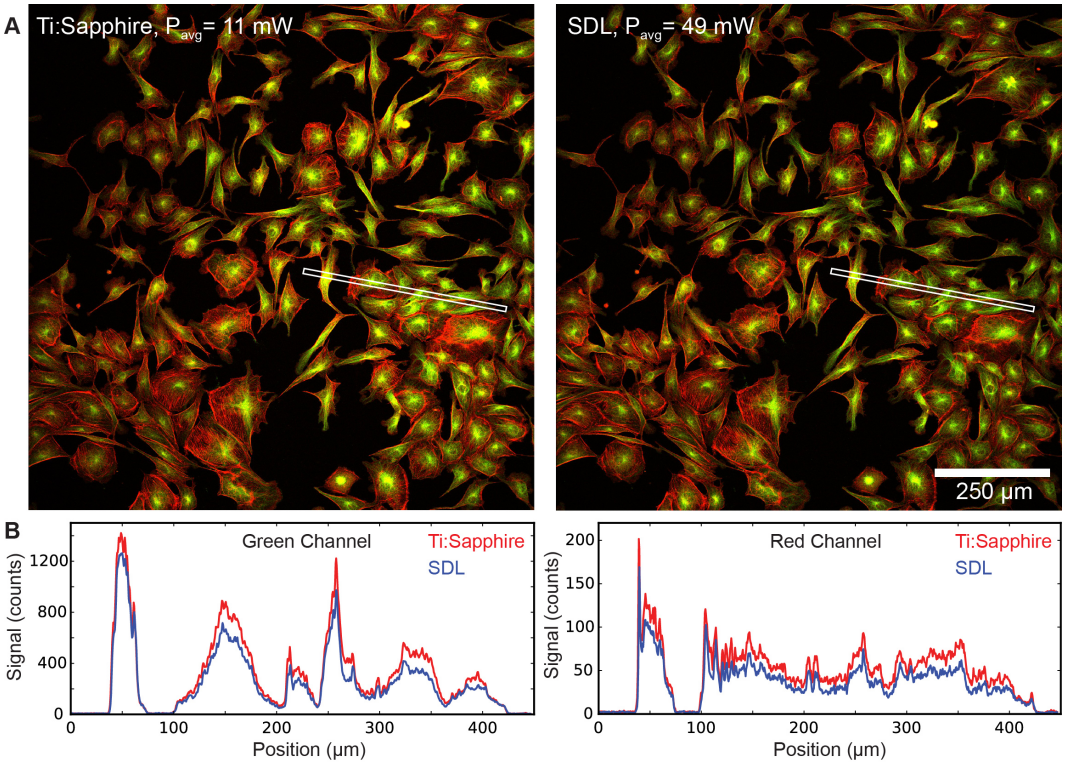

Figure 2.7: Imaging comparison between the SDL and the Ti:Sapphire laser. The power levels were set to a ratio of ≈4.5 to create approximately the same signal based on the ratio of repetition rates [48]. The images are sum projections over a stack of 10 slices (taken at 2048 x 2048 pixel with 10 µs pixel dwell time) using 1 µm z-spacing. A) Comparison images of fixed BPAE cells (similar histogram settings). Green channel: Microtubules, red channel: F-Actin. B) Comparison of the signal counts created by the SDL and the Ti:Sapphire laser along the line profiles highlighted in A.

time over 100 seconds at a frame rate of 15 Hz. The average powers of the Ti:Sapphire laser and the SDL were set to create similar signal counts (14.4 mW and 66.5 mW below the objective, respectively; corresponding to a ratio of ≈4.6). For each laser, the bleaching tests were repeated 4 times (Figure 2.8A). The bleaching traces observed with the SDL did not exhibit any signs of damage processes related to the higher average power level compared to the Ti:Sapphire laser. To properly fit the time-dependent fluorescence signal during bleaching, a tri-exponential function was necessary (Figures 2.8A and B) indicating that at least three different bleaching processes with separate dynamics are involved. Simpler fitting functions such as a single- and bi-exponential fit exhibit oscillatory behavior when comparing the residues on normalized traces (Figure 2.8D). The time constants (τ_1, τ_2, τ_3) extracted from the fits then allowed us to calculate the coefficient of photo-

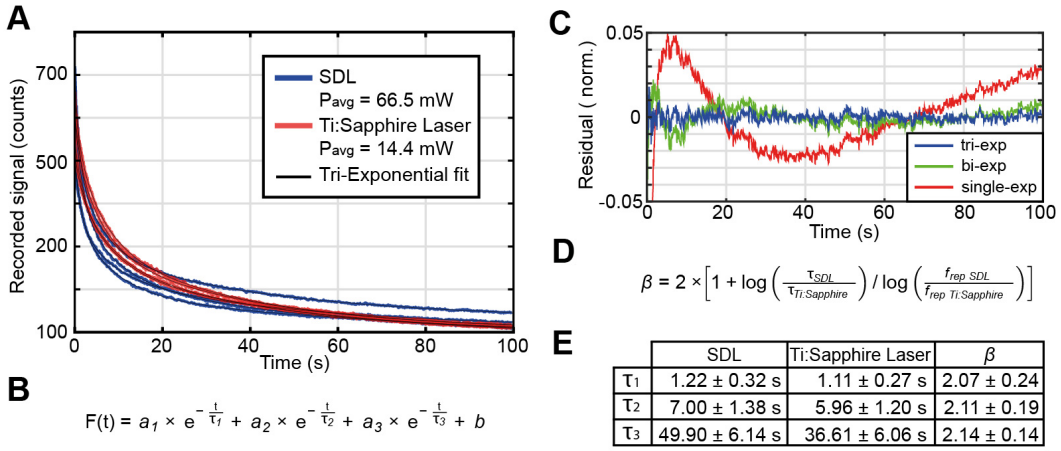

	SDL	Ti:Sapphire Laser	β
τ_1	1.22 ± 0.32 s	1.11 ± 0.27 s	2.07 ± 0.24
τ_2	7.00 ± 1.38 s	5.96 ± 1.20 s	2.11 ± 0.19
τ_3	49.90 ± 6.14 s	36.61 ± 6.06 s	2.14 ± 0.14

Figure 2.8: Comparison of bleaching rates in a Drosophila larva labeled with mKate2. A) Raw bleaching time courses for the SDL (blue) and for the Ti:Sapphire laser (red) at a power ratio of 4.6 giving a similar generated signal as expected by theory. B) Tri-exponential function used to fit bleaching curves in A. As shown in C), this function was the most adequate to obtain an accurate and robust fit because a single or bi-exponential function cannot fully fit the data. D) Formula to calculate the photodamage coefficient β using the approach in [48]. E) Taking into account the three time constants of the bleaching curves (τ_1, τ_2 and τ_3), can be obtained in each case. The average β value across all three extracted time constants is centered at 2.10 with a standard deviation of 0.51.

damage (β, Figure 2.8D) using the same approach as in (Ji et al., 2008). At $\beta = 2.1 \pm 0.51$, the difference of the SDL and the Ti:Sapphire was very slight, corresponding to a 10-15% improvement in the bleaching rates, which is lower than previously reported values (Ji et al., 2008).

2.2.6 In vivo multiphoton imaging using the SDL

In this section we demonstrate the multiphoton imaging capabilities of the SDL for routine in vivo imaging experiments in developmental biology and neuroscience. All images shown in this section were acquired with the ultrafast SDL.

In vivo multiphoton imaging in Drosophila

To demonstrate the compatibility of the SDL with MPM in living organisms, we imaged a Drosophila larva labeled with mKate2 in muscle cells (same line as described in subsection 2.2.5). A 3rd instar larva was selected for imaging, dissected and placed in a custom imaging chamber with calcium-free HL3 buffer to reduce motion artifacts. The excited fluorescence signal above 552 nm was

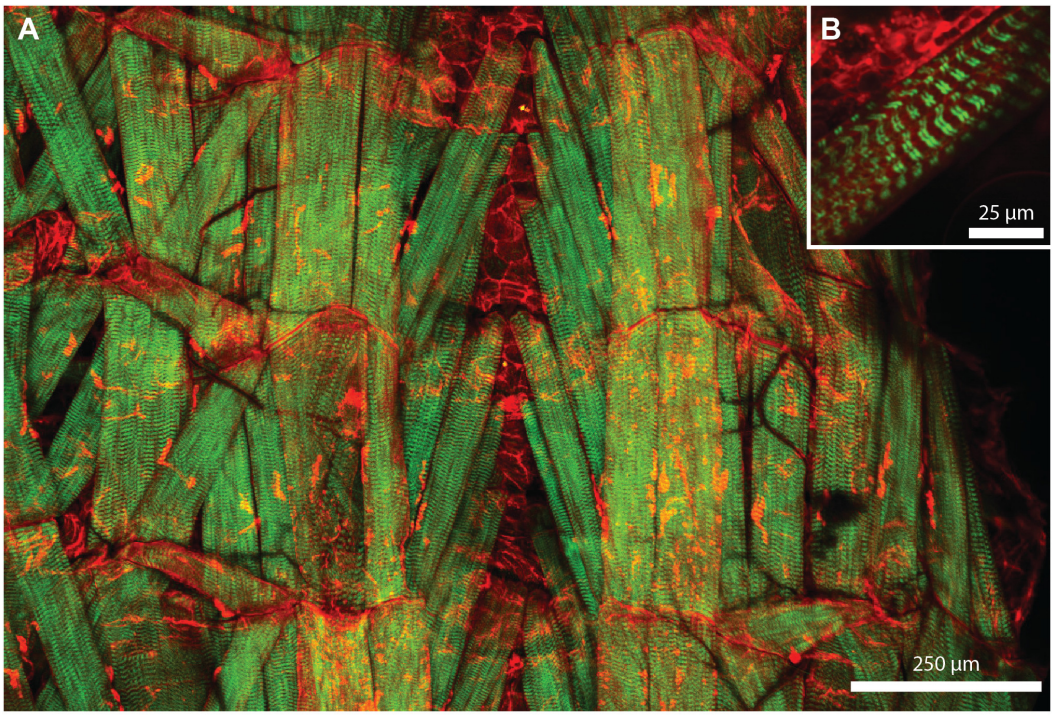

Figure 2.9: Multiphoton imaging in a Drosophila larva using the ultrafast SDL. A) Maximum intensity projection of a stack covering a range of 160 µm (Average laser power: 17 mW, 1696 x 1142 pixel, 10 µs dwell time). Red channel: Fluorescence from mKate2, Green channel: SHG signal. The SHG signal is predominantly originating from sarcomeres in the muscles. B) Image of the sarcomeres at higher zoom showing the characteristic double-band structure (6 mW, 1024 x 1024 pixel, 10 µs dwell time, 4x averaging).

collected together with the forward-directed SHG signal by the transmission detection system. A strong red fluorescence signal from muscle cells, together with SHG generated by sarcomeres was detected down to a depth of several hundred microns (Figure 2.9). The SDL thus provides high enough peak power to generate sufficient two-photon excited fluorescence and SHG signal levels for imaging in small organisms. In fact, the average power levels needed in this experiment (i.e., 17 mW and 6 mW in Figure 2.9) were so low that we reasoned that the SDL should be capable of allowing multiphoton imaging under more challenging conditions, for example in samples with higher levels of scattering or using other fluorophores.

In vivo two-photon imaging of mouse vasculature in the neocortex

We then tested the imaging capabilities of the SDL for structural imaging in the living mouse brain. We prepared a chronic cranial window in a C57BL/6 mouse and injected Texas Red conjugated to a high molecular weight dextran (70 kDa molevular weight, Invitrogen) into the tail vein to label the blood plasma. This type of experiment is routinely used to study the structure and function of the brain vasculature, for example to evaluate the coupling between neuronal activity and associated changes in blood flow (neurovascular coupling) (Kleinfeld et al., 1998). During isoflurane anesthesia, the tail vein was dilated by heating in warm water. The end of the tail was softly clamped and a bolus of dye-containing solution (0.1 ml at 5% wt/vol) was slowly injected. For in vivo imaging sessions, isoflurane anesthesia was maintained and the animal's body temperature was kept steady at 36°C. Using the 16x objective and 60 mW of SDL average power, we were able to acquire two-photon images of blood vessels and fine capillaries down to 400 µm depth (Figure 2.10). At 10-30 µm depth, we also detected the SHG signal created by the collagen-rich dura mater just below the cranial window. All animal procedures were carried out according to the guidelines of the Center for Laboratory Animals of the University of Zurich and were approved by the Cantonal Veterinary Office. This experiment demonstrates that in vivo imaging with the SDL is feasible in the superficial layers of the mouse brain despite the lower average power output compared to Ti:Sapphire lasers. The SDL should thus also be applicable for measurements studying the dynamics of blood flow by line scans across single blood vessels (Kleinfeld et al., 1998) and for structural imaging at comparable depths.

In vivo two-photon imaging of neuronal activity in mice

A key application of two-photon microscopy in modern neuroscience is functional imaging of the activity of neuronal populations in a living brain through cranial windows. For such recordings across tens to thousands of neurons, fluorophores reporting changes in intracellular calcium concentration are commonly employed (Grienberger and Konnerth, 2012). As the center wavelength of the SDL at 1027 nm predominantly allows excitation of red fluorophores, we used the

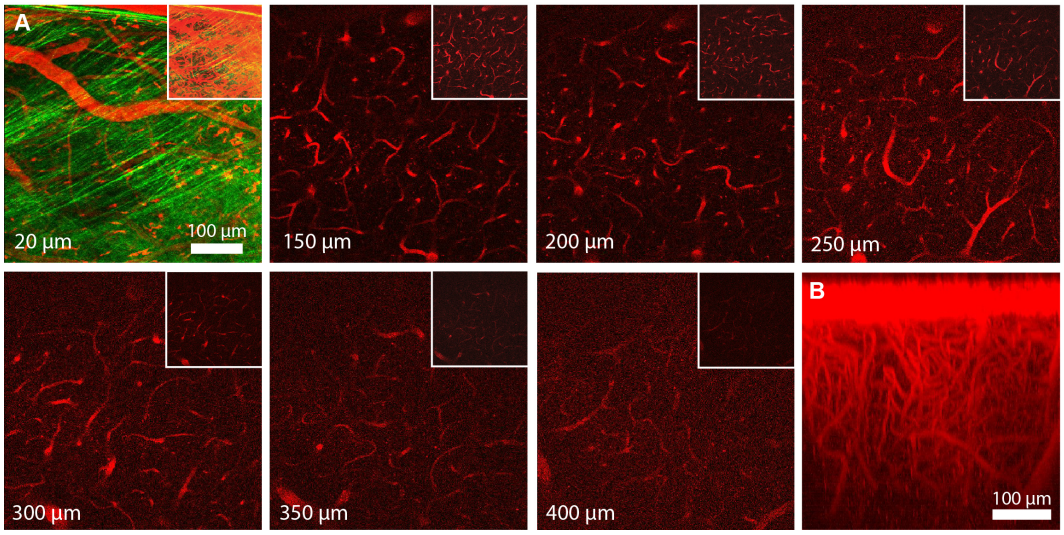

Figure 2.10: In vivo two-photon imaging of blood vessels filled with Texas Red Dextran using the ultrafast SDL. A) Selected frames from a z-stack at different depths as measured from the brain surface (512 x 512 pixel, 10 µs pixel dwell time). For each z-plane, the histogram was adjusted for better visibility. The top right insets show the same z-positions with the identical histogram settings throughout to compare signal strength. The SHG signal from the dura mater is visible at 20 µm. B) YZ-side-projection of the same data set (red channel only).

red-shifted genetically encoded calcium indicator R-CaMP1.07 (Ohkura et al., 2012) We expressed R-CaMP1.07 in neurons of the mouse brain by using several intracortical stereotaxic injections of an adeno-associated viral serotype 1 (AAV1) vector driving expression under the control of the unspecific EF-α1 promoter (AAV1-EFα1-R-CaMP1.07). For each injection site, 200 nl of virus were injected through glass micropipettes in a C57BL/6 mouse under isoflurane anesthesia in the superficial layers of the somatosensory barrel cortex (100-800 µm depth). After recovery, a cranial window (d = 4 mm) was implanted and in vivo imaging recordings were started 10 days post-operation. Using the 20x objective, we were able to visualize R-CaMP1.07-expressing neurons down to a depth of 360 µm with the SDL (Figure 2.11A). At a depth of 125 µm, we recorded functional signals at a frame rate of 10.68 Hz on a field-of-view (FOV) of 120 µm x 120 µm which allowed us to resolve calcium transients from a set of neurons (Figure 2.11B). For plotting neuronal ΔF/F signals, imaging frames were registered to correct for motion artifacts using the template matching and slice alignment plugin in Fiji (Schindelin et al., 2012) and regions of interest around

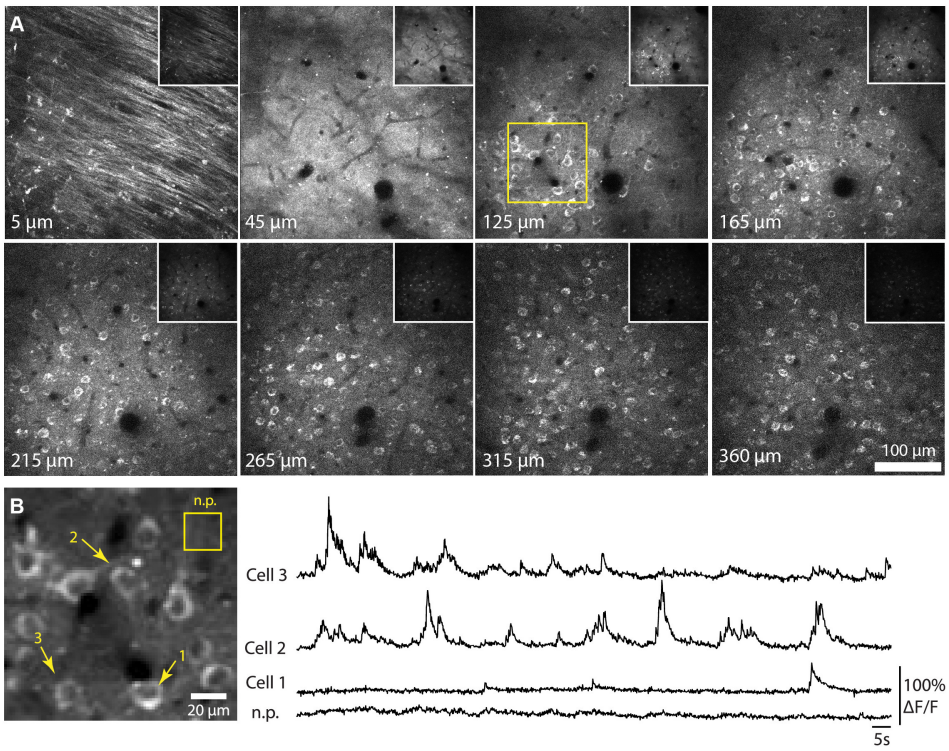

Figure 2.11: In vivo imaging of R-CaMP1.07-expressing neurons in mouse neocortex using the ultrafast SDL. A) Single z-planes from a stack starting at the dura down to a depth of 360 µm (72 mW laser power, 1024 x 1042 pixel, 10 µs dwell time). For each z-plane, the histogram was adapted for better visibility. The insets show the same z-positions with the same histogram settings. Neurons are visible as hollow rings as the calcium indicator does not enter the cell nucleus. The yellow frame at a depth of 125 µm indicates the functional imaging region in B). B) Calcium imaging in a subset of neurons (acquired at 72 mW laser power, 100 x 100 pixel, 6 µs dwell time). Average projection and example traces of three neurons and a neuropil (n.p.) region of interest are shown with a frame rate of 10.68 Hz. For this experiment, an HPD recorded all available signal without additional filters except an IR rejection filter.

cell bodies were selected manually. The SDL allowed recordings of neuronal activity at signal to noise levels comparable to recordings obtained with Ti:Sapphire lasers (Pilz et al., 2016). These results demonstrate that two-photon calcium imaging in the superficial layers of mouse neocortex at 100-350 µm depths, which is a major type of experiments in current neuroscience, is feasible with an ultrafast SDL.

In vivo two-photon imaging of neuronal activity in mice with OGB-1

Finally, we examined whether despite of the long wavelength of 1027 nm of our ultrafast SDL, calcium imaging with indicators normally excited in the 800-900 nm region is feasible as well. For this purpose, we used a VIP-tdTomato mouse, in which inhibitory interneurons expressing vasointestinal polypeptide (VIP) co-express the red marker protein tdTomato. A postnatal day 8 (P8) mouse was sedated by chlorprothixene (0.1 g/kg, intraperitoneal (i.p.); Sigma-Aldrich Chemie GmbH, Buchs, Switzerland) and lightly anesthetized with urethane (0.25-0.5 g/kg, i.p.). A custom-built head plate was glued to the skull over the left brain hemisphere with dental cement (Paladur, Heraeus Kulzer GmbH) to secure and stabilize the animal. A small cranial window of 1.5 × 1.5 mm^2 was opened above the cortical barrel map (guided via intrinsic imaging) with a sharp razor blade and neuronal ensembles in the superficial layers were bolus-loaded with the AM-ester form of Oregon Green BAPTA-1 by pressure injection (OGB-1; 1 mM solution in calcium-free Ringer'solution; 2-min injection at 150-200 µm depth (Stosiek et al., 2003)). The craniotomy was filled with agarose (Type III-A, 1% in Ringer's solution; Sigma) and covered with a glass plate. Using the SDL and the 16x objective, we could efficiently excite tdTomato and OGB-1 and record both large-FOV structural images (Figure 2.12A) and functional calcium signals (Figure 2.12)). For functional recordings, we selected a smaller FOV and detected calcium transients from putative excitatory neurons, astrocytes as well as dual-labelled VIP-positive interneurons (Figure 2.12B), supplementary Visualization 5). The neuronal populations displayed a highly synchronized activity pattern, which is typical for the maturing neocortex in this early postnatal period (Golshani et al., 2009). Our prototype ultrafast SDL is thus suitable for imaging of a wide range of fluorophores, even though a SDL tailored towards green fluorophores by lowering the laser wavelength would certainly be better suited for such imaging applications.

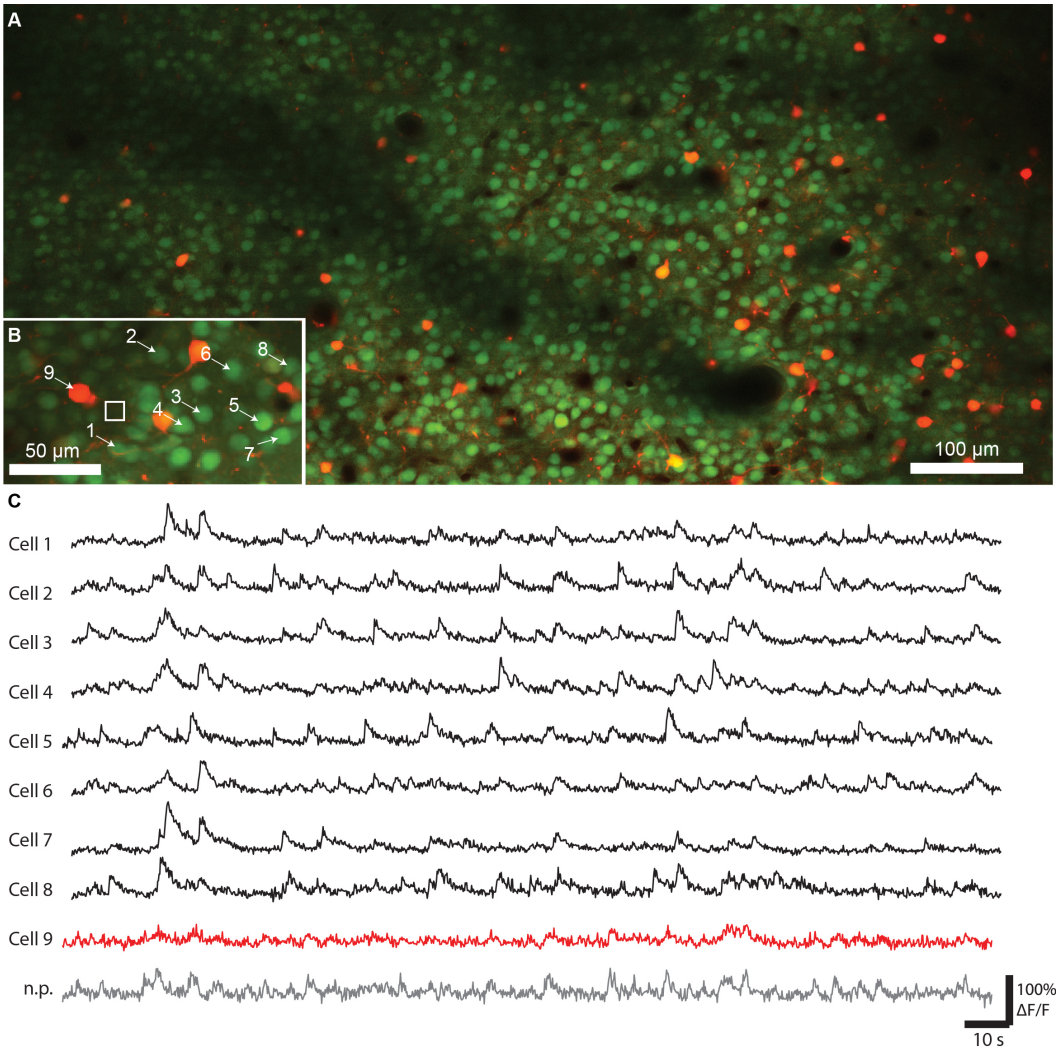

Figure 2.12: In vivo calcium imaging in a young (P8) mouse with the ultrafast SDL. In vivo calcium imaging in a young (P8) mouse with the ultrafast SDL: A) Overview image (924 µm x 465 µm) of tdTomato-expressing VIP-positive interneurons (red) and the surrounding cell population labeled with the calcium indicator OGB-1 (green) at a depth of 140 µm (51.4 mW average power, 3492 x 1598 pixel, 10 µs pixel dwell time, 4x average). Shadows in the image originate from superficial blood vessels. B) Field-of-view selected for calcium imaging (164 µm x 89 µm, 155 µm depth, 55.8 mW laser power, 200 x 100 pixel, 5 µs pixel dwell time) and calcium transients recorded from several neurons (6.42 Hz frame rate). Cell 9 is a VIP-positive interneuron co-labeled with tdTomato. n.p.: Neuropil.

2.2.7 Conclusions

We have demonstrated the utility of a femtosecond semiconductor disk laser (SDL) for a broad selection of multiphoton imaging applications, ranging from two-photon excited fluorescence to second harmonic generation in Drosophila and mice. In all of our experiments, the ultrafast SDL provided sufficient signal levels to make this laser an attractive alternative to a standard Ti:Sapphire laser for a wide range of experiments in developmental biology and neuroscience. As predicted by theory (Denk et al., 1990), imaging of the same sample with a SDL and a Ti:Sapphire laser with matched parameters (pulse duration, center wavelength, and spatial resolution) resulted in comparable signal levels when the SDL average power was appropriately scaled (ratio ≈4.5). In this work, the power levels provided by the laser at 1027 nm were sufficient to image a variety of red fluorophores but also the green calcium indicator OGB-1 (which is typically excited at 800 or 920 nm). Images were obtained from a depth of hundreds of microns in scattering tissue in vivo, highlighting that for many imaging applications the complexity and cost of a Ti:Sapphire laser are not necessary. In our SDL experiments, we did not observe heating-induced damage of the samples (due to linear absorption), which could have occurred due to the higher average power compared to the Ti:Sapphire laser. In addition, we stayed far below the threshold for long-lasting damage of brain tissue of 250 mW that has been recently reported (Podgorski and Ranganathan, 2016). While Ji et al. (2008) would predict a two-fold improvement in bleaching rate when using a 20x higher repetition rate, we could not confirm this prediction experimentally. We could nonetheless confirm that the 4.5-fold increased SDL average power did not cause increased photodamage compared to the Ti:Sapphire laser. The absence of an effect of the repetition rate on bleaching may also be caused by differences in samples and fluorophores. The ultrafast SDL produced equally good imaging results as a Ti:Sapphire laser with similar operation parameters except repetition rate and power even though the two-photon figure of merit (Resan et al., 2014) of the SDL is lower than the FOM for a Ti:Sapphire laser. The reason is that in the majority of biological imaging experiments, the maximum FOM of the laser is not even close to be utilized due to onset of tissue damage and the high absorption cross section of modern fluorophores. Whereas

the current generation of ultrafast SDLs is not suitable for very deep multiphoton imaging as performed with high-peak-power sources, a cost-efficient and reliable ultrafast source at GHz repetition rates could also be interesting for implementing frequency-type two- photon fluorescence lifetime imaging (FLIM) approaches or to improve photon statistics for fast scanning techniques with pixel dwell times in the <100 ns domain such as low-power temporal oversampling (LOTUS, Chen et al. (2011)). While the SDL presented here excites a green fluorophore (OGB-1) with reasonable efficiency, future SDLs will be bandgap-engineered towards center wavelengths in the 750- 970 nm region, thus allowing to make full use of the wide range of fluorescent markers currently imaged using Ti:Sapphire lasers. In summary, we have demonstrated that the current generation of ultrafast SDLs can be successfully used for nonlinear imaging applications. The SDL can thus fulfill the need for a simple, small, and reliable MPM laser source covering a wide range of applications. It will be especially attractive for configuring or upgrading a confocal microscope with multiphoton capabilities at low cost.

Should the experiments aimed at achieving a satisfactory method to stain nerves in the intact object be successful, so would this in combination with clearing allow us to considerably extend our knowledge on the distribution of nerves.

Werner Spalteholz, Über das Durchsichtigmachen von menschlichen und tierischen Präparaten, 1911

3

Tissue clearing and light-sheet microscopy

3.1 Tissue clearing

In 1911, the anatomist Werner Spalteholz published a book entitled "Über das Durchsichtigmachen von menschlichen und tierischen Präparaten" chronicling his efforts over the preceding years in making tissue transparent (Spalteholz, 1911). He noted that the key ingredient to making samples as clear as possible is to find an immersion medium that matches the average refractive index of the sample as closely as possible. Spalteholz tested a variety of organic solvents ranging from benzene ($n_D = 1.496$) to carbon disulfide ($n_D = 1.627$) and created mixtures to properly index-match the average index of tissues*. He noted that different species, different organs, and samples of different ages all require modifications of the clearing protocol. In the end, he settled on using

*Refractive indices of optical materials used in the visible part of the spectrum are usually measured at the Sodium D-Line $\lambda = 587.5618$ nm and denoted as n_D.

a mixture of methyl salicylate ($n_D = 1.536$) and benzyl benzoate ($n_D = 1.568$). Clearing using these organic solvents took only a few days for small cm-sized specimens, but it took weeks to months for larger samples including whole human embryos. Nonetheless, it resulted in excellent transparency even for bone specimens. Spalteholz primary application was the production of anatomical preparations for exhibitions and educational institutions, he did not pursue further quantification of his samples (Keller and Dodt, 2012). The approach by Spalteholz saw some application in embryology in the late 20th century (Klymkowsky and Hanken, 1991) with the major modification of replacing the methyl salicylate in the original protocol with benzyl alcohol. The combination of benzyl alcohol and benzyl benzoate (BABB) is often referred to as Murray's clear and allowed the combination with immunostaining in whole-mount preparations of Xenopus embryos (Dent et al., 1989). In the early 1990s, clearing was combined for the first time with light-sheet microscopy (see section 3.2) to obtain cochlear reconstructions (Voie et al., 1993). After the introduction of optical projection tomography (OPT, Sharpe et al. (2002)), BABB-clearing and immunolabeling were used to study gene expression patterns in whole mouse embryos. At the same time, the Spalteholz method continued to be used for clearing large samples, for example to prepare a whole human larynx (Steinke and Wolff, 2001). In 2007, light-sheet microscopy was used for the first time to image a cleared sample labeled with fluorescent proteins (Dodt et al., 2007). This highlighted the possibility of using whole-mount preparations for studies of neuronal connectivity without the need for tissue slicing. In the years since, a wide variety of clearing techniques became available. While the details of the physical and chemical processes differ, clearing techniques contain a series of basic steps (reviewed in (Richardson and Lichtman, 2015; Tainaka et al., 2016)):

- Tissue fixation for sample preservation. Often, aldehyde fixation is used for this purpose, for example using paraformaldehyde or glutaraldehyde.

- Treatment for sample dehydration, permeabilization, or delipidation. Dehydration aids in avoiding tissue damage in the Spalteholz method. Permeabilization makes the cytosol accessible and delipidation removes highly scattering membranes.

- Decolorization to reduce the impact of pigments, for example to remove heme or melanin.
- Refractive index matching – this is the actual ”clearing” step as the sample turns transparent after matching its refractive index with the immersion medium.
- Staining or antibody labeling. Depending on the clearing protocol, this needs to happen before index matching or can be performed after the clearing step.

Clearing techniques can be grouped into methods based on hydrophobic solutions – often referred to as organic solvent clearing – and methods based on hydrophilic reagents (Richardson and Lichtman, 2015; Tainaka et al., 2016; Vigouroux et al., 2017). The following sections and Table 3.1 provide an overview of the properties and capabilities of a variety of clearing methods while Figure 3.1 summarizes the key chemical compounds involved in them.

Protocol	Fixation	Key steps	RI match	RI	Reference
BABB	PFA	Dehydration with Ethanol	BABB	1.56	Dodt et al. (2007)
FluoClearBABB	PFA	1-Propanol or tert-Butanol for dehydration pH increased to 9.5 by adding Triethylamine	BABB (pH 9.5)	1.56	Schwarz et al. (2015)
3DISCO	PFA	THF/DCM: Delipidation	DBE	1.56	Becker et al. (2012) Ertürk et al. (2012a)
iDISCO/iDISCO+	PFA	iDISCO: THF for dehydration and delipidation iDISCO+: Methanol series before and after bleaching with H_2O_2 & DCM for delipidation Both: Immunolabeling with passive diffusion	DBE	1.56	Renier et al. (2014) Renier et al. (2016)
uDISCO	PFA	tert-Butanol for dehydration DCM for delipidation	BABB	1.56	Pan et al. (2016)
vDISCO	PFA	Pressure perfusion with nanobodies THF/DCM for delipidation	BABB	1.56	Cai et al. (2018)
PEGASOS	PFA	Decalcification with EDTA Decolorization with Quadrol Dehydraton & delipidation with tert-Butanol / Polyethlyenglycol (PEG)	BABB/PEG	1.54	Jing et al. (2018)
Scale	PFA	ScaleA2 (Urea/Glycerol/Triton X-100)	ScaleA2	1.38	Hama et al. (2011)
ScaleS	PFA	ScaleS (Urea/Sorbitol/DMSO)	ScaleS	1.44	Hama et al. (2015a)
SeeDB	PFA	Fructose / α-thioglycerol	SeeDB	1.49	Ke et al. (2013)
CUBIC	PFA	ScaleCUBIC1 (Urea/Aminoalcohol/Triton X100)	ScaleCUBIC2 (Sucrose/ Aminoalcohol/ Urea/Triton X-100)	1.49	Tainaka et al. (2014) Susaki et al. (2015)
CUBIC-X	PFA	Delipidation by ScaleCUBIC-1 Expansion by CUBIC-X1 (20% imidazole)	CUBIC-X2 (5% Imidazole + 55% Antipyrine)	1.47	Murakami et al. (2018)
CLARITY	PFA/Acrylamide/ Bis-acrylamide	Passive SDS flow or active electrophoresis (electrophoretic tissue clearing, ETC)	FocusClear or Glycerol/Water	1.45	Chung et al. (2013) Tomer et al. (2014)
PACT/PARS	PFA/Acrylamide	Passive (PACT) or perfusion-assisted clearing (PARS) with SDS	RIMS: Histodenz	1.45	Yang et al. (2014)
Expansion microscopy	PFA/Acrylamide/ Bis-acrylamide/ Sodium acrylate	Protease for digestion 4.5x expansion after adding deionized water	Deionized Water	1.33	Chen et al. (2015)
SWITCH	Glutaraldehyde	SDS Delipidation at higher temperatures Multi-round antibody labeling	Diatrizoic acid/ Iodixanol	1.47	Murray et al. (2015)
SHIELD	P3PE	SDS Delipidation	Diatrizoic acid/ Iodixanol	1.46	Park et al. (2019)

Table 3.1: Overview of selected clearing methods. On the top, techniques using organic solvents are shown whereas the bottom lists hydrophilic methods.

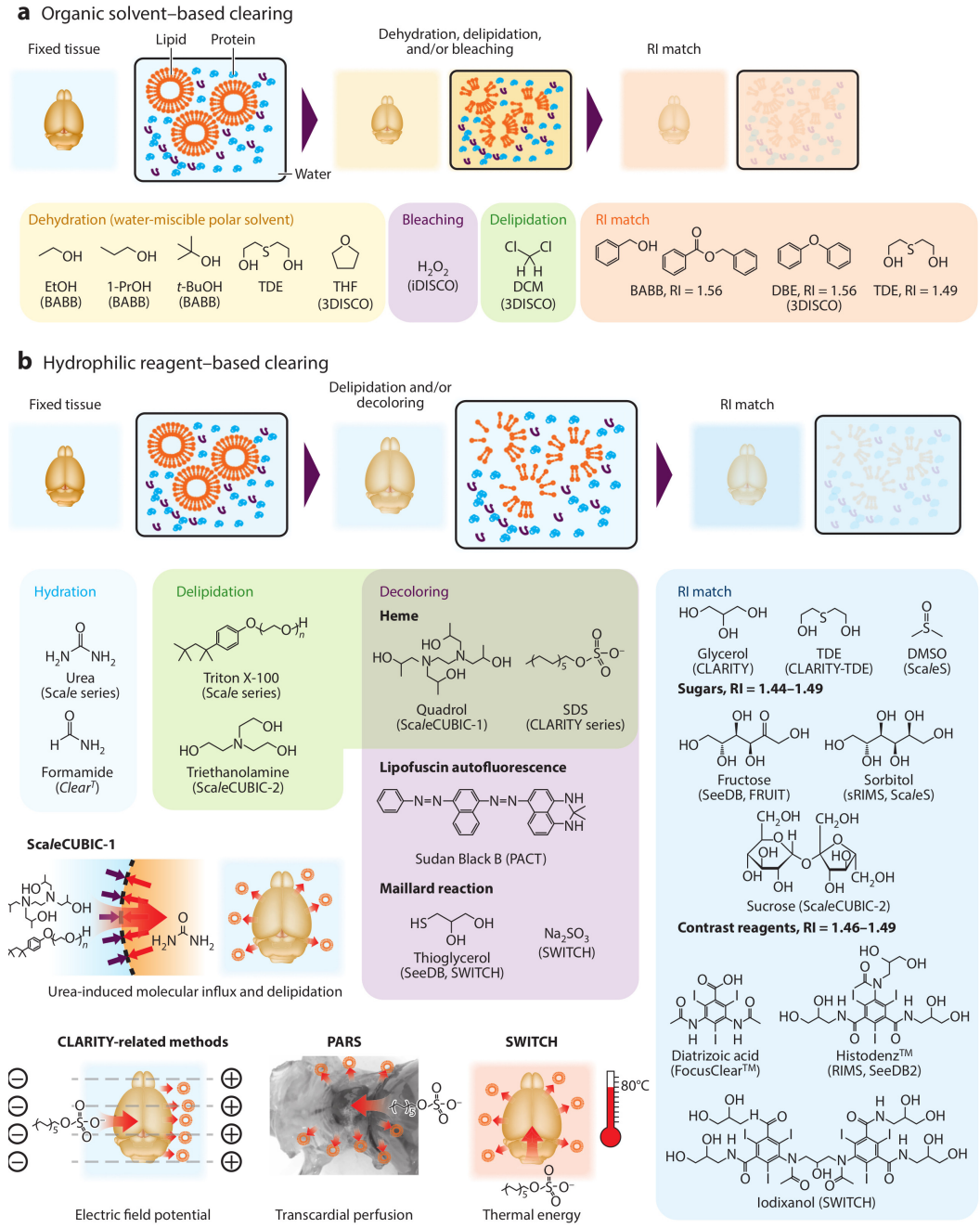

Figure 3.1: Overview of tissue-clearing chemistry. (a) Organic solvent–based clearing methods include dehydration, delipidation, bleaching, and refractive index (RI) matching steps. b) Hydrophilic reagent–based clearing methods utilize similar steps. A variety of compounds can be utilized for delipidation and decoloring and RI matching. Figure adapted from Tainaka et al. (2016)

3.1.1 Methods based on organic solvents

As outlined above, clearing methods based on organic solvents which delipidate and match the refractive index of samples form the oldest class of techniques. While the original protocols by Spalteholz (1911) and Dodt et al. (2007) are simple to perform and lead to good clearing results, fluorescent proteins are quickly degraded – for example, GFP fluorescence is lost within a few days. To ameliorate the issue, it was suggested to change the dehydration procedure from an ethanol series to tetrahydrofuran (THF) and exchange BABB for dibenzylether (DBE) as the clearing and index matching medium (Becker et al., 2012) which led to the 3DISCO (3D imaging of solvent-cleared organs) protocol (Ertürk et al., 2012a). This technique was used to study axon regeneration in spinal cord injury models (Ertürk et al., 2012b). 3DISCO clearing was later extended to the whole-mount immunolabeling techniques iDISCO (Renier et al., 2014) and iDISCO+ (Renier et al., 2016) by the addition of a methanol/hydrogen peroxide bleaching step to reduce background autofluorescence and enhance antibody penetration. iDISCO+ features reduced tissue distortions compared to iDISCO – as all clearing methods based on organic solvents need dehydration, samples tend to shrink and harden. This allows easy handling and mounting in a microscope, but can lead to distortions due to non-isotropic shrinkage. Apart from obtaining immediate early gene expression maps of whole mouse brains (Renier et al., 2016), iDISCO allowed the quantification of β-amyloid plaques in mouse models of Alzheimers disease and in brain tissue of Alzheimer patients (Liebmann et al., 2016). iDISCO has also been used to study the development of muscles, vasculature, and the nervous system in human embryos (Belle et al., 2017).

Later, the 3DISCO protocol was further optimized to preserve endogenous fluorescence by using tert-butanol for dehydration and additions of diphenyl ether (DPE) and vitamin E to the BABB imaging solution (Pan et al., 2016). This uDISCO protocol allowed whole-body clearing in adult mice. To allow whole-body immunolabeling, another DISCO-variant, vDISCO, was recently developed which uses pressure perfusion of nanobodies (Cai et al., 2018). With a molecular weight of 15 kDa, camelid-derived nanobodies (Muyldermans, 2013) diffuse more readily through

tissue than immunoglobulin G (IgG) antibodies at 150 kDa. Together with other whole-body clearing techniques such as PEGASOS (Jing et al., 2018), there is an ever-increasing palette of organic solvent methods. Beyond increasing the sample size, studies have investigated replacing toxic solvents such as BABB with less harmful compounds. Klingberg et al. proposed the usage of ethyl cinnamate (ECi) and demonstrated clearing and quantification of kidneys from nephritic mice (Klingberg et al., 2017). This technique was recently combined with nuclear staining protocols and applied to human cortex (Hildebrand et al., 2018). While the retention of fluorescent proteins has been drastically improved – for example by pH engineering in the FluoClearBABB method (Schwarz et al., 2015), generally, clearing methods based on organic solvents suffer from a loss in endogenous fluorescence compared to methods based on aqueous solutions. For example, in vDISCO, GFP expression is visualized using anti-GFP nanobodies. While the need to immunostain fluorescent proteins adds an additional level of complexity to the clearing technique, signal levels can be drastically increased by secondary amplification and the signal-to-noise ratio can be improved by using red fluorophores which suffer less from autofluorescence background.

3.1.2 Methods based on aqueous solutions

An alternative strategy to organic solvent-based clearing is the usage of hydrophilic reagents which promise better retention of fluorescent proteins while retaining good compatibility with immunolabeling. One of the earliest methods is FocusClear (Chiang et al., 2001; Chiang, 2002), a mixture of diatrizoic acid (an X-ray contrast medium with high index and excellent solubility in water and thus used for index matching) and dimethyl sulfoxide (DMSO, a polar aprotic solvent). FocusClear allowed whole-mount immunohistochemistry and imaging of the Drosophila brain. Other approaches employed sucrose and Triton X-100, a potent detergent to permeabilize cells, to increase the penetration depth of two-photon microscopy for the mapping of vasculature in mouse brain slices (Tsai and Kleinfeld, 2009). Due to the hyperosmolarity of the sucrose solution, this lead to shrinkage of the tissue.

These early studies on small samples formed the basis for the first widely publicized aqueous whole-brain clearing technique, Sca*l*e (Hama et al., 2011). The basic of Sca*l*e is the serendipitous observation that urea solutions can have a clearing effect on membranes. Urea is a small molecule that readily penetrates lipid bilayers, partially denaturates, and hydrates proteins (Hua et al., 2008). This hyperhydration of the hydrophobic core of proteins lowers and homogenizes the refractive index throughout the tissue preparation. The major disadvantages of the original Sca*l*e protocol are long clearing times (multiple weeks for samples larger than a few mm), sample swelling due to osmotic flux, and insufficient clearing performance for adult mouse brains given that lipids are retained inside the sample. Nonetheless, these protocols were developed further – the fructose-based approach by Tsai et al. evolved into SeeDB (Ke et al., 2013) and Sca*l*e was developed into Sca*l*eS (Hama et al., 2015b) which uses a combination of sorbitol and urea for better clearing results. Given that clearing methods of the Sca*l*e family do not remove lipids, Sca*l*eS is one of the few methods that preserve ultrastructure and allow for electron microscopic imaging of the same sample. Hama et al. used this to perform correlative light and electron microscopy of amyloid β plaques in cleared human specimens (Hama et al., 2015b).

The need for hydrophilic clearing methods capable of delipidation has prompted studies screening thousands of compounds for their clearing efficiency in brain homogenates which resulted in the CUBIC family of protocols (clear, unobstructed brain imaging cocktails and computational analysis, Susaki et al. (2014, 2015)). In the original CUBIC protocol, delipidation was performed using a cocktail based on Sca*l*e (termed Sca*l*eCUBIC-1) which contains high concentrations of quadrol, Triton X-100, and urea. Index-matching was carried out using Sca*l*eCUBIC-2, a mixture of sucrose, triethanolamine, urea, and Triton X-100 and resulted in a final refractive index of $n_D = 1.49$. CUBIC allowed the clearing and nuclear staining of a marmoset brain hemisphere and was later scaled up to whole body clearing (Tainaka et al., 2014). This was aided by the discovery that beyond delipidation, quadrol solubilizes and elutes endogenous heme which acts as a decolorization step for heme-rich organs such as liver or kidney.

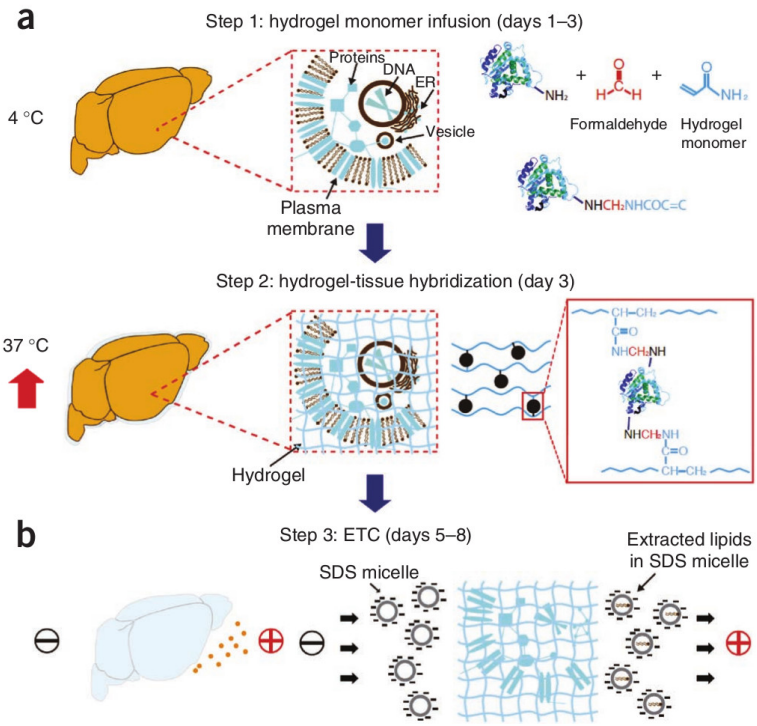

Figure 3.2: The CLARITY protocol. a): Initially, the tissue is infused with hydrogel monomers and crosslinkers and polymerization initiated by an increase in temperature. b) Lipids are then removed by electrophoretic transport of SDS. Figure adapted from (Chung and Deisseroth, 2013).

A DIFFERENT APPROACH to hydrophilic clearing protocols was published in 2013 by the Deisseroth lab (Chung et al., 2013): In CLARITY[†], the animal is perfused with acrylamide and bisacrylamide in addition to paraformaldehyde (PFA). In combination with an azo initiator such as VA-044, raising the temperature then leads to the covalent anchoring of molecules of interest such as proteins, RNA, or DNA to a hydrogel scaffold. Lipids can then be removed by electrophoretic tissue clearing (ETC) using a sodium dodecyl sulfate (SDS) as a strong detergent (Figure 3.2). Index-matching can be carried out using FocusClear or a glycerol/water solution.

THE CREATION OF A TISSUE-HYDROGEL HYBRID and subsequent molecular phenotyping and modification allows a wide range of applications (Gradinaru et al., 2018). One example is the re-

[†]Clear Lipid-exchanged Acrylamide-hybridized Rigid Imaging/ Immunostaining/In situ hybridization-compatible Tissue-hYdrogel

cent use of hydrogels for in situ RNA sequencing which allowed spatial transcriptomics of 1020 genes in a small slab (1.4 x 1.7 x 0.1 mm) of mouse brain tissue (Wang et al., 2018b). To simplify CLARITY, passive CLARITY procedures were developed (Tomer et al., 2014; Yang et al., 2014) which avoid the ETC procedure (termed "active CLARITY"). In the case of PACT (passive CLARITY technique, Yang et al. (2014)), the composition of the hydrogel monomers was changed by removing bis-acrylamide. As the density of crosslinks in the hydrogel depends on the acrylamide/bis-acrylamide concentration ratio, this step increased pore size and facilitated lipid extraction and subsequent immunohistochemistry. The same publication also introduced PARS (perfusion-assisted agent release in situ), a method using long-term perfusion of the SDS solution via cerebrospinal or systemic circulation for several days-to-weeks for whole-body clearing, and a refractive index matching solution (RIMS) based on histodenz, a gradient medium for centrifugation. After the initial publication of CLARITY, hydrogel-based clearing protocols were used for a wide range of applications, for example to disentangle the projection identities of dopaminergic neurons with Rabies virus tracing (Menegas et al., 2015; Lerner et al., 2015), or to unravel the role of a projection from prefrontal cortex to the basomedial amygdala in the top-down control of anxiety and learned freezing (Adhikari et al., 2015).

A SPEEDUP OF LIPID REMOVAL for the passive SDS-based clearing step is possible by increasing the temperature – provided the sample can sustain it. By using a different fixative, glutaraldehyde, in a protocol termed SWITCH[‡] rapid SDS clearing at 60-80°C was made possible (Murray et al., 2015). In SWITCH, the sample is first placed in a low-pH buffer to infuse the glutaraldehyde solution while avoiding the fixation reaction and then transferred to a high-pH buffer which initiates molecular cross-linking. SWITCH features low protein loss, preserves antigenicity, and the strong fixation conditions allow harsh elution treatments. This enabled up to 22 rounds of antibody labeling in a sample of human visual cortex.

[‡]System-wide control of interaction time and kinetics of chemicals.

To enhance the efficacy of the ETC step, stochastic electrotransport was introduced by the Chung laboratory (Kim et al., 2015). By placing the sample in a rotating electric field, the diffusion of SDS micelles is enhanced which speeds up the clearing process. The technique can be applied to the staining with small dyes and antibodies and is compatible with other clearing methods such as iDISCO and CUBIC.

Recently, the Chung group further explored the possibilities of improved fixation protocols and introduced SHIELD[§] which stabilizes fluorescent proteins using epoxide cross-linkers (Park et al., 2019). SHIELD avoids an increase in background autofluorescence which is a disadvantage of the SWITCH method. SHIELD also preserves mRNA which allows fluorescence in situ hybridization (FISH) and allows immunolabeling in combination with stochastic electrotransport.

If the hydrogel-based fixation is carried out with a swellable polymer such as sodium polyacrylate that expands upon absorption of water, the anchored biomolecules are moved apart which acts as a mechanical magnification process. This idea forms the basis of Expansion Microscopy (ExM, Chen et al. (2015)) which can be seen as an mechanical superresolution method (Karagiannis and Boyden, 2018; Wassie et al., 2019). As the final product after 4.5-fold expansion is 99% water, it has excellent transmission, the refractive index of water ($n_D = 1.33$) and can be imaged using standard water-immersion objectives. The initial ExM protocol required a harsh proteolytic treatment to homogenize the mechanical properties of the hydrogel which in turn necessitated a special fluorophore and labeling technique. Later improvements to the method (Tillberg et al., 2016) allowed the use of common fluorescent proteins and antibodies by crosslinking them to the gel and combined ExM with FISH to allow imaging of RNA (Chen et al., 2016a). Expansion microscopy has been used to image entire Drosophila brains and small slabs of mouse cortex at an effective resolution of 60 x 60 x 90 nm with lattice light-sheet microscopy (Gao et al., 2019). The capabilities of expansion microscopy have led to the development of expansion variants of other clearing methods, for example ePACT (Treweek et al., 2015) and CUBIC-X (Murakami et al., 2018).

[§]Stabilization to harsh conditions via intramolecular epoxide linkages to prevent degradation.

3.2 Light-sheet microscopy

At the turn of the twentieth century, the chemist Richard Zsigmondy at Schott teamed up with the physicist Henry Siedentopf at Zeiss to design a microscope capable of measuring nanometer-sized gold particles in ruby glasses and collodial solutions (Mappes et al., 2012). The challenge lay in visualizing the small particles at all given that they scattered only tiny amounts of light and were much smaller than the diffraction limit. Together, they developed a variant of dark-field microscopy: By directing a focused beam of light onto the sample from the side, the strong illumination beam never entered the detection objective and the tiny amount of scattered radiation from each particle could be seen through the microscope (Figure 3.3). Individual particles would become visible as moving dots on a dark background. The instrument was called the "ultramicroscope" as it allowed visualizing particles down to sizes of 6-250 nm for the first time (Siedentopf and Zsigmondy, 1902).

A SIMILAR TECHNIQUE was used in the 1960s to increase the depth of field for photomicrography (Simon, 1965). In 1993, light-sheet imaging was combined for the first time with fluorescence imaging and tissue clearing (Voie et al., 1993) to obtain three-dimensional reconstructions of a guinea pig cochlea. The method was termed orthogonal-plane fluorescence optical sectioning (OPFOS). Apart from the standard approach of acquiring parallel optical sections by translating the sample through the light-sheet, the instrument also allowed data acquisition by rotating the sample through the illumination plane (Voie and Spelman, 1995), similar to a tomographic scan – but without the need for back-projection. In these studies, a key aspect of light-sheet illumination was highlighted: Unlike a wide-field fluorescence microscope, images using light-sheet illumination do not suffer from out-of-focus background as the parts of the sample giving rise to background are not illuminated. Despite its advantages, however, in the decade after the introduction of OPFOS, light-sheet microscopy remained a fringe imaging technology that did see only very few applications such as microbial oceanography (Fuchs et al., 2002), imaging the entire cleared guinea pig auditory bone (Voie, 2002), or macrophotography (Huber et al., 2001).

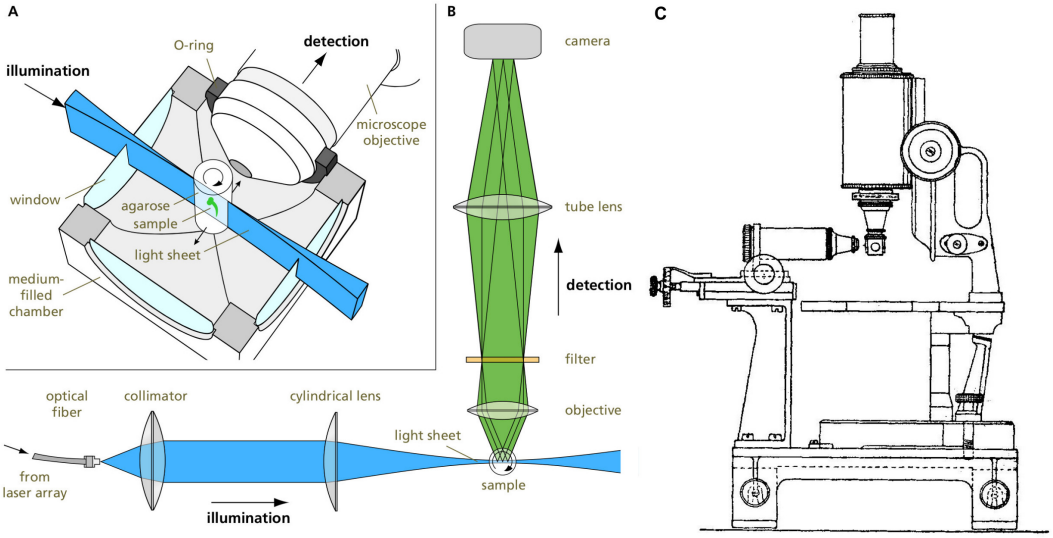

Figure 3.3: The concept of selective plane illumination microscopy (SPIM) A) The sample is mounted in a chamber filled with immersion liquid and illuminated from a direction orthogonal to the detection objective. B) The light-sheet is generated from a fiber-coupled laser, a collimator and a cylindrical lens. To allow multi-view imaging of the sample, it can be rotated around its axis. Three-dimensional datasets are generated by translating the sample along the detection axis and recording a series of images. Figure adapted from (Huisken, 2004). C) Original design of the ultramicroscope (Siedentopf and Zsigmondy, 1902).

This changed in 2004 with the development of selective plane illumination microscopy (SPIM, Huisken (2004)) which turned light-sheet microscopy into an *in vivo* imaging technique capable of studying embryogenesis in large transparent specimens (Figure 3.3). Thanks to the availability of transgenic Medaka embryos and *Drosophila melanogaster* larvae, 3D time-lapse datasets could be acquired over the time course of 24 hours. Apart from the optical sectioning capability, SPIM has two further advantages: Firstly, the parallel illumination of the whole FOV leads to lower peak laser intensities compared to a confocal microscope which reduces phototoxicity. Orthogonal illumination also means that structures above or below the focal plane cannot be bleached as they are not illuminated. Secondly, the image readout is done with a camera which enables much faster image acquisition than a point-scanning microscope. In addition, multi-view datasets could be acquired and fused together (Swoger et al., 2007) as the vertical orientation of the light-sheet allowed for sample rotation (Figure 3.3A). Imaging methods based on SPIM or other forms of light-sheet generation are referred to as light-sheet fluorescence microscopy (LSFM) techniques.

In the years after the publication of this landmark paper, SPIM was used for a wide variety of biological applications, for example to track all cells in the early stages of Drosophila melanogaster larvae (Tomer et al., 2012; Krzic et al., 2012), zebrafish embryos (Keller et al., 2008), and mouse embryos both in the pre-implantation stage (Strnad et al., 2016) and during gastrulation and early organogenesis (McDole et al., 2018). Owing to the intrinsic fast acquisition rates, light-sheet microscopy is also ideally suited to capture dynamic processes such as blood flow in a beating zebrafish heart at high temporal resolution. (Mickoleit et al., 2014; Weber et al., 2017). Using genetically encoded calcium indicators as an optical readout of neuronal activity, light-sheet imaging provided whole brain activity maps of 80000 neurons in zebrafish larvae (Ahrens and Keller, 2013). Light-sheet based whole brain imaging was recently extended to screening applications in the search for antiepileptic drugs (Lin et al., 2018). In addition, the excellent signal-to-background ratio (SBR) of LSFM makes it well suited for detecting and tracking weak emitters down to the level of single molecules. In this domain, it was applied to study interactions and kinetics of single molecules in living cells (Tokunaga et al., 2008), combined with fluorescence correlation spectroscopy (Wohland et al., 2010; Capoulade et al., 2011) to study diffusion processes, and integrated with localization-based superresolution microscopy (Cella Zanacchi et al., 2011). Light-sheet microscopy was also combined with other modalities to optically manipulate the sample, for example with optogenetics (Arrenberg et al., 2010) and laser microsurgery (Engelbrecht et al., 2007).

3.2.1 Light-sheet generation and parameters

In the original SPIM publication (Huisken, 2004), the light-sheet was generated by directing a Gaussian beam through a cylindrical lens. This approach is extraordinarily simple and easy to set up, but it suffers from several drawbacks: Reshaping a Gaussian beam into an elliptical beam retains the Gaussian intensity profile which means that the illumination intensity varies across the FOV unless the beam is truncated by an aperture or the light-sheet is made much wider than the detection FOV. In addition, to change the width of the illuminated stripe, the intermediate optical system has to be modified or a zoom system has to be used (Ritter et al., 2011). An approach

to circumvent these issues is to create a "virtual light-sheet" by rapidly scanning a Gaussian beam across the FOV with a scan mirror in a digitally scanned light-sheet microscope (DSLM, Keller et al. (2008)). In a DSLM, the illumination intensity is constant across the FOV and the width of the light-sheet can be adjusted by changing the amplitude of the galvo scan. Since the illumination beam exposes each line on the detection camera for only a small fraction of the exposure time, the illumination intensity has to be increased accordingly. The higher peak intensities can lead to higher phototoxicity (Power and Huisken, 2017). Nonetheless, a DSLM can be used for long-term studies in embryonic development (Tomer et al., 2012; Krzic et al., 2012) without adverse effects. A DSLM setup is also well suited to accomodate improvements aimed at increasing the optical sectioning capabilities of the instrument in thick scattering specimen, for example by incoherent structured illumination (Keller et al., 2010) or by using a physical slit for the rejection of out-of-focus light in a confocal light-sheet microscope (Silvestri et al., 2012). A sectioning effect similar to a confocal slit can also be created by synchronization of the scanned beam with the rolling shutter of the camera (Baumgart and Kubitscheck, 2012).

In a DSLM setup, the radius $\omega(z)$ of the cross section of the Gaussian beam propagating along the z-axis varies as (Saleh and Teich, 2007):

$$\omega(z) = \omega_0 \cdot \sqrt{1 + \left(\frac{z - z_0}{z_R}\right)^2} \tag{3.1}$$

Here, ω_0 is the waist radius at $1/e$ E-field amplitude or $1/e^2$ intensity, z_0 is the location of the focus and z_R is the Rayleigh range:

$$z_R = \frac{n \cdot \pi \cdot \omega_o^2}{\lambda_0} \tag{3.2}$$

where n is the refractive index of the medium and λ_0 is the wavelength. One Rayleigh range z_R away from the focus, the beam diameter has increased by $\sqrt{2}$. As a measure of the axial elongation of the focal region, $2 \cdot z_R$ is often called the "depth of focus" or "confocal parameter".

The full-width at half amplitude (FWHM) size of a Gaussian beam is related to the waist radius ω_0 by:

$$\mathrm{FWHM} = \sqrt{2 \cdot \ln(2)} \cdot \omega_0 \approx 1.178 \cdot \omega_0 \tag{3.3}$$

Apart from Gaussian beams, other excitation modes can be used as well, for example Bessel beam (Fahrbach et al., 2010; Planchon et al., 2011) and Airy beams (Vettenburg et al., 2014) which have higher depths of focus than a Gaussian beam. In addition, a light-sheet can be generated using multiphoton processes such as two-photon (Truong et al., 2011) and three-photon excitation (Escobet-Montalbán et al., 2018). By combining these modalities, synergies can occur: For example, single-photon excitation with Bessel beams suffers from side-lobes as a Bessel function has a series of maxima around the central peak. These additional rings can be suppressed using two-photon excitation. Recently, another approach to reduce the side-lobes emerged: In a linear array of Bessel beams, destructive interference leads to the suppression of the side-lobes if the periodicity is chosen correctly. This realization forms the basis of lattice light-sheet microscopy (LLSM, Chen et al. (2014)). The generation of optical lattices in the excitation path was recently simplified by a field synthesis approach (Chang et al., 2019).

A simpler approach to render the excitation light-sheet more uniform is axially scanned light-sheet microscopy (ASLM, Dean et al. (2015). In ASLM, the waist of the Gaussian excitation beam is translated through the specimen using a remote focusing arrangement. The motion of the waist is synchronized with the rolling shutter of the camera. This method allowed isotropic imaging in single cells at 390-nm resolution throughout a 216×162×100 μm^3 imaging volume

3.2.2 Light-sheet configurations

The decoupling of the illumination and detection paths in a light-sheet instrument allows a wide variety of geometrical configurations – a light-sheet microscope can (and should) be designed around the sample (Huisken, 2012). Depending on the size and optical properties of the specimen and the required environmental conditions (immersion media, perfusion, temperature control)

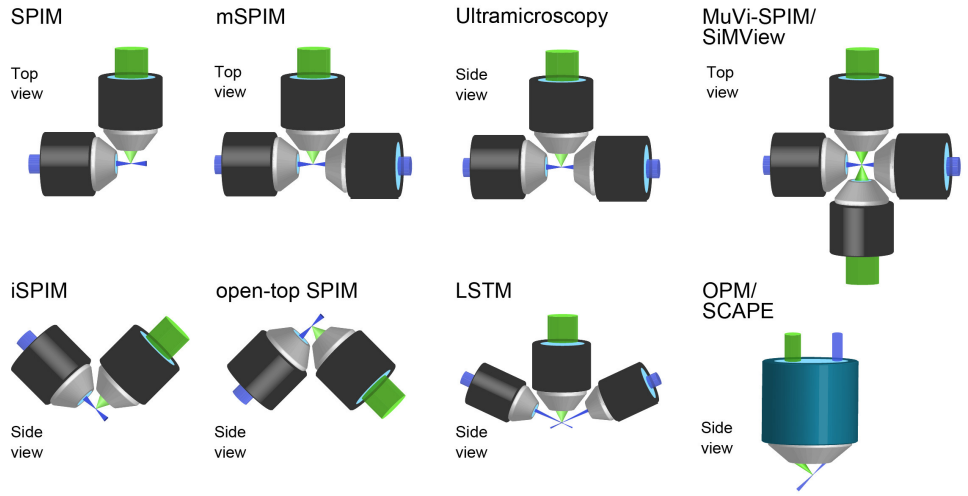

Figure 3.4: Various light-sheet configurations. Top row: Selective plane illumination (SPIM, Huisken (2004)), multidirectional SPIM (Huisken and Stainier, 2007), Ultramicroscopy (Dodt et al., 2007), multiview (MuVi, Krzic et al. (2012)) and simultaneous multiview (SIMview, Tomer et al. (2012)) setups. Bottom row: Inverted SPIM (iSPIM, Wu et al. (2011)), open-top light-sheet (OTLS) microscopy (McGorty et al., 2015), light-sheet theta microscopy (LSTM, Migliori et al. (2018)) and oblique plane microscopy (OPM, Dunsby (2008)) or swept confocally-aligned planar excitation (SCAPE, Bouchard et al. (2015))

it requires, a custom arrangement of the illumination and detection axis can be chosen. This leads to a wide variety of light-sheet microscope designs (reviewed in Power and Huisken (2018)), a selection of which are shown in Figure 3.4.

The original SPIM concept (Huisken, 2004) features horizontal excitation and detection paths which make it possible to rotate the sample around a vertical axis for multiview imaging. To increase the uniformity of the illumination and to reduce shadowing artifacts, the specimen can be illuminated from multiple directions hence the name multidirectional SPIM (mSPIM, Huisken and Stainier (2007)). Modern ultramicroscopy features a similar geometry, but has a vertical detection path (Dodt et al., 2007). This allows the use of immersion lenses, but renders sample rotation more complicated as the rotation axis has to be horizontal, which can lead to gravity-induced distortions in soft samples. To speed up time-lapse imaging in developmental biology, an additional detection path opposite the first was added to the SPIM design, which resulted in the multiview SPIM (MuVi-SPIM, Krzic et al. (2012)) and the simultaneous multiview

light-sheet microscope (SiMView, Tomer et al. (2012)). The second detection path is especially helpful in highly scattering samples such as Drosophila larvae as one of the two views will show higher image quality due to shorter path length inside the sample. In addition, having two simultaneously recorded views reduces the number of required rotations for multiview imaging. This concept was further scaled up to the isotropic multiview microscope (Chhetri et al., 2015), a setup in which each of the four objectives arranged around the sample can be part of an excitation or detection path.

To ALLOW LIGHT-SHEET IMAGING in a petri dish and make it compatible with a standard inverted microscope, the inverted SPIM (iSPIM, Wu et al. (2011)) geometry was created. It is very well suited for imaging flatworms such as *Caenorhabditis elegans* on a planar substrate both during development and in the adult stage. Just as in the case of multi-view setups in the horizontal plane, multi-view modifications of the iSPIM exist (Wu et al., 2013; Kumar et al., 2014). The iSPIM geometry can also be inverted to create an open-top light-sheet instrument (McGorty et al., 2015; Glaser et al., 2017). The iSPIM geometry can lead to very compact light-sheet instruments (Yang et al., 2016) and can also be used for two-photon excitation (Piksarv et al., 2017). When extending the upright light-sheet configuration to larger samples, the working distances and physical size of the excitation and detection objectives impose geometrical restrictions. To allow high-NA detection in large samples such as thick (multi-mm) cleared coronal slices of the human brain, the light-sheet theta microscope was conceived (Migliori et al., 2018). To accomodate samples ten to hundred-fold larger than the detection FOV, it does away with the strict orthogonal arrangement of the illumination and detection axes of standard light-sheet microscopes – similar to the original confocal theta microscope more than 20 years earlier (Stelzer et al., 1995). Deviating from an orthogonal design is also common for light-sheet microscopes designed for high-resolution imaging in single cells to accomodate the highest possible illumination and detection NAs (Theer et al., 2016).

Often, further mechanical restrictions apply and it is beneficial to do light-sheet imaging with all its advantages using only a single objective for both illumination and detection. This means that both the illumination and detection path have to share the available NA of a single objective. An optical setup tailored to achieve this was first implemented by Dunsby as oblique plane microscopy (Dunsby, 2008; Kumar et al., 2011) and later extended into "swept confocally-aligned planar excitation" (SCAPE) microscopy by the Hillman group (Bouchard et al., 2015). These setups require an additional pair of microscope objectives apart from the imaging objective to focus the tilted image plane onto a detector. Scanned oblique plane illumination (SOPi) forms a related single-objective technique that avoids volume distortions during the light-sheet sweep (Kumar et al., 2018; Kumar and Kozorovitskiy, 2019).

3.2.3 Shadow artifacts

A very common artifact in light-sheet microscopy are stripes or shadows: Every part of the sample that absorbs, scatters or refracts the light-sheet on its way through the sample will cast a shadow across the detection field-of-view (Figure 3.5). In this thesis, I refer to techniques that reduce or eliminate shadow artifacts as shadow reduction techniques. Reducing shadows actually begins long before imaging: In cleared specimens, for example, care should be taken to reduce the number of bubbles when mounting or index-matching samples. Nonetheless, even with sufficient clearing and index-matching, light-sheet generation with a cylindrical lens still leads to considerable shadow artifacts (Stefaniuk et al., 2016). Conceptually, the simplest modification of the microscope hardware is to illuminate the sample from opposing directions (Dodt et al., 2007) which also helps to counteract bulk absorption of the light-sheet inside tissue and forms the basis of multidirectional SPIM (mSPIM, Huisken and Stainier (2007)).

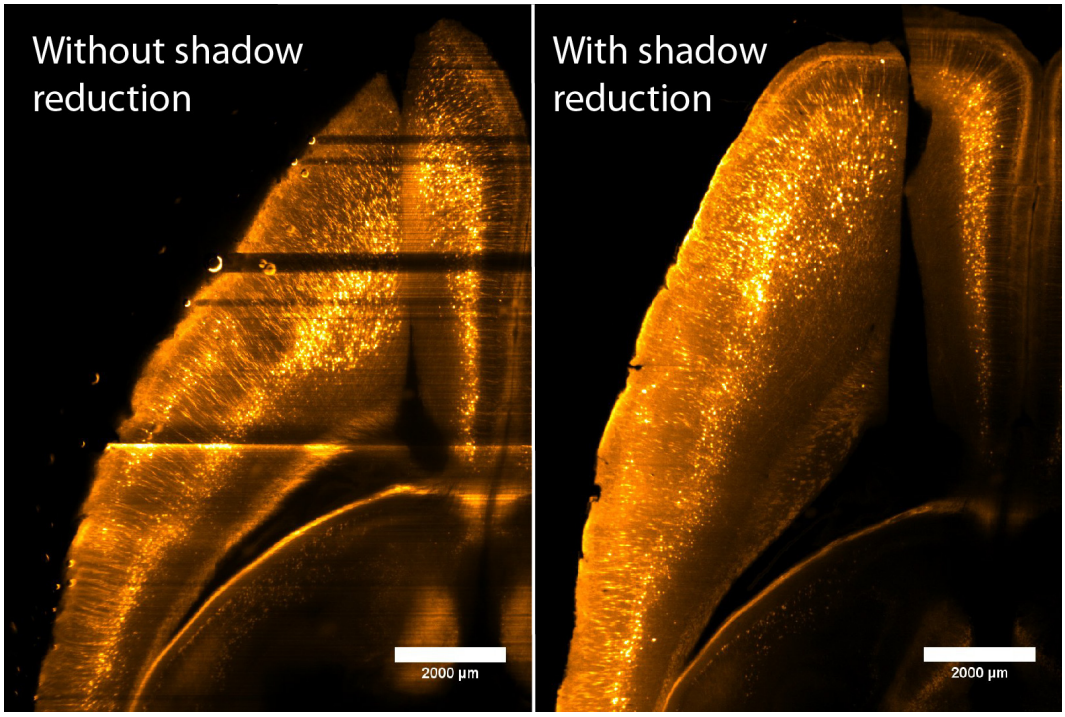

Figure 3.5: Shadow reduction in light-sheet microscopy. Left: Single horizontal plane acquired in a CLARITY-cleared Thy1-YFP mouse brain with an early mesoSPIM prototype. Due to bubbles on the surface of the sample, the image is full of shadow artifacts. Right: By using a scanned Gaussian beam, shadows are less apparent which leads to more uniform data quality.

In mSPIM, shadow artifacts are further reduced by rapidly pivoting the light-sheet in the focal plane. While at any given moment in time, shadows will be cast across the FOV, their direction will vary and shadow regions will be averaged out in sufficiently long exposures. To avoid any aliasing effects, the driving frequency of the pivoting mirror should be higher than the frame rate of the camera. Therefore, multi-kHz resonant scanners are often used in mSPIM setups. In a microscope where the light-sheet is created using a scanned Gaussian beam such as in a DSLM setup (Keller et al., 2008), shadow artifacts are reduced as well: The focused illumination beam allows "filling in" of the shadow cone behind absorbing structures (Fahrbach et al., 2010). While many DSLM setups use a rotationally symmetric Gaussian beam to create the virtual light-sheet, this is not necessary: By choosing the in-plane excitation NA higher than the NA perpendicular to the light-sheet, shadow artifacts can be further reduced (Glaser et al., 2018).

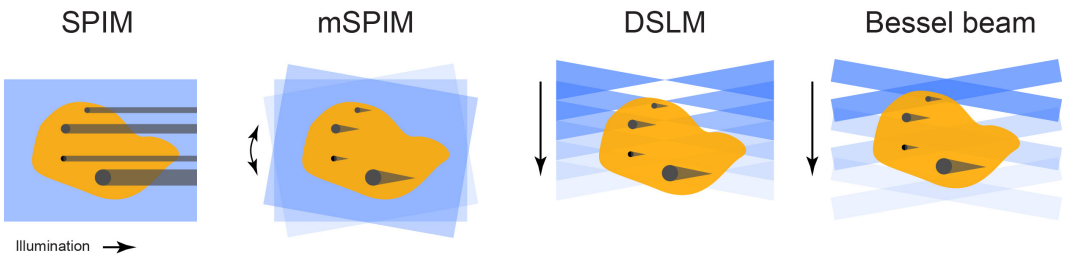

Figure 3.6: Comparison of various shadow reduction techniques. In a SPIM setup, there are no provisions to avoid shadows. Absorbing structures in the sample cast shadows across the FOV. By pivoting the light-sheet in a multidirectional SPIM (mSPIM, (Huisken and Stainier, 2007), shadows are shortened. In a DSLM (Keller et al., 2008), a Gaussian beam is scanned to create the light-sheet. The illumination cone of the exctiation beam reduces shadows. In a microscope utilizing a scanned Bessel beam (Fahrbach et al., 2010) for illumination, shadows are shortened as the Bessel beam is created by the interference of plane waves from different directions. This angular diversity shortens shadows and allows the Bessel beam to reconstitute itself behind an obstruction in a process known as self-reconstruction or self-healing.

Other excitation beams such as Bessel and Airy beams are also beneficial for reducing shadows (Fahrbach et al., 2010; Müllenbroich et al., 2018a) – these beams are often called self-reconstructing or self-healing beams (Bouchal et al., 1998) as they can recover their original beam profile if part of the illumination beam is blocked by an absorber or scatterer. Shadow reduction is also of interest for functional imaging – for example for calcium imaging (Müllenbroich et al., 2018b) as the dynamic shadows cast by passing red blood cells can introduce additional noise in brain activity maps of zebrafish embryos. A different solution is not to modify the excitation beam, but to translate the sample through the light-sheet so that the position of shadow-generating parts of the sample shifts. Shadow artifacts can then be reduced using image processing (Dong et al., 2014). Apart from this combined hard- and software approach to shadow reduction, there are pure computational solutions as well, for example methods based on wavelet and Fourier filtering (Münch et al., 2009), variational stationary noise removal (VSNR, Fehrenbach et al. (2012)) and multidirectional stripe remover algorithms (MDSR, Liang et al. (2016)). While these methods allow a reduction in stripes without affecting image quality too much by the introduction of additional artifacts, they can come with considerable processing time. In addition, information from other modalities such as an absorption map of the specimen acquired using OPT can be integrated into a shadow correction algorithm (Mayer et al., 2018).

3.2.4 Light-sheet microscopes for cleared tissue

As even the first fluorescence-based light-sheet microscope (Voie et al., 1993) was intended for cleared tissue preparations, there is a long history of designing LSFM instruments for such samples. Compared to the *in vivo* case, imaging in fixed samples does away with the need for high temporal resolution but comes with a series of engineering challenges as well:

- The samples are usually much larger than mm-sized embryos and can reach the size of a whole mouse (Susaki et al., 2015; Pan et al., 2016).
- The refractive indices of the imaging media are much higher than water ($n_D = 1.33$) – for example, $n_D = 1.45$ for CLARITY and $n_D = 1.56$ for BABB. Ideally, the illumination and detection optical paths should be corrected for the immersion medium.
- While many clearing techniques lead to highly transparent and optically homogenous tissue, the optical path lengths of the excitation light-sheet into the tissue and for the emitted fluorescence out of the sample are larger due to the larger sample sizes. Compared to *in vivo* imaging, scattering due to local index mismatches in the sample is less of a problem, but absorption can still be an issue.
- While temporal resolution is not a concern in fixed samples, throughput is: Ideally, the high acquisition speeds in LSFM are used as an advantage to collect data from larger imaging volumes or more samples.
- The optical resolution should be as uniform as possible and ideally isotropic.

Light-sheet microscopes for cleared tissue generally fall into two categories:

- Instruments based on standard microscope optics (using an objective / tube lens combination) with small to medium (<10 mm) FOVs (Silvestri et al., 2012; Tomer et al., 2014; Müllenbroich et al., 2015). In this category, the numerical aperture of the detection path

can be large (up to NA 1.0), but manufacturers offer very few low-magnification objectives with long working distance – therefore, the instruments are limited in maximum FOV.

- Instruments based on macroscopes, often with intermediate zoom optics (Santi et al., 2009; Mertz and Kim, 2010; Schwarz et al., 2015) and FOVs larger than 10 mm. Most manufacturers offer macroscopes with maximum FOVs larger than 50 mm and long working distances, but there are no immersion objectives available. The maximum NA is usually 0.5, which is reached across FOVs of 1 or 2 mm.

To combine the benefits of both approaches, some studies employ optical systems from both categories (Dodt et al., 2007).

Setup improvements beyond the capabilities of a standard SPIM instrument include means for shadow reduction (Schwarz et al., 2015), improvements to to the optical sectioning capability by rejecting out-of-focus background – for example by confocal detection (Silvestri et al., 2012) or structured illumination (Mertz and Kim, 2010). Optical sectioning can also be enhanced by thinner and more uniform light-sheets created using aspherical elements (Saghafi et al., 2014; Dodt et al., 2015). To increase microscope throughput, the detection path can be modified as well, for example by extending the detection point-spread function (PSF) axially through the introduction spherical aberration (Tomer et al., 2015). In combination with subsequent deconvolution, this allows to increase the volumetric imaging rate. Improved sample mounting strategies can be highly benefical as well. To this end, the CLARITY-optimized light-sheet microscope (COLM, Tomer et al. (2014)) introduced quartz cuvettes borrowed from spectroscopy as sample containers. As quartz has approximately the same refractive index as an index-matched CLARITY sample ($n_D = 1.45$), this creates only a minimum of additional aberrations. In addition, the small cuvette volume keeps the required amount of mounting medium low which is valuable as many water-based refractive index matching media tend to have a lot of striae (index inhomogeneities). A small sample cuvette thus reduces the optical path length of the light-sheet which lowers the amount of aberrations introduced by the immersion medium.

The following chapter introduces the mesoSPIM, a light-sheet instrument which combines macroscopic detection, COLM-inspired cuvette mounting of samples, and uniform axial resolution. It extends previous work aimed at creating open-source imaging platforms for cleared tissue such as the openSPIM (Pitrone et al., 2013; Stefaniuk et al., 2016) and the openSPIN (Gualda et al., 2013).

A simple system may or may not work.

A complex system that works is invariably found to have evolved from a simple system that worked. A complex system designed from scratch never works and cannot be patched up to make it work. You have to start over, beginning with a working simple system.

John Gall, *General Systematics, 1975*

4

The mesoscale selective plane illumination microscope (mesoSPIM)

The mesoSPIM project started in late 2015 when the lab of Adriano Aguzzi approached the Helmchen lab with a request for help in the selection of a light-sheet microscope for CLARITY-cleared mouse brains. Initially, a commercial (the LaVision Ultramicroscope I) and a custom setup (the COLM by Tomer et al. (2014)) were tested. Both had advantages and disadvantages: For example, the large FOV of the Ultramicroscope was excellent (based on a zoom macroscope) which could easily visualize a whole mouse brain. However, the Ultramicroscope sample mounting technique was based on clamping holders which are excellent for the small, hard samples prepared with organic solvent-based methods, but less than ideal for the soft and expanded samples resulting from CLARITY. In addition, the working distance of the dipping objective and the travel range of the sample stages were 10 mm and thus too small for CLARITY samples. This is partly due to

the Ultramicroscope being designed around 2009 – at a time before hydrogel-based clearing techniques became commonplace. On the other hand, the COLM setup featured a very simple sample mounting technique by placing CLARITY-samples in quartz cuvettes with approximately the same refractive index ($n_D = 1.45$). The horizontal light-sheet detection path allowed quick sample exchange and sample rotation which is unavailable on the Ultramicroscope due to its vertical detection path. The main shortcoming of the COLM was its small FOV – based on standard microscope objectives, it could achieve a maximum FOV of 3-6 mm, which is much smaller than a whole cleared mouse brain. This meant that every whole-brain acquisition required a mosaic or tiling acquisition – which resulted in long acquisition times and large datasets. We noted that the COLM instrument delivers excellent image quality, however, the high resolution was unnecessary for some of the planned imaging projects – for example to localize virus injection sites or to visualize sparse expression patterns in a mouse brain. In addition, it became apparent that establishing any clearing technique is a long-term process and usually, the first batches of cleared samples are not satisfactory. Therefore, I reasoned, a light-sheet macroscope capable of using sample cuvettes would be ideal for our needs. Originally, this setup was intended as a low-cost side project, but over the course of the past years it was developed into a facility-grade instrument.

4.1 mesoSPIM capabilities

As in many other fields of engineering, coming up with clear specifications for a new device is a challenging task. In the case of the mesoSPIM, it became apparent that users can appreciate good data when they see it – but they provide conflicting priorities on how to achieve good data quality: Understanding which engineering trade-offs need to be made to arrive at an instrument that users enjoy to use is not straightforward. For example, users are unanimously in favor of higher resolution, but often fail to realize that doubling the x/y and z-resolution leads to an eightfold increase in data size and often a similar increase in acquisition times – both of which will drastically affect how they plan their imaging studies. In the end, I arrived at a coarse list of top-level requirements I deemed necessary for a large-FOV light-sheet mesoscope:

- Compatibility with all clearing techniques
- Quick exchange of samples within seconds and usage of sample cuvettes.
- Uniform axial resolution across cm-sized fields of view.
- The ability to image at least a whole mouse central nervous system without cutting or remounting.
- Multiview imaging (easy sample rotation)
- Overview scans of whole cleared mouse brains at cellular resolution within minutes.
- Dual-sided light-sheet illumination with a minimum of shadow artifacts to simplify post-processing.
- Modular and open hard- and software

These requirements evolved in a series of iterations of the microscope hardware. For example, early on, it turned out that shadow reduction and quick sample exchange are highly beneficial to allow the fast screening of cleared samples without much postprocessing of data, thus providing users with quick feedback. Later, when processing datasets from early generation mesoSPIMs, we noticed that uniform axial resolution and ideally, isotropy across cm-sized FOVs makes segmentation and visualization of features much easier.

During the development phase we realized that such requirements are of considerable interest for other research groups seeking light-sheet instruments for cleared tissue. I thus decided to turn the mesoSPIM project into an open hardware initiative to make the microscope as accessible as possible. This follows in the footsteps of open-source light-sheet microscopes such as the openSPIM (Pitrone et al., 2013) and the openSPIN (Gualda et al., 2013). The idea of the mesoSPIM initiative (mesospim.org) is to provide instructions, guidelines, and software for developers and users to build, operate and improve light-sheet mesoscopes for cleared tissue.

The following manuscript provides an overview of the features and capabilities of the instrument. For this project, I initiated the research, designed all mesoSPIM variants, wrote the microscope software, wrote hard- and software documentation and the manuscript, set up three mesoSPIM microscopes and helped setting up two more. With samples provided by my collaborators, I performed measurements and analyzed data. Given that the project has the character of a resource, the manuscript was submitted as a correspondence and is rather short. Therefore, the extensive supplementary notes describing and characterizing the instrument are included in the main text of this thesis.*

* The manuscript with supplementary material (including supplementary videos) is available as a preprint on bioRχiv: biorxiv.org/content/10.1101/577122v1

4.2 The mesoSPIM initiative: open-source light-sheet mesoscopes for imaging in cleared tissue

Fabian F. Voigt, Daniel Kirschenbaum, Evgenia Platonova, Stéphane Pagès, Robert A. A. Campbell, Rahel Kastli, Martina Schaettin, Ladan Egolf, Alexander van der Bourg, Philipp Bethge, Karen Haenraets, Noémie Frézel, Thomas Topilko, Paola Perin, Daniel Hillier, Sven Hildebrand, Anna Schueth, Alard Roebroeck, Botond Roska, Esther Stoeckli, Roberto Pizzala, Nicolas Renier, Hanns Ulrich Zeilhofer, Theofanis Karayannis, Urs Ziegler, Laura Batti, Anthony Holtmaat, Christian Lüscher, Adriano Aguzzi, and Fritjof Helmchen

Over the course of the past decade, tissue clearing methods have reached a high level of sophistication with a wide variety of approaches now available (Richardson and Lichtman, 2015). To image large cleared samples, light-sheet microscopes have proven to be ideal due to their excellent optical sectioning capability in transparent tissue (Dodt et al., 2007). Such instruments have recently seen extensive technological and commercial development. However, despite this progress, the community is lacking instruments capable of exploring large samples with near-isotropic resolution within minutes. Here, we introduce the mesoscale selective plane-illumination microscopy (mesoSPIM) initiative, an open-hardware project that provides researchers with instructions and software to easily build and operate light-sheet microscopes for centimeter-sized cleared samples (mesospim.org).

A wide range of commercial light-sheet microscopes have become available since the invention of SPIM (Huisken and Stainier, 2007), most of them optimized towards time-lapse imaging in transparent developing embryos or – if designed for cleared tissue – tailored for only a narrow selection of clearing techniques and immersion media. To overcome these limitations, we set out to design a modular light-sheet mesoscope (Figure 4.1a) that combines simple and versatile sample handling with large fields-of-view (FOV) of 2-20 mm. Large-FOV light-sheet micro-

scopes typically suffer from non-uniform axial resolution due to the varying thickness of the light sheet (Figure 4.1b). To address this issue, we use a tunable lens to shift the excitation beam waist through the sample in synchrony with the rolling shutter of the camera, a method called "axially scanned light-sheet microscopy" (ASLM, Dean et al. (2015)) (Figure 4.1b). For whole mouse brains ($\approx$ 1 cm^3), typical datasets are isotropic (6.5 µm) small (12-16 GB), and they are recorded quickly (7-8 minutes) with minimal shadow artifacts. Together with standardized quick-exchange holders, these features allow for the fast screening of samples. With a travel range of 44×44×100 mm, very large samples such as a whole mouse central nervous system can be imaged. After acquiring overview datasets, users can zoom in and record multidimensional data at higher resolution by mosaic acquisitions, for example revealing cellular distribution and long-range axonal projections of Purkinje cells in the mouse cerebellum ((Figure 4.1c-e) or fine neurites in the developing nervous system of a chick embryo (Figure 4.1f). The instrument has been tested in combination with all common clearing methods ranging from CLARITY (Chung et al., 2013), CUBIC (Susaki et al., 2014) to organic solvent approaches such as iDISCO (Renier et al., 2014) and BABB (Dodt et al., 2007). Due to the modular design of the mesoSPIM, switching between different imaging media can be done in less than a minute. The mesoSPIM setup, performance characterization, and example applications are presented in detail in Supplementary Notes including Supplementary Figures 1-30. Inspired by the openSPIM (Pitrone et al., 2013) and openSPIN (Gualda et al., 2013) projects, documentation for the mesoSPIM hardware and software (written in Python) is freely available (github.com/mesoSPIM). Currently, there are 5 mesoSPIM setups in operation across Europe. The mesoSPIM is the ideal instrument to quickly bridge scales from the µm- to the cm-level, and serves as an excellent tool for detailed three-dimensional anatomical investigations in neuroscience and developmental biology.

Code availability The mesoSPIM software and documentation are available on Github (github.com/mesoSPIM). mesoSPIM-control is licensed under the GNU General Public License v3.0 (GPL v3).

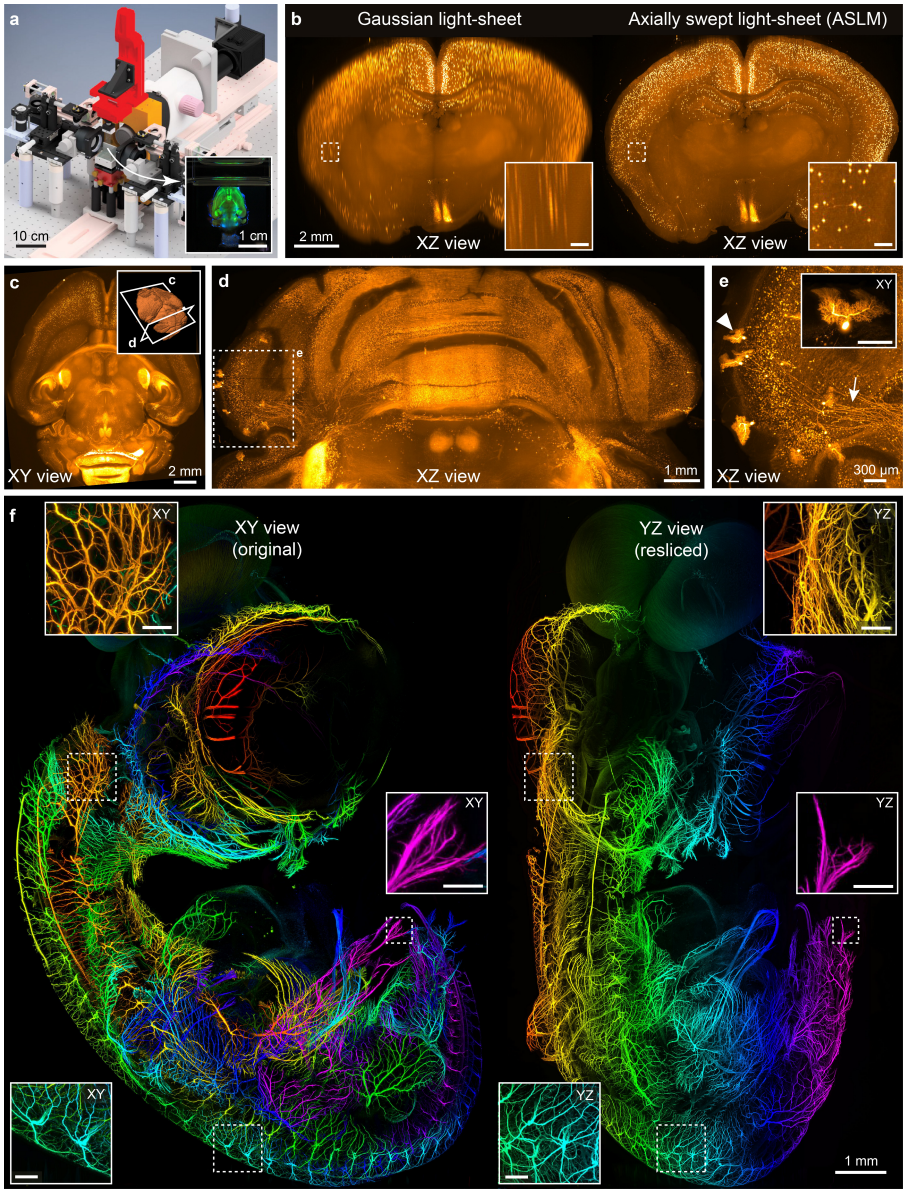

Figure 4.1: Example demonstrations of the mesoSPIM light-sheet mesoscope. a) Overview of the mesoSPIM instrument. Inset: Photograph of a Thy1-YFP mouse brain during image acquisition. b) Comparison of axial image quality achieved in a CLARITY-cleared VIP-tdTomato mouse brain for scanning with a Gaussian beam (left) and for the axially swept light-sheet mode, ASLM (right). Images are maximum intensity projections over 250-µm range. c) Overview image of a CLARITY-cleared TPH2Cre-tdTomato mouse brain. Inset shows 3D orientation of views in c and d. d) XZ maximum intensity projection of a high-resolution dataset (4× zoom, range: 500 µm) taken in the cerebellum of the sample in c. e) Volume rendering of sparsely labeled Purkinje cells and their axonal projections (arrow). Inset: individual Purkinje cell (arrow head, scale bar: 200 µm). f) Depth-coded original XY (left) and resliced YZ (right) projections of a dataset taken from a 7-day old chicken embryo (neurofilament labeling) cleared using BABB. Throughout the dataset (acquired at 1.6×1.6×2 μm^3 sampling), neurites are visible in great detail. Because of the ASLM mode this same holds true for the original (transverse) and the resliced (axial) direction. The assignment of color to Z-position is similar for both the XY and YZ view. Scale bars of all insets: 200 µm.

4.3 Supplementary material

4.3.1 Supplementary Note: The mesoSPIM initative – overview and mesoSPIM features

Overview

The 'mesoscale selective plane illumination microscopy' (mesoSPIM) initiative aims to provide the imaging community with open-source light-sheet microscopes for large cleared samples. On the one hand, it is aimed at neuroscientists and developmental biologists seeking high-quality anatomical data from cleared samples, on the other hand, it strives to provide instrumentation developers with an imaging platform that can be tailored towards specific needs – i.e. to accommodate uncommonly large samples or different illumination schemes. To achieve these goals, we have designed the mesoSPIM to be compatible with all major clearing techniques, ranging from hydrogel-based approaches such as CLARITY to organic-solvent based clearing techniques such as BABB and iDISCO (see subsection 4.3.7). Both the immersion cuvettes and sample holders are highly modular to allow quick sample exchange and customization (see subsection 4.3.4). In addition, we noted that in a light-sheet microscope, data acquisition, visualization and analysis are greatly facilitated if the microscope generates raw data at high and uniform axial resolution across the FOV. The mesoSPIM achieves this by incorporating an axially scanned light-sheet microscopy (ASLM) mode (see subsection 4.3.2). ASLM facilitates data acquisition as every generated raw image has uniform axial resolution which mean that fewer tiles are necessary to cover a sample compared to a microscope with varying light-sheet thickness (where only a narrow stripe along the light-sheet waist has the best axial resolution). Scanning fewer tiles leads to smaller datasets and faster acquisition times. Having near-isotropic raw data also allows visualization without extensive post-processing or deconvolution and aids in segmenting structures of interest. While the mesoSPIM initative will evolve to include improved features in the instruments, we believe that the current configuration already satisfies a wide range of application requirements.

Existing setups

As of February 2019, five mesoSPIM V4 (Version 4) setups are operational across various research labs and imaging facilities in Europe:

- Brain Research Institute, University of Zurich (Helmchen group)
- Institute of Neuropathology, University Hospital Zurich (Aguzzi group)
- Wyss Center Geneva (Advanced Lightsheet Imaging Center 'ALICE')
- Center for Microscopy and Image Analysis, University of Zurich
- Sainsbury Wellcome Center for Neural Circuits and Behavior London (Advanced Microscopy Facility)

Several additional mesoSPIM V4 and V5 instruments are currently under construction. Version 5 is the latest (and recommended) design, it incorporates better sample stages with larger travel range. All data in this manuscript was acquired using a mesoSPIM V4.

Core features

- Horizontal detection path as in the original SPIM (Huisken, 2004) – which allows for sample rotation by suspending the sample from the top without changing the direction of gravity acting on the sample.
- Macro-zoom system (Olympus MVX-10) in the detection path, enabling large FOVs of 2-21 mm in combination with a 1× air objective (Olympus MVPLAPO1×).
- Dual-sided illumination
- Exitation path designed for minimal shadowing artifacts (stripes cause by refraction, scatting, and absorption inside the sample) by using an illumination scheme which delivers comparable results to the multidirectional SPIM (mSPIM, Huisken and Stainier (2007)).

- Uniform axial resolution across such FOVs by axially scanned light-sheet microscopy (ASLM, Dean et al. (2015)) based on a tunable lens.

- Large travel range (44.5 mm × 44.5 mm × 100 mm) to accommodate specimens such as a whole cleared mouse CNS without the need for remounting or cutting.

- Compatibility with all major clearing techniques ranging from hydrogel-based methods such as CLARITY (Chung et al., 2013), hydrophilic reagent-based techniques such as CUBIC (Susaki et al., 2014) to organic solvent approaches such as 3DISCO (Ertürk et al., 2012b,a) and BABB (Spalteholz, 1911; Dodt et al., 2007).

- Switching between different imaging media optimized for specific clearing methods is accomplished by quick-exchange immersion cuvettes on magnetic mounts and can be done in tens of seconds. Samples are suspended in the immersion cuvettes from the top.

- Sample mounting can be done either in sample cuvettes (as for the COLM setup (Tomer et al., 2014) or using 3D-printed sample clamps (i.e. for iDISCO (Renier et al., 2014)). Magnetic sample holders allow for quick sample exchange within tens of seconds.

- Open and modular hardware and software to adapt the instrument to custom imaging requirements.

Comparison to commercial and open-source light-sheet instruments

In the light-sheet community several open-source light-sheet projects exist, for example the openSPIM (Pitrone et al., 2013)) and openSPIN (Gualda et al., 2013) projects, which aim to provide scientists without prior knowledge in building optical systems with low-cost entry-level light-sheet microscopes. Simlilarly, the mesoSPIM initiative aims to build a community of users and developers of mesoSPIM setups to foster the exchange of ideas and solutions around imaging technologies for cleared tissue. We hope that the mesoSPIM design provides a starting point for other developers to add and share their own improvements and modifications.

However, open-source instrumentation also has issues: Achieving consistent data quality and sample throughput appropriate for publication with low-cost setups is challenging (Girstmair et al., 2016). For example, the openSPIM project is highly successful as a tool to train microscopists on how to build and use a light-sheet microscope. However, only a small fraction (Kolesová et al., 2016; Costa et al., 2016; Stefaniuk et al., 2016; Rühland et al., 2015; Mendonca et al., 2018; Lloyd-Lewis et al., 2016; Wang et al., 2018a) of the 152 citations (as of March 2019) of the original openSPIM publication present original biological research acquired with an openSPIM.

With the mesoSPIM initiative, we hope to provide a mesoscopic imaging instrument for cleared tissue en par or better than existing options. The setup is thus suitable for research groups or imaging facilities in search of alternatives to the existing palette of commercial instruments. Typically, we recommend the mesoSPIM to teams in which at least one team member has experience in setting up custom microscopes such as a two-photon microscope or a lattice light-sheet instrument. In addition, we would like to emphasize that in the long run—as with every custom microscope – a mesoSPIM is only as good as its support staff and that experienced local support is absolutely necessary.

Compared to the current generation of commercial light-sheet instruments suitable for cleared tissue, the mesoSPIM is most similar to the LaVisionBiotec Ultramicroscope II. They share the usage of the Olympus MVX-10 macro zoom system to achieve large FOVs in the cm-range. Whereas the Ultramicroscope has a vertical detection path and a light-sheet parallel to the horizontal plane (which simplifies the usage of dipping objectives), the mesoSPIM has a horizontal detection path and a vertical light-sheet (which allows quick exchange of samples and immersion cuvettes and allows sample rotation around a vertical rotation axis). Other commercial instruments such as the Zeiss Z.1 or Luxendo MuVi SPIM CS share this vertical light-sheet geometry but only fit small samples due to travel range limitations (<10 mm in XYZ vs. 44.5 mm × 44.5 mm × 100 mm of the mesoSPIM V4). However, these instruments can be used with high-NA immersion objectives and thus allow higher imaging resolution. This option is currently not

implemented in the mesoSPIM and would require the design of special imaging chambers. Another instrument is the ct-diSPIM by Applied Scientific Instrumentation (ASI), which is based on the inverted SPIM (iSPIM) geometry (Wu et al., 2011) and can fit samples of comparable size to the mesoSPIM but only with a maximum thickness of 5 mm (limited by the working distance of the objectives). With its multi-immersion objectives (nD = 1.33-1.56) this microscope is also one of the few commercial instruments that is compatible with all clearing techniques without major modifications. However, owing to its light-sheet geometry it lacks a rotation stage for multi-view acquisitions. In addition, it is currently not available with FOVs in the cm-range.

Several existing commercial microscopes also feature imaging modes yielding uniform axial resolution across the FOV. For example, the LaVisionBiotec Ultramicroscope II has a "dynamic focus" mode that mechanically translates the waist location while merging subsequent images. This approach is, however, much slower than the ASLM implementation used in the mesoSPIM. Other commercial light-sheet instruments such as the LifeCanvas SmartSPIM and the 3I light-sheet microscope feature imaging modes with uniform axial resolution that are faster, for example by adopting a tiling light-sheet approach in the 3I instrument (Gao, 2015; Fu et al., 2016) using spatial light modulators. Both instruments are using vertical detection paths like the LaVisionBiotec Ultramicroscope and the mesoSPIM.

A key advantage of the mesoSPIM compared to all existing commercial setups is that it supports imaging samples immersed in sample cuvettes, an idea that was introduced by Tomer et al. in the CLARITY-optimized light-sheet microscope (COLM Tomer et al. (2014)). Because developing mounting strategies for different types of samples (Weber and Huisken, 2011; Huisken, 2012; Reynaud et al., 2015) is a key aspect of using a light-sheet microscope, being able to quickly image samples by putting them in an imaging cuvette renders mesoSPIM usage highly ergonomic. Restricting the volume needed for index-matching the sample is beneficial if the refractive index matching solution (RIMS) is costly. Furthermore, if the excitation light-sheet has to pass through

less medium solution, the refractive index inhomogeneities of water-based high-index RIMS media do not degrade light-sheet quality as much as compared to immersing the sample in a larger chamber. For example, the LaVision Ultramicroscope with its large (10 cm) imaging cuvette is less suited for imaging CLARITY samples for that reason. In summary, we believe that the combination of mesoSPIM features is unique and only partially available commercially and that the mesoSPIM constitutes a highly capable multi-user imaging platform for large cleared samples.

mesoSPIM Budget

While the parts lists for both mesoSPIM version 4 and 5 can be used to prepare a detailed budget, a coarse overview is provided in table 4.1.

Component	Cost (USD)
Optical table	8000
Camera	17000
Olympus MVX-10	11500
Filter wheel	7400
Laser engines	40000-110000
Mechanical stages	26000
Imaging computer	9000
Electronics	10000
Optics & Optomechanics	32200
Total	169600-239600

Table 4.1: mesoSPIM V4/V5 budget overview. The laser engine (fiber-coupled laser combiner with multiple laser lines) is the most expensive single item. For this list, it is assumed that the mesoSPIM will be built in a full configuration with dual-sided illumination and a wide variety of excitation laser lines and emission filters. Prices are based on quotations we obtained for setting up several mesoSPIM instruments in Switzerland and were converted to USD at an exchange ratio of 1:1 (as of February 2019). Owing to import, customs, and shipping expenditures, costs are likely to be considerably different in other countries.

4.3.2 Supplementary Note: Axially scanned light-sheet microscopy (ASLM): A key mesoSPIM imaging mode

Users of early light-sheet setups such as the orthogonal-plane fluorescence optical sectioning (OPFOS) instrument by Voie et al. (Voie et al., 1993; Voie and Spelman, 1995) or the selective plane

illumination microscope (SPIM) by Huisken et al. (Huisken, 2004) noted that the quality of the 3D reconstruction of specimens were critically dependent on the effective thickness of the optical sections. As these first-generation fluorescence-based light-sheet instruments relied on Gaussian beams in their illumination paths, the variation of the beam profile along the excitation direction caused images to be sharp in the center but increasingly blurry towards the edges if the datasets were viewed from the side (in the XZ-plane). Therefore, the illumination path was usually set up in a way that the Rayleigh-range z_R of the illumination beam was approximately twice the FOV size provided by the camera. In this way, the light-sheet thickness varied only by $\sqrt{2}$ cross the FOV. However, this is unsatisfactory at low magnification (<20×) as the sub-µm lateral resolution provided by the emission path outweighs the multi-µm axial resolution provided by the light-sheet (Engelbrecht and Stelzer, 2006).

A SIMPLE SOLUTION is to restrict the readout of the 2D imaging detector to a region around the center of the light-sheet waist and move the sample through this region while taking sequential images (Voie, 2002) – essentially performing extensive tiling acquisitions. This takes more time because for each z-plane the sample has to be moved several times in the lateral direction. Essentially, the parallel 2D readout (which massively speeds up volume acquisition in a SPIM compared to a point-scanning microscope) is reduced to a quasi-1D readout if the best axial resolution is desired. Nonetheless, the slow acquisition allows the resulting datasets to exhibit a high degree of axial uniformity. As most of the sensor area is thus not used for collecting data, it made sense to simplify the sensor from a 2D array to a Time Delay and Integration (TDI) detector where the movement of the sample is synchronized with the readout of the camera – an idea first implemented in a thin-sheet laser imaging microscope (TSLIM) in 2010 (Schacht et al., 2010). During the same time, other groups explored the usage of a confocal slit as a spatial filter (similar to a confocal microscope) to improve the axial resolution and uniformity of light-sheet microscopes (Silvestri et al., 2012) in a digitally scanned light-sheet microscope (DSLM) (Keller et al., 2008). As the detector 'sees' only ballistic photons from the light-sheet, this approach helps to reduce

the impact of scattering. With the introduction of scientific sCMOS cameras into microscopy, it was noted that the rolling-shutter readout mode of such a camera could be used to approximate a confocal slit (Baumgart and Kubitscheck, 2012). The rolling shutter restricts the active line to a few rows, which can be synchronized with the DSLM scanning motion to create a light-sheet. At the same time, several groups explored the capabilities of other excitation geometries to create thinner as well as more uniform light-sheets by employing two-photon excitation (Truong et al., 2011), non-diffracting Bessel (Fahrbach et al., 2010; Planchon et al., 2011), and Airy beams (Vettenburg et al., 2014) and combinations thereof (Fahrbach et al., 2013a). In 2014, Dean et al. (Dean and Fiolka, 2014) used a tunable acoustic gradient (TAG) lens to create an extended focus out of a Gaussian beam for more uniform axial resolution. In 2015, the same group combined the remote focusing system by Botcherby et al. (Botcherby et al., 2007) with the externally (controlled) rolling-shutter readout of a modern sCMOS camera to form an axially swept light sheet microscopy (ASLM) instrument (Dean et al., 2015). Briefly, the waist motion through the sample was synchronized with the readout of the rolling shutter so that during the sweep the waist location tracked the active line on the camera (see Figure 4.2). This instrument yielded isotropic 390-nm resolution throughout a 216×162×100 μm^3 imaging volume. The major drawback is similar to earlier approaches, namely a longer acquisition time for the creation of 3D data because for each z-plane, additional time has to be spent sweeping the light-sheet across the FOV to collect a sufficient number of signal photons. With tunable optical elements, as employed in the mesoSPIM systems, however, there are no heavy mechanical parts that have to be moved, which leads to a considerable speedup. However, each plane has to be illuminated for a longer time to perform the axial sweep, which can lead to increased photobleaching.

In 2016, Hedde and Gratton (Hedde and Gratton, 2016) used an electrically tunable lens (ETL) as the remote focusing device for ASLM, a device which can also be used to tune the excitation light-sheet to the shape of the sample (Chmielewski et al., 2015) by positioning the waist at regions of interest, for example to illuminate the outline of a Drosophila embryo as efficiently

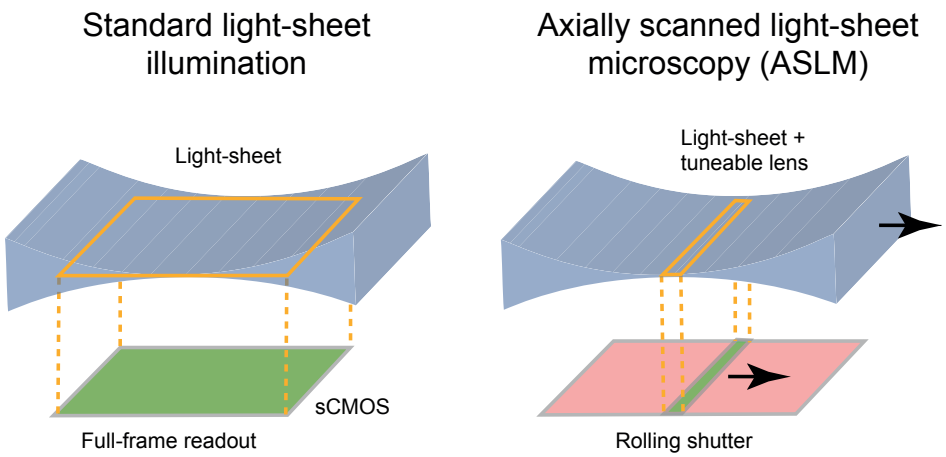

Figure 4.2: Comparison of standard light-sheet illumination and axially scanned light-sheet microscopy. With standard illumination, the whole frame is read out at once, which leads to non-uniform axial resolution across the FOV. In ASLM mode, the readout of the camera is synchronized with the motion of the light-sheet waist through the sample. The final image contains only signal from the waist region which leads to uniform axial resolution across the FOV.

as possible. A comparable effect to ASLM can be achieved by tiling the excitation beam waist (Gao, 2015; Fu et al., 2016) using spatial light-modulators (SLM). A further option is to use lattice light-sheet illumination (Chen et al., 2014; Liu et al., 2018) which has not been implemented yet for cm-sized FOVs.

While testing early mesoSPIM prototypes (Version 1 to 3), which employed cylindrical lenses or scanned Gaussian beams to create the light-sheet, we noted that especially in large (cm-sized) samples, achieving uniform axial resolution is a key requirement. At 488 nm and at $n_D = 1.45$, even a light-sheet with a 5-µm (FWHM) waist in the center expands to approximately 400 µm at the edges of a 13.4 mm FOV (a size, which is for example needed to image a whole CLARITY-cleared mouse brain). As noted above, this loss of axial resolution means that most light-sheet instruments are used with extensive tiling acquisitions (Tomer et al., 2014; Doerr et al., 2017; Stefaniuk et al., 2016) yielding hundreds of GB per brain. We reasoned that implementing a light-sheet illumination mode with more uniform axial resolution would both lead to higher data quality and easier data analysis and allow users to screen samples at near-isotropic resolution

before committing to generate TB-sized datasets. We noted that for many labs in the early stages of adopting a clearing method, sample quality was usually not sufficient to warrant generation of high-resolution data across the whole sample. However, visualizing at which locations inside a whole-brain sample clearing or labeling quality were insufficient was not straightforward at low magnification because a light-sheet with 40-100 µm thickness (with a Rayleigh range z_R) tuned to large FOVs) led to extensive axial blurring of features. Therefore, we reasoned that achieving a thinner and more uniform effective light-sheet thickness would allow better visualization of features at low magnification and possibly also improve data quality at higher magnification. Among the possible options (ASLM, tiled light-sheets, nonlinear excitation, Bessel or Airy-beams, or a lattice light-sheet approach) we selected ASLM. Given that our macro-light-sheet instrument was supposed to have FOVs ranging from 2-20 mm and be capable of exciting a wide variety of fluorophores, we deemed ASLM as the simplest single-photon approach to be most appropriate and cost-efficient. Given our positive previous experiences with electrically tunable lenses in microscopy (Grewe et al., 2011; Fahrbach et al., 2013b), we decided to include ETLs as remote focusing units in the optical path as suggested by Hedde and Gratton (Hedde and Gratton, 2016).

To demonstrate that the resulting mesoSPIM configuration allows a substantial increase in axial resolution uniformity across the FOV, we cleared mouse brains, in which vasoactive intestinal peptide (VIP) interneurons express tdTomato, with a passive CLARITY protocol (see section 4.4). When scanning this sample with a Gaussian beam with the ASLM-mode switched off, labeled neurons could be distinguished in the axial direction in the center of the FOV whereas at the edges of the 13.29 mm FOV (zoom 1×) cells overlapped in Z (Figures 4.1b, 4.3a,c,e). After switching the ASLM mode on, however, neurons could easily be distinguished in the XZ plane (Figures 4.1b, 4.3b,d,f). In a volume rendering, the same effect is apparent (Supplementary Videos 1 & 2). These datasets were acquired within 8 minutes (2-µm z-step size).

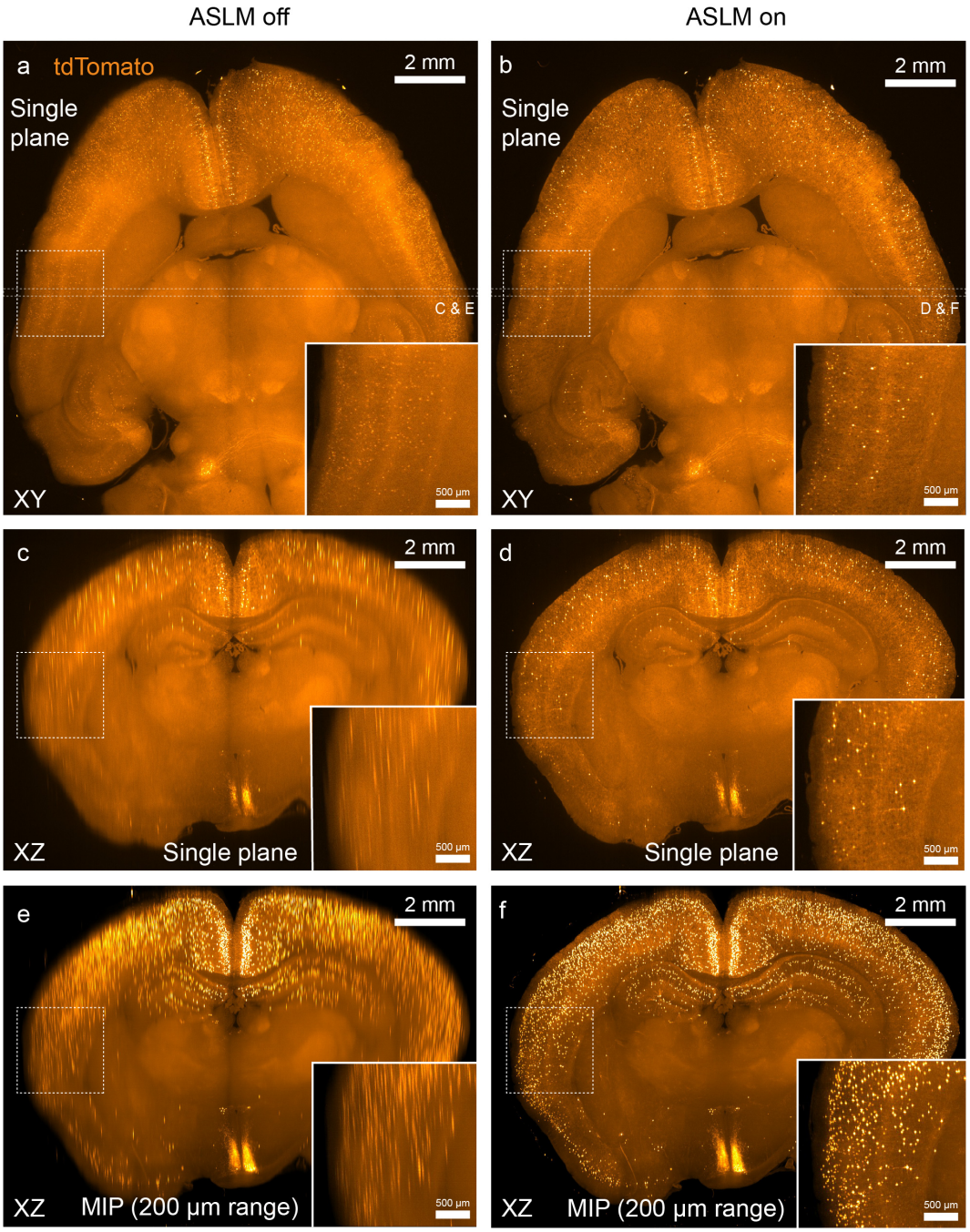

Figure 4.3: Comparison of whole-brain VIPCre-tdTomato datasets acquired with and without ASLM at 1× magnification. a) & b) Single planes acquired from a passive CLARITY-cleared VIPCre-tdTomato mouse brain with ASLM switched off (left) and ASLM switched on (right). Whereas in the center, both images look similar, with ASLM on, far fewer cells are visible because the optical section is thinner. c) & d) Single resliced (XZ) plane at the location indicated in a) & b): Due to ASLM, the uniformity of the axial resolution is much better which renders single cells visible in the XZ plane at the edges of the FOV. e) & f): Comparison of maximum intensity projections at the same location.

At 4× magnification and 1.6 µm × 1.6 µm × 2 µm sampling, switching the ASLM mode on allows for the visualization of axons in the XZ-plane across the entire 3.3-mm FOV (Figure 4.5, Supplementary Video 3) Allowing for ASLM also means that unlike most other light-sheet microscopes, a mesoSPIM allows users to control the effective thickness of the light-sheet to a high degree. This freedom comes with a considerable learning curve as users have to learn how to optimize the ASLM sweep parameters from the live (XY) image. Sub-optimal settings of the ASLM parameters will result in a loss of optical sectioning quality (see Figure 4.6).

The ETL parameters (ETL amplitude and offset of the ramp, see Supplementary Figure 12) depend on a variety of imaging conditions:

- A change in zoom leads to a change in ETL amplitude: For example, smaller FOVs at higher magnification mean that the ASLM sweep should cover a smaller distance along the illumination direction which corresponds to a reduction in ETL amplitude.
- The ETL offset mostly depends on the bulk refractive properties of the imaging medium – switching to a different clearing medium (with different n_D) also leads to a required change in offset.
- Switching the excitation wavelength requires changing the ETL offset as the dispersion of the immersion medium is wavelength-dependent.

For all of the above, the mesoSPIM software provides reasonable presets that have to be calibrated for a certain immersion medium when setting up the instrument. However, the following should be noted:

- Both ETL amplitude and zoom can depend on the local refractive properties of the sample – we noticed that even extremely well cleared and index-matched samples still show some variation of optimal ETL parameters in mosaic acquisitions.

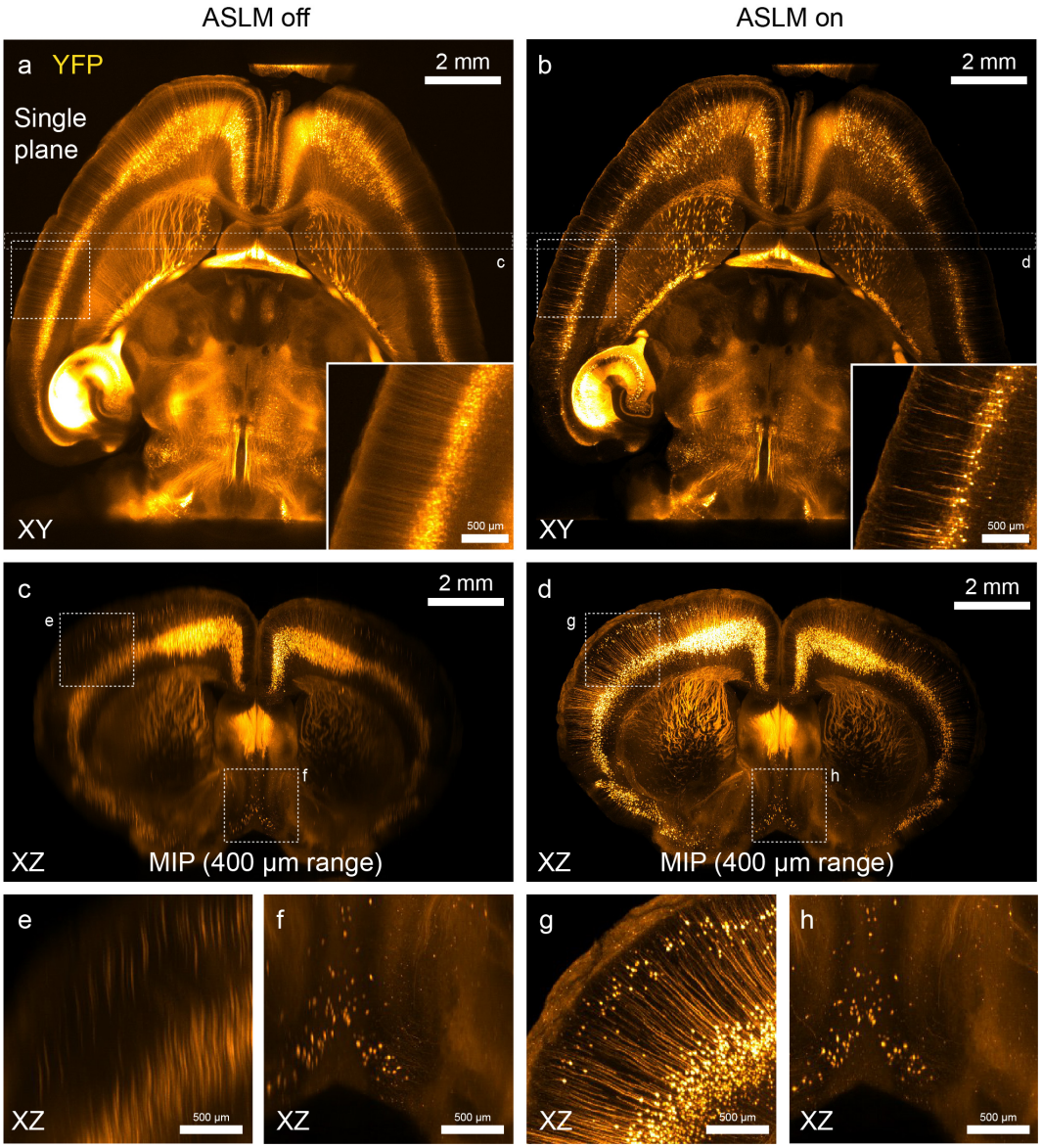

Figure 4.4: Comparison of whole-brain Thy1-YFP datasets acquired with and without ASLM at 1× magnification. a) & b) Single planes acquired from an active CLARITY-cleared Thy1-H-YFP mouse brain with ASLM switched off (left) and ASLM switched on (right) at low magnification (Zoom 1×). Whereas in the center, both images look similar, with ASLM on, far fewer cells are visible because the optical section is thinner (insets). In addition, sections of single dendrites become visible. c) & d) Comparison of maximum intensity projections (MIP) in the XZ plane. The location of the coronal MIP is indicated in subpanels a) and b). e)-h) Details from subpanels c) & d): Whereas along the midline (subpanels f) and h)), the improvement in axial resolution is less pronounced, there is a drastic increase in axial resolution at the edges of the FOV (subpanel e) vs. g)) which renders single dendrites visible in the XZ plane.

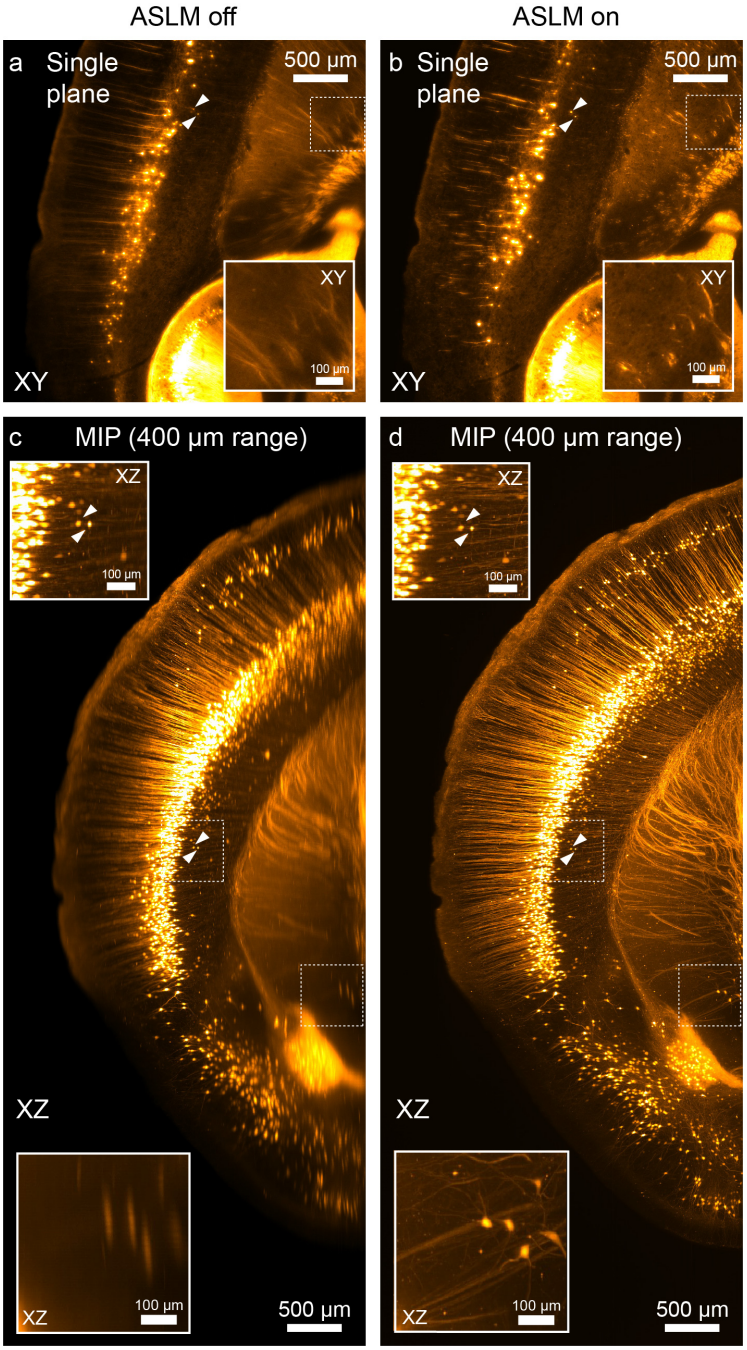

Figure 4.5: Comparison of Thy1-YFP datasets acquired with and without ASLM at 4× magnification. a) & b) Comparison of single planes acquired with ASLM switched off (left) and ASLM switched on (right). The more uniform thickness of the optical section reduces the blur around features at the edges of the 3.3-mm FOV. c) & d): Comparison of XZ maximum intensity projections. Whereas cells close to the location of the light-sheet waist in the ASLM-off condition (marked by arrows) do not show a loss of axial resolution in ASLM mode (top insets), neurons at the edge of the FOV (bottom insets) show a massive improvement in axial resolution. Passing axons at that location are virtually invisible without ASLM.

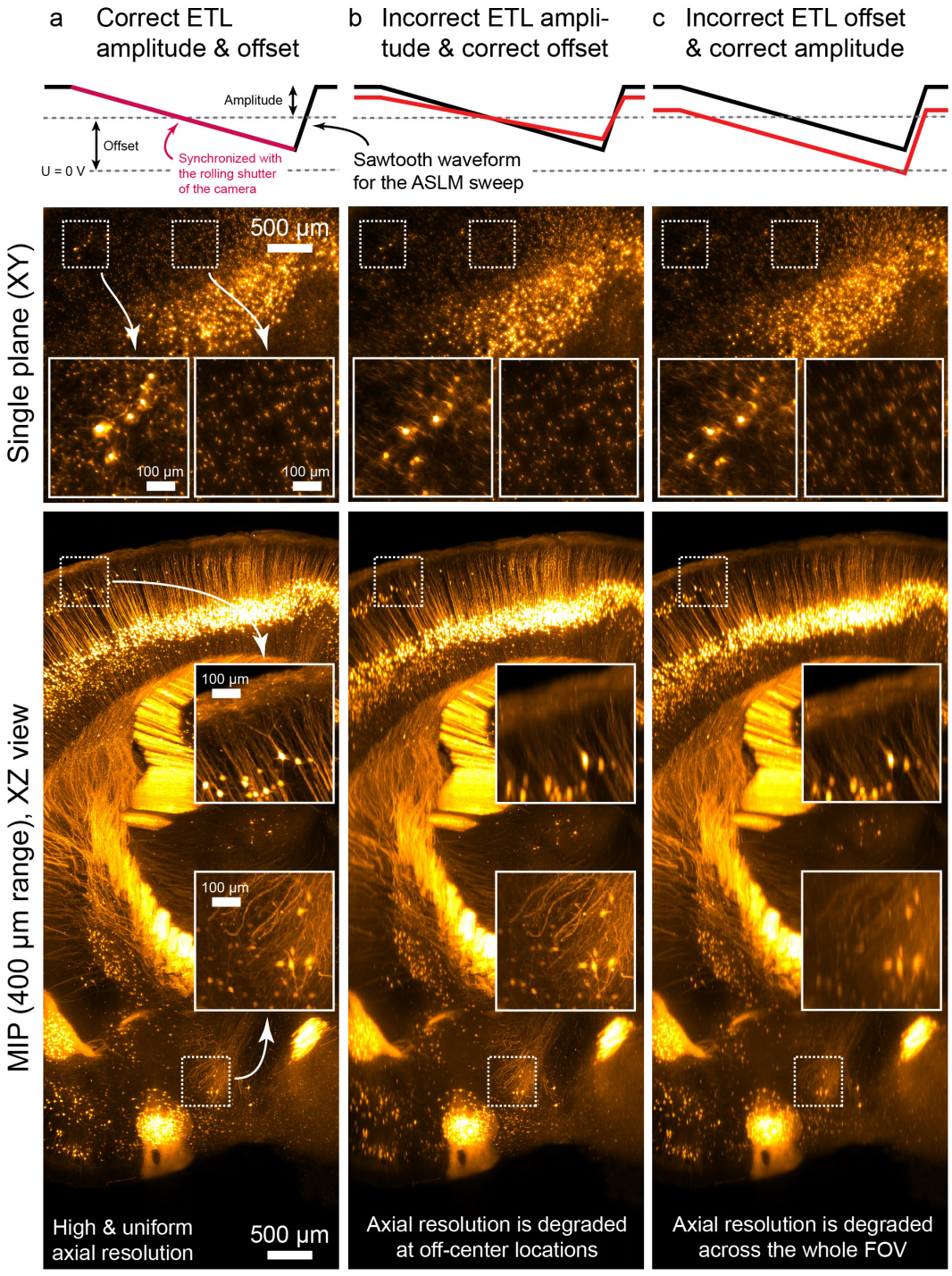

Figure 4.6: Choosing the correct ETL parameters is important to achieve uniform axial resolution. Shown is a comparison of z-stacks in both the XY and XZ planes acquired at 4× magnification in a CLARITY-cleared Thy1-YFP mouse brain. The slow linear section of the ETL waveform is synchronized with the rolling shutter of the sCMOS camera. a) The optimal choice of the ETL parameters yields high and uniform axial resolution across the FOV. If either the ETL amplitude (b) or offset (c) are chosen incorrectly, axial resolution is degraded.

In our experience, despite extensive index-matching, every cleared sample still behaves like a lens. This is not surprising given that even very small index variations across slightly tilted interfaces can lead to detectable refraction across cm-sized samples. For an experienced user imaging a familiar sample, manually optimizing the thickness of the light-sheet locally is a process that takes only a few seconds. However, we also noted that in samples with insufficient signal intensity or unsatisfactory clearing quality, an optimum can be extremely hard to find. If a user has never seen a certain type of labeling before, understanding how to read the XY image as an indication of optical sectioning thickness requires some experience and interpretation. For example, in samples with a uniform nuclear staining or with fluorescent beads, the number of visible spots can be used as a simple indication of light-sheet thickness – the fewer spots, the better. This also means that lower bulk image intensity is better. In samples in which neurons are labeled in their entirety, the effective light-sheet thickness is the better the shorter the visible sections of dendrites and axons appear in the XY image. However, especially in regions of interest (ROIs) that contain background autofluorescence and a small subset of passing axons, it is important to optimize for the axons only and not for general image contrast – a process that can be complicated by the rapid bleaching of background autofluorescence in CLARITY-cleared samples. As we noted that especially difficult-to-optimize subregions of specific samples require quite some background knowledge from the user, we currently have not automated the choice of ETL parameters. Nonetheless, we foresee that automation should be possible in a subset of samples by using on-line optimization similar to the techniques implemented in the current generation of smart light-sheet microscopes for developmental biology (Royer et al., 2016). In fact, an optimization step for the overlap of illumination and detection for tiled acquisitions in cleared samples was already implemented in the COLM setup software by Tomer et al. (Tomer et al., 2014), but it comes with considerable overhead in acquisition time.

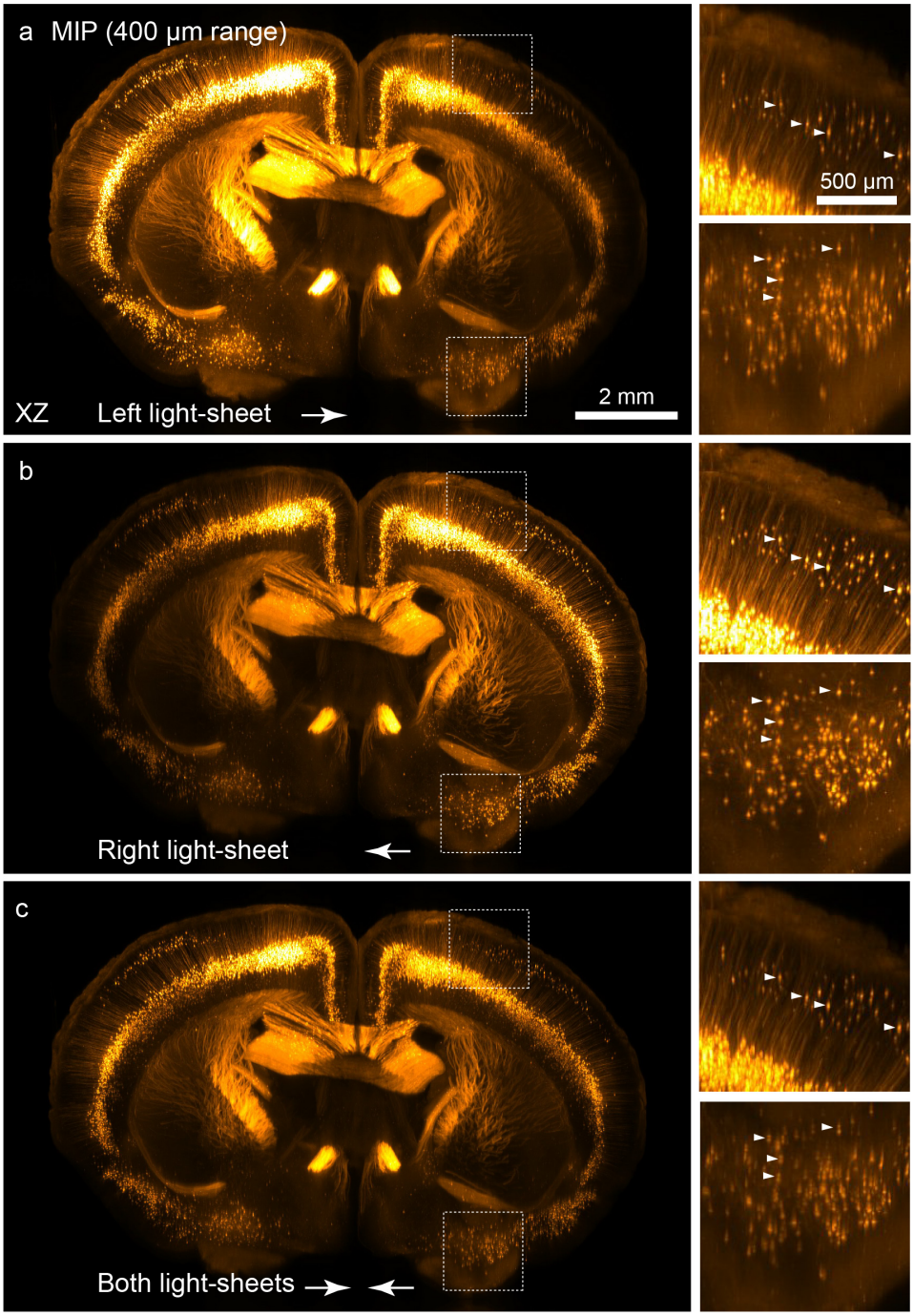

Figure 4.7: Double-sided illumination can lead to location-specific doubling of axial features. Shown is a 1× overview stack taken from a CLARITY-cleared Thy1-YFP mouse brain. a) & b): Maximum-intensity projected (MIP) reslices (XZ plane) from datasets taken with illumination from the left or right. A direction-dependent intensity and resolution gradient is visible. c) When acquiring data with both light-sheets, the illumination is more uniform, however, cells which are located in ventral regions appear twice (bottom inset). This artifact is not visible in the dorsal part of the datasets (top inset) which indicates that in well-cleared specimens, light-sheet co-alignment is strongly dependent on the local refractive properties of the sample.

The local refractive properties of cleared samples we highlighted above also lead to an important consideration on how to acquire data with a mesoSPIM: We strongly recommend acquiring data from well-cleared samples with a single illumination direction only, as stacks taken with double-sided illumination in the ALSM mode can show axial doubling of cells (see Figure 4.7), indicating that the light-sheets are not overlapping properly. Importantly, this happens even though the light-sheets were co-aligned in some other part of the sample along the z-axis (see Figure 4.7). Especially when using light-sheets with an effective thickness below 10 µm such effects are highly prevalent, but tend to be hidden when thicker light-sheets are used. If two illumination directions are required, they should be acquired sequentially and merged during data processing.

4.3.3 Supplementary Note: Optical design of the mesoSPIM setup

Key design decisions during the optical design for the mesoSPIM included:

- Olympus MVX-10 macroscope in the detection path with a MVPLAPO 1× objective for FOVs of 2-21.8 mm (inspired by the LaVision Ultramicroscope I).
- Horizontal detection path as in the original SPIM (Huisken, 2004) to simplify sample exchange (from the top) and sample rotation (direction of gravity acting on the sample does not change during rotation).
- Use of a Hamamatsu Orca Flash 4.0 V2 or V3 to allow the usage of the rolling shutter ("light-sheet mode") for axially scanned light-sheet microscopy (ASLM).
- The light-sheet has to be at least as wide as the FOV of the microscope.
- The remote focusing system to translate the waist location trough the sample needs to have a tuning range >22 mm with typical immersion media (to allow ASLM even at the lowest detection zoom settings).
- To generate z-stacks, the light-sheet is stationary and the sample is translated through the sheet.

- The light-sheet illumination should be multidirectional (mSPIM, Huisken and Stainier (2007)) to minimize the amount of shadowing artifacts.

- The microscope should support single-photon excitation wavelengths from 405 nm to 650 nm and into the NIR region, if possible.

- Co-alignment of both light-sheets should be easy.

The choice of the Olympus MVX-10 macroscope as the core component of the detection path led to the following decisions:

- As the MVPLAPO 1× is an air objective, the samples need to be immersed in an immersion cuvette of sufficient size to allow sample translation and rotation. We opted to use standard glass or quartz macro-fluorescence cuvettes from vendors such as Hellma or Portmann Instruments which are available in sizes ranging from 30x30x35, 40x40x45 to 50x50x50 mm^3 and can be custom made to user requirements.

- As samples come in all kinds of sizes and shapes, the distance between the wall of the immersion cuvette needs to be adjustable to keep the amount of medium between the light-sheet and the objective to a minimum, but allow for enough travelling range to take a z-stack of the region of interest.

- This in turn requires two translation stages along the detection axis: One for translating the sample through the light-sheet to generate z-stacks and one for focusing the detection optics.

- n addition, the MVX-10 requires the use of 32-mm filters in the detection filter wheel to have sufficient free aperture (necessitating custom filters).

The parameters of the detection system thus dictated the design of the illumination optics to a high degree. Early tests with light-sheet illumination using cylindrical lenses showed that

shadow artifacts can lead to many stripes in the images, which we deemed inacceptable. For example, in a modified openSPIM for cleared tissue (Stefaniuk et al., 2016), shadow artifacts lead to a severe degradation in image quality. Therefore, we concluded that shadow reduction – for example in the form of multidirectional SPIM (mSPIM, Huisken and Stainier (2007)) – is necessary. In this solution, the light-sheet is rapidly pivoted by a resonant scanner so that the shadows cast by absorbing structures in the sample are averaged out. While designing a mSPIM for 2-20 mm FOVs is feasible, we adopted a design similar to an digitally scanned light-sheet microscope (DSLM, Keller et al. (2008)). In a DSLM, the light-sheet is created by rapidly scanning a Gaussian beam in a plane. Typically, in a DSLM the NA of the laser beam is chosen such that the Rayleigh length is on the order of half of the FOV of the microscope camera so that the resolution variation of the axial resolution across the FOV is not too severe. This leads to low excitation NAs for large FOVs. As noted by Fahrbach et al. (Fahrbach et al., 2010), a scanned Gaussian beam leads to a reduction in shadow artifacts – though not as strongly as using Bessel beam excitation. The effectiveness of shadow reduction is related to the NA of the Gaussian illumination beam: The higher the NA, the shorter the shadow cone behind an absorbing object. For large FOVs, the necessary low excitation NAs can thus lead to severe shadow artifacts. In an ASLM setup, however, there is no trade-off between NA and FOV: The higher the illumination NA, the smaller the beam waist which in turn is converted to a low effective light-sheet thickness by the ASLM sweep. A side effect of ASLM is thus that it allows using higher excitation NAs (compared to a standard DSLM with the same FOV) which in turn lead to decreased shadow artifacts.

Initial tests with mesoSPIM prototypes showed that a scanned Gaussian beam with an excitation NA of 0.14 - 0.15 yielded acceptable reduction of shadow artifacts over the FOV. The scan lens path has to be telecentric, otherwise the height of the light-sheet (in the Y direction) does not stay constant during remote focusing as required for ASLM. Any change in height will also be a nuisance as the light-sheet intensity will vary across the FOV: If the light-sheet height is not constant, the available laser power will be more concentrated in certain parts of the FOV (see see

Figure 4.8) In typical DSLM instruments, the excitation path is similar to typical confocal excitation paths with a combination of scanners, a scan and tube lens and a microscope objective. As we needed more than 20-mm FOV due to our large detection FOV, we deemed standard microscope optics as inadequate as there are no low-magnification objectives with sufficient working distance (> 25 mm) and NA (>0.1). One of the closest approximations to the mesoSPIM requirements, the Olympus XLFLUOR 4× NA 0.28 with a working distance of 29.5 mm is designed for a field number of 22, corresponding only to a 5.5 mm FOV. However, the design of the scan path can be simplified by removing the tube lens and objective altogether: By combining a single-axis galvo scanner with a scan lens of sufficient NA and working distance, creating a light-sheet of more than 20-mm height after the scan lens should be feasible (Figure 4.8).

Therefore, we were faced with the challenge of requiring a scan lens with the following parameters (Figure 4.8):

- NA 0.15
- Focal length in the range from 40 mm to 80 mm (larger focal lengths lead to overly large galvo scanners).
- Telecentric (on the finite conjugate side) to generate a light-sheet with uniform height for ASLM.
- Achromatic from 405 to 650 nm
- Corrected for field curvature to have a straight waist for ASLM.
- Ideally, diffraction limited across a 22-mm FOV / image circle.
- Sufficient working distance

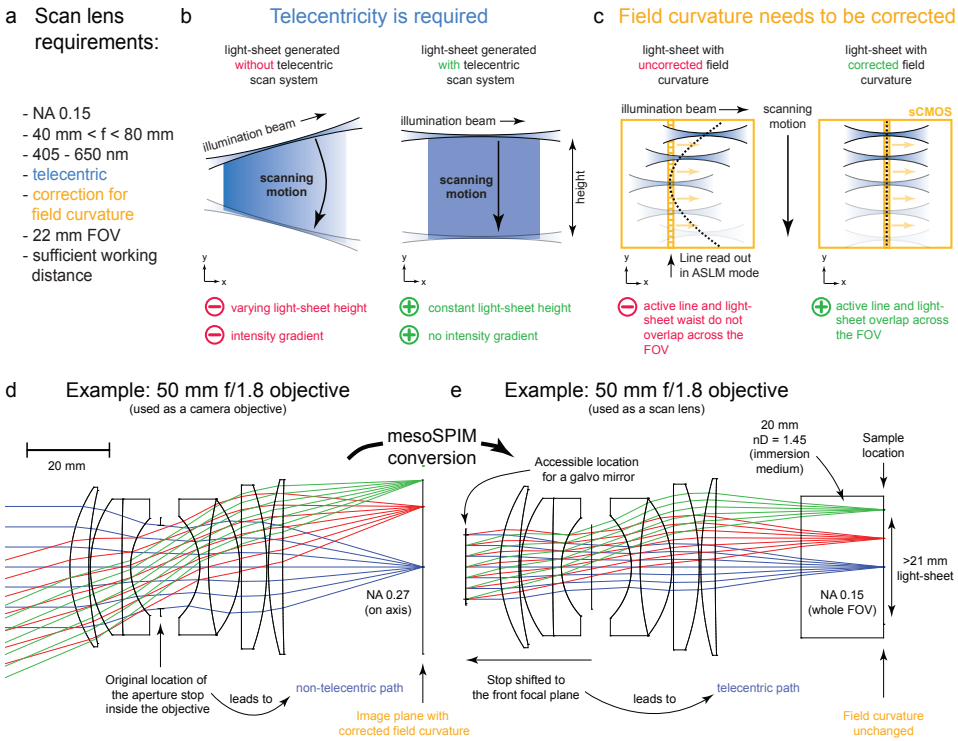

Figure 4.8: Challenges and solutions in the optical design of the mesoSPIM excitation scan lens. a) List of scan lens requirements. b) The scan system has to be telecentric to avoid a varying height of the light-sheet and the associated intensity gradient. c) Field curvature has to be corrected allow for the ASLM mode to work properly for large FOVs. d) Example design of a 50 mm f/1.8 objective (from Laikin (2012)) showing the original design conditions for this camera lens. e) Conversion of the lens into a scan lens. Please note this design is close to the Nikon 50 mm f/1.4 G objectives used in the mesoSPIM to show the concept of shifting a stop, but currently, the design of the lenses used in the mesoSPIM is unavailable to the authors.

For comparison, standard scan lenses for confocal microscopy have specifications close to the Thorlabs SL50-CLS2:

- f = 50 mm
- NA 0.04 (4-mm input beam)
- Telecentric
- Field flattened
- Correction from 450 to 1100 nm
- 26.4 mm working distance
- 15.5 mm image circle at 587.6 nm

In optical design, scaling up such a field-flattened telecentric scan lens (to obtain 3x the NA and 25% larger FOV) is a formidable challenge that will result in a costly custom design. Apart from the upscaled NA, a key factor in the cost of such a design is the achromaticity requirement. Moreover, such a scan lens design cannot be carried out in a fully achromatic fashion without movable elements if it is supposed to work with varying immersion media: As the dispersion of clearing media and immersion oils varies significantly between different clearing media, the scan lens would have to contain a correction collar which in turn leads to cost increases. Upon closer inspection, however, we noted that in fixed and cleared tissue, it is unlikely that simultaneous illumination with multiple laser lines is required: We were planning to use only a single detection camera and in fixed tissue, different color channels can be acquired by successive z-stacks if the sample does not drift or change over time. In addition, we were planning to have a tunable lens in the path to allow for ASLM, which is basically a remote focusing arrangement. Hence, if there has to be a tunable lens anyway and if we plan to use only one excitation wavelength between 405-650 nm at a time, the axial chromatic aberration of the scan lens can be corrected by simply applying an offset to the ETL driving signal. This drastically simplifies the optical design.

In light of these modified requirements, the opportunity for an optics "hack" opened up: In optical design, custom designs tend to be costly and take long to manufacture, but things are much easier when mass-produced optical systems can be creatively repurposed for the required application. We noted that the requirement for working distance, field flattening, and FOV are basically covered by camera lenses: Typical consumer DSLR (digital single-lens reflex camera) lenses have long image-side working distances (to make space for the moving mirror, typically 44-46 mm) and a flattened 24×36 mm field to cover full-format CMOS detectors (Figure 4.8d).

In addition, there is a massive selection of focal lengths in the 40-70 mm range available as these are considered "standard" or "portrait" lenses. Typical 50-mm DSLR lenses have an f-Number (f/#) of 1.4 (or NA 0.35, $f/\# = 1/(2 \cdot \mathrm{NA})$ but are not diffraction-limited under such conditions.

However, such a lens can be "stopped down" to NA 0.15 (corresponding to approx. 15-mm beam diameter), which yields a reasonable size for a galvo mirror when using this lens as a scan lens. Therefore, such DSLR lenses were promising candidates for the mesoSPIM excitation path. The missing requirement from our initial list is telecentricity – DSLR lenses are usually not single- or double-telecentric (except some macroscopy lenses) and have an inaccessible aperture stop inside the lens. However, a lens can be forced to perform as a telecentric system by placing the aperture stop at a particular position. In the case of a laser scanning system, the galvo scanner creates a stop location (where ray bundles directed at different image locations originate). If the position of the scanner coincides with the front or back focal plane of the optical system, the system will perform telecentrically (Figure 4.8e). Importantly, forcing an optical system to accept a different stop location will result in introducing additional off-axis aberrations such as coma or astigmatism, the degree of which can be calculated using stop-shift formulae (Kingslake, 2010). We deemed this risk acceptable as NA 0.15 is much lower than the original design NA of DSLR enses. From this point on, the challenge was to find a 50-mm DSLR lens, which had an external front focal plane (FFP) and a sufficient distance between FFP and front lens (at least 7.5 mm to place a 15-mm scan mirror there). We therefore screened a series of consumer DSLR lenses for accessible FFPs using an autocollimator and found a lens with approximately 12 mm distance between the FFP and the vertex of the front lens in the Nikon AF-S 50 mm f/1.4 G. In this lens, however, the FFP is located within the lens hood which means that several plastic parts have to be removed before a scan mirror can be placed close enough. The modification process is documented on the mesoSPIM wiki.

Be aware that this modification is likely to void the warranty of the lenses and will render their autofocus unusable in a standard DSLR as the focus encoder has to be removed. Nonetheless, we consider this acceptable as each objective / scan lens costs only around 0.2% (or approx. 500 USD) of the total cost of a mesoSPIM with 6 laser lines.

Therefore, the combination of this 50-mm DSLR/"scan lens" and 15-mm beam diameter (NA 0.15) was chosen as basic components for designing the rest of the excitation path. 15-mm scanners from galvo suppliers such as Citizen Chiba, Cambridge Technologies or Scanlab are made-to-order items with long lead times and require custom power supplies and driver boxes. Therefore, the mesoSPIM excitation path is also compatible with 10-mm scanners such as the Thorlabs GVS211/M, which are off-the-shelf items but lead to a reduced excitation NA of 0.1. To ensure telecentric conditions during refocusing/translation of the waist of the excitation light-sheet, the ETL has to be placed in a conjugate pupil relative to the galvo scanner (Fahrbach et al., 2013b), which can be achieved by a 4f system. To allow for the maximum possible tuning range, the magnification of the relay should be as low as possible. Therefore, we opted to use a 1:1 relay and an ETL with 16-mm free aperture (EL-16-40-TC-VIS-5D-1C, Optotune AG). ETLs with large free apertures tend to have slow step responses and are thus not suitable for very fast focusing, but we reasoned that the frame rate of the microscope would rarely exceed 10-20 Hz and thus, the 30-ms step response and settling time of the EL-16 does not constitute a major limitation. The ETLs were selected for low wavefront aberrations by the manufacturer. For optimum performance, ETLs should be placed in a vertical section of the optical path because otherwise gravity-induced sag of the liquid leads to non-rotationally symmetric deformation of the lens membrane, which in turn leads to additional aberrations such as coma. This necessitated the inclusion of additional fold mirrors between ETLs and galvo scanners. The final mesoSPIM V4 optical path is shown in Figure 4.9. The optical path of the mesoSPIM V5 is identical.

In setting up most light-sheet microscopes with dual-sided illumination paths, co-alignment of both light-sheets is a challenge. This is caused by the need to include enough degrees of freedom in the excitation path to vary the position of the light-sheet along the detection axis and its tilt as independently as possible. While the tilt of the light-sheet can easily be adjusted using a fold mirror with kinematic mount upstream of the galvo scanners, adjusting the tilt angle requires translating the footprint of the excitation beam on the scan lens along the detection axis. We therefore in-

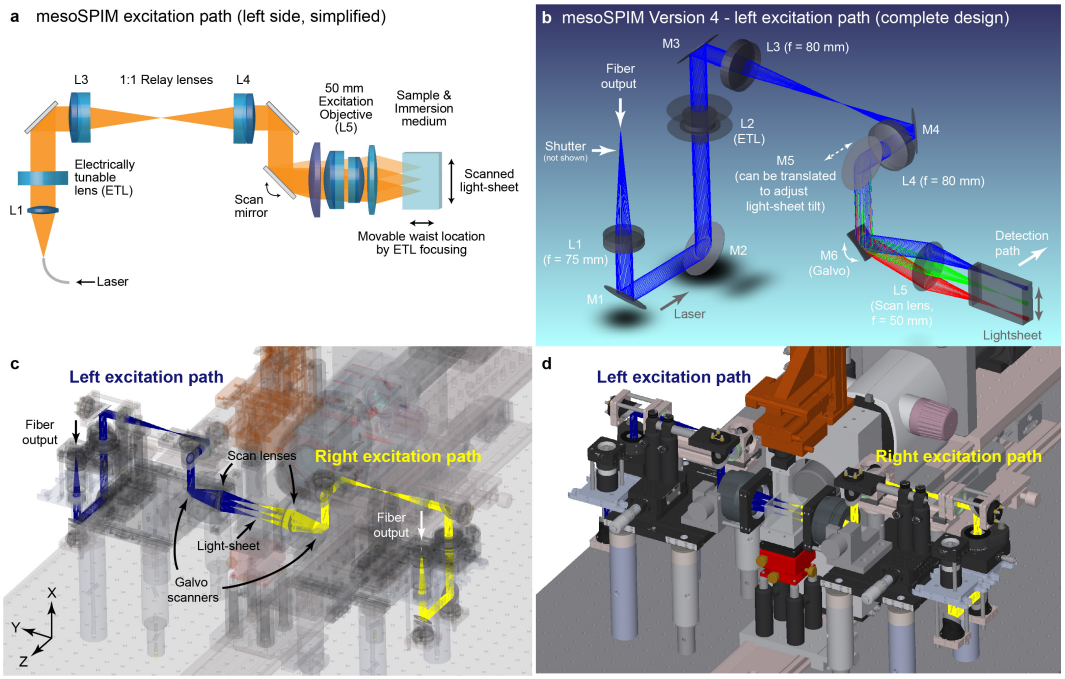

Figure 4.9: Optical design of the mesoSPIM excitation path. a) Simplified optical path: Laser light from a single-mode fiber is collimated and then sent to an electrically tunable lens (ETL). The ETL is placed in the conjugate pupil of the galvo scan mirror via a 1:1 relay system (4f system) composed of two achromats (L3 and L4). The galvo scanner creates the light-sheet in combination with a f = 50 mm scan lens. The location of the light-sheet waist along the excitation direction can be changed by changing the ETL focus. b) Full design of the left excitation path showing additional fold mirrors which were required to place the ETL in a vertical section of the optical path to avoid gravity-induced sag and to allow for adjustment of the light-sheet tilt using the translation of mirror 5 (M5). c) & d) CAD renderings showing how the left and right optical paths are placed inside the mechanical design.

cluded a fold mirror that can be manually translated and adjusted in angle to simplify this process (Figure 4.9b). Additionally, it is aided by a light-sheet alignment mode in the microscope software that interleaves the illumination direction between subsequent frames in live mode.

4.3.4 Supplementary Note: Description of the mesoSPIM setup

Detailed parts lists, drawings and CAD files for mesoSPIM version 4 and 5 are available on the mesoSPIM hardware documentation repository.

Guidelines: For the optomechanical design, we adhered to the following guidelines:

- The microscope has to be as modular as possible to allow for future modifications.
- Extensive use of rail systems (Qioptiq X95, FLS95 and FLS40) and cage systems (Qioptiq Microbench & Thorlabs 30-mm cage) to aid in modularity and ease of alignment.
- The number and complexity of custom parts has to be kept to a minimum (a mesoSPIM V4 contains only 15 custom parts).
- The detection axis is located 225 mm above the plane of the optical table to allow for sufficient vertical movement of samples.
- The excitation system is located on a horizontal breadboard 185 mm above the plane of the optical table (40 mm below the detection for FLS40 compatibility).

Optical table: With a weight in excess of 50 kg, we recommend placing a mesoSPIM on a dedicated optical table. The total footprint of a mesoSPIM is approximately 1.1 m x 0.75 m x 0.7 m (length x width x height). The detection axis of the microscope is defined by a central FLS-95 rail, which carries the detection system and immersion cuvette (see Figure 4.10).

Excitation lasers: The excitation path consists of a laser combiner unit coupled to two single-mode fibers, one for each excitation path. Two of the existing mesoSPIM instruments have Omicron SOLE-6 laser with 405, 488, 515, 561, 594 and 647 nm excitation lines and a 50:50 split between fibers. Three mesoSPIMs have two Toptica MLE laser combiners with 405, 488, 561, 640 nm lines, one for each excitation path. In general, it is recommended to use laser combiners with

the highest available output powers, each line should have at least 30 mW on the sample to properly illuminate the full FOV (which can be up to 22 mm). The laser selection should take the following considerations into account:

- Relatively high laser powers are required for imaging endogenous labels in samples cleared with methods with loss of fluorescent proteins (in our experience especially passive and active CLARITY).

- In contrast, well-stained samples – for example, after amplification with secondary antibodies such as in iDISCO – generally leads to high signal levels and thus can be imaged at lower laser intensities.

- If it can be anticipated that only very little imaging will be done in samples requiring FOVs of more than 5 mm, lower laser power specifications will be sufficient as the available power will be concentrated onto a smaller light-sheet.

- We do not recommend having a 405-nm laser line unless it is absolutely needed – in general, the penetration depth even in cleared samples at this wavelength is very low (Cai et al., 2018) and it is recommended to use red labels instead of UV-excitable dyes.

- White-light laser sources are not recommended (though not tested) as it can be expected that the axial chromatic aberration of the mesoSPIM excitation path will lead to worse effective light-sheet thickness because ETL sweep parameters depend on the dispersion of the immersion medium.

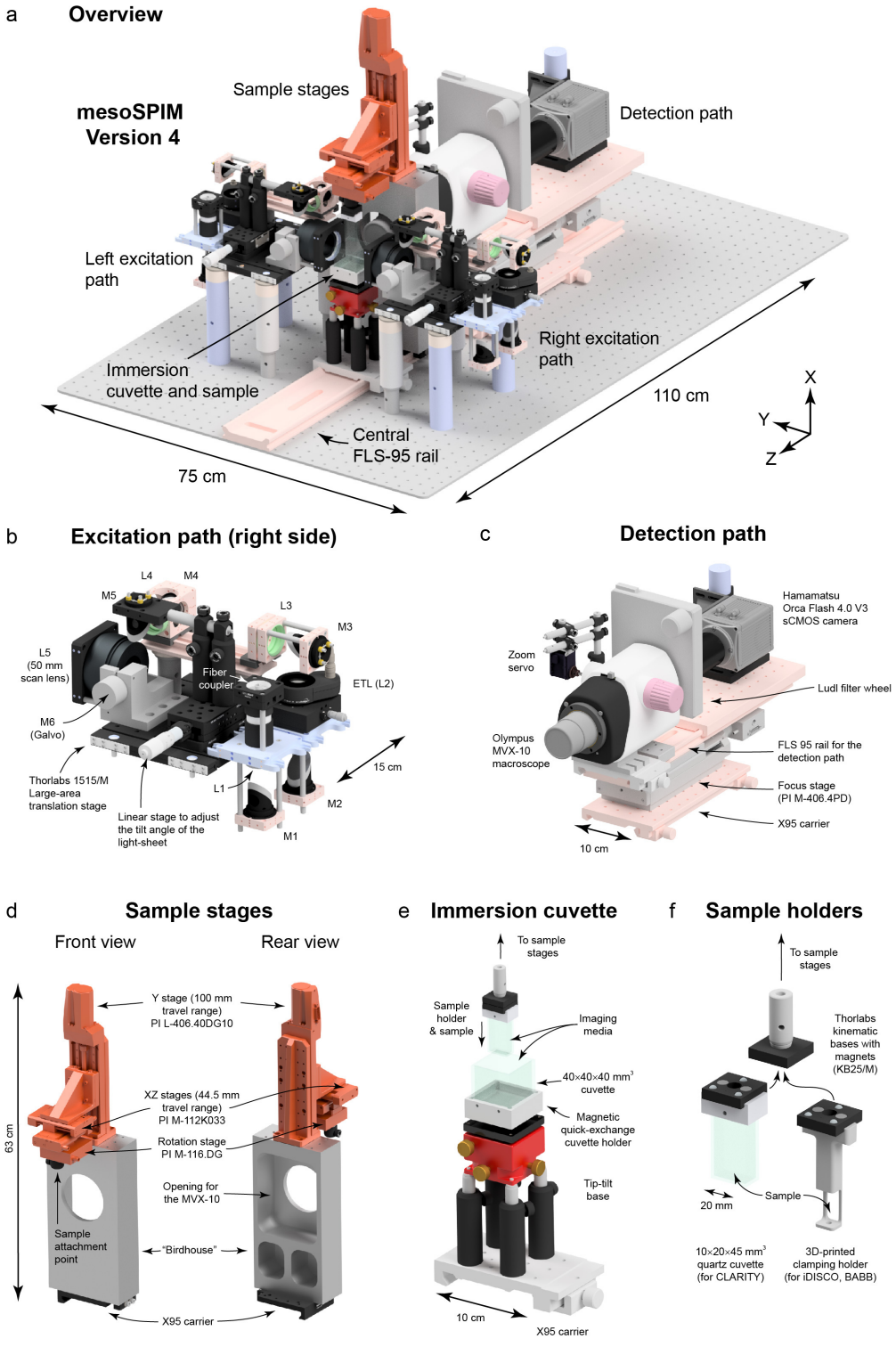

Figure 4.10: mesoSPIM mechanical design. a) Overview rendering. b-f): Core mesoSPIM components ranging from the excitation path to the sample holders. For a mesoSPIM Version 4, a total of 15 custom parts are necessary.

Most existing mesoSPIMs are part of either research labs or imaging facilities with a wide range of clearing methods available. Having sufficient laser powers and a wide selection of laser lines available therefore is beneficial to support all kinds of imaging needs. Nonetheless, high-power laser combiners with 4 or 6 wavelengths are a major cost factor and account for 30-50% of the total cost of a mesoSPIM setup. If a mesoSPIM has to be built on a lower budget, we recommend starting with a single laser line and a single excitation path. If multiple lines are required, building an open-source laser combiner might be an option (Nicovich et al., 2017).

Excitation path: Light from the laser combiners is directed to each excitation path (left & right) via a single-mode fiber (Figure 4.9). After passing a shutter (Thorlabs SHB025), the laser light is collimated by an achromat (f = 75 mm; Thorlabs AC254-075-A-ML) to approximately 15-mm beam size. It is then directed to an electrically tunable lens (ETL, Optotune EL-16-40-TC-VIS-5D-1C), which can create both a converging and diverging beam in combination with a Optotune EL-E-4-i lens driver that is configured for external control via an analog input. The beam is then directed through a 1:1 relay comprising two visible achromats (f = 80 mm; Qioptiq G063200000). Via a series of elliptical 1-inch fold mirrors (Thorlabs BBE1-E02), the beam is directed towards a galvo scanner for which the following options exist:

- Thorlabs GVS211/M scanner with 10 mm beam size (resulting in an excitation NA of 0.1) – these are standard Thorlabs items and have short lead times and are recommended for building a mesoSPIM quickly.
- Citizen Chiba GCM-2280-1500 scanner allowing a 15 mm beam (NA 0.15) – legacy option implemented in several mesoSPIM V4.
- Scanlab 14/1 dynaxis 3M scanner with a custom air-cooled galvo mount (NA 0.14) – this option has longer lead time and requires custom electronics and housing.

The galvo scanner creates the light-sheet by scanning the Gaussian input beam through a f=50 mm consumer single-lens reflex (DSLR) objective (Nikron AF-S 50 mm f/1.4 G) that was “hacked”

into a telecentric scan lens (see section 4.3.3). Typically, the galvo scanners are driven with a symmetric sawtooth signal at f=99 or f=199.9 Hz. The amplitude of the galvo driver signal dictates the height of the light-sheet (Figure 4.13). Each excitation path is located on a Thorlabs TB1515/M large-area translation stage (see Figure 4.10) to allow changing the distance between the detection axis and the excitation objectives to accommodate immersion cuvettes of varying sizes. In practice, the EL-16 tunable lenses in combination with a f = 50 mm scan lens have a tuning range in excess of >100 mm in air, so that all distance changes can be done by changing the driving signal to the ETLs.

Immersion cuvettes: We typically keep the immersion medium in an quadratic glass or quartz macro-fluorescence cuvette which are 30×30×30 mm^3, 40×40×40 mm^3, or 50×50×50 mm^3 in size (Portmann Instruments or Hellma AG). The immersion cuvettes are mounted on plastic cuvette mounts milled from polyoxymethylene (POM). At the bottom, the cuvette mounts are attached to a KB25/M kinematic base (Thorlabs). This quick-detachable magnetic base with a ball and V-groove design allows quick exchange between immersion cuvettes filled with different immersion media (Supplementary Figure 9e). For example, for imaging in CLARITY, we fill the cuvette with an immersion oil (Cargille 50350, $n_D = 1.45$) whereas for imaging in iDISCO-cleared and stained-samples, the cuvette is filled with dibenzyl ether ($n_D = 1.562$). If a mesoSPIM is supposed to be used with many different immersion media within a day of imaging, we recommend having dedicated immersion cuvettes filled with each medium ready.

Sample holders: The sample XYZ & rotation stages carry a KB25/M kinematic base (Thorlabs) as well. This allows quick exchange of samples – they can be "clicked" in and suspended below the stages within seconds. For mounting samples, we either use cuvettes or sample clamps: For example, CLARITY cleared whole-mouse brains are usually immersed in 10×20×45 mm^3 quartz cuvettes (Portmann Instruments) in a refractive-index matching solution (RIMS). The same approach is recommended for all samples that are swollen or fragile. Samples cleared with organic

solvents (i.e. DISCO, iDISCO, or BABB) tend to shrink and harden in the clearing process and can be clamped in a holder (either milled from aluminum or 3D-printed). As immersion media such as BABB or DBE tend to dissolve plastic, we recommend using nylon (polyamide) screws and 3D-printed parts for this purpose –– in our hands, these tend to be very resistant. An overview of the Pros and Cons of the different sample mounting strategies is shown in Figure 4.11.

Sample stages: The travel range of the sample stages (see Supplementary Figure 9d) is currently 44.5 mm × 100 mm × 44.5 mm (X/Y/Z, mesoSPIM V4). The stages are produced by Physik Instrumente, Germany: M-112K033 (for X & Z movement), L-406.40DG10 (Y movement), M-116.DG (sample rotation) and controlled by a C-884 controller. In the mesoSPIM Version 4, the sample XYZ & rotation stages are mounted on a massive aluminum block (150×65×300 mm^3) that has a central hole for the detection objective (termed the 'bird house'). As this aluminum block requires a large milling machine for manufacturing, it has been replaced by a gantry built from X95-profiles (Qioptiq) in mesoSPIM V5. Version 5 also features slightly larger travel ranges (52 mm × 52 mm × 102 mm) by using PI L-509 stages.

Detection path: The mesoSPIM detection path (Figure 4.10b) consists of an Olympus MVX-10 macroscope with a MVPLAPO 1× objective, which allows FOVs of 2-20 mm in combination with a Hamamatsu Orca Flash 4.0 V3 camera. Due to its zoom system, the Olympus MVX-10 does not have a classical infinity-corrected space between objective and tube lens/zoom body that could be varied for focusing. Therefore, we opted to translate the entire detection path (MVX10 + filter wheel + camera assembly) for focusing by mounting it on a heavy-duty linear stage (PI M-406.4PD). The focusing stage carries an additional FLS-95 rail so that the detection system can be highly modular. The stage also aids in refocusing between different zoom settings as the MVX-10 has a large focus drift with magnification (> 150 µm for a change from 1× to 4×). The MVX-10 has a manual zoom wheel which we motorized by attaching a Robotis Dynamixel MX-28R servo to it.

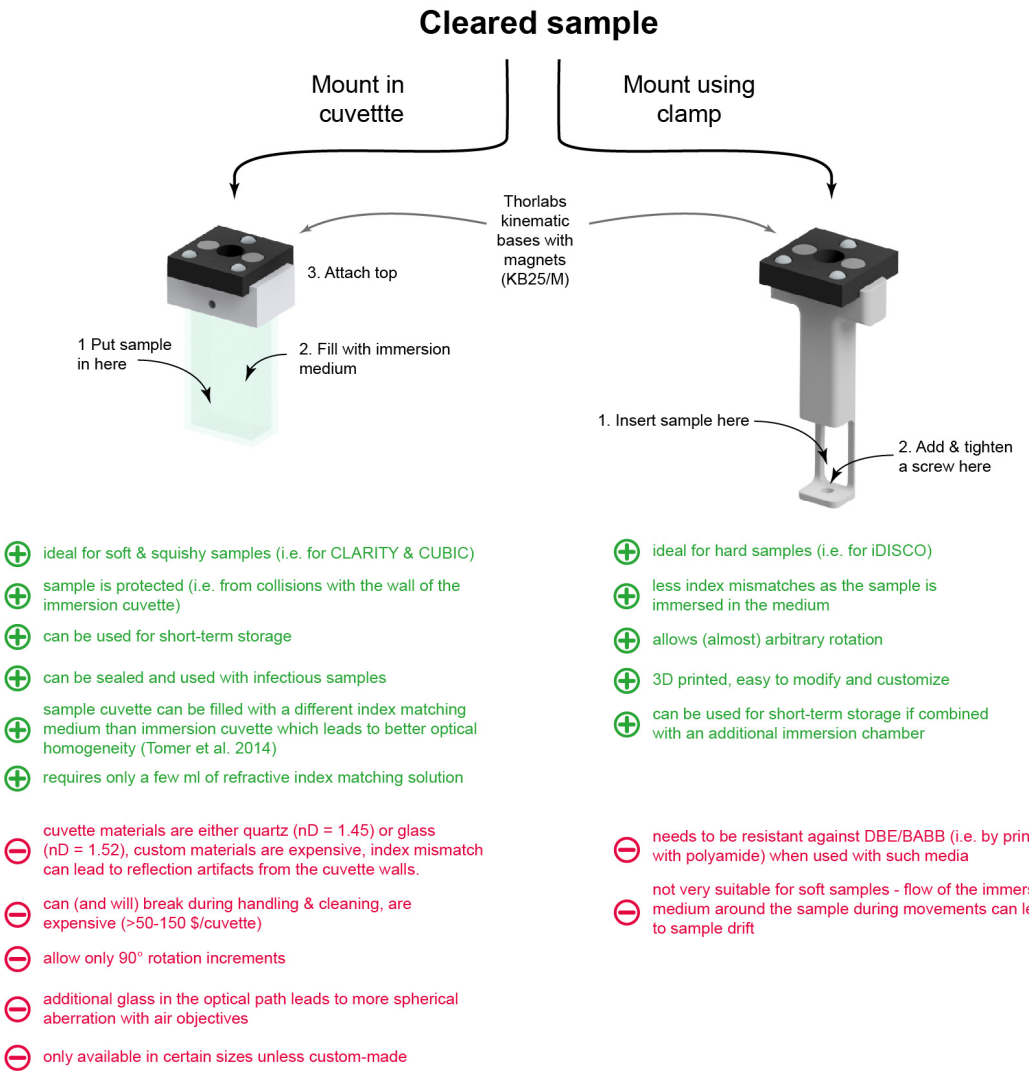

Figure 4.11: Comparison of mesoSPIM sample mounting approaches. Samples are mounted using either an imaging cuvette (left) or a sample clamp (right), which both have a wide range of advantages and disadvantages. Beyond these standard sample holders, any custom holder can be fitted to a mesoSPIM as long as it interfaces with the Thorlabs KB25/M kinematic base with magnets.

The MX-28R is computer-controlled via a serial RS-485 connection and has an internal rotation encoder with a resolution of 4096 steps/revolution, which we deemed to be adequate for the approximately 160 degrees of rotation necessary to change the zoom setting from 0.63× to 6.3×. For higher magnification, the Olympus MVPLAPO 2x objective can be used, but it has large distortion in the corners of the FOV. At the rear port of the MVX-10, we attached a Ludl 96A350 filter wheel with ten 32-mm filter positions. The filter wheel is controlled by a MAC-6000 controller which is connected via RS-232 to the imaging computer. The rear port of the filter wheel housing interfaces with a Olympus MVX-TLU tube lens and a MVX-TV1×C C-mount adapter to which the camera is attached. The camera is rotated by 90° around the detection axis because in an ALSM instrument, the read-out direction of the rolling shutter and the translation of the waist have to be parallel.

Waveform generation and electronics: The control signals for the galvo scanners and tunable lenses are generated by a National Instruments (NI) PXI-6259 card housed in a NI PXIe-1073 chassis connected to the imaging computer by a MXI-bus. An additional PXI-6733 card controls the laser intensities (up to 8 lines) via the analog inputs of the laser engines. All waveforms are generated by the mesoSPIM-control software (see section 4.3.5), buffered in advance and triggered by a master trigger routed to all NI cards. The camera is triggered via a counter output on the PXI-6259. A detailed overview of the electronic mesoSPIM components is given in Figure 4.12 whereas the timing and shape of the mesoSPIM waveforms is shown in Figure 4.13.

Installation instructions: Detailed instructions for setting up a mesoSPIM can be found on the mesoSPIM wiki.

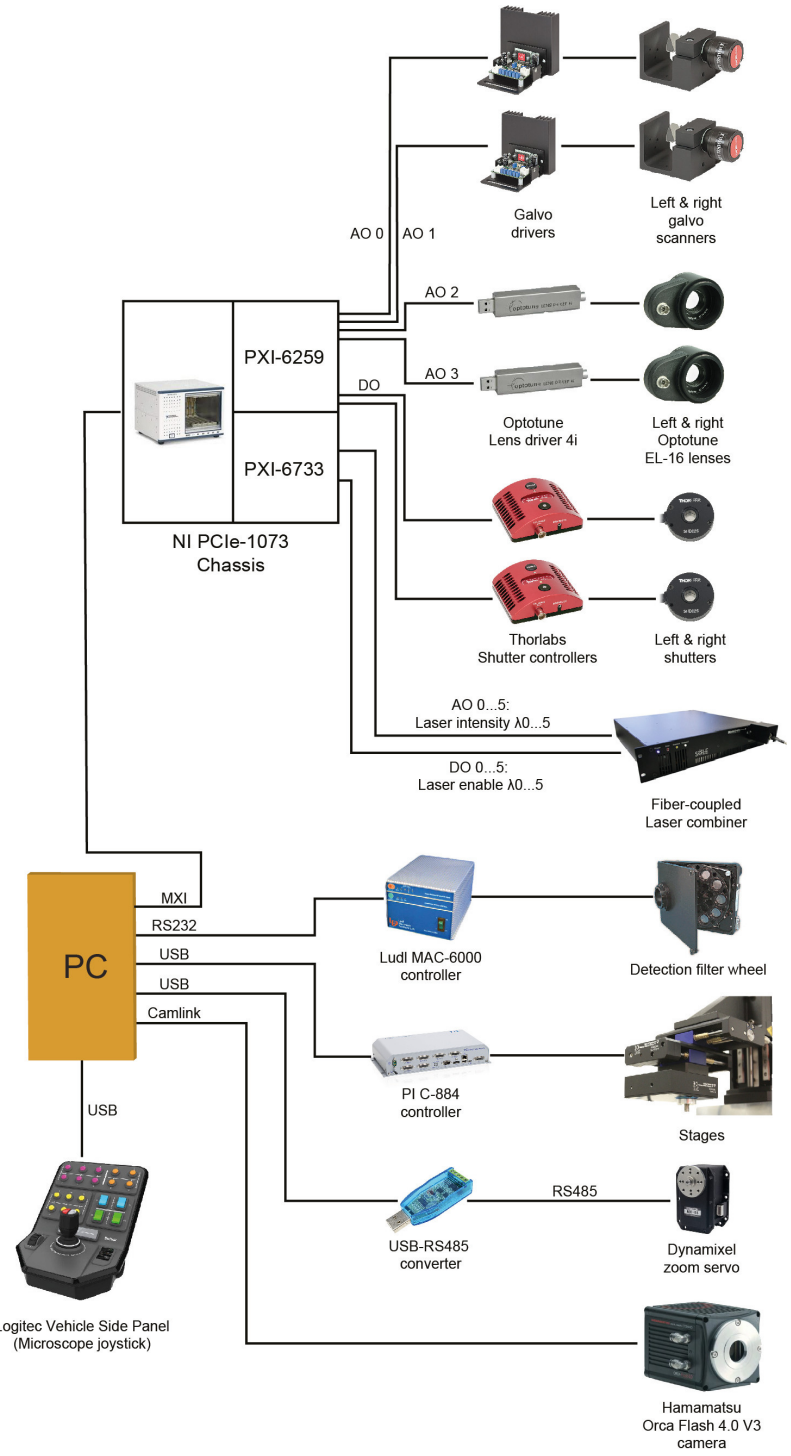

Figure 4.12: Block diagram of the mesoSPIM electronics. The sCMOS camera, zoom servo, mechanical stages and filter wheel all have dedicated connections to the imaging computer (PC) whereas the waveform generation (ETL ramps, galvo signals, shutter control, and laser intensity control) is done via a National Instruments PCIe-1073 PXI chassis.

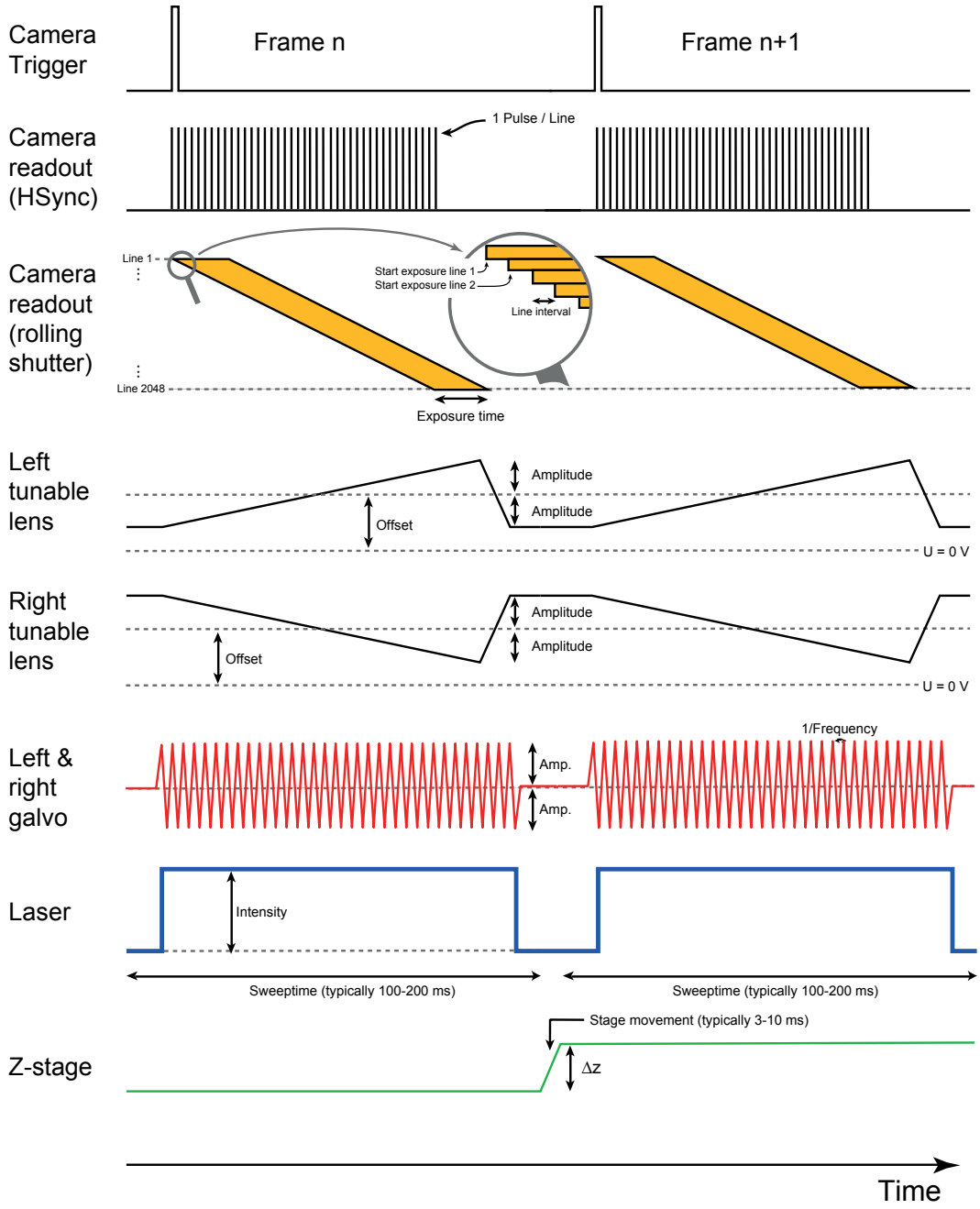

Figure 4.13: Timing diagram of the mesoSPIM waveforms. The camera trigger starts the rolling shutter, which is synchronized to a sweep of the tunable lenses. At the same time, the light-sheet is created by rapidly scanning a Gaussian beam using the galvo scanners. While the exposure is running, the laser is set to a constant intensity and switched off between frames. During the same time, the camera frame is read out and the z-stage can advance.

4.3.5 Supplementary Note: Microscope software: mesoSPIM-control

A wide range of custom light-sheet microscopes (e.g. the openSPIM instrument) are controlled by Micromanager (Edelstein et al., 2010, 2014), an open source microscope control software based on ImageJ (Schneider, 2012). As a significant fraction of early mesoSPIM hardware components were not supported by Micromanager, we opted to control the instrument with custom-written software in Python. The mesoSPIM-control software software runs on Python >3.6 and was tested both on Windows 7 and Windows 10. It utilizes the PyQt5 bindings for Qt V5, a set of cross-platform C++ libraries that implement high-level APIs for accessing many GUI functions. In addition, we are using the QThread class of Qt5 for multithreading to allow the user interface to stay responsive while the microscope is acquiring images. The Camera Window and histogram controls are using the ImageView class of the pyqtgraph graphics and user interface library. Installation instructions are documented in the software documentation. After startup, users are prompted to select a microscope configuration file. This file contains assignments of digital and analog output channels to microscope actuators (i.e. stages, galvo scanners, tunable lenses etc.) and configuration data for all major microscope components (i.e. filter assignments to filter wheel positions). The configuration files are user-editable and contain all parameters in the form of Python dictionaries. If necessary, the microscope then carries out referencing movements of the translation stages. The microscope software consists of three windows (Figure 4.14): "Main Window", "Camera Window" and the "Acquisition Manager". The "Main Window" contains all user controls for sample movement, microscope focus, and user-adjustable parameters such as emission filters and laser intensity. After clicking the "Live" button, the "Camera Window" displays images acquired with the current set of parameters without saving them.

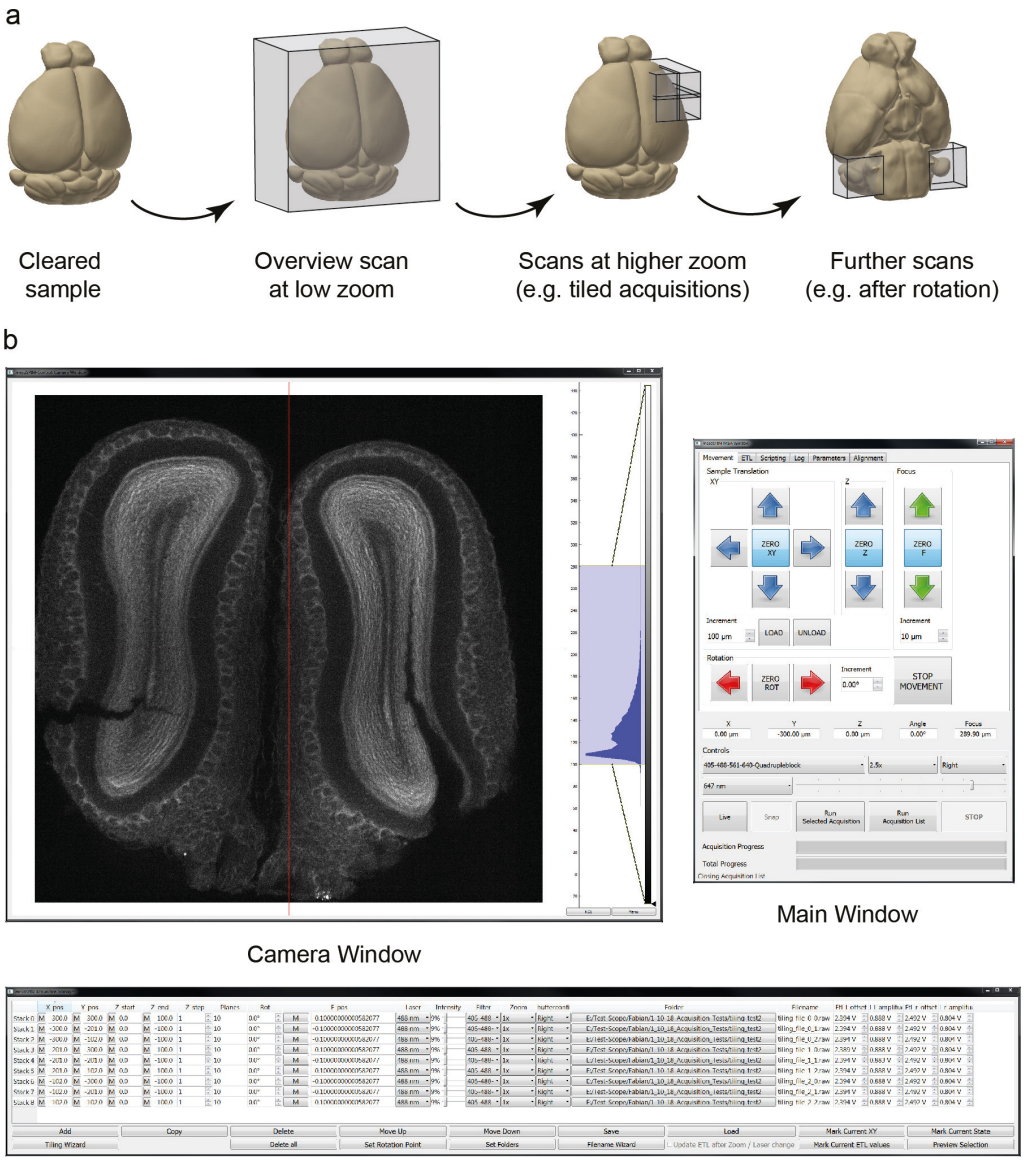

Figure 4.14: mesoSPIM-control. a) Possible user-defined series of data acquisitions: Starting from a cleared sample, users typically perform overview scans to evaluate the quality of the labeling and clearing. Subregions (or the entire sample) can then be scanned with tiled acquisitions. By rotating the sample, multi-view datasets can be generated. b) The mesoSPIM-control user interface consists of three windows: A Main Window with microscope controls (i.e. for sample position, laser selection, laser intensity etc.), a Camera Window with histogram controls and an Acquisition Manager, a table-based tool to plan a series of z-stacks.

As most mesoSPIM users aim for the thinnest possible optical sections using the ASLM mode, the "Main Window" provides extensive control over ETL parameters in the ETL tab: Firstly, sets of predefined ETL parameters ("ETL configuration files") for each combination of zoom, excitation wavelength, and light-sheet direction (left or right) can be saved and loaded as `.csv`-files. As ETL parameters (offset and amplitude) depend on the refractive index of the medium inside the immersion cuvette and its size, a dedicated ETL configuration file should be generated for each combination of clearing method and immersion cuvette the setup is supposed to be used with. In addition, individual clearing methods might require more fine-grained presets: As refractive indices can vary with preparation and temperature, it is recommended for each user/project to have their individual ETL parameter file. In contrast, clearing methods based on organic solvents such as BABB or iDISCO tend to have much more uniform refractive indices across different batches of samples.

To optimize the effective light-sheet thickness, we recommend the following procedure: After setting up the desired zoom and excitation wavelength, users can deactivate the ASLM mode by toggling the "Amp=0" buttons in the ETL tab. This sets the ETL amplitude to zero and saves the current amplitude (which can be reloaded by de-toggling the button). Effectively, this turns the mesoSPIM in a standard light-sheet microscope with a scanned Gaussian beam (DSLM) for light-sheet generation. Users can then manually place the waist location (visible as the vertical stripe with the lowest signal or the least amount of sample features) in the center of the camera FOV (aided by crosshairs in the camera window). In samples with insufficient clearing, visually localizing this region can be a challenge. As soon as the waist is placed in the center of the FOV, users can switch the ASLM mode back on and optimize the ETL amplitude. In the ideal case, the amplitude is just right for the ETL-actuated waist and the rolling shutter of the camera to track each other perfectly across the FOV of the microscope. If this is not the case, for example, when the ETL amplitude is too small or too large for a given zoom/FOV setting, the center of the image will display good axial confinement of the light-sheet whereas the left and right edges will appear

more blurry or contain more sample features as the effective light-sheet thickness is larger in these regions (see Figure 4.6). By observing the left and right edges of the image while changing the ETL amplitude, an optimum can be found.

After finding the optimum ETL parameters for a certain region of the sample, users can generate complex multidimensional acquisition sequences using the "Acquisition Manager" window, which contains a table of z-stacks. Each stack (or "acquisition") is represented by a row in this table and can have a user-defined startpoint (defined by its XYZ and rotation coordinate) and an endpoint at a different z-location. The software then automatically calculates the number of planes for a selected z-spacing. In addition, users can define the laser line, laser intensity, emission filter, zoom and shutter configuration (left/right/both light-sheets). In addition, a filename and a folder location can be specified. The tunable lens offset and amplitude values can be specified as well for each row. A series of "Mark" buttons allows the user to copy elements of the current microscope state (i.e. filter and laser intensity or ETL parameters) into a table row to simplify setting up acquisitions.

Tables for mosaic acquisitions can be generated using a "Tiling Wizard" which guides users through a series of steps (starting from the definition of a bounding box for the list of acquisitions). A preview button allows users to visually inspect a single selected acquisition in "Live mode" by moving the sample to the starting position and setting up the desired excitation wavelength, laser intensity, filter, shutter configuration and ETL parameters. This aids in checking whether the imaging parameters are correct for each individual stack. By selecting a table row and clicking the "Run selected acquisition" button in the main GUI, a single z-stack can be acquired. By clicking "Run Acquisition List", the microscope acquires all acquisitions specified in the table from top to bottom. Acquisition manager tables can also be saved and reloaded, i.e. to apply the same tiling pattern to a different sample. If the user specified a sample rotation between subsequent z-stacks, the microscope will move in X,Y, and Z to a safe rotation position, rotate

the sample, move back, and continue with the next z-stack. This is necessary as large samples can collide with the immersion cuvette during rotation. The rotation position can be inspected and specified in the main user interface. By specifying multiple rotation positions, multi-view acquisitions can be generated (see Figure 25 4.26). Currently, the microscope saves acquisitions in a raw-format with an additional metadata file. A "Parameter" tab in the main GUI allows access to other microscope configuration parameters such as the delays, rise and fall times for the ETL ramps, camera exposure time and line interval. In addition, the Main Window has a "Alignment" tab that allows running the microscope in a mode that simplifies co-alignment of both light-sheets by interleaving the illumination directions frame-by-frame.

4.3.6 Supplementary Note: Resolution measurements and microscope characterization

To GENERATE TEST-SAMPLES, we embedded Fluoresbrite YG Microspheres (1-µm diameter; Polysciences) in 1% agarose (Sigma-Aldrich 9012-36-6). For resolution measurements at low zoom settings (1×), we used 1:10000 dilution, for 4× 1:1000. We cured the agarose/bead mixture in molds made out of 10 ml syringes with cut-off tips. Using the plunger, removing the agarose from the mold was straightforward. The agarose cylinders were then transferred to a 20 ml RIMS (Yang et al., 2014) solution to begin index matching. After 24 hours, the samples were transferred into 10×20×45 mm^3 quartz cuvettes and the RIMS was exchanged. We noted that full index-matching could take up to a week. It is recommended to keep such test-samples for long time periods in the imaging cuvette to periodically check the microscope performance. To allow this, the cuvettes should be covered to avoid evaporation and can be placed in a fridge at 4°C. The RIMS was prepared at an index of nD=1.45 using a refractometer (Krüss DR301-95). We then placed the samples in the immersion cuvette filled with a fused silica immersion oil (Cargille 50350). This allowed resolution measurements under conditions for imaging CLARITY samples. We acquired z-stacks over a range of 200 µm at 1-µm z-spacing after manually optimizing the ETL parameters.

The datasets were then converted to .tif and analyzed using the Jupyter notebook for mesoSPIM PSFanalysis (github.com/mesoSPIM/mesoSPIM-PSFanalysis), which is based on the PSF analysis code developed by Nicolas Sofroniew for the Thorlabs two-photon mesoscope. Briefly, after smoothing using a Gaussian filter, maxima (corresponding to beads) are detected by the scikit-image `peak_local_max` function. Maxima locations that are too close in 3D than a predefined bounding box (window size) in X x Y x Z (20 × 20 × 40 µm3 at zoom 1×; and 5 × 5 × 20 μm^3 at zoom 4×) are discarded to allow for measurements on single beads. A Gaussian function is then fitted to the lateral and axial intensity profiles. For lateral PSFs, the X and Y full-width at-half-maximum (FWHM) are averaged. The resulting data are shown in Figures 4.15 and 4.16.

By switching the ASLM mode off the resolution of the microscope could be estimated in a scanned Gaussian beam mode. At 488 nm, we estimated the FWHM of the non-scanned light-sheet as 3.514 ± 0.013 µm (n = 198 beads), which corresponds to a Rayleigh length of approximately 83 µm. When switching on the ASLM mode at zoom 4×, the average axial FWHM was 5.568 ± 0.027 µm (n = 2170 beads) across a 3.29-mm FOV (Figure 4.16). To achieve these values, the lateral galvo sweep frequency was set to 199 Hz and the exposure time to 5 ms.

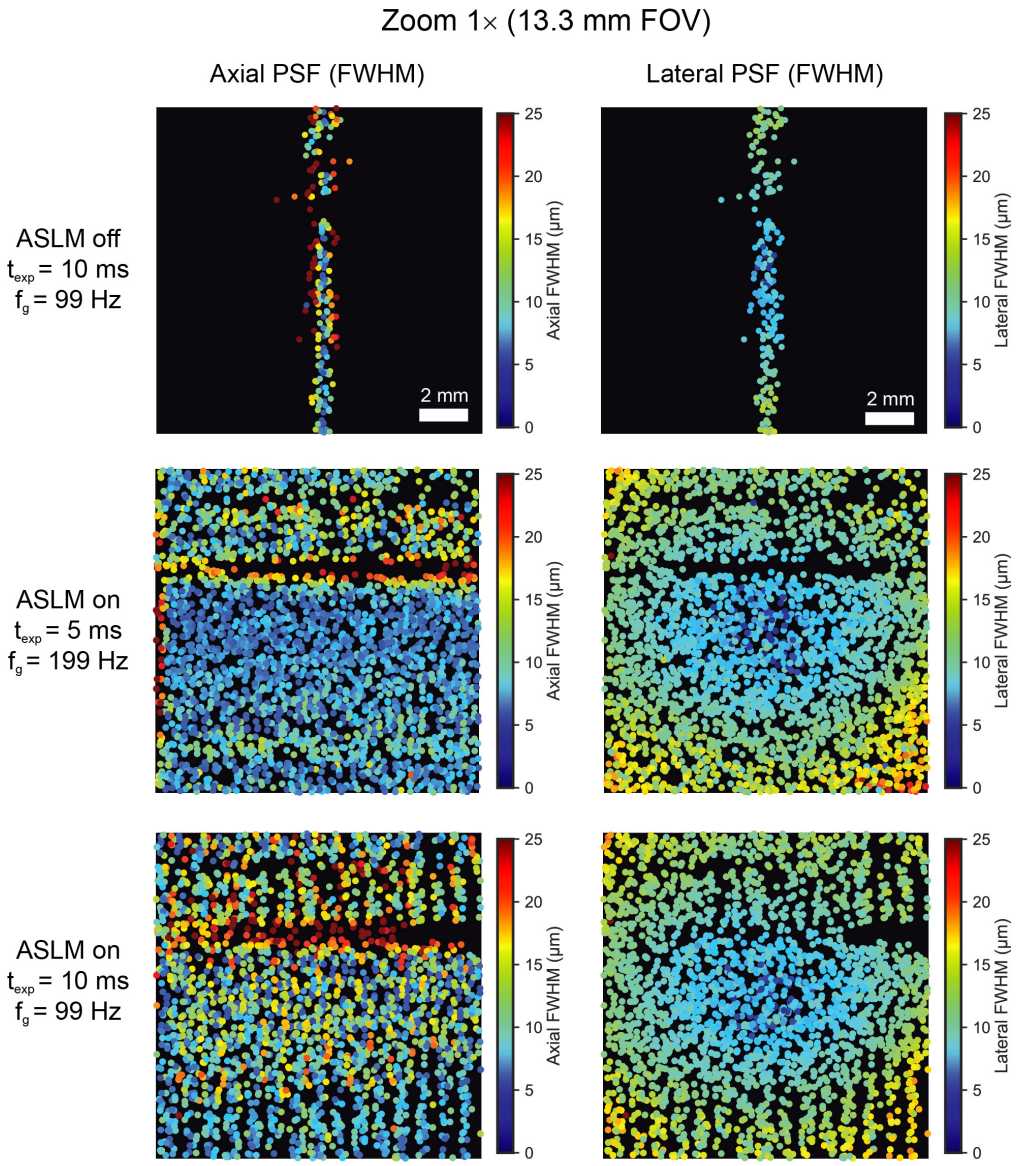

Figure 4.15: Axial and lateral resolution at low zoom (1×). Color-coded FOV-maps of the axial (left) and lateral (right) point-spread-function (PSF) full-width at half-maximum (FWHM) at zoom 1×. With the ASLM mode switched off, beads were detected only along the light-sheet waist as the axial FWHM increased rapidly beyond the window size. The beads were diluted 1:10000 in 1% agarose and index matched to a final index of $n_D = 1.45$. The excitation wavelength was 488 nm, the emission light was filtered using a 520/35 band pass filter. Cracks in the agarose block deteriorate the light-sheet confinement and lead to shadow regions, along which beads could not be fitted. Note that compared to the ASLM-off condition, running the ASLM mode at a galvo scanner frequency f_g= 199 Hz and 5-ms exposure time allowed a uniform axial resolution <7 µm across the whole lateral FOV in the central region of the sample. As the Olympus MVX-10 was originally designed for visual use, an inside-out gradient of the lateral resolution is visible. In addition, the lateral resolution measurements are sampling-limited due to a pixel size of 6.55 µm. At lower f_g, the pattern of detected beads shows stripes due to detoriation of the axial resolution, leading to fewer detected beads.

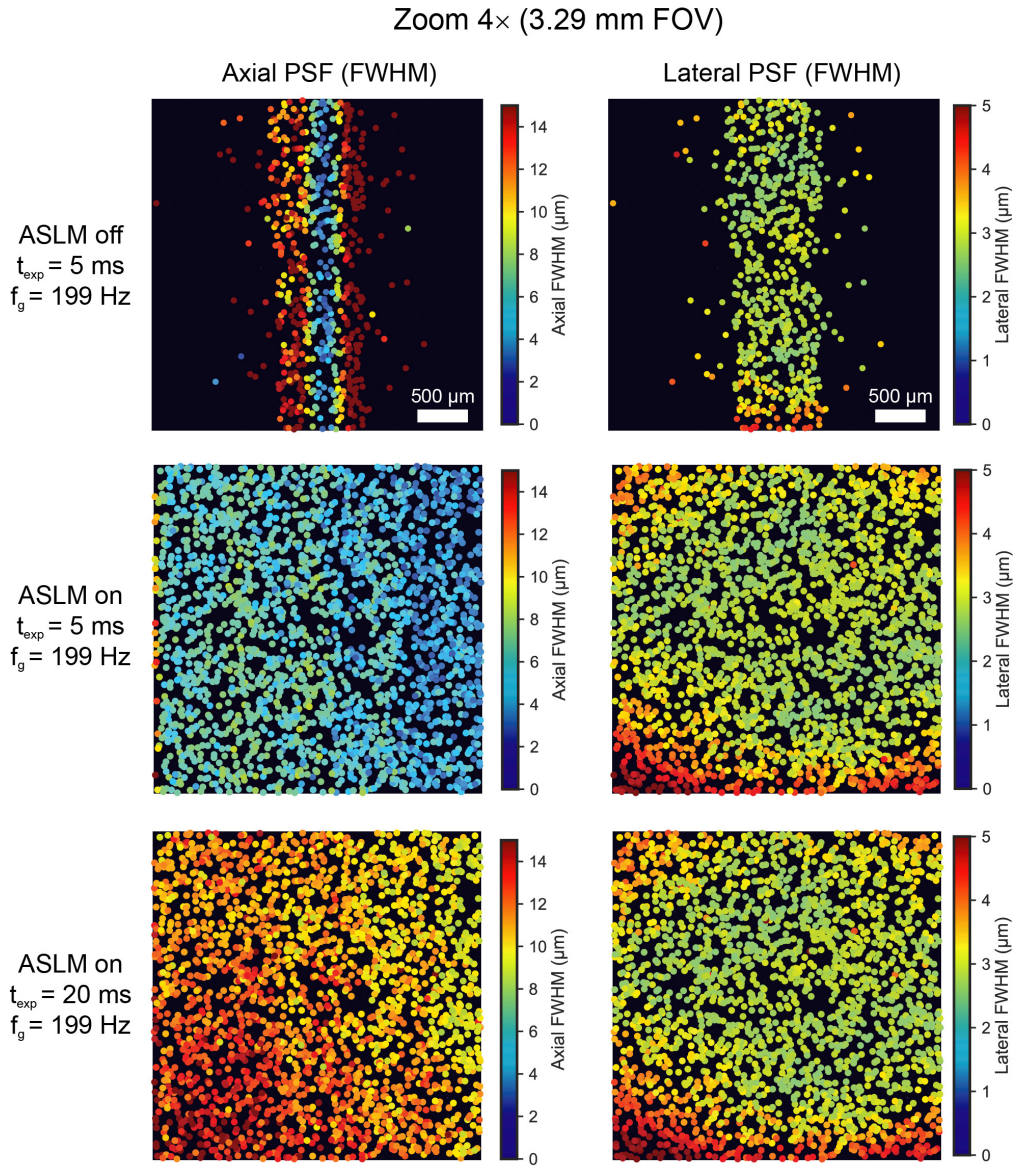

Figure 4.16: Axial and lateral resolution at high zoom (4×). Color-coded FOV-maps of the axial (left) and lateral (right) point-spread-function (PSF) full-width at half-maximum (FWHM) at zoom 4×. Each dot represents a single detected 1 µm bead of which the axial and lateral intensity profiles were extracted and fitted with a Gaussian. To allow proper fitting of the PSF, only a single bead was allowed within a volume of 5 × 5 × 20 µm^3. With the ASLM mode switched off, beads were detected only along the light-sheet waist as the axial FWHM increased rapidly beyond the window size. The beads were diluted 1:1000 in 1% agarose and index matched to a final index of nD = 1.45. The excitation wavelength was 488 nm, the emission light was filtered using a 520/35 band pass filter. Note that compared to the ASLM-off condition, running the ASLM mode at a galvo frequency f_g = 199 Hz and 5 ms exposure time allowed a uniform axial resolution of 4.097 ± 0.013 µm across the whole FOV. The axial resolution degrades with increasing exposure time as each active line on the sCMOS sensor then samples more axial variation of the passing light-sheet waist region. At this magnification, the lateral resolution is more uniform compared to 1× zoom, but shows an inside-out gradient as well.

While these values are higher than the non-ASLM z-PSF, it should be noted that even a Gaussian beam with a 5.5 µm FWHM waist has a Rayleigh range of 203 µm; the usable FOV of the light-sheet microscope ($FWHM_{axial} < \sqrt{2} \cdot FWHM_{center}$) was thus increased at least 8-fold. At lower zooms, it was also possible to achieve a considerable increase in uniformity of the axial PSF across the FOV: In the central region (13.29 mm in X × 1.3 mm in Y or 2048 × 200 pixels) of the 1× FOV, a resolution of 6.519 ± 0.074 µm (n = 322 beads) across a FOV of 13.29 mm was measured (Figure 4.15). A Gaussian light-sheet with a 6.5 µm waist would have a Rayleigh range of 284 µm – enabling the ASLM mode thus corresponds to a 23.4-fold increase in FOV. However, such resolution measurements at low zoom suffer from inhomogeneities and cracks in the agarose, which make generation of stable test samples for large FOVs difficult.

The effective detection NA of the MVX-10/MVPLAPO 1× combination varies with zoom and can be estimated as NA = 0.075 at 1× and 0.22 at 4× (Olympus, personal communication). Based on these values, the diffraction-limited lateral resolution would be 3.5 µm and 1.18 µm, respectively. With 6.55 µm/pixel and 1.6 µm/pixel sampling, the mesoSPIM is undersampled at both zooms which results in much larger measured resolution values. In addition, at both zooms, a radial gradient of the lateral FWHM values is visible.

With longer and longer exposure times at constant ETL sweeptime (see Figure 4.13), the effective light-sheet thickness (or axial FWHM) across the FOV increases: As each line of the detector collects photons for a longer time, it samples a wider stripe of the axial light-sheet profile. This means that in practice, a trade-off has to be found between exposure time (collecting sufficient signal) and light-sheet thickness. For example, for imaging antibody-stained samples in BABB (Figures ??) or samples cleared and stained with iDISCO (Figure 4.28), exposure times could be reduced to 10 ms or even 5 ms because the secondary amplification in the staining procedure yields high signal levels. When imaging endogenous fluorescence, however (Figures 4.1 , 4.20, 4.21), typical exposure times were 20 ms. To demonstrate this trade-off, we imaged the same

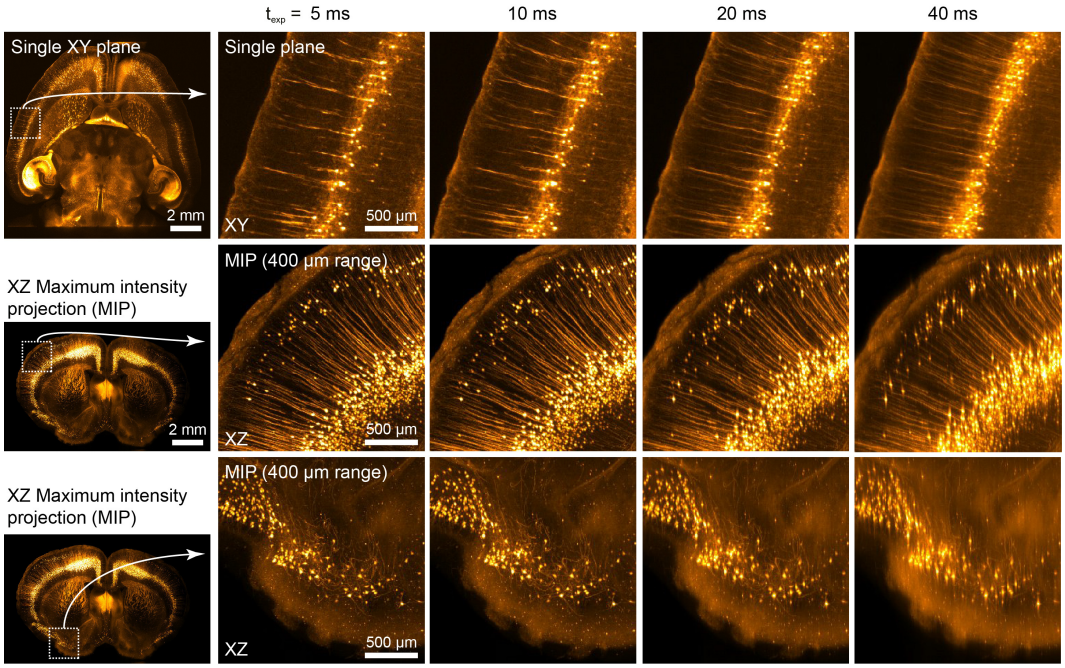

Figure 4.17: In ASLM, axial resolution depends on exposure time at low zoom (1×). Comparison of example stacks taken in a CLARITY-cleared Thy1-YFP whole mouse brain. The galvo frequency was set to $f_g = 199$ Hz and the sweeptime to 200 ms. Increasing the exposure time yielded worsening of axial resolution. Note that despite the loss of axial resolution, it is uniform across the FOV; even 40-ms exposure time (which is 1/5 of the sweeptime) leads to a better axial resolution at the edges of the FOV compared to switching off the ASLM mode entirely (compare to Figure 4.5). As the microscope collects more light with increasing exposure time, users have to select a tradeoff between exposure time and axial resolution depending on their requirements.

CLARITY-cleared Thy1-H-mouse brain under a variety of imaging conditions: At zoom 1× (Figure 4.17, increasing the exposure time from 5 to 40 ms led to a drastic reduction in axial resolution. At 4× magnification (Figure 4.18, the loss in axial resolution was less severe. In these experiments, the sweeptime was kept constant at 200 ms which led to an effective frame rate of 4.8 Hz.

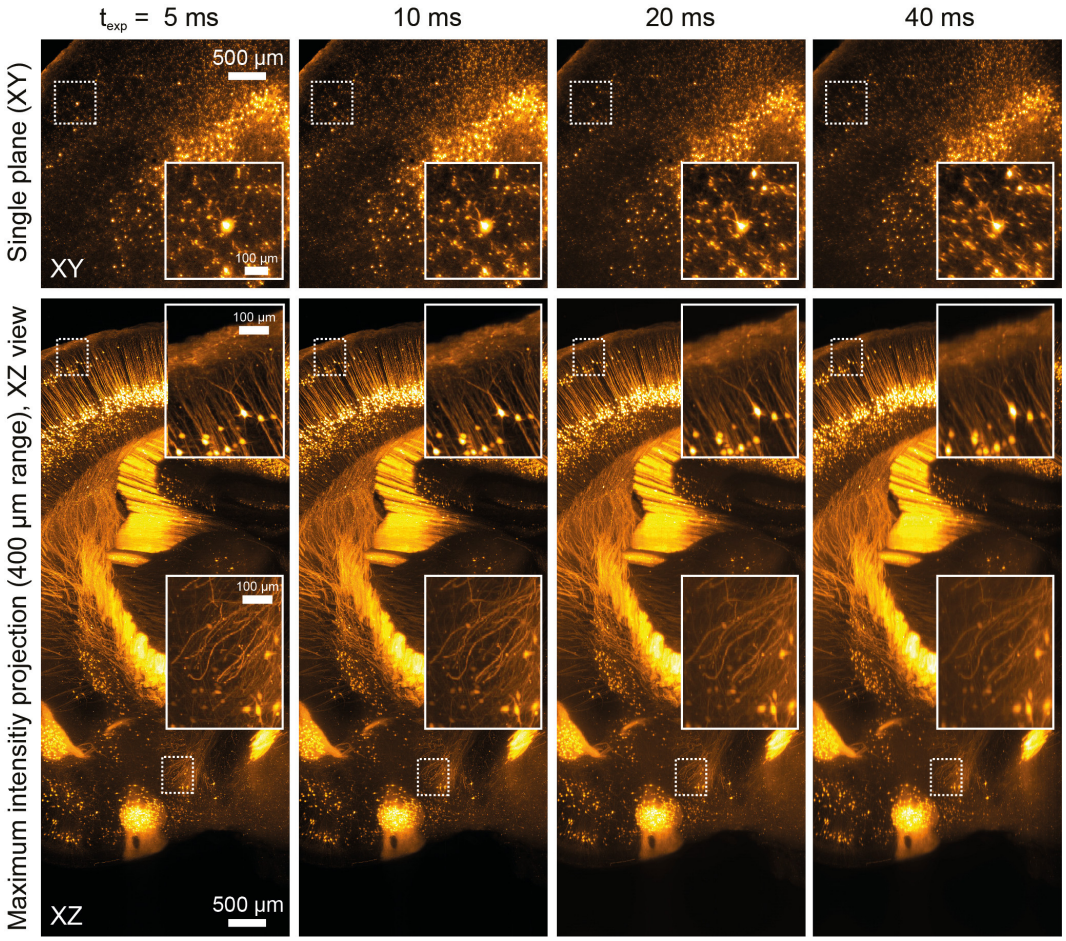

Figure 4.18: In ASLM, axial resolution depends on exposure time at high zoom (4×). Comparison of example stacks taken in a CLARITY-cleared Thy1-YFP whole mouse brain. The galvo frequency was set to $f_g = 199$ Hz and the sweeptime to 200 ms. Increasing the exposure time yielded worsening of axial resolution. Note that despite the loss of axial resolution, it is uniform across the FOV; even 40-ms exposure time (which is 1/5 of the sweeptime) leads to better axial resolution at the edges of the FOV compared to switching off the ASLM mode entirely (compare to Figure 4.5.

4.3.7 Supplementary Note: Imaging examples: Compatibility with different clearing techniques

A key advantage of the modular and open design of the mesoSPIM is the compatibility with all major clearing techniques. As different clearing techniques require immersion media with a wide range of refractive indices and different physical properties, typical light-sheet microscopes have to be modified extensively to allow for imaging across a wide range of media. For example, many CLARITY immersion media such as RIMS (Yang et al., 2014) are not very homogenous in refractive index (evident by visible striae in the medium). This is not surprising given that the RIMS by Yang et al. is based on Histodenz, which is originally a gradient density medium. Other media such as BABB (benzyl alcohol-benzyl benzoate) can lead to damage of the front lens of microscope objectives which is why very few objectives capable of imaging in BABB exist. An overview of all tested clearing techniques is given in Table 4.2. As a reference, table 4.4 lists all mouse lines used in this study. In addition, table 4.3 provides an overview of the imaging parameters.

Clearing technique	Sample	Figure
CLARITY (passive)	Mouse brain (VIPCre-tdTomato)	Figures 4.1b, 4.3
CLARITY (passive)	Mouse brain (TPH2Cre-tdTomato)	Figure 4.1c-e
CLARITY (passive)	Mouse brain (Rbp4Cre-YCX2.60)	Figures 4.19-4.21
CLARITY (active)	Mouse brain (Thy1-YFP)	Figures 4.4-4.7, 4.17-4.18
X-CLARITY (active)	Mouse brain (GlyT2-EGFP)	Figures 4.22
CUBIC-X	Mouse brain (Ntsr1Cre-tdTomato)	Figures 4.23-4.24
BABB	Chicken embryo (Neurofilament)	Figures 4.1f, 4.25-4.26
BABB	Drosophila melanogaster	Figure 4.27
iDISCO	Mouse brain (IgG)	Figures 4.28-4.29
iDISCO	Rat brain (To-Pro)	Figure 4.30
MASH (iDISCO/ECi)	Human cortex	Figure 4.31

Table 4.2: Overview of clearing techniques tested with the mesoSPIM. References to the figures are provided.

The mesoSPIM is compatible with hydrogel-based clearing techniques such as active and passive CLARITY: The CLARITY (Chung et al., 2013) family of clearing techniques is based on

crosslinking proteins in a hydrogel and using sodium dodecyl sulfate (SDS) as detergent to remove lipids from the sample. Lipid removal can be done 'actively', using electrophoretic assistance in a custom chamber (Chung et al., 2013) or using 'passive' or flow-assisted immersion in SDS (Tomer et al., 2014; Lerner et al., 2015). Samples cleared with CLARITY tend to be slightly expanded after the index-matching step in the refractive index matching solution (RIMS) we employed (based on the Histodenz approach by Yang et al. (Yang et al., 2014)). As noted by Tomer et al. (Tomer et al., 2014) , the refractive index of cleared samples is close to the index of quartz, which means that samples can be placed in quartz cuvettes for imaging. In addition, as many immersion media for CLARITY samples such as glycerol-water solutions and RIMS tend to be inhomogeneous in refractive index, placing the cuvette in an imaging chamber filled with an immersion oil at the index of quartz/fused silica (such as Cargille 50350) means that the light-sheet has to pass through a minimum of RIMS, which reduces the impact of local index variations in the quality of the light-sheet. For imaging CLARITY-cleared samples, we adopted the same technique and immersed whole mouse brains in a 10×20×45 mm^3 quartz cuvette filled with RIMS and then immersed this imaging cuvette in turn in an immersion cuvette (typically a 40×40×45 mm^3 quartz macro fluorescence cuvette made by Portmann Instruments). As CLARITY-cleared samples tend to float, we glued a small weight to the brain (typically a M4 nut) using quick glue.

To showcase the imaging quality achievable with the mesoSPIM in a mouse brain processed using active CLARITY, we imaged an Thy-1 YFP sample(Feng et al., 2000) (Figures 4.4, 4.5, 4.6). In this sample, the mesoSPIM can resolve single neurons in sparse subregions at 1× zoom, which corresponds to a 13.29-mm FOV

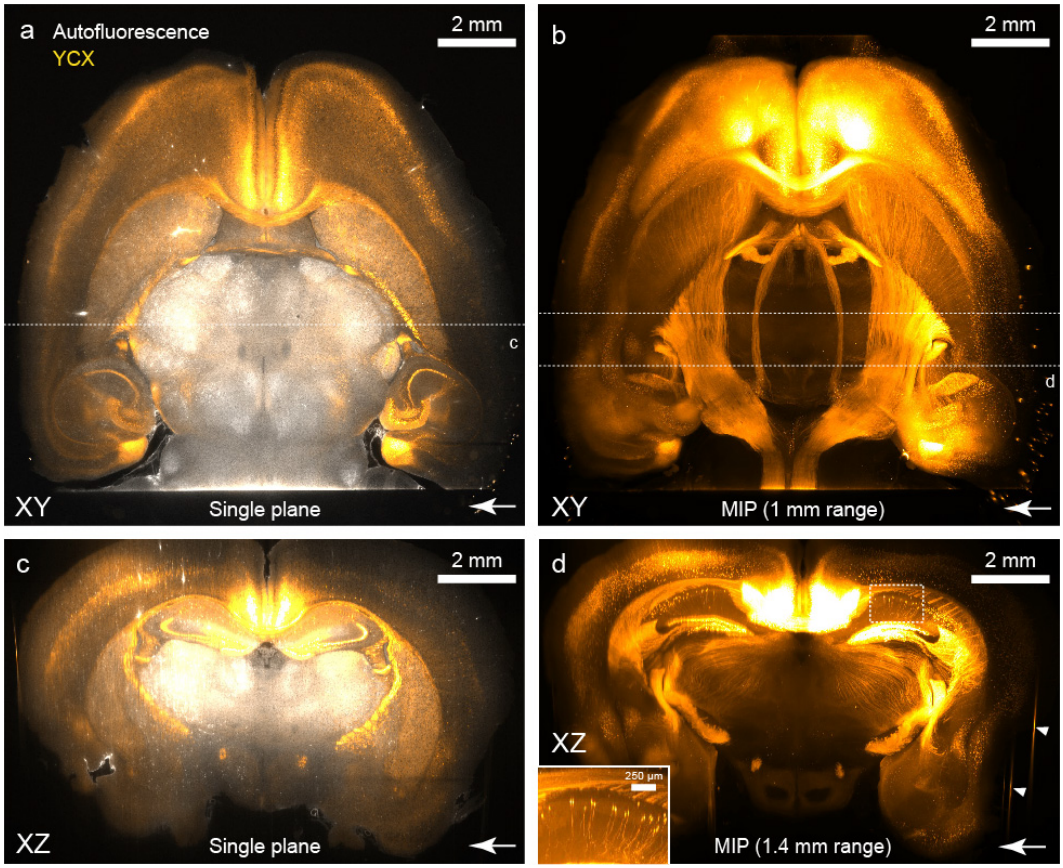

Figure 4.19: Low-resolution overview images (Zoom 1×) of a passive CLARITY-cleared mouse brain. a) Single horizontal plane taken from an overview dual-color stack of a mouse expressing the calcium indicator Yellow Cameleon X 2.60 (YCX) in excitatory neurons in layer 5 (Rbp4Cre-YCX2.60) of the neocortex. b) Maximum intensity projection (MIP) over the basal half-section of the imaging volume in a). Long-range projections from the cortex to the spinal cord are visible. c) Single resliced plane (XZ view) from the dataset (location indicated in a). d) MIP over a range of 1.4 mm. Despite the large pixel size (6.55 m), dendrites from YCX-expressing neurons in the hippocampus are visible in the XZ view (inset). The bottom right arrow indicates the light-sheet direction (illumination from the right side). Degradation of the light-sheet inside the tissue leads to the lower resolution in the left hemisphere. The arrow heads indicate Z-streaks caused by bubbles on the surface of the sample which scatter the excitation laser light.

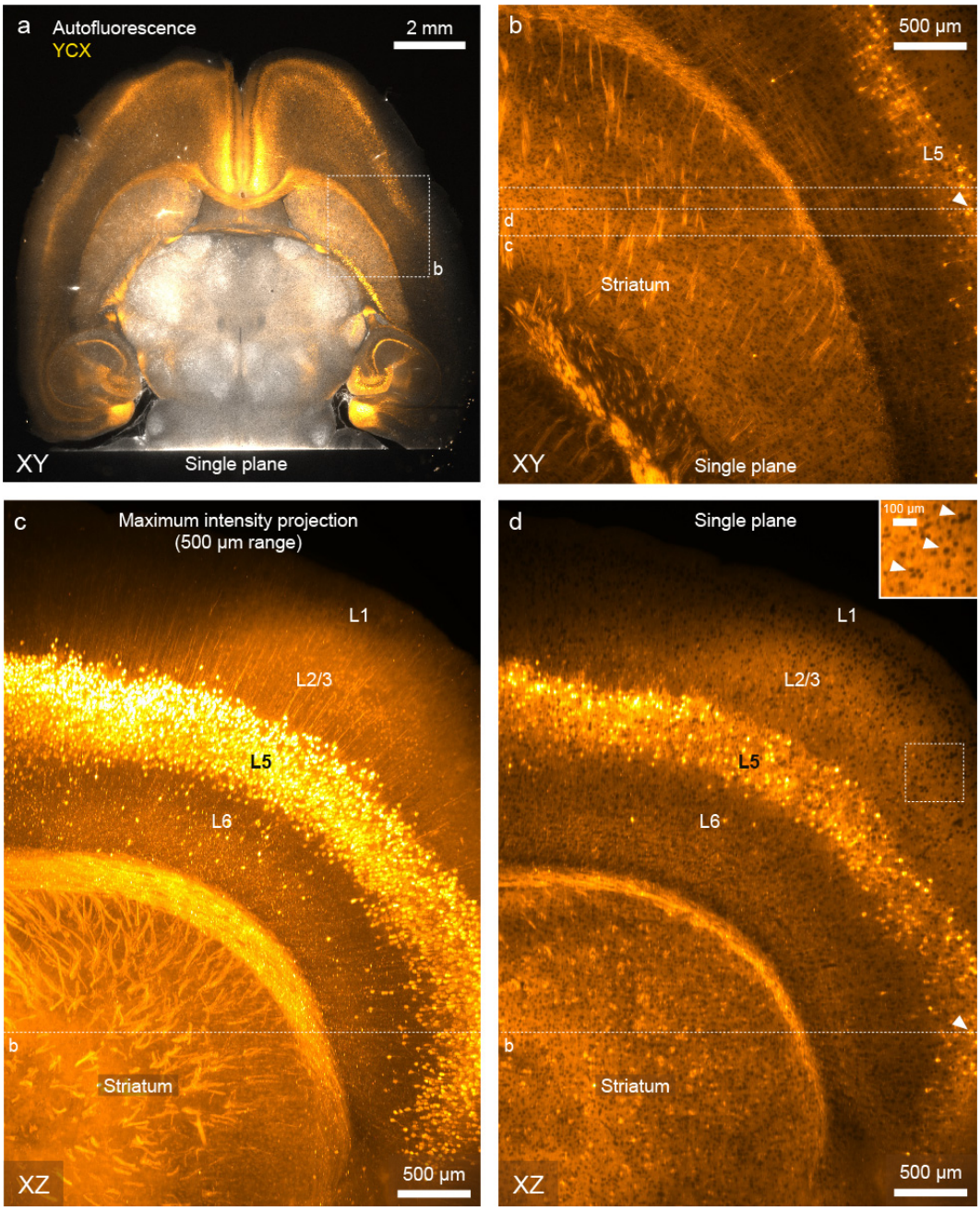

Figure 4.20: A mouse brain expressing the calcium indicator Yellow Cameleon X 2.60 (Rbp4Cre-YCX2.60) was cleared using passive CLARITY. a) Single plane taken from an overview dual-color stack. b) Single plane acquired at 4× zoom of the subregion shown in a). The arrow head indicates the same cell in subpanels b) and d) c) MIP in the XZ-plane (reslice) of the subvolume indicated in b). d) Single plane (location indicated in b) of the resliced dataset. The expression occurs predominantly in cortical layer 5 (L5). Long-range projections are visible in the striatum. A wide variety of counterstained cell bodies is visible throughout the volume and can be identified even in the XZ plane (inset).

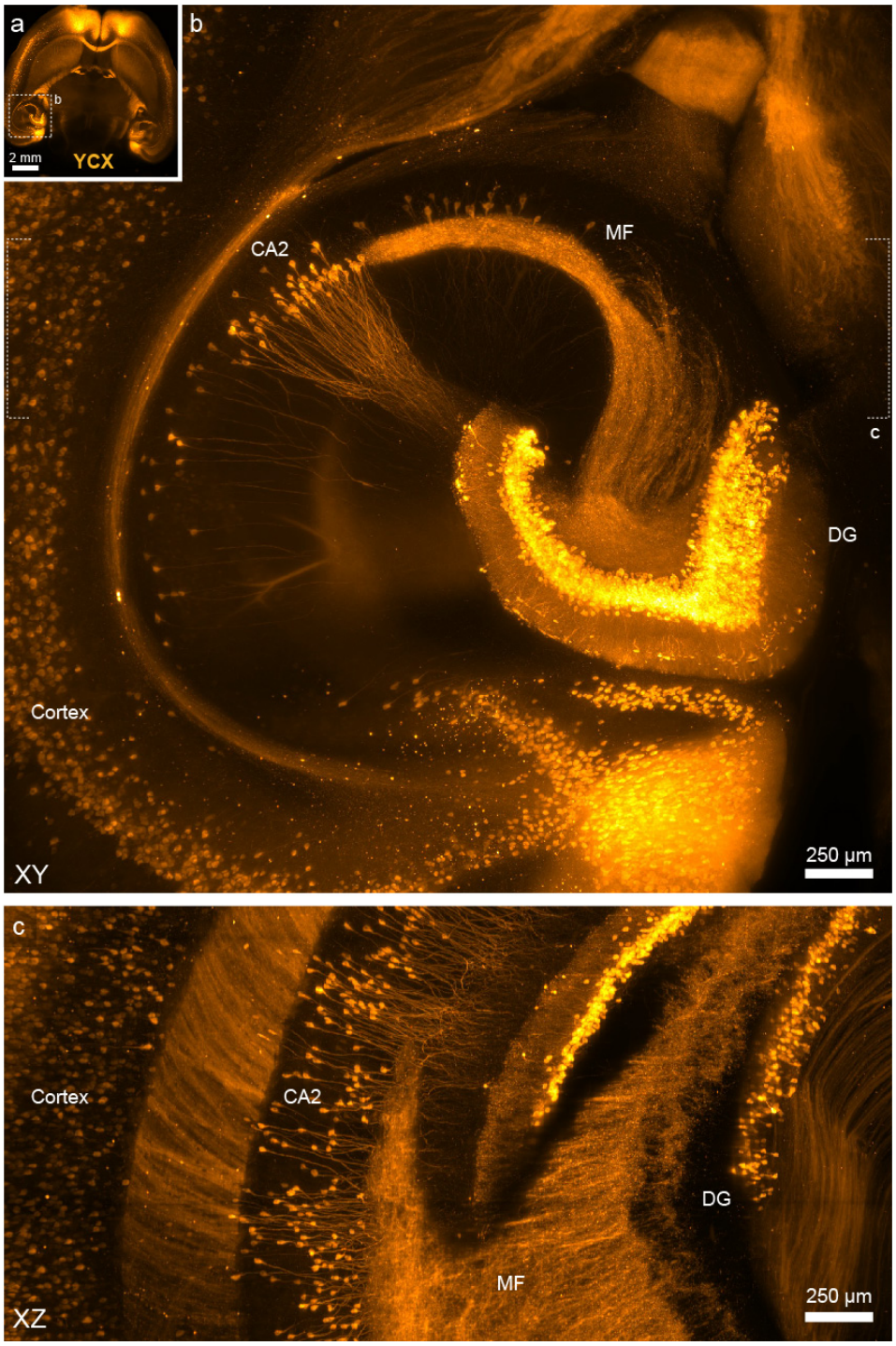

Figure 4.21: Multi-scale imaging with subcellular resolution (Zoom 4×) in a mouse brain cleared with a passive CLARITY protocol. a) Overview image of a mouse brain expressing the calcium indicator Yellow Cameleon X 2.60 (Rbp4Cre-YCX2.60). b) MIP of a 600-µm thick virtual slice. In addition to the cortical expression, this mouse line shows sparse labeling in CA2 region of the hippocampus and strong labeling of granule cells in the dentate gyrus (DG). Furthermore, the mossy fiber pathway (MF) is labeled. c) MIP of a subvolume (indicated in subpanel a) of b). Single CA2 neurons and their dendrites are well resolved in the XZ plane.

and 6.55-µm pixel size (Figure 4.4, Supplementary Video 2). At higher magnification (zoom 4×, 3.3-mm FOV, 1.6-µm pixel size) axons can be imaged and are well resolved in the XZ plane (Figure 4.5 Supplementary Video 3). The preparation of this sample is described in a dedicated supplementary note (section 4.4).

A SIMPLIFIED CLARITY PROTOCOL utilizes either passive immersion or pumping of SDS through the clearing chamber without electrophoresis (Tomer et al., 2014). This "passive" CLARITY approach takes much longer (up to 4-6 weeks for a whole mouse brain), but many samples can be processed in parallel. As an example, we processed and imaged a whole mouse brain expressing tdTomato in VIP neurons, a subclass of inhibitory interneurons (Figure 4.1b). Owing to the sparse expression pattern of this mouse line, single neurons can be visualized across the whole brain in the axial direction even at low magnifications such as 0.8x if the ASLM mode of the mesoSPIM is engaged (Figures 4.1b, 4.3, Supplementary Video 1). In addition, we applied the passive CLARITY protocol to a mouse brain expressing tdTomato in serotonergic neurons driven by a TPH2Cre line (Tryptophan Hydroxylase 2). In this sample, expression is not restricted to structures such as the Raphe nuclei, but widespread (Fig. 4.1c,d, Supplementary Video 4) – for example, both the hippocampi and the optic nerves between the optical chiasm and the lateral geniculate nuclei are strongly labeled. In addition, a small subset of Purkinje neurons showed labeling in dendrites, soma and axons (Figures 4.1d,e Supplementary Videos 5 & 6).

A KEY ADVANTAGE OF CLARITY, compared to clearing techniques that quench fluorescence within a few days (such as 3DISCO), is that no additional staining is required to visualize expression patterns. For example, in two-photon microscopy, genetically encoded calcium indicators are often used to measure neuronal activity (Grienberger and Konnerth, 2012). In such experiments, it is of considerable interest to link the functional response properties of neurons imaged in vivo to their anatomical identity and projection profiles. A key step in a cleared whole-mount sample is to achieve sufficient resolution of indicator expression so that single neurons can be

identified. To demonstrate this, we processed mouse brains expressing the calcium indicator Yellow Cameleon YCX2.60 (Madisen et al., 2015) in excitatory neurons in layer 5 (L5) of the neocortex (Rbp4Cre-YCX2.60) using passive CLARITY (details on the sample processing are provided in section 4.4). YCX2.60 is a calcium indicator based on fluorescence resonance energy transfer (FRET) and contains a ECFP/EYFP pair. For anatomical imaging, we excited EYFP at 515 nm and recorded background autofluorescence with 647-nm excitation (Figure 4.19). Overview images at low magnification (zoom 1×) reveal that in this mouse line, a wide range of long-range projections are labeled (Figure 4.19a-c). In addition, in certain subregions, for example in the hippocampus, single neurons and their dendrites are readily visible in the XZ (Figure 4.19d). At 4× magnification, it is possible to detect single neurons in L5 in both the XY and XZ plane (Figure 4.20a-c). In addition, the dense neuropil labeling by the calcium indicator leads to non-labeled cells visible due to counterstaining (Figure 4.20d). As the ability to visualize such non-expressing cells is critically dependent on the effective light-sheet thickness, ETL parameters can be tuned in the sample by optimizing the contrast of these negatively stained cells. In addition, it is possible to visualize singe neurons and their dendrites in deeper regions of the brain such as the hippocampus (Figure 4.21a,b). Interestingly, the Rbp4Cre line shows a sparse expression confined to the hippocampal region CA2 as well as strong expression in granule cells of the dentate gyrus (DG) and their axons forming the mossy fiber pathway (MF). Most importantly, the ASLM mode allows visualizing the same structures in the XZ plane with ease (Figure 4.21c).

4.3.8 The mesoSPIM is capable of imaging a whole mouse central nervous system

A key advantage of the mesoSPIM compared to existing commercial setups is that much larger cleared samples can be accommodated. To demonstrate this capability, we dissected a whole central nervous system (CNS) from a GlyT2-EGFP mouse (Zeilhofer et al., 2005) which expresses EGFP in glycinergic neurons in the spinal cord, brainstem, cerebellum, and thalamus. We processed the sample using the X-CLARITY clearing machine (Bucher Biotec AG). For mounting, we transferred the sample in RIMS in a custom 10×20×120 mm^3 quartz cuvette (Portmann Instruments) filled with RIMS and immersed it in a 40×40×120 mm^3 quartz cuvette filled with an immersion oil at nD = 1.45 (Cargille 50350). The large travel range of the sample stages (44.5 × 44.5 × 100 mm^3) then allowed scanning the entire sample without remounting or cutting (Figure 4.22). Using this approach, single interneurons expressing the glycine transporter 2 (GlyT2) could be visualized in the spinal cord and hindbrain (Figure 4.22, Supplementary Video 8).

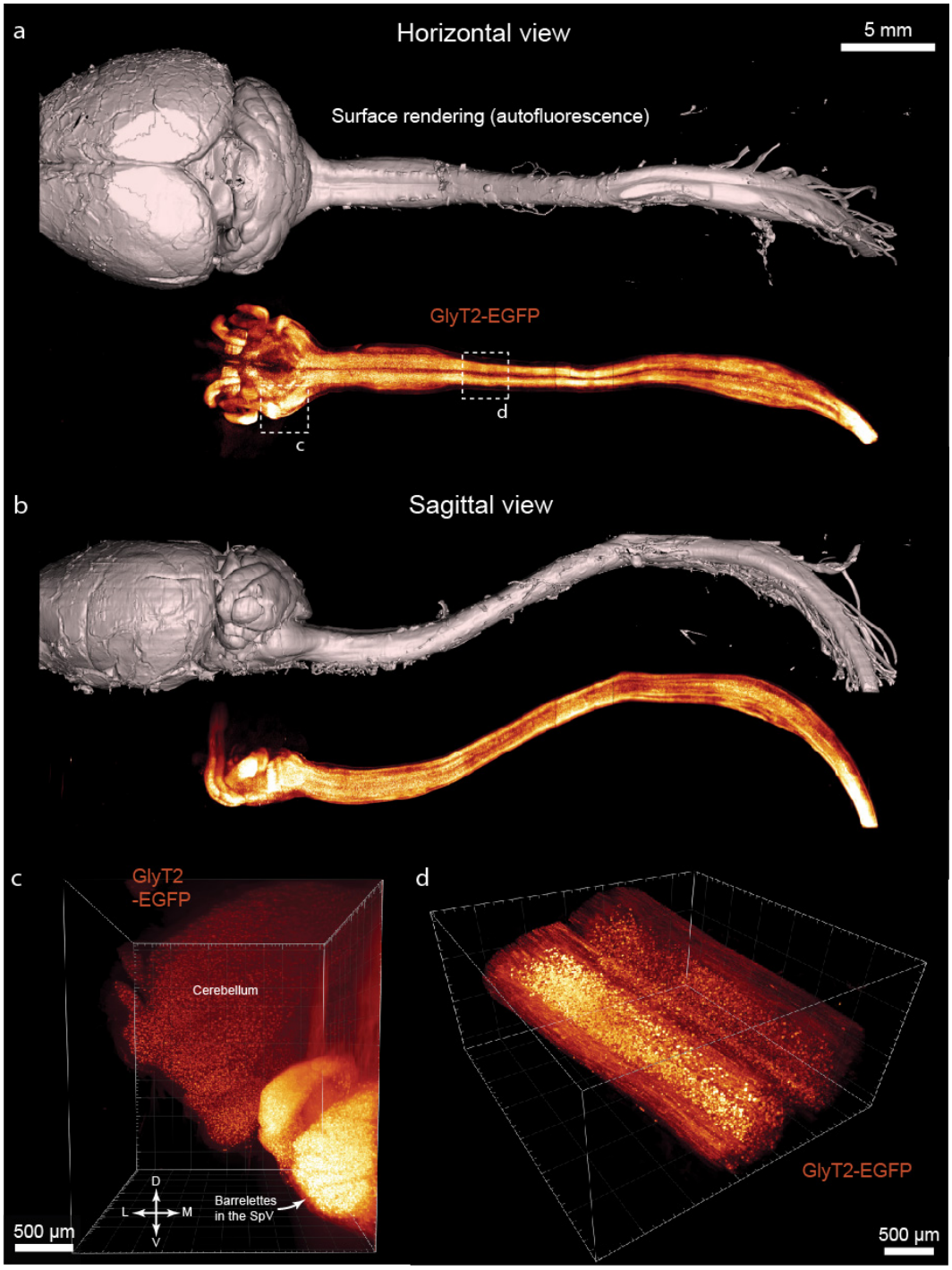

Figure 4.22: Whole-CNS imaging with the mesoSPIM. a) A whole central nervous system was dissected from a Glycine Transporter-2 EGFP (GlyT2-EGFP) mouse and cleared using the X-CLARITY protocol. Shown is a stitched overview dataset taken at 1× zoom (13.29-mm FOV). As GlyT2 expression is restricted to the hindbrain and spinal cord, the forebrain does not show much signal. b) Sagittal view of the data in a). c) Volume rendering of a subvolume acquired using 4× magnification in the ventral hindbrain and cerebellum. Barrelettes in the trigeminal nucleus (SpV) are visible. d) Volume rendering of a volume acquired at 4× magnification in the spinal cord. Individual Glyt2-positive neurons are visible.

4.3.9 The mesoSPIM is compatible with CUBIC-cleared samples

Apart from CLARITY, another family of clearing methods that retain endogenous fluorescence is a combination of "clear, unobstructed brain imaging cocktails and computational analysis" based on amino alcohols (CUBIC, Susaki et al. (2014); Tainaka et al. (2014); Susaki et al. (2015); Nojima et al. (2017). To demonstrate the compatibility of the mesoSPIM with CUBIC-cleared samples, we processed a Ntsr1Cre-tdTomato mouse brain with the CUBIC-X protocol (Murakami et al., 2018), a recent improvement to the original CUBIC which can also be tuned for sample expansion. After clearing, the sample was transferred to a 10×20×45 mm^3 quartz cuvette similar to the ones used for imaging CLARITY samples. The imaging cuvette was then filled with the CUBIC-X2 index matching medium, a combination of 5% (w/v) imidazole and 55% (w/v) antipyrine. To keep the sample from floating to the surface of the imaging medium, a 10×20×10 mm^3 plug made out of 2% agarose was then inserted above the sample. The imaging cuvette was then submerged in a 40×40×45 mm^3 quartz cuvette filled with the same CUBIC-X2 solution. While the original approach of embedding the samples in 2% agarose for imaging can also be utilized with a mesoSPIM, we noted that the approach using cuvettes tends to be much simpler and safer as the sample was very fragile. As the Ntsr1Cre-tdTomato line has an expression pattern restricted to a subset of layer 6 (L6) excitatory neurons, overview images at low zoom show strong labeling in this region and in thalamus (Figure 4.23). At 4× magnification, it is possible to visualize commissural axons in the hindbrain (Figure 4.24).

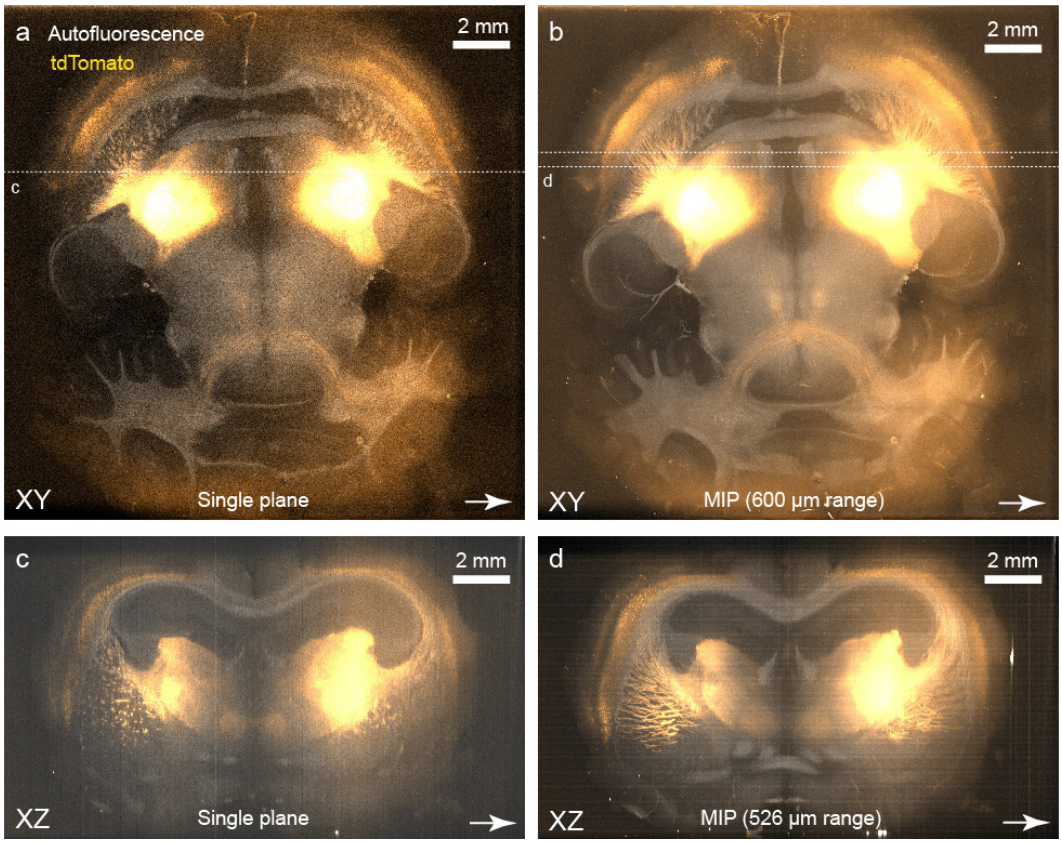

Figure 4.23: Low-resolution overview images (Zoom 0.63x) of a cleared mouse brain cleared using CUBIC-X. A mouse expressing tdTomato in a subset of layer 6 (L6) neurons (Ntsr1-Cre;CAG-tdTomato) was cleared using the CUBIC-X protocol and imaged with the mesoSPIM. a) Single horizontal plane taken from an overview dual-color stack. b) Maximum intensity projection (MIP) over a 600- m range of the imaging volume in a). Long-range projections from the cortex to the thalmus are visible. c) Single resliced plane (XZ view) from the dataset (location indicated in a). d) MIP over a range of 526 m. The bottom right arrow indicates the light-sheet direction (illumination from the left side). Degradation of the light-sheet inside the tissue leads to the lower image resolution on the right half of the brain. Due to low signal levels, the images are very noisy and stripes from single camera pixels are visible.

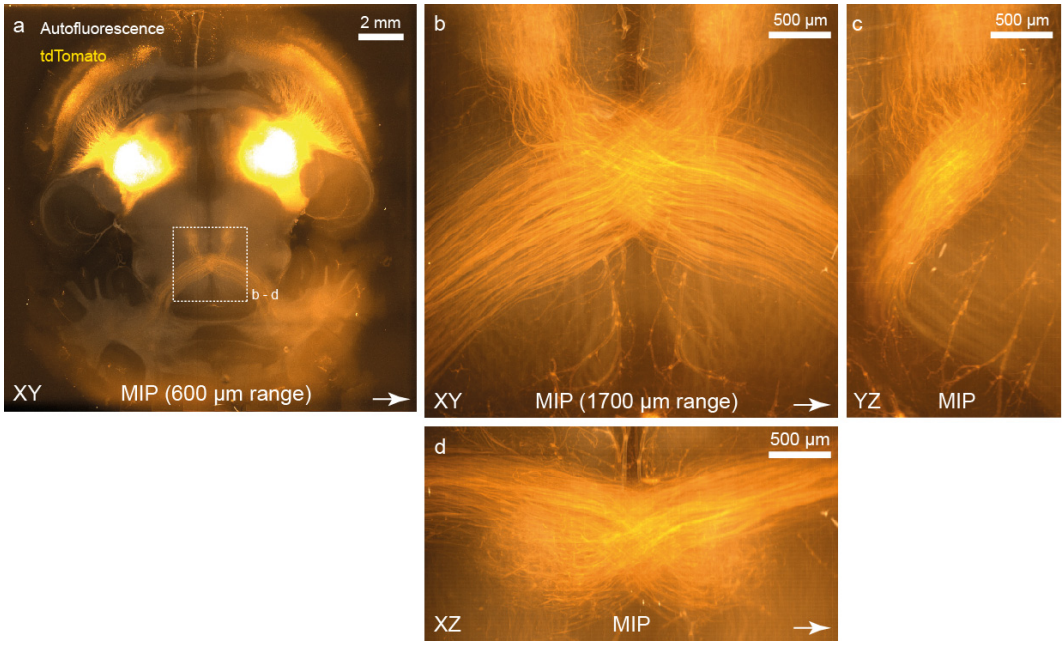

Figure 4.24: Imaging long-range projections in a CUBIC-X-cleared mouse brain. a) Low-resolution overview image (Zoom 0.63x) of a cleared mouse brain (using CUBIC-X2) expressing tdTomato in a subset of layer 6 (L6) neurons (Ntsr1-Cre;CAG-tdTomato) b) Maximum intensity projection (MIP) over a 1700- m z-range of the midline-crossing axons in the sample (location indicated in a). c & d: YZ and XZ projections of the same volume. Due to low signal levels, the images are very noisy and stripe artifacts from single camera pixels are visible. The arrow in the lower right corner indicates the direction of the light-sheet illumination.

4.3.10 The mesoSPIM is compatible with BABB-cleared samples

The combination of benzyl alcohol and benzyl benzoate is among the oldest clearing techniques and was introduced in the early 20th century by Spalteholz (Spalteholz, 1911; Dodt et al., 2007). It forms the ancestor of a wide variety of clearing techniques based on dehydration, delipidation and index matching using organic solvents – including 3DISCO (Ertürk et al., 2012a,b; Ertürk and Bradke, 2013), iDISCO (Renier et al., 2014), iDISCO+ (Renier et al., 2016), uDISCO (Pan et al., 2016), vDISCO (Cai et al., 2018), and PEGASOS (Jing et al., 2018). Compared to CLARITY and CUBIC, the refractive index of the employed organic solvents is usually >1.5, for example $n_D = 1.56$ for BABB. As an example for imaging results achievable with the mesoSPIM, we stained a 7-day old chicken embryo (Hamburger Hamilton stage HH31) for neurofilament with secondary antibodies conjugated to Cy3 and mounted the sample in a 10×10×45 mm^3 glass cuvette (Portmann Instruments) filled with BABB. The imaging cuvette was then immersed in a 40×40×45 mm^3 immersion cuvette filled with BABB. With 561-nm excitation, the developing nervous system could be visualized in its entirety (Figure ??). Using 405-nm excitation and a quadruple-band emission filter (QuadLine Rejectionband ZET405/488/561/640, AHF), it is possible to visualize the anatomy of the embryo using autofluorescence (Figure 4.26). As the mesoSPIM contains a rotation stage, it is possible to perform multi-view acquisitions by specifying rotation increments in the Acquisition Manager Window of the mesoSPIM-control software. Especially for sample features that are highly absorbing and therefore cast shadows—such as the melanin-rich eyes—multidirectional acquisitions can allow "filling in" of missing information. In addition, multidirectional datasets can be fused to achieve more isotropic resolution, a technique common in developmental light-sheet microscopy (Swoger et al., 2007) that has recently been applied to cleared samples (Pende et al., 2018). As the sample was mounted in a quadratic cuvette, we recorded overview stacks at 90° intervals to avoid imaging through the corners of the cuvette (Figure 4.26). If the sample is mounted in a clamping holder, more rotation angles (views) can be collected. By zooming in 4× and tiling the embryo in the 180° orientation, fine neurites in the developing nervous system can be discerned across the whole embryo (Figures 4.1f and 4.26. For

this, a 5x7 mosaic of stacks at zoom 4× was taken using 2-µm z-step size and fused into a single 670 GB dataset using Bigstitcher (Hörl et al., 2018). Single long-range axons can be discerned both in the developing brain (Figure 4.25b) and the trunk (Figure 4.25c-e). Reslicing the datasets of a single substack in the XZ direction reveals that fine processes can also be discerned in the axial direction (igure 4.25d-e), highlighting that the mesoSPIM allows near-isotropic imaging quality in such a sample (see also Supplementary Video 9).

As a further example for the imaging quality achievable with a mesoSPIM in a BABB-cleared sample, we cleared a white-eyed Drosophila melanogaster according to the protocol by Dodt et al. (Dodt et al., 2007). We then placed the sample in a 10×10×45 mm^3 glass imaging cuvette (Portmann Instruments) filled with BABB and immersed this cuvette in a 40×40×45 mm^3 immersion cuvette filled with BABB as well. Using the 1× objective, we scanned the head of the fly using 488-nm excitation (Figure 4.27 and Supplementary Video 10). In a surface rendering of the resulting dataset (Figure 4.27a), a wide range of external anatomical features can be discerned, ranging from single ommatidia in the compound eyes to antennae and sensiliae around the head. Both in the XY and the XZ plane, a wide variety of internal anatomical features can be visualized as well – ranging from the internal structure of the mouthparts to subdivisions of the brain such as the layers of the optic lobe (Figure 4.27 b,c). Despite its comparatively small size, it is thus possible to visualize details of the anatomy of D. melanogaster with a mesoSPIM using a 1× objective.

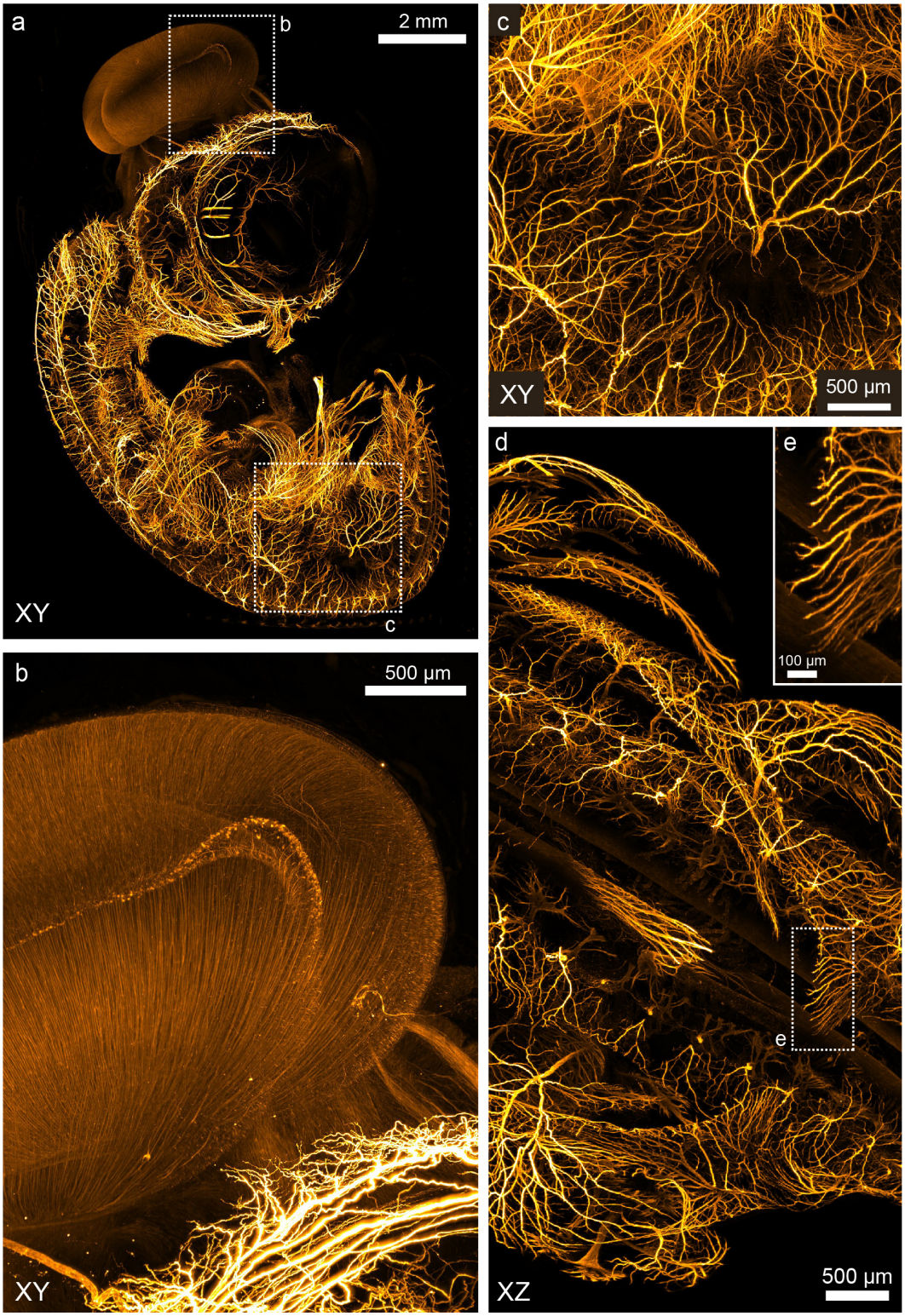

Figure 4.25: Multi-scale imaging in a BABB-cleared and neurofilament-stained 7-day old chicken embryo. a) Overview image of the whole sample (Maximum intensity projection) taken at zoom 0.8x (Same sample as in Figure 1). b) & c) Higher magnification images (MIPs) taken at 4×. d) & e) Reslice (XZ view, MIP) of the substack shown in c).

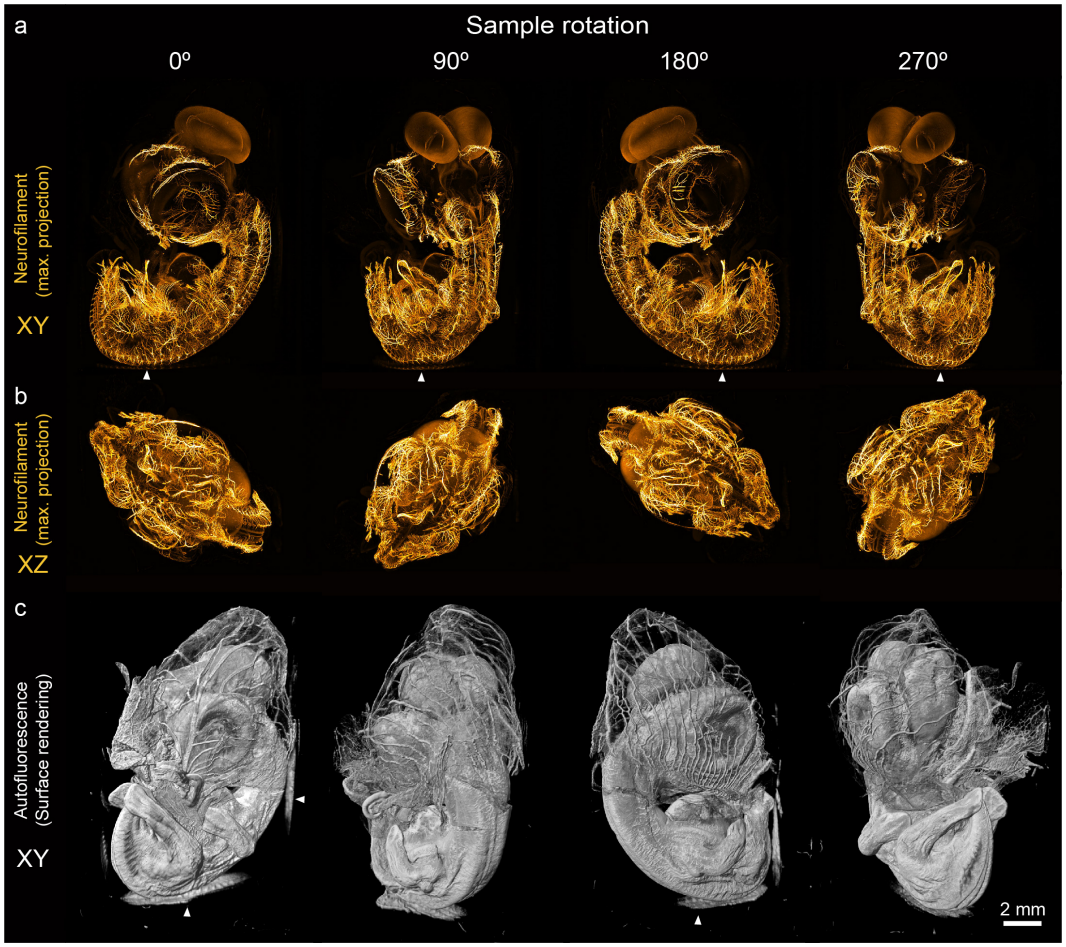

Figure 4.26: Multi-view imaging in a BABB-cleared and neurofilament-stained 7-day old chicken embryo. a) MIPs of z-stacks (0.8× magnification) taken at different rotation angles of the sample (Cy3), excited at 561 nm. b) MIPs of the XZ (resliced) view of the datasets in a). c) Surface rendering of the autofluorescence signal excited at 405 nm. Due to the index mismatch between BABB and the quartz material of the cuvettes, reflections off the cuvette walls can occur (indicated by arrows).

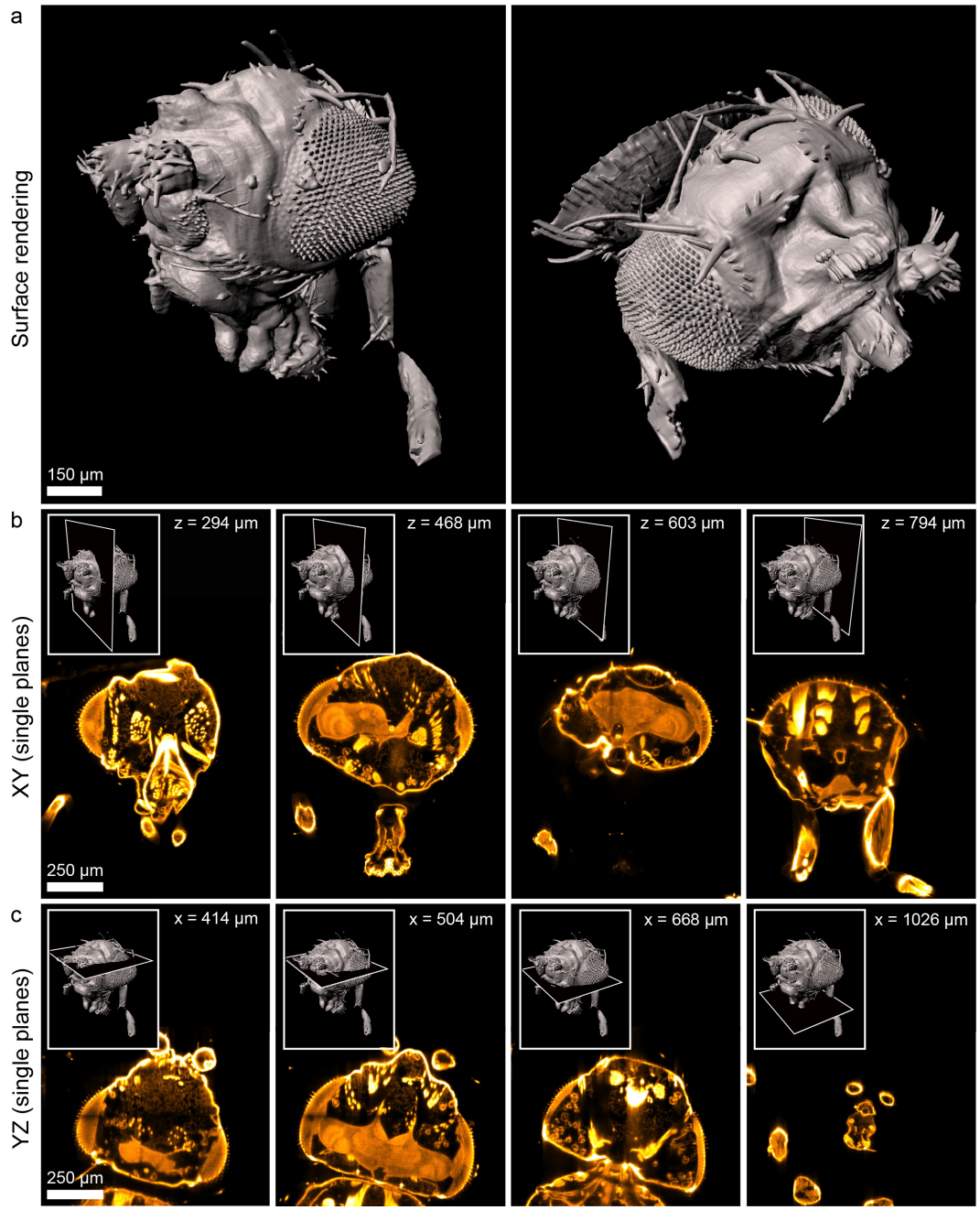

Figure 4.27: Anatomical imaging in a BABB-cleared Drosophila melanogaster. A white-eyed fly was dehydrated and cleared with the BABB protocol. a) Surface renderings from a dataset acquired at 6.3× zoom using the 1× objective (1-µm pixel size). Cuticle and tissue autofluorescence was excited at 488 nm. b) Single XY planes at different axial locations (indicated by the insets). c) Single planes from the resliced view (YZ) view of the same dataset. A wide variety of fine anatomical features can be distinguished.

4.3.11 The mesoSPIM is compatible with iDISCO-cleared samples

In recent years, the combination of 3DISCO clearing (Ertürk et al., 2012a,b; Ertürk and Bradke, 2013) and immunolabeling led to the iDISCO technique (Renier et al., 2014) which allows immunostaining in whole mouse brains for a wide range of antibodies. iDISCO samples are commonly imaged in dibenzylether (DBE), a high-index medium ($n_D = 1.562$), which can dissolve plastics. As DISCO-samples tend to be small and hard, we clamp such samples in a 3D-printed custom sample holder made from polyamide (nylon) with nylon screws. In our hands, nylon is stable even during prolonged immersion in DBE. To demonstrate the compatibility of the mesoSPIM with iDISCO samples, we performed whole-brain immunostaining against immunoglobulin G (IgG) in a non-perfused mouse brain (Figure 4.28a-b). Without perfusion, the vasculature retains IgG in the serum which can be stained using secondary antibodies. Even in low-magnification overviews taken at zoom 1.25×, details of the vasculature can be discerned in the XY and XZ views (Figure 4.28c-e). We noted that given the high transparency of the tissue and excellent labeling quality, imaging with a single light-sheet was sufficient as there was no intensity gradient visible across the sample. In addition, optimizing the tunable lens parameters was straightforward as the length of the blood vessel sections visible in every XY plane is a good indicator for the effective thickness of the light-sheet. As the staining is done using passive diffusion of the antibody, there is a labeling gradient from outside to inside, but even in the central parts of the sample, the labeling quality is sufficient to discern small capillaries in higher resolution datasets taken at 4× magnification (3.29 mm FOV; Figure 4.29, Supplementary Video 11). To demonstrate that the mesoSPIM is capable both of imaging rat brain tissue and doing multi-color acquisitions in iDISCO samples, we performed a nuclear stain on a wildtype rat using To-Pro (Figure 4.30).

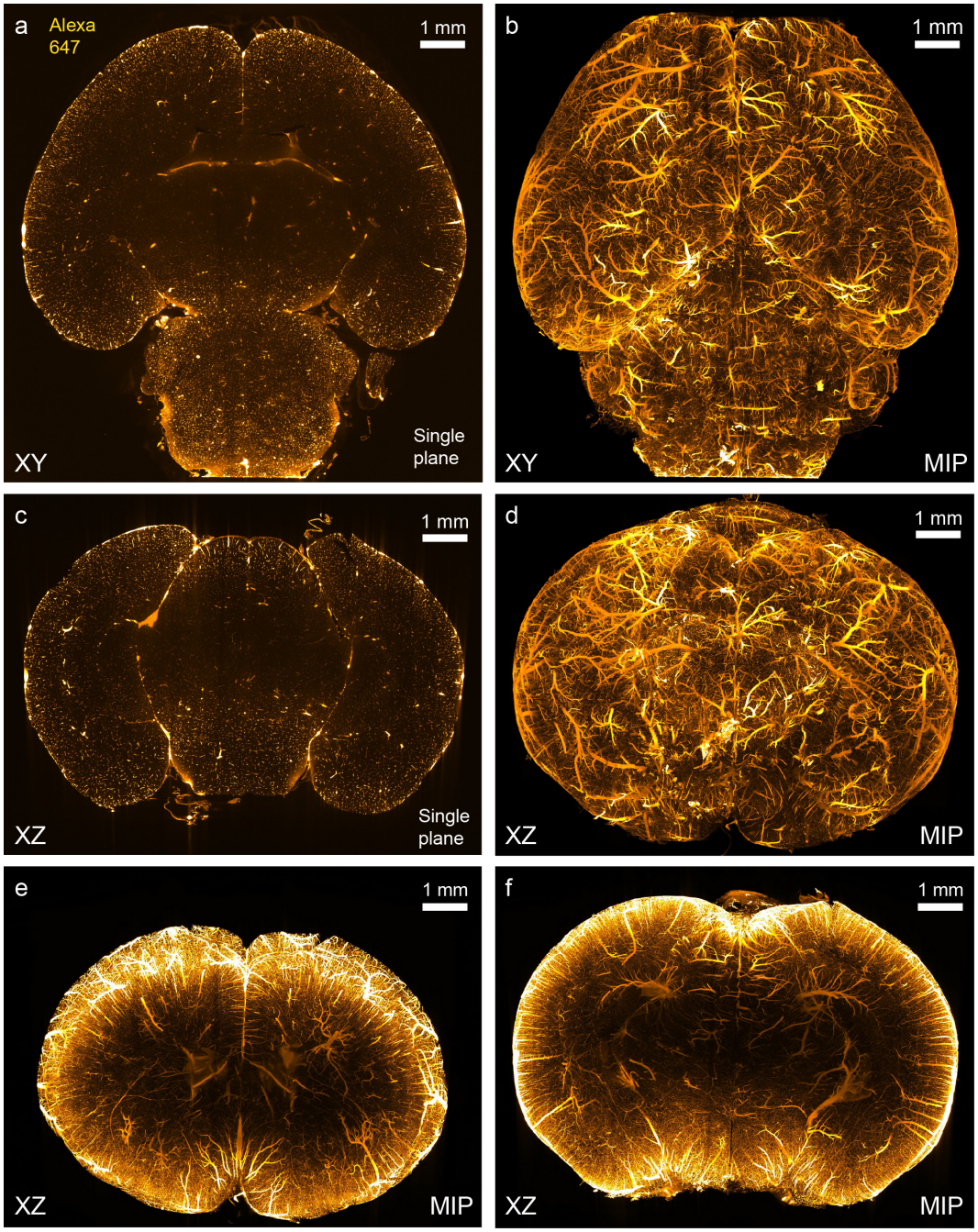

Figure 4.28: The mesoSPIM is compatible with iDISCO-cleared samples. A whole mouse brain was stained for immunoglobulin G (IgG) conjugated to Alexa 647 antibodies and cleared using the iDISCO protocol. a) Single plane taken from a low-resolution overview stack (Zoom 1.25×). b) Maximum intensity projection (MIP) covering the dorsal aspect of the brain. Large vessels on the surface are prominent. c) Single resliced plane (XZ view) from the dataset. d) MIP of the frontal aspect of the sample. e) and f) MIP (500- m range) in the coronal plane. As antibody penetration is limited by diffusion, an inside-out intensity gradient is visible.

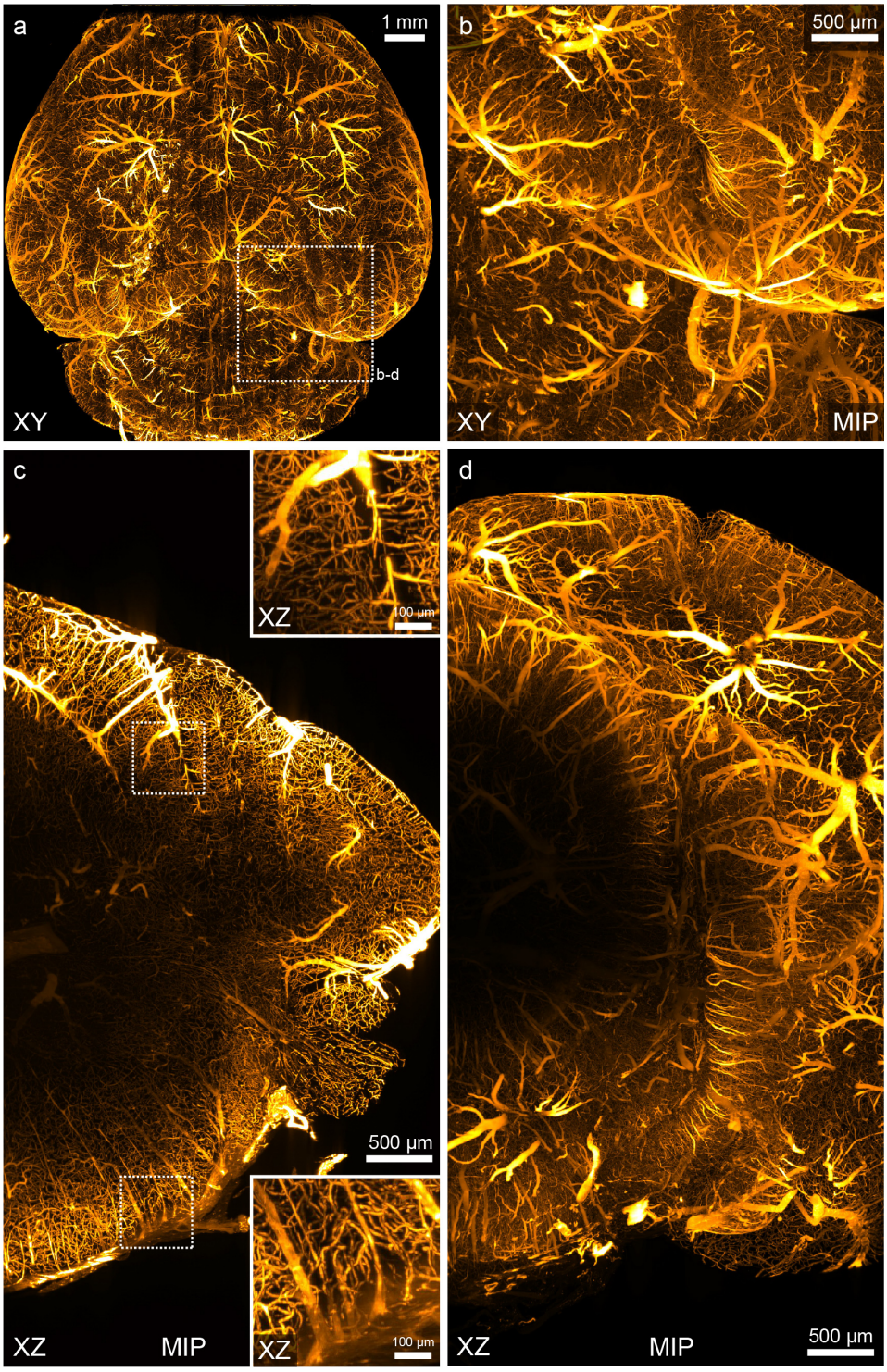

Figure 4.29: Near-isotropic imaging in an iDISCO-cleared mouse brain stained for vasculature. a) The same sample as in Figure **proper ref** was scanned at zoom 4× (3.29-mm FOV) at the indicated location. b) Maximum projection (MIP) of the whole stack. c) and d) MIPs (250-µm range) of the acquired dataset. The insets in c) demonstrate that even in the XZ view, fine capillaries are well separated from each other.

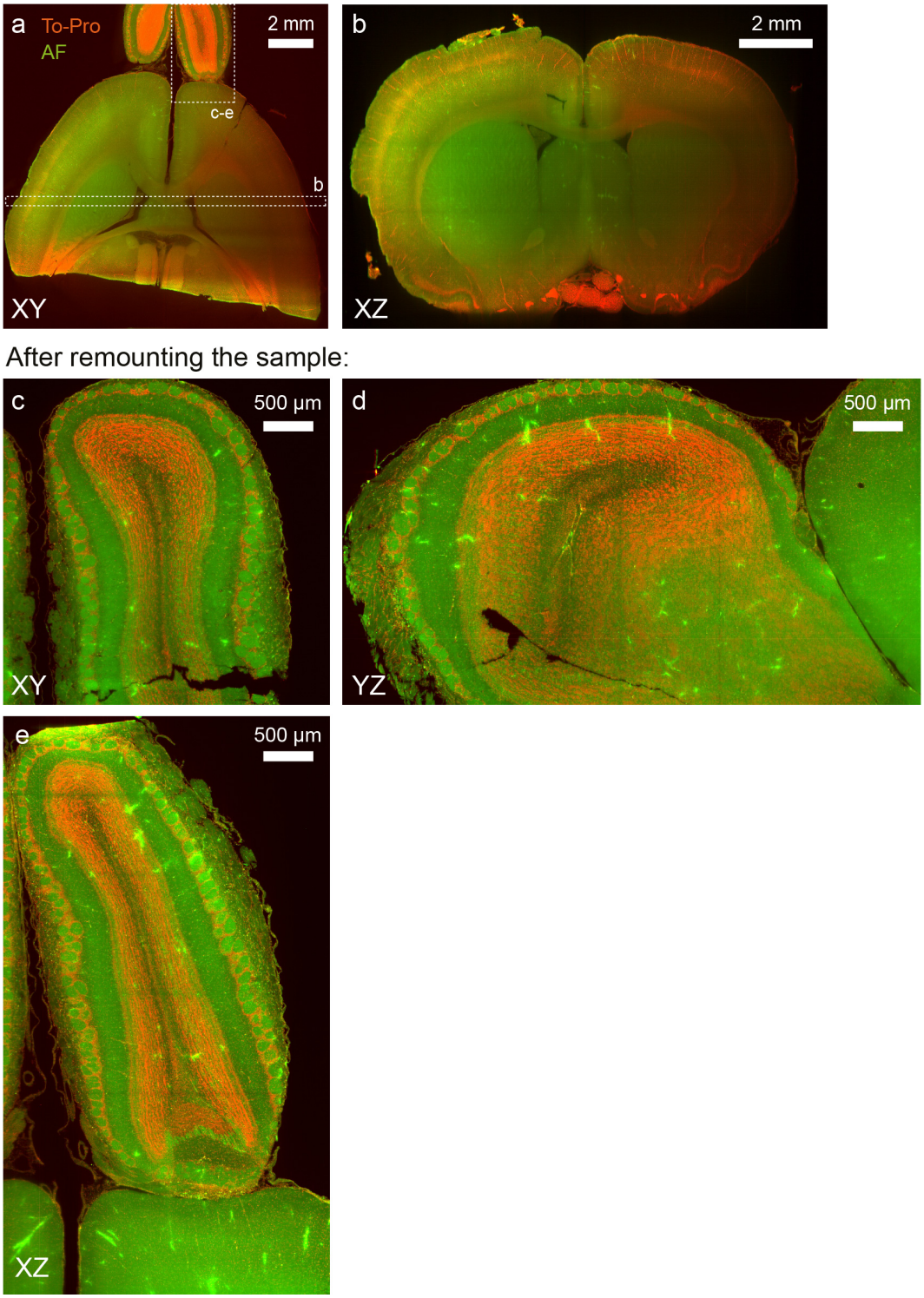

Figure 4.30: Multicolor imaging in an iDISCO-cleared and To-Pro-stained rat brain. a) Overview image (maximum projection, 0.5 mm range) of a rat forebrain. The nuclear stain (To-Pro) is shown in red and the autofluorescence (AF) in green. b) Reslice (XZ view) of a subvolume of the sample in a). After remounting the sample (coronal planes parallel to the light-sheet), the olfactory bulb was imaged again (c-e). In all sectioning planes, single glomeruli can be seen.

4.3.12 The mesoSPIM is compatible with MASH (iDISCO/ECi)-processed samples

Given the size and complexity of the human brain, clearing techniques capable of rendering human samples sufficiently transparent for large-scale studies are of considerable interest for neuroscience and pathology. However, owing to its myelination and sheer size, clearing human brain tissue is challenging. In addition, samples are usually much older than the mouse brains used in the demonstration of clearing techniques, which leads to increased levels of autofluorescence (for example due to an increase in lipofuscin). However, a variety of clearing methods was shown to be compatible with human tissue, for example OPTIClear (Lai et al., 2018). Recently it was shown that 'multiscale architectonic staining of human cortex' (MASH, Hildebrand et al. (2018)) is possible by a modified iDISCO+ clearing protocol and with the possibility of using ethyl cinnamate (ECi) for index matching. Compared to other index matching solutions, the non-toxicity of ECi, which was established in 2017 (Klingberg et al., 2017), makes it very user-friendly. Using this technique in combination with the cell nucleus label MASH-MG (based on known protocols with Methyl Green) and cell body label MASH-NR (based on standard protocols for Nissl staining with Neutral Red) staining, we were able visualize the structure of the human neocortex (see Figure 4.31). The 10×20×5 mm^3 slab of MASH-processed tissue was placed inside a 10×20×45 mm^3 glass cuvette filled with ECi and submerged in an immersion cuvette filled with ECi. Imaging at low zoom allowed localizing cortical folds (Supplementary Video 12) while datasets taken at 4× zoom reveal the distribution of) neurons across the layers of the neocortex (Supplementary Video 13).

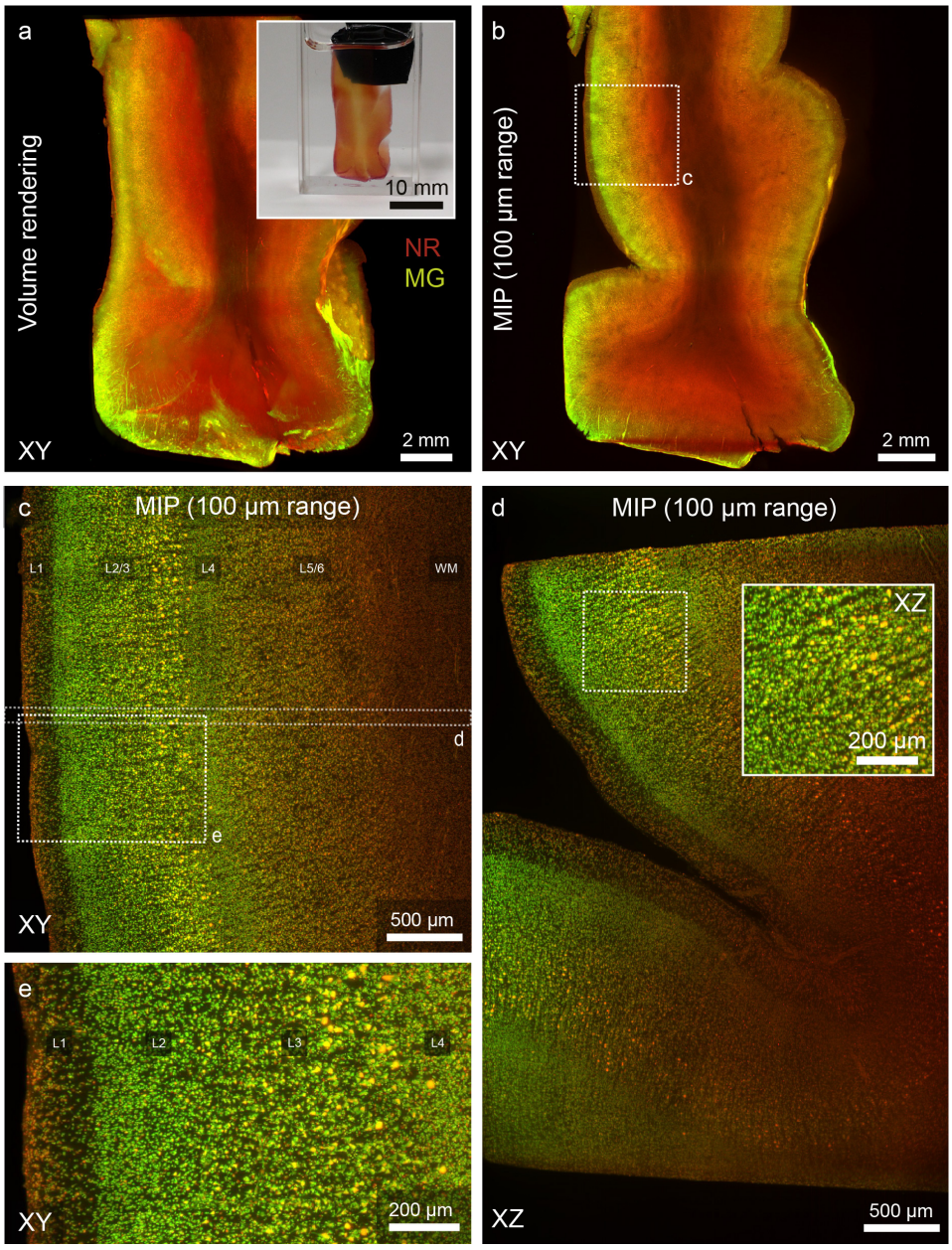

Figure 4.31: The mesoSPIM is compatible with MASH (iDISCO/ECi)-processed human neocortex samples. a) Volume rendering of data acquired from a slab of human cortex cleared using ethyl cinnamate (ECi) and stained with Neutral Red (NR) and Methyl Green (MG) using the multiscale architectonic staining of tissue protocol (MASH)78. The inset shows the sample immersed in ECi in the imaging cuvette. b) Maximum intensity projection (MIP) of a part of the dataset in a) c) MIP of a dataset acquired at 4× magnification (location shown in b). d) Reslice of a part of the dataset (location) indicated in c). Even in the axial direction, cells can be resolved easily. In the XZ view, the better penetration of the red wavelengths is visible. e) Detail of c). Cortical layers 1 to 6 (L1 to L6) and white matter (WM) are indicated.

Figure	Panel	Obj.	Zoom	Sample	Clearing method	Ill. Dir.	Excitation	Filter	t_{sweep} t_{exp}	f_{galvo}	Pixel size (X×Y×Z)	Tiles/Conditions × X × Y × Z	t_s [min]	t_{tot} [min]	File size	File size (total	Comment
1	b	1×	1×	VIP-tdTomato mouse brain	Passive CLARITY	Right	561 nm	561LP	200 m 20 ms	99.9 Hz	6.55 × 6.55 × 5 µm^3	2 × 2048 × 2048 × 1937	7.37	14.85	11.9 GB	23.8 GB	
	c	1×	0.63×	TPH2::Cre;Rosa26^{tdTomato} mouse brain	Passive CLARITY	Right	561 nm	561LP	200 m 20 ms	99.9 Hz	10.5 × 10.5 × 5 µm^3	1 × 2048 × 2048 × 2107	8.03	8.03	15.58 GB	15.58 GB	
	d/e	1×	4×	TPH2::Cre;Rosa26^{tdTomato} mouse brain	Passive CLARITY	Right	561 nm	561LP	200 m 20 ms	199 Hz	1.6 × 1.6 × 2 µm^3	5 × 2048 × 2048 × 3100	12.54	62.7	17.62 GB	88.1 GB	
	f	1×	4×	Chick embryo (7d)	BABB	Right	561 nm	561LP	200 m 5 ms	199 Hz	1.5 × 1.5 × 2 µm^3	24 × 2048 × 2048 × 4700	17.82	429	38.5 GB	880 GB	
Supplementary Figures																	
2	a-f	1×	1×	VIP-tdTomato mouse brain	Passive CLARITY	Right	561 nm	561LP	200 m 20 ms	99.9 Hz	6.55 × 6.55 × 5 µm^3	2 × 2048 × 2048 × 1937	7.37	14.85	11.9 GB	23.8 GB	Same dataset as in 1b
3	a-h	1×	1×	Thy1-YFP mouse brain	Active CLARTIY	Right	488 nm	542/27	200 m 20 ms	99.9 Hz	6.55 × 6.55 × 2 µm^3	2 × 2048 × 2048 × 4200	15.95	31.9	34.4 GB	68.8 GB	
4	a-d	1×	4×	Thy1-YFP mouse brain	Active CLARTIY	Right	488 nm	542/27	200 m 10 ms	199 Hz	1.6 × 1.6 × 2 µm^3	2 × 2048 × 2048 × 4200	15.95	31.9	34.4 GB	68.8 GB	
5	a	1×	4×	Thy1-YFP mouse brain	Active CLARTIY	Right	488 nm	542/27	200 m 10 ms	199 Hz	1.6 × 1.6 × 2 µm^3	3 × 2048 × 2048 × 4200	15.95	47.85	34.4 GB	103.2 GB	
6	a-c	1×	1×	Thy1-YFP mouse brain	Active CLARTIY	Left/Right/Both	488 nm	542/27	200 m 20 ms	99.9 Hz	6.55 × 6.55 × 3 µm^3	3 × 2048 × 2048 × 2800	13.42	40.26	22.9 GB	68.7 GB	
14		1×	1×	1 µm bead test sample at nD=1.45	n/a	Right	488 nm	520/35	200 m 5 & 10 ms	99 & 199 Hz	6.55 × 6.55 × 1 µm^3	3 × 2048 × 2048 × 200	0.77	2.75	1.6 GB	4.8 GB	
15		1×	4×	1 µm bead test sample at nD=1.45	n/a	Right	488 nm	520/35	200 m 5 & 10 ms	99 & 199 Hz	1.6 × 1.6 × 1 µm^3	3 × 2048 × 2048 × 200	0.77	2.75	1.6 GB	4.8 GB	
16		1×	1×	Thy1-YFP mouse brain	Active CLARTIY	Right	488 nm	520/35	200 m 5-40 ms	199 Hz	6.55 × 6.55 × 2 µm^3	4 × 2048 × 2048 × 4200	15.95	64.9	34.4 GB	137.6 GB	
17		1×	4×	Thy1-YFP mouse brain	Active CLARTIY	Right	488 nm	520/35	200 m 5-40 ms	199 Hz	1.6 × 1.6 × 2 µm^3	4 × 2048 × 2048 × 4200	15.95	64.9	34.4 GB	137.6 GB	
18	a-d	1×	1×	YCX 2.60 mouse brain	Passive CLARITY	Right	515 nm & 647 nm	515LP & QB	200 m 20 ms	99.9 Hz	6.55 × 6.55 × 5 µm^3	2 × 2048 × 2048 × 1674	6.38	12.65	13 Gb	26 GB	
19	a	1×	1×	YCX 2.60 mouse brain	Passive CLARITY	Right	515 nm & 647 nm	515LP & QB	200 m 20 ms	99.9 Hz	6.55 × 6.55 × 5 µm^3	2 × 2048 × 2048 × 1674	6.38	12.65	13 Gb	26 GB	
	b-d	1×	4×	YCX 2.60 mouse brain	Passive CLARITY	Right	515 nm	515LP	200 m 20 ms	199 Hz	1.6 × 1.6 × 5 µm^3	1 × 2048 × 2048 × 1310	5.06	5.06	10.2 GB	10.2 GB	
20	b-c	1×	4×	YCX 2.60 mouse brain	Passive CLARITY	Right	515 nm	515LP	200 m 20 ms	199 Hz	1.6 × 1.6 × 3 µm^3	1 × 2048 × 2048 × 766	2.97	2.97	6 GB	6 GB	
21	a-b	1x	1x	GlyT2-EGFP mouse CNS	Active CLARTIY	Left/Right	488 nm &561 nm	520/35 @ 561LP	200 m 20 ms	199 Hz	6.55 × 6.55 × 5 µm^3	16 × 2048 × 2048 × 1679	7.5	165	13.771 GB	220 GB	
21	c	1x	4x	GlyT2-EGFP mouse CNS	Active CLARTIY	Right	488 nm	520/35	200 m 20 ms	199 Hz	1.6 × 1.6 × 2 µm^3	1 × 2048 × 2048 × 2469	10.24	10.24	19.2 GB	19.2 GB	
21	d	1x	4x	GlyT2-EGFP mouse CNS	Active CLARTIY	Left/Right	488 nm	520/35	200 m 20 ms	199 Hz	1.6 × 1.6 × 2 µm^3	2 × 2048 × 2048 × 994	4.1	8.2	8.14 GB	15.5 GB	
22	a-d	1×	0.63×	Ntsr1-Cre;CAG-tdTomato) mouse brain	CUBIC-X	Left	561 nm & 488 nm	561LP	200 m 20 ms	99.9 Hz	10.5 × 10.5 × 3 µm^3	2 × 2048 × 2048 × 3566	13.53	29.48	29.2 GB	58.4 GB	
23	a-d	1×	4×	Ntsr1-Cre;CAG-tdTomato) mouse brain	CUBIC-X	Left	561 nm & 488 nm	561LP	200 m 20 ms	199 Hz	1.6 × 1.6 × 2 µm^3	2 × 2048 × 2048 × 4700	17.93	36.3	38.5 GB	77 GB	
24	a-d	1×	4×	Chick embryo (7d)	BABB	Right	561 nm	561LP	200 m 5 ms	199 Hz	1.5 × 1.5 × 2 µm^3	24 × 2048 × 2048 × 4700	17.82	429	38.5 GB	880 GB	Same dataset as in 1f
25		1×	0.8×	Chick embryo (7d)	BABB	Right & Both	405 nm & 561 nm	QB & 561LP	200 m 20 ms	99.9 Hz	7.8 × 7.8 × 2 µm^3	8 × 2048 × 2048 × 5200	19.8	2.64	42 GB	319 GB	4 rotation angles
26		1×	4×	D. melanogaster	BABB	Right	488 nm	QB	200 m 10 ms	99.7 Hz	1 × 1 × 1 µm^3	1 × 2048 × 2048 × 1700	6.49	6.49	13.4 GB	13.4 GB	
27		1×	1.25 ×	Mouse brain (vasculature)	iDISCO	Right	647 nm	QB	200 m 10 ms	199 Hz	5 × 5 × 2 µm^3	1 × 2048 × 2048 × 4072	15.4	15.4	31.8 GB	31.8 GB	
28		1×	4×	Mouse brain (vasculature)	iDISCO	Right	647 nm	QB	200 m 10 ms	199 Hz	1.55 × 1.55 × 2 µm^3	16 × 2048 × 2048 × 3186	12.1	191.4	24.8 GB	398 GB	
29	a-b	1×	1×	Rat brain (TO-PRO)	iDISCO	Right	488 nm & 647 nm	QB & QB	200 m 20 ms	99.9 Hz	6 × 6 × 3 µm^3	2 × 2048 × 2048 × 2966	14.19	28.38	24.3 GB	48.6 GB	
	c-d	1×	4×	Rat brain (TO-PRO)	iDISCO	Right	488 nm & 647 nm	QB & QB	200 m 10 ms	199 Hz	1.55 × 1.55 × 1 µm^3	2 × 2048 × 2048 × 5800	22	44	47.5 GB	95 GB	
30	a-b	1×	0.8×	Human cortex	MASH (iDISCO/ECi)	Both	561 nm & 647 nm	561LP & QB	200 m 20 ms	99.9 Hz	7.8 × 7.8 × 2 µm^3	2 × 2048 × 2048 × 2500	9.46	19.14	20.5 GB	41 GB	
	c-e	1×	4×	Human cortex	MASH (iDISCO/ECi)	Left	561 nm & 647 nm	561LP & QB	200 m 10 ms	199 Hz	1.6 × 1.6 × 1 µm^3	2 × 2048 × 2048 × 5000	18.92	37.95	41 GB	82 GB	

Table 4.3: Overview of all imaging parameters. All datasets were taken with the MVPLAPO1× objective (Obj.). In addition, illumination direction (Ill.dir.), sweeptime (total waveform generation time, t_{sweep}), exposure time (t_{exp}), galvo frequency (f_{galvo}), and the acquisition time for a single stack in a multi-color or tiled acquisition (t_{s}) and for the entire acquisition (t_{tot}) are indicated. In addition, the size of the dataset for a single stack and for the entire acquired dataset are given. QB refers to a quadrupleband blocking filter (QuadLine Rejectionband ZET405/488/561/640, AHF). 561LP refers to a 561 nm longpass.

4.4 Sample preparation

An overview of all mouse lines used for this study is given in Table 4.4. Crosses were performed as indicated in the text.

Short name	Official strain name	Repository stock number
VIPCre	Viptm1(cre)Zjh/J	JAX 010908
Ai14 (tdTomato)	B6.Cg-Gt(ROSA)26Sortm14(CAG-tdTomato)Hze/J	JAX 007914
TPH2Cre	Tg(Tph2-cre)RH35Gsat/Mmucd	MMRRC 036634-UCD
Camk2a-tTA	B6.Cg-Tg(Camk2a-tTA)1Mmay/DboJ	JAX 007004
Ai92(YCX2.60)	B6.Cg-Igs7tm92.1(tetO-ECFP*/Venus*)Hze/J	JAX 026262
Rbp4Cre	Tg(Rbp4-cre)KL100Gsat/Mmucd	MMRRC 031125-UCD
Thy1-YFP	B6.Cg-Tg(Thy1-YFP)HJrs/J	JAX 003782
GlyT2-EGFP	Tg(Slc6a5-EGFP)1Uze	MGI 3835459
Ntsr1Cre	B6.FVB(Cg)-Tg(Ntsr1-cre)GN220Gsat/Mmucd	MMRRC 030648-UCD
Ai9 (tdTomato)	B6;129S6-Gt(ROSA)26Sortm9(CAG-tdTomato)Hze/J	JAX 007905

Table 4.4: Overview of mouse lines used in this study.

4.4.1 Passive CLARITY clearing of mouse brains

To demonstrate the compatibility of the mesoSPIM with passive CLARITY clearing, we cleared mouse brains from VIPCre-tdTomato ((Viptm1(cre)Zjh/J); B6.Cg-Gt(ROSA)26Sortm14(CAG-tdTomato)Hze/J) (Taniguchi et al., 2011; Madisen et al., 2010), TPH2Cre-tdTomato (Tg(Tph2-cre)RH35Gsat/Mmucd; B6.Cg-Gt(ROSA)26Sortm14(CAG-tdTomato)Hze/J) (Gong et al., 2003), and Yellow-Cameleon YCX2.60 (Camk2a-tTA;Rbp4-Cre;TITL-YCX2.60) (Madisen et al., 2015). The method used for hydrogel-based tissue clearing is described in detail elsewhere (Chung et al., 2013; Tomer et al., 2014; Yang et al., 2014). In short, the animals were transcardially perfused first with PBS followed by an ice-cold hydrogel solution (1% PFA, 4% acrylamide, 0.05% bis-acrylamide). The brains were dissected and post-fixed in the same hydrogel solution for 24h at 4°C. The samples were then degassed using a dessicator before hydrogel polymerization was induced at 37°C for 2-3hours. Following the polymerization, excess hydrogel was removed from the brains and they were immersed in 40mL of 8% SDS and kept shaking at room temperature until the tissue was cleared sufficiently (30+ days for an adult animal). Finally, after 2-4 washes in PBS, the brains were put into a self-made refractive index matching solution (RIMS) (Yang

et al., 2014) for the last clearing step. They were left to euqilibrate in 5mL of RIMS for at least 4 days before being imaged. After clearing, brains were attached to a small weight and loaded into a 10×20×45 mm^3 quartz cuvette (UQ-205, Portmann Instruments), then submerged in RIMS and imaged using the mesoSPIM. The sample cuvette was immersed in a 40×40×40 mm^3 quartz cuvette (UQ-753, Portmann Instruments) filled with index-matching oil (Code 50350, Cargille, nD=1.45), which allows sample XYZ movements and rotations without refocusing the detection path. This set of animal experiments and procedures were performed in accordance with standard ethical guidelines and were approved by the Cantonal Veterinary Office of the Canton of Zurich.

4.4.2 Active CLARITY clearing of Thy1-YFP mouse brains

Nine-weeks-old Thy1-YFP mice (Feng et al., 2000) were deeply anaesthetized with intraperitoneal injection of a mixture of 150 µl Ketamine (Ketalar, Bayer AG), 75 µl Xylazine (Rompun, Parke-Davis) and 75 µl sterile water. When mice seized to breath and no toe reflex was present, mice were transcardially perfused with 20 ml ice cold phosphate buffered saline (PBS) after which 20 ml ice cold hydrogel monomer-fixative (4% acrylamide, 1% paraformaldehyde, 0.05% bis-acrylamide, 1% VA-044 initiator in phosphate buffered saline, Chung et al. (2013)) was infused. Harvested brains were fixed in 20 ml ice-cold hydrogel monomer fixative overnight. Brains were degassed in a vacuum exicator for 20 minutes at -0.8 bar, followed by purging with nitrogen gas. The hydrogel monomer was polymerized at 37°C for 2.5 hours in tightly closed tubes. Samples were extracted from the hydrogel and transferred into clearing solution (8% sodium-dodecyl-sulphate, 200 mM boric acid, pH 8.5). Brains were optically cleared with clearing solution based on the CLARITY method degassed in a vacuum exicator for 20 minutes at -0.8 bar, followed by purging with nitrogen gas. The hydrogel monomer was polymerized at 37°C for 2.5 hours in tightly closed tubes. Samples were extracted from the hydrogel and transferred into clearing solution (8% sodium-dodecyl-sulphate, 200 mM boric acid, pH 8.5). Brains were optically cleared with clearing solution based on the CLARITY method in a custom-built electrophoretic setup in 5 hours. Samples were washed in PBS three times and then transferred into RIMS., RIMS was replaced

once to reach RI 1.46. Samples were stored light-protected at 4°C until imaged. After curing, the sample was immersed in a 10×20×45 mm^3 quartz cuvette for imaging. This set of animal experiments and procedures were performed in accordance with standard ethical guidelines and were approved by the Cantonal Veterinary Office of the Canton of Zurich.

4.4.3 Whole-CNS imaging of X-CLARITY cleared samples

Mice (GlyT2::eGFP (Tg(Scl6a5-EGFP)1Uze, Zeilhofer et al. (2005)) were perfused transcardially with 10 ml of artificial cerebrospinal fluid (ACSF: 125 mM NaCl, 2.5 mM KCl, 1.25 mM NaH_2PO_4, 25 mM $NaHCO_3$, 1 mM $MgCl_2$, 2 mM $CaCl_2$, 20 mM glucose equilibrated with 95% O_2, 5% CO_2) at room temperature (RT) followed by 20 ml of RT 4% paraformaldehyde (PFA, in 0.1 M sodium phosphate buffer, pH 7.4). The perfusion was performed using a gravity perfusion setup. Brain and spinal cord attached were dissected and put in 4% PFA overnight. They were then put in 4% acrylamide (161–0140; Bio-Rad) and 0.25% VA-044 (017–19362; Novachem) in PBS at 4°C. They were then incubated for 3 hours at 37°C for acrylamide polymerization, washed overnight at 37°C in clearing solution (200 mM SDS (L3371; Sigma-Aldrich) and 200 mM boric acid (L185094; Sigma-Aldrich), pH 8.5), and electrophoresed in clearing solution using an X-CLARITY Tissue Clearing System (Logos Biosystems) for 8 hours at 1.2 A constant current, temperature <37°C, and 100 rpm pump speed. The samples were incubated in approximately 88% Histodenz (D2158; Sigma-Aldrich) solution in PBS (refractive index adjusted to 1.457) overnight, and mounted for imaging in the same solution. To accommodate the whole CNS, the sample was placed in a custom quartz imaging cuvette (10×20×120 mm^3, Portmann Instruments AG) and then placed in a custom 40×40×120 mm3 quartz immersion cuvette (Portmann Instruments AG). To ease mounting inside the sample cuvette, the sample was attached to a 1×13 cm strip of black aluminium foil (Thorlabs BKF12) using quick glue. This set of animal experiments and procedures were performed in accordance with standard ethical guidelines and were approved by the Cantonal Veterinary Office of the Canton of Zurich.

4.4.4 CUBIC-X clearing and imaging

The clearing process followed the protocol described in Murakami et al. (Murakami et al., 2018). Adult animals (Ntsr1-cre, strain: B6.FVB(Cg)-Tg(Ntsr1-cre)GN220Gsat/Mmcd,; crossed with LSL-tdTomato, strain: B6;129S6-Gt(ROSA)26Sortm9(CAG-tdTomato)Hze/; aged P50) were perfused for five minutes with cold PBS, then for five minutes with cold 4% PFA. Brains were dissected after perfusion and incubated in 4% PFA overnight. Brains were delipidated for 14 days. After delipidation, brains were washed in PBS overnight then incubated in 30 mL of 20% imidazole (VWR, AAA10221-36) at 4°C for 2.5 days. An expanded brain was immersed in 40 ml of CUBIC-X2 (5% (w/v) imidazole and 55% (w/v) antipyrine (VWR AAA11089-36) cocktail at room temperature for 1.5 days. Cleared swollen brains were embedded in CUBIC-X2 with 2% agarose. This set of experiments and procedures were performed in accordance with standard ethical guidelines (European Communities Guidelines on the Care and Use of Laboratory Animals, 86/609/EEC) and were approved by the Cantonal Veterinary Office of the Canton of Basel-Stadt.

4.4.5 Neurofilament staining of a whole-mount chicken embryo.

The embryo was sacrificed at day 7 of development and incubated in 4% paraformaldehyde for 2 hours at room temperature. For best results, the embryo was kept in constant, gentle motion throughout the staining procedure. Incubation was at 4°C. The tissue was permeabilized in 1% Triton X-100/PBS for 15 hours, followed by an overnight incubation in 20 mM lysine in 0.1 M sodium phosphate, pH 7.3. Then the embryo was rinsed with five changes of PBS. Non-specific binding was blocked using 10% FCS (fetal calf serum) in PBS for 48 hours. The primary antibody mouse anti-neurofilament (1:1500, RMO270, Invitrogen 13-0700) was added for 60 hours. The primary antibody was removed and the tissue rinsed with ten changes of PBS and an additional incubation overnight. After re-blocking in FCS/PBS for 15 hours, the embryo was incubated with the secondary antibody goat anti-mouse IgG-Cy3 (1:500, Jackson ImmunoResearch 115-165-003) for 48 hours. In a next step, the embryo was washed ten times with PBS followed by incubation overnight in PBS. For imaging the tissue was dehydrated in a methanol gradient (25%, 50%, 75%

in H2O and 2x 100%, 2 hours each step) and cleared using 1:2 benzyl alcohol: benzyl benzoate (BABB) solution overnight (again gentle shaking is recommended for dehydration and clearing). The tissue and staining are stable for months when kept at 4°C in the dark. This set of animal experiments and procedures were performed in accordance with standard ethical guidelines and were approved by the Cantonal Veterinary Office of the Canton of Zurich.

4.4.6 BABB-clearing of Drosophila Melanogaster

We sacrificed a white-eyed D. Melanogaster after ether anesthesia and fixed the tissue in 4% PFA. Sample preparation followed the protocol by Dodt et al9. Briefly, after washing in PBS, the sample was dehydrated in an ethanol series (50%, 70%, 80%, 2x 100%) for 2h each and then transferred to the clearing solution (1:2 benzyl alcohol: benzyl benzoate, BABB). Imaging was performed in a 10 × 10 × 45 mm^3 glass cuvette (filled with BABB) which was submerged in a 40 × 40 mm^2 quartz immersion cuvette filled with BABB.

4.4.7 iDISCO clearing and staining of mouse vasculature

For vasculature staining, brain tissue from 1 month old C57bl6/N males was fixed in 4% PFA without perfusion to preserve the endogenous immunoglobulins. Dye-conjugated secondary antibodies (1:100 dilution) against the tissue species were then used without need of primary antibodies. The protocol followed the one by Liebmann et al (Liebmann et al., 2016). This experiment was approved by the Institutional Animal Care and Use Committee of ICM Brain and Spine Institute, Paris.

4.4.8 iDISCO clearing and staining of rat samples

The brain from a female Wistar rat (age 16 weeks) was processed for enhanced autofluorescence and nuclear staining using iDISCO clearing protocol (adapted from Renier et al. (2014)). The brain was fixed transcardially and postfixed overnight (4% PFA in PBS). After cryoprotection (30% sucrose in PBS), in order to enhance autofluorescence, the brain sample was additionally

postfixed with 10% PFA in PBS for one week before clearing. Clearing was performed following the protocol on the iDISCO webpage, with n=4 days. Although no immunolabeling was performed, the sample underwent all incubation steps indicated in the protocol, simply omitting antibodies in the solutions. On the beginning of day 4 of the "secondary Ab" incubation, TO-PRO (Thermo Fisher) was added at 1:2500 dilution. After 24 hours, the sample was washed twice with PTwH (30 min) to ensure removal of non-bound TO-PRO, and then the protocol resumed.

4.4.9 Human brain tissue preparation

Brain tissue samples were taken from one human body donor (no known neuropathological diseases) of the body donation program of the Department of Anatomy and Embryology, Maastricht University. The tissue donor gave informed and written consent to the donation of their body for teaching and research purposes as regulated by the Dutch law for the use of human remains for scientific research and education ("Wet op de Lijkbezorging"). Accordingly, a handwritten and signed codicil from the donor posed when still alive and well, is kept at the Department of Anatomy and Embryology Faculty of Health, Medicine and Life Sciences, Maastricht University, Maastricht, The Netherlands. The brain was first fixed in situ by full body perfusion via the femoral artery. Under a pressure of 0.2 bar the body was perfused by 10 l fixation fluid (1.8 vol % formaldehyde, 20 % ethanol, 8.4 % glycerine in water) within 1.5-2 hours. Thereafter the body was preserved at least 4 weeks for post-fixation submersed in the same fluid. Subsequently, the brain was recovered by calvarian dissection and stored in 4% paraformaldehyde in 0.1 M phosphate buffered saline (PBS) for 25 months. All tissue was manually blocked with anatomical trimming blades, then cut into 5 mm thick slices in coronal orientation and immediately processed.

4.4.10 Clearing and labelling of human brain tissue

All human tissue samples were prepared following the MASH protocol (Hildebrand et al., 2018). As long as not indicated otherwise, samples were incubated in a volume of 5 ml in 6 well cell culture plates respectively. Samples were dehydrated in 20 %, 40 %, 60 %, 80 % and 100 % methanol

(MeOH) for 1h each at room temperature (RT). After that samples were incubated for 1h in 100 % MeOH at 4^0C and bleached in chilled, freshly prepared 5 % H_2O_2 in MeOH overnight at 4^0C in the dark. Samples were then rehydrated 1h each in 80 %, 60 %, 40 %, 20 % MeOH and twice in phosphate buffered saline (PBS) containing 0.2 % Triton X-100 at RT. This was followed by another bleaching step in freshly filtered aqueous 50 % potassium metabisulfite solution and washing in distilled water for 1h each at RT. Staining was performed in 6 ml solution containing 0.001 % neutral red and a 1:7500 dilution of a 2 % methyl green stock solution81 in PBS at pH 4 for 2.5 days. After that, the samples were turned on the other side, the solution was exchanged and incubation was continued for another 2.5 days. Then samples were washed 1h twice in PBS at pH 4, dehydrated once more in 20 %, 40 %, 60 %, 80 % and twice in 100 % MeOH. Samples were then transferred into 50 ml tubes and delipidated overnight in 66% dichloromethane (DCM)/33 % MeOH. Before immersion in ethyl cinnamate (ECi), sample were washed twice in 100 % DCM for 1h each. Samples were kept on a shaker during every step.

As the births of living creatures at first are ill-shapen, so are all innovations, which are the births of time.

Francis Bacon, *Of Innovations, 1625*

5

Conclusion and outlook

A key challenge for technology developers in microscopy is to bring novel methods and improvements to the community. This is often a process that ends at an intermediate stage as only a fraction of published microscopy methods show enough promise to warrant further commercial development. In other cases, a technology is developed far enough for instruments to reach the market, but widespread adoption has to wait for progress in other fields such as fluorophore development, sample preparation techniques, or image processing. In superresolution microscopy, an example for this effect is the first generation of commercial stimulated excitation and depletion (STED, Hell and Wichmann (1994); Hell (2007)) microscopes such as the Leica TCS STED which used continous-wave (CW) excitation and depletion in the red and near-infrared parts of the spectrum (Willig et al., 2007) and was thus limited to a small selection of fluorophores. This situation changed with the rapid improvement of dyes and labeling techniques for superresolution microscopy (Fernández-Suárez and Ting, 2008; van de Linde et al., 2012) and today, commercial STED setups are a common sight in many imaging facilities.

This thesis presents two projects aimed at making imaging technologies more accessible. In the project presented in Chapter 2, the suitability of femtosecond semiconductor disk lasers for *in vivo* multiphoton microscopy was demonstrated with a wide range of application examples. In the second project (presented in Chapter 4), the open-source mesoscale selective plane illumination microscope (mesoSPIM), an open hardware instrument, was developed, characterized and shown to be capable of delivering high image quality in a broad selection of cleared samples. Most importantly, the mesoSPIM was developed from a prototype into a facility-grade instrument and brought into the imaging community with (as of March 2019) five operational setups across Europe.

5.1 Microscopy with pulsed semiconductor disk lasers

In our SDL experiments, we performed a thorough characterization of the laser and matched its operating parameters with a commercial Ti:Sapphire laser. This allowed an image quality comparison and we found that the SDL has similar pulse lengths and beam quality which led to equal PSFs in our microscope. The only major difference was the SDL repetition rate of 1.63 GHz versus 80 MHz for the Ti:Sapphire laser. The 20.3× higher repetition rate requires to increase the average power of the SDL on the sample by 4.5× to reach comparable signal levels. In line with previous studies of two-photon imaging at high repetition rate (Ji et al., 2008), we found that the operating parameters of our SDL allowed extended imaging sessions as we avoided average laser powers leading to heating-induced damage (Podgorski and Ranganathan, 2016). Unlike (Ji et al., 2008), however, we did not find a considerable reduction in photobleaching rate. It is still an open question under which excitation conditions and with which fluorophores molecular photophysics allow such a reduction (Tong-Sheng et al., 2003; Eggeling et al., 2005; Kalies et al., 2011). Recently, another report highlighted that imaging at a repetition rate of 750 MHz reduces the photobleaching rate two-fold compared to 94 MHz excitation (Niu et al., 2019) in Rhodamine B films.

We demonstrate the suitability of a femtosecond SDL for structural and functional multiphoton in vivo imaging in both Drosophila larvae and mice for a variety of fluorophores (including mKate2, tdTomato, Texas Red, OGB-1, and R-CaMP1.07) and for SHG in muscle cell sarcomeres. For multiphoton imaging, a main disadvantage of SDLs is the need to operate at high repetition rates in the GHz regime due to fact that the the carrier lifetime ($\approx$ ns) is much shorter than the lifetimes of solid state materials in the µs domain. While high repetition rates are ideal for frequency combs (Udem et al., 2002; Maddaloni et al., 2009; Picqué and Hänsch, 2019) and telecommunication applications, the low peak powers lead to increased average powers for imaging. A possible solution is to use a multipass cavity where during each roundtrip, a pulse interacts with the gain chip multiple times (Zaugg et al., 2012).

In the time since the publication of our SDL paper another type of semiconductor disk lasers, a modelocked integrated external-cavity surface emitting laser (MIXSEL) reached sub-150 fs pulses (Alfieri et al., 2019). In a MIXSEL, the gain chip and SESAM are integrated into a single semiconductor structure. The cavity thus consists only of an output coupler and the MIXSEL chip, an even simpler concept than a VECSEL. Apart from optical pumping, such a laser can also be pumped electrically (Barbarin et al., 2011) by injecting a current into the gain structure which could lead to highly compact and versatile sources for microscopy in the future.

As both the SDL gain chip and the SESAM are manufactured using standard semiconductor engineering methods, SDLs can be mass-produced thanks to wafer-scale integration. In addition, they can be scaled to higher output powers by increasing the beam footprint on the gain medium. In combination with the possibility of engineering devices with a emission wavelength between 0.8-1.2 µm, they have considerable potential to allow multiphoton imaging at low cost.

5.2 From mesoSPIM prototypes to applications

The mesoSPIM initative aims to provide the imaging community with instructions and software to allow researchers to set up and operate versatile light-sheet microscopes for cleared tissue. With the combination of an excitation path designed for both uniform axial resolution and minimal shadowing artifacts, suitability for large samples, compatibility with all major clearing techniques, and straightforward sample handling we have arrived at a very promising instrument configuration. Going from a cleared and cuvette-mounted whole mouse brain to an isotropic dataset at 6.5 µm sampling within less than 10 minutes allows users to get quick feedback about sample and clearing quality. As the data does not have to be pre-processed for further analysis, users can (and will) start exploring datasets immediately, for example to localize injection sites. The isotropy makes visualization with tools such as ClearVolume (Royer et al., 2015) or using virtual reality straightforward and allows planning of high-resolution acquisitions which the instrument can carry out at comparable acquisition speeds of other instruments based on macro-detection optics (Niedworok et al., 2012; Schwarz et al., 2015; Doerr et al., 2017).

Our decision to showcase compatibility of the mesoSPIM with all major clearing techniques reflects the state of the clearing field: there is a wide variety of clearing methods available (an overview is given in Chapter 3.1) with variations of existing protocols being published in quick succession. At the present stage, however, no single clearing method seems to combine good retention of endogenous fluorescent markers, straightforward immunolabeling in whole mouse brains or larger anatomical structures, excellent clearing performance, and – most importantly – is proven to be reproducible and working across a wide range of experimental conditions (age-groups etc.). All methods have certain pitfalls and incompatibilities. One example is uDISCO (Pan et al., 2016), which preserves GFP fluorescence, but degrades tdTomato (Qi et al., 2019). From planning to data analysis, all stages of a clearing experiment have to take such limitations into account. It is unlikely that the present confusing diversity of clearing techniques will lead to standardization in the near future. Nonetheless, we can assume that given the simplicity of

exchanging immersion media and modifing sample holders, the mesoSPIM is ready for future clearing techniques.

As part of the mesoSPIM initiative, we also transitioned the setups from the proof-of-concept stage showcasing application examples to supporting biological projects. In one application, the mesoSPIM helped to visualize the projection from HVC to the robust nucleus of the arcopallium (RA) using lentiviral expression of tdTomato in CUBIC-cleared Zebrafinch brains (Rocha et al., 2019). In the brain of birds, HVC is a key nucleus involved in the learning and production of birdsong (Bolhuis and Gahr, 2006). Previously, there has been only a single report in the literature (Fujii et al., 2016) demonstrating clearing of the adult Zebrafinch brain with SeeDB – this study extends the range of clearing methods proven to work in this species and is the first to combine it with light-sheet microscopy.

In a different project, the Keller and Aguzzi groups used *Pdgfb*$^{ret/ret}$ mice, which possess a highly permeable blood-brain-barrier (BBB) (Armulik et al., 2010; Villaseñor et al., 2016) to investigate whether prions in blood may enter the brain via blood vessels (Keller et al., 2018). They discovered that *Pdgfb*$^{ret/ret}$ mice have similar disease incubation times as the control group, which suggests that crossing of the BBB is not a major infection route. In this study, the combination of active CLARITY clearing and mesoSPIM imaging was used to demonstrate the extravasation of an injected vascular tracer (70 kDa dextran conjugated to TexasRed) in *Pdgfb*$^{ret/ret}$ mice.

The same mouse line also exhibits brain vessel calcifications comparable to those found in cases of primary familial brain calcification (PFBC) in humans (Keller et al., 2013). In a recent study, it was used to characterize the cellular environment surrounding calcifications (Zarb et al., 2019). Cells around calcifications express markers for osteoblasts, osteoclasts and osteocytes. In the context of this project, mesoSPIM imaging was utilized to obtain three-dimensional ossification maps from whole *Pdgfb*$^{ret/ret}$ mouse brains cleared with active CLARITY and stained for calcifications using Fluor 647-labeled risedronate (Roelofs et al., 2010).

The combination of immunolabeling, tissue clearing and light-sheet microscopy is especially helpful for structures that have a complex anatomy with many of interwoven components and where classical tissue sectioning methods would introduce too much damage. One such example is the inner ear with the cochlea and vesibular labyrinth. It can even be argued that the need for imaging techniques allowing to study the inner ear at cellular resolution fostered the development of fluorescence-based light-sheet microscopy in combination with clearing (Voie et al., 1993; Voie and Spelman, 1995; Voie, 2002). An aspect that is especially challenging to investigate with traditional methods are the neuroimmune interactions of the auditory brainstem, meninges, choroid plexus, and inner ear structures such as the endolymphatic duct because brainstem meninges are disrupted by standard dissection methods. In a study investigating the capabilities of iDISCO clearing and immunolabeling of the rat auditory brainstem (Perin et al., 2019), the mesoSPIM was employed to image $7 \times 7 \times 7$ mm^3 tissue blocks which contained the cochlea, labyrinth, part of the brainstem, cerebellum and the surrounding bone. With this preparation, it was possible to image the distribution of microglia in the cochlea and to reconstruct the inner ear in three dimensions (Figure 5.1). In the auditory brainstem, the mesoSPIM revealed the presence of chorid plexus contacts with the dorsal cochlear nucleus (DCN) which could act as neuroimmune gates.

5.2.1 Future mesoSPIM development

The open design of the mesoSPIM hard- and software are intended to provide a template for further developments. The following paragraphs provide an overview of possible avenues for the continued development of the mesoSPIM platform.

One of the key lessons from the mesoSPIM project is that good microscope performance is essentially useless if it is too difficult to use – but figuring out what users need is challenging as it is difficult for them to verbalize what needs to be changed. One of the few approaches that worked was user observation, a common practice in user interface design. mesoSPIM usability improvements fall into three categories: Improvements for instrument developers, improvements in sample handling and software usability upgrades.

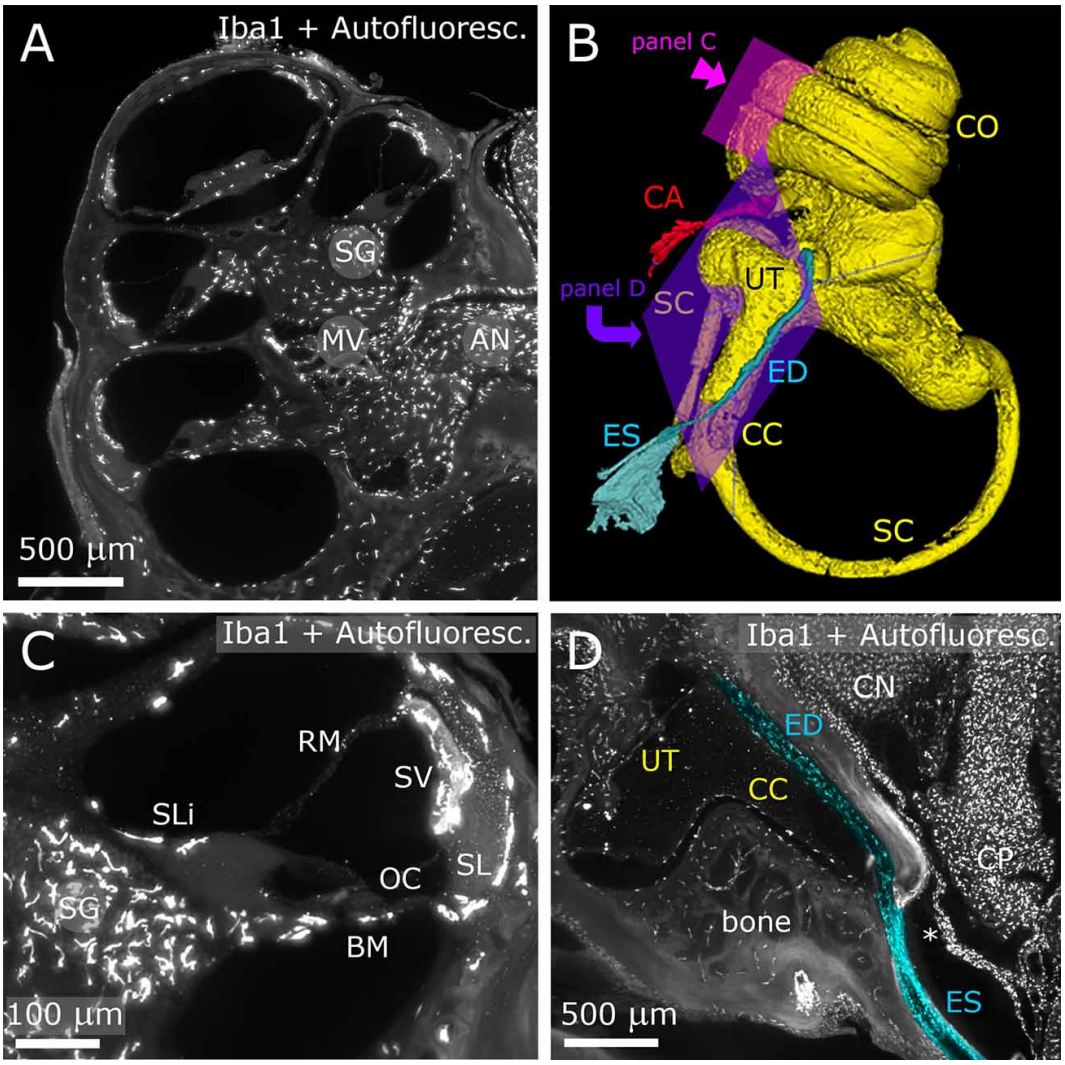

Figure 5.1: Imaging of the inner ear with the mesoSPIM. A) Maximum projection (10 µm) of a z-stack of the cochlea showing both autofluorescence and the microglia (Iba1) B) 3D reconstruction of the inner ear. C) Higher magnification detail of a single cochlear turn. D) Longitudinal section of ED and ES (pseudocolored blue). AN, auditory nerve; BM, basilar membrane; CA, cochlear aqueduct; CC, crus commune; CN, cochlear nucleus; CO, cochlea; CP, choroid plexus; ED, endolymphatic duct; ES, endolymphatic sac; MV, modiolar vein; OC, organ of corti; RM, reissner membrane; SC, semicircular canal; SG, spiral ganglion; SL, spiral ligament; SLi, spiral limbus; SV, stria vascularis. Figure adapted from Perin et al. (2019).

Improvements for instrument developers

Simplified alignment and improved feedback of the alignment state would help during the setup phase. The mesoSPIM excitation path design contains a lot of fold mirrors – partly to make alignment of the light-sheet tilt easier and partly due to the need for a vertically scanned light-sheet

in combination with a tunable lens that needs to be placed in a vertical section of the optical path to avoid gravity-induced deformations of the flexible membrane. In future versions, this design could be stretched out a bit by using larger breadboards for the excitation path which would also allow easier modifications of the instrument.

Sample handling

Improvements to sample handling include a better selection of 3D-printed sample clamps and mounting aids. The current generation of cuvette mounts is based on clamping with screws or using a pressure plate to attach the cuvette to a top plate. Both approaches work, but clamping has to be carried out very carefully to avoid breakage of cuvettes. This is made worse by the combined tolerances of cuvettes and 3D-printed cuvette holders which mean that some batches of cuvettes are incompatible with some holders and trying to attach them will lead to cracks in the cuvette. A possible solution would be a cuvette holder with an integrated spring built from a compliant mechanism.

Software usability

Users would benefit from better feedback on the current light-sheet thickness and axial resolution, improved planning tools for complicated acquisitions (i.e. multi-view tiling acquisitions) and safety features (i.e. warnings ahead of sample collisions with the wall of the immersion cuvette). Navigating a complex three-dimensional sample such as a cleared mouse brain at high magnification is also a challenge – in a well cleared sample, there is no immediate feedback where the FOV is located. If users are not familiar with anatomical landmarks or if the plane of the optical section does not correspond to a known anatomical plane (i.e. due to sample rotation), mesoSPIM users can experience a feeling of being ”lost” inside their own sample. A possible solution is to add a new component to the user interface, a sample explorer that displays the current FOV and location relative to a low-resolution dataset acquired previously. This tool could also add in setting up complicated acquisitions by visualizing the geometry of the planned z-stacks. Another helpful feature would be the addition of autofocusing tools both for focusing the detection path

and for setting up the tunable lens sweep. For this, online processing of acquired images needs to be integrated and robust measures of image quality have to be found. Image quality metrics that are shown to work in timelapse imaging of Drosophila embryos (Royer et al., 2016, 2018) are a possible starting point. In addition, closer integration with open microscopy exchange formats (Allan et al., 2012) and streamlining the pipeline for stitching using open-source tools (Hörl et al., 2018; Bria and Iannello, 2012) and later registration to the Allen Brain Atlas (Jones et al., 2009) will be helpful. While the mesoSPIM frame rates are comparatively low compared to light-sheet microscopes used for imaging zebrafish or Drosophila development, online compression could be implemented as well (Amat et al., 2015).

Integration of other modalities

Apart from light-sheet imaging, the mesoSPIM could also serve as a platform for other imaging modalities suitable for cleared samples such as optical projection tomography (OPT, Sharpe et al. (2002)). The mesoSPIM hard- and software could be integrated with existing open-source OPT projects (Gualda et al., 2013; Wong et al., 2013), for example to generate an absorption map of the sample (Bassi et al., 2015) which can help to further improve shadow reduction by post-processing (Mayer et al., 2014). The mesoSPIM could also be combined with Raman light-sheet microscopy (Müller et al., 2016) to better utilize intrinsic contrast mechanisms.

Support for larger samples

In recent years, tissue clearing and labeling methods have been scaled up to larger and larger samples, including whole mice (Tainaka et al., 2014; Pan et al., 2016; Cai et al., 2018). As these samples are considerably larger than the whole mouse CNS imaging example in Figure 4.22, a mesoSPIM variant capable of imaging such large samples would require much larger immersion cuvettes and sample stages with a much bigger travel range. Figure 5.2 shows a draft design of a mesoSPIM with 100 × 100 × 200 mm^3 travel range. Nonetheless, for immersion cuvettes with a footprint of up to 90 × 90 mm^2 , the current working distances of the excitation and detection optics would be sufficient. While the current mesoSPIM software is able to support this application, tools to

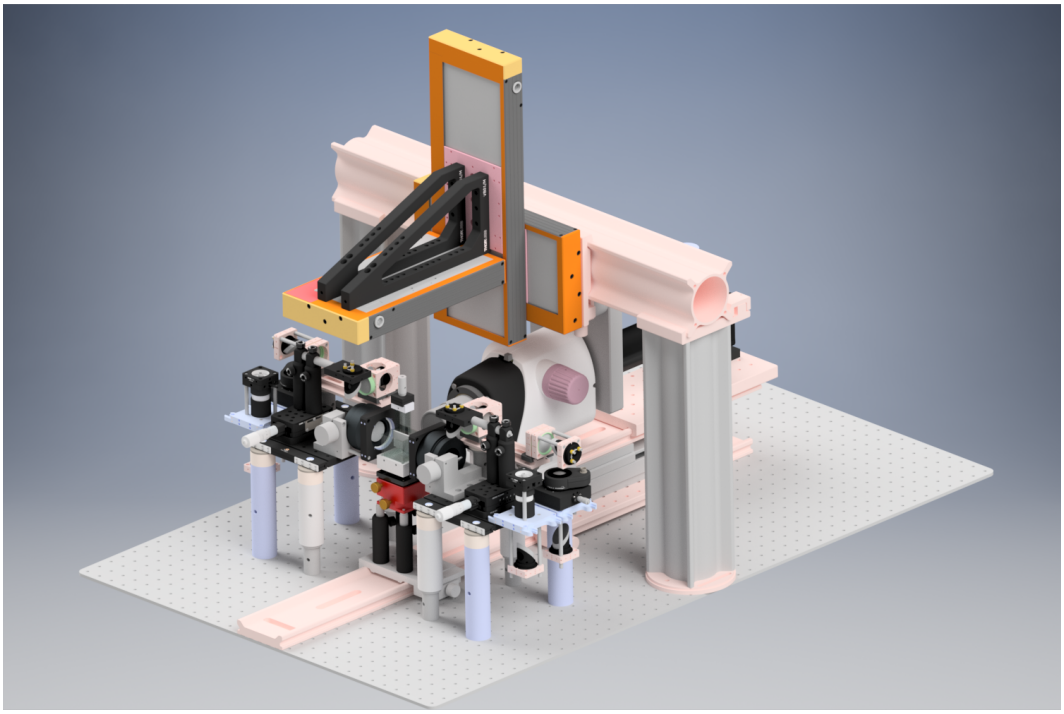

Figure 5.2: Design of a mesoSPIM with 100 × 100 × 200 mm travel range. Here, the 200 mm stage is oriented in the vertical direction. The sample stages are mounted on a gantry built from X95-profiles which renders the instrument more modular.

efficiently navigate a whole-body sample would be highly beneficial in this domain as well. As there is currently no commercial instrument capable of imaging a whole cleared mouse without remounting or cutting (Cai et al., 2018), this is a highly promising direction for further development.

Improvements to the optical design

The capabilities of the current generation of mesoSPIM setups could be further extended by increased optical performance. Some of the possible directions are:

The current excitation NA of 0.15 should – in theory – provide light-sheet thicknesses of 1.6 µm at 488 nm which is a fraction of the currently achieved values (6.55 µm over 13.3 mm FOV and 5.6 µm for a 3.3 mm FOV). The reason for this discrepancy is spherical aberration of the excitation beam due to the interface of the immersion cuvette. Future mesoSPIM excitation paths should

be aberration-corrected for a wide variety of immersion media ranging from water ($n_D = 1.33$) to BABB ($n_D = 1.56$). Note that better optical sectioning leads to stacks with more z-steps which can reduce the sample throughput. Lower lightsheet thickness could also be achieved with two-photon Bessel beam excitation (Fahrbach et al., 2010; Planchon et al., 2011), but this would require laser sources with high peak power to achieve a FOV of 13 mm or more and thus increase the cost of the setup.

Similar to the excitation path, the detection path would benefit from spherical aberration correction to increase the lateral resolution. As it is unlikely that dipping objectives with correction collars for commercial macro-zoom instruments will be available in the near future, this is likely to require a custom optical system. To design such a system, one could use a design strategy for adding post-objective correctors to existing commercial objectives (Saghafi et al., 2015).

Especially for samples with very weak expression of fluorescent proteins and thus very low emission intensities, the current generation mesoSPIM allows only imaging with very low SNR at low zoom setting. Under these conditions, any increase of laser power leads to high bleaching. The reason for this behavior is the inherent trade-off in microscopy between detection NA and FOV. High-NA objectives have small FOVs whereas macroscopic systems have low NA. As the image brightness or photon collection efficiency scales as NA^2, only a small fraction of the emitted light is focused on the detector. Therefore, future mesoSPIM generations should be designed for higher detection NAs, for example by adopting the mesolens design (McConnell et al., 2016).

To increase throughput, it would be beneficial if the acquisition speeds of the instrument could be increased. Currently, frame rates are typically 4.3 Hz with the main limitation being the need to scan the Gaussian excitation beam in two dimensions (to create the light-sheet and to perform ASLM) which requires time. If the light-sheet generation could be parallelized while retaining both the ability to change light-sheet width from 2-21 mm and to have shadow-reduced

illumination, acquisition speeds could be drastically increased. There is a report available on using engineered diffusors for shadow reduction (Taylor et al., 2018) which could consitute a direction for further development.

Another approach to increase throughput is to utilize cameras with higher pixel counts. With the Hamamatsu Lightning and the Photometrics Iris 15, sCMOS cameras with 12 to 15 megapixels are becoming available. Importantly, both sensors have a rectangular shape with an aspect ratio of approximately 16:9 which matches well with a horizontal section of a mouse brain. This would allow the design of a screening-mesoSPIM that could scan a whole mouse brain at 4 µm sampling within 5-8 minutes which is 2× to 1.5× the resolution of current mesoSPIM overview datasets. The remaining challenge is to design the detection optics to allow diffraction-limited imaging over the required 15 mm FOV with high numerical aperture.

5.3 Summary

With a wide variety of applications and options for setup improvements, the mesoSPIM has been introduced successfully into the microscopy community and will serve both users and instrument developers as a versatile platform to carry out their experiments. Future mesoSPIM generations are likely to become smart microscopes (Scherf and Huisken, 2015) which will actively help researchers answering questions using cleared samples and aid in the quest for better models of life.

References

Adhikari, A., Lerner, T. N., Finkelstein, J., Pak, S., Jennings, J. H., Davidson, T. J., Ferenczi, E., Gunaydin, L. A., Mirzabekov, J. J., Ye, L., Kim, S.-Y., Lei, A., and Deisseroth, K. (2015). Basomedial amygdala mediates top-down control of anxiety and fear. *Nature*, 527(7577):179–185.

Ahrens, M. B. and Keller, P. J. (2013). Whole-brain functional imaging at cellular resolution using light-sheet microscopy. *Nat Meth*, pages –.

Alfieri, C. G. E., Waldburger, D., Nürnberg, J., Golling, M., and Keller, U. (2019). Sub-150-fs pulses from an optically pumped broadband modelocked integrated external-cavity surface emitting laser. *Optics Letters*, 44(1):25–28.

Allan, C., Burel, J.-M., Moore, J., Blackburn, C., Linkert, M., Loynton, S., MacDonald, D., Moore, W. J., Neves, C., Patterson, A., Porter, M., Tarkowska, A., Loranger, B., Avondo, J., Lagerstedt, I., Lianas, L., Leo, S., Hands, K., Hay, R. T., Patwardhan, A., Best, C., Kleywegt, G. J., Zanetti, G., and Swedlow, J. R. (2012). OMERO: Flexible, model-driven data management for experimental biology. *Nature Methods*, 9(3):245–253.

Amat, F., Höckendorf, B., Wan, Y., Lemon, W. C., McDole, K., and Keller, P. J. (2015). Efficient processing and analysis of large-scale light-sheet microscopy data. *Nature Protocols*, 10(11):1679–1696.

Amos, W. and White, J. (2003). How the Confocal Laser Scanning Microscope entered Biological Research. *Biology of the Cell*, 95(6):335–342.

Antal, P. G. and Szipőcs, R. (2012). Tunable, low-repetition-rate, cost-efficient femtosecond Ti:sapphire laser for nonlinear microscopy. *Applied Physics B*, 107(1):17–22.

Armulik, A., Genové, G., Mäe, M., Nisancioglu, M. H., Wallgard, E., Niaudet, C., He, L., Norlin, J., Lindblom, P., Strittmatter, K., Johansson, B. R., and Betsholtz, C. (2010). Pericytes regulate the blood–brain barrier. *Nature*, 468(7323):557–561.

Arrenberg, A. B., Stainier, D. Y. R., Baier, H., and Huisken, J. (2010). Optogenetic control of cardiac function. *Science*, 330(6006):971–974.

Aviles-Espinosa, R., Filippidis, G., Hamilton, C., Malcolm, G., Weingarten, K. J., Südmeyer, T., Barbarin, Y., Keller, U., Santos, S. I. C. O., Artigas, D., and Loza-Alvarez, P. (2011). Compact ultrafast semiconductor disk laser: Targeting GFP based nonlinear applications in living organisms. *Biomed. Opt. Express*, 2(4):739–747.

Barad, Y., Eisenberg, H., Horowitz, M., and Silberberg, Y. (1997). Nonlinear scanning laser microscopy by third harmonic generation. *Applied Physics Letters*, 70(8):922–924.

Barbarin, Y., Hoffmann, M., Pallmann, W. P., Dahhan, I., Kreuter, P., Miller, M., Baier, J., Moench, H., Golling, M., Südmeyer, T., Witzigmann, B., and Keller, U. (2011). Electrically Pumped Vertical External Cavity Surface Emitting Lasers Suitable for Passive Modelocking. *IEEE Journal of Selected Topics in Quantum Electronics*, 17(6):1779–1786.

Bassi, A., Schmid, B., and Huisken, J. (2015). Optical tomography complements light sheet microscopy for in toto imaging of zebrafish development. *Development*, 142(5):1016–1020.

Baumgart, E. and Kubitscheck, U. (2012). Scanned light sheet microscopy with confocal slit detection. *Opt. Express*, 20(19):21805–21814.

Becker, K., Jährling, N., Saghafi, S., Weiler, R., and Dodt, H.-U. (2012). Chemical Clearing and Dehydration of GFP Expressing Mouse Brains. *PLOS ONE*, 7(3):e33916.

Belle, M., Godefroy, D., Couly, G., Malone, S. A., Collier, F., Giacobini, P., and Chédotal, A. (2017). Tridimensional Visualization and Analysis of Early Human Development. *Cell*, 169(1):161–173.e12.

Bolhuis, J. J. and Gahr, M. (2006). Neural mechanisms of birdsong memory. *Nature Reviews Neuroscience*, 7(5):347–357.

Botcherby, E. J., Juskaitis, R., Booth, M. J., and Wilson, T. (2007). Aberration-free optical refocusing in high numerical aperture microscopy. *Optics Letters*, 32(14):2007–2009.

Bouchal, Z., Wagner, J., and Chlup, M. (1998). Self-reconstruction of a distorted nondiffracting beam. *Optics Communications*, 151(4):207–211.

Bouchard, M. B., Voleti, V., Mendes, C. S., Lacefield, C., Grueber, W. B., Mann, R. S., Bruno, R. M., and Hillman, E. M. C. (2015). Swept confocally-aligned planar excitation (SCAPE) microscopy for high-speed volumetric imaging of behaving organisms. *Nature Photonics*, advance online publication.

Bracegirdle, B. (1981). A History of Microtechnique. *Journal of the History of Biology*, 14(2):355–355.

Bracegirdle, B. (1991). The microscopical tradition. In *Companion Encyclopedia of the History of Medicine*, pages 102–119. Routledge.

Bria, A. and Iannello, G. (2012). TeraStitcher - A tool for fast automatic 3D-stitching of teravoxel-sized microscopy images. *BMC Bioinformatics*, 13(1):1.

Cai, R., Pan, C., Ghasemigharagoz, A., Todorov, M. I., Förstera, B., Zhao, S., Bhatia, H. S., Parra-Damas, A., Mrowka, L., Theodorou, D., Rempfler, M., Xavier, A. L. R., Kress, B. T., Benakis, C., Steinke, H., Liebscher, S., Bechmann, I., Liesz, A., Menze, B., Kerschensteiner, M., Nedergaard, M., and Ertürk, A. (2018). Panoptic imaging of transparent mice reveals whole-body neuronal projections and skull–meninges connections. *Nature Neuroscience*, page 1.

Cajal, R. (1893). Neue Darstellung vom histologischen Bau des Centralnervensystems. In *Archiv Fur Anatomie Und Physiologie, Anatomische Abteilung*. G. Eichler, Berlin.

Capoulade, J., Wachsmuth, M., Hufnagel, L., and Knop, M. (2011). Quantitative fluorescence imaging of protein diffusion and interaction in living cells. *Nature Biotechnology*, 29(9):835–839.

Caviglia, S., Brankatschk, M., Fischer, E. J., Eaton, S., and Luschnig, S. (2016). Staccato/Unc-13-4 controls secretory lysosome-mediated lumen fusion during epithelial tube anastomosis. *Nature Cell Biology*, 18(7):727–739.

Cella Zanacchi, F., Lavagnino, Z., Perrone Donnorso, M., Del Bue, A., Furia, L., Faretta, M., and Diaspro, A. (2011). Live-cell 3D super-resolution imaging in thick biological samples. *Nature Methods*, 8(12):1047–1049.

Chang, B.-J., Kittisopikul, M., Dean, K. M., Roudot, P., Welf, E. S., and Fiolka, R. (2019). Universal light-sheet generation with field synthesis. *Nature Methods*, 16(3):235.

Chen, B.-C., Legant, W. R., Wang, K., Shao, L., Milkie, D. E., Davidson, M. W., Janetopoulos, C., Wu, X. S., Hammer, J. A., Liu, Z., English, B. P., Mimori-Kiyosue, Y., Romero, D. P., Ritter, A. T., Lippincott-Schwartz, J., Fritz-Laylin, L., Mullins, R. D., Mitchell, D. M., Bembenek, J. N., Reymann, A.-C., Böhme, R., Grill, S. W., Wang, J. T., Seydoux, G., Tulu, U. S., Kiehart, D. P., and Betzig, E. (2014). Lattice light-sheet microscopy: Imaging molecules to embryos at high spatiotemporal resolution. *Science*, 346(6208):1257998.

Chen, F., Tillberg, P. W., and Boyden, E. S. (2015). Expansion microscopy. *Science*, page 1260088.

Chen, F., Wassie, A. T., Cote, A. J., Sinha, A., Alon, S., Asano, S., Daugharthy, E. R., Chang, J.-B., Marblestone, A., Church, G. M., Raj, A., and Boyden, E. S. (2016a). Nanoscale imaging of RNA with expansion microscopy. *Nature Methods*, 13(8):679–684.

Chen, J. L., Voigt, F. F., Javadzadeh, M., Krueppel, R., and Helmchen, F. (2016b). Long-Range population dynamics of anatomically defined neocortical networks. *eLife*, 5:e14679.

Chen, X., Leischner, U., Rochefort, N. L., Nelken, I., and Konnerth, A. (2011). Functional mapping of single spines in cortical neurons in vivo. *Nature*, 475(7357):501–505.

Chhetri, R. K., Amat, F., Wan, Y., Höckendorf, B., Lemon, W. C., and Keller, P. J. (2015). Whole-animal functional and developmental imaging with isotropic spatial resolution. *Nature Methods*, 12(12):1171–1178.

Chiang, A.-s. (2002). Aqueous tissue clearing solution.

Chiang, A.-S., Liu, Y.-C., Chiu, S.-L., Hu, S.-H., Huang, C.-Y., and Hsieh, C.-H. (2001). Three-dimensional mapping of brain neuropils in the cockroach, Diploptera punctata. *The Journal of Comparative Neurology*, 440(1):1–11.

Chmielewski, A. K., Kyrsting, A., Mahou, P., Wayland, M. T., Muresan, L., Evers, J. F., and Kaminski, C. F. (2015). Fast imaging of live organisms with sculpted light sheets. *Scientific Reports*, 5.

Chu, S.-W., Chen, I.-H., Liu, T.-M., Chen, P. C., Sun, C.-K., and Lin, B.-L. (2001). Multimodal nonlinear spectral microscopy based on a femtosecond Cr:forsterite laser. *Optics Letters*, 26(23):1909–1911.

Chung, K. and Deisseroth, K. (2013). CLARITY for mapping the nervous system. *Nat Meth*, 10(6):508–513.

Chung, K., Wallace, J., Kim, S.-Y., Kalyanasundaram, S., Andalman, A. S., Davidson, T. J., Mirzabekov, J. J., Zalocusky, K. A., Mattis, J., Denisin, A. K., Pak, S., Bernstein, H., Ramakrishnan, C., Grosenick, L., Gradinaru, V., and Deisseroth, K. (2013). Structural and molecular interrogation of intact biological systems. *Nature*, 497(7449):332–337.

Costa, M., Manton, J. D., Ostrovsky, A. D., Prohaska, S., and Jefferis, G. S. X. E. (2016). NBLAST: Rapid, Sensitive Comparison of Neuronal Structure and Construction of Neuron Family Databases. *Neuron*, 91(2):293–311.

de Chadarevian, S. and Hopwood, N. (2004). *Models: The Third Dimension of Science*. Stanford University Press.

Dean, K. M. and Fiolka, R. (2014). Uniform and scalable light-sheets generated by extended focusing. *Optics Express*, 22(21):26141–26152.

Dean, K. M., Roudot, P., Welf, E. S., Danuser, G., and Fiolka, R. (2015). Deconvolution-free Subcellular Imaging with Axially Swept Light Sheet Microscopy. *Biophysical Journal*, 108(12):2807–2815.

Denk, W., Strickler, J., and Webb, W. (1990). Two-photon laser scanning fluorescence microscopy. *Science*, 248(4951):73–76.

Dent, J. A., Polson, A. G., and Klymkowsky, M. W. (1989). A whole-mount immunocytochemical analysis of the expression of the intermediate filament protein vimentin in Xenopus. *Development*, 105(1):61–74.

Dodt, H.-U., Leischner, U., Schierloh, A., Jährling, N., Mauch, C. P., Deininger, K., Deussing, J. M., Eder, M., Zieglgänsberger, W., and Becker, K. (2007). Ultramicroscopy: Three-dimensional visualization of neuronal networks in the whole mouse brain. *Nature Methods*, 4(4):331–336.

Dodt, H.-U., Saghafi, S., Becker, K., Jährling, N., Hahn, C., Pende, M., Wanis, M., and Niendorf, A. (2015). Ultramicroscopy: Development and outlook. *Neurophotonics*, 2(4):041407–041407.

Doerr, J., Schwarz, M. K., Wiedermann, D., Leinhaas, A., Jakobs, A., Schloen, F., Schwarz, I., Diedenhofen, M., Braun, N. C., Koch, P., Peterson, D. A., Kubitscheck, U., Hoehn, M., and Brüstle, O. (2017). Whole-brain 3D mapping of human neural transplant innervation. *Nature Communications*, 8:14162.

Dong, D., Arranz, A., Zhu, S., Yang, Y., Shi, L., Wang, J., Shen, C., Tian, J., and Ripoll, J. (2014). Vertically scanned laser sheet microscopy. *Journal of Biomedical Optics*, 19(10):106001–106001.

Drobizhev, M., Makarov, N. S., Tillo, S. E., Hughes, T. E., and Rebane, A. (2011). Two-photon absorption properties of fluorescent proteins. *Nat Meth*, 8(5):393–399.

Dunsby, C. (2008). Optically sectioned imaging by oblique plane microscopy. *Opt. Express*, 16(25):20306–20316.

Durfee, C. G., Storz, T., Garlick, J., Hill, S., Squier, J. A., Kirchner, M., Taft, G., Shea, K., Kapteyn, H., Murnane, M., and Backus, S. (2012). Direct diode-pumped Kerr-lens mode-locked Ti:sapphire laser. *Optics Express*, 20(13):13677–13683.

Economo, M. N., Clack, N. G., Lavis, L. D., Gerfen, C. R., Svoboda, K., Myers, E. W., and Chandrashekar, J. (2016). A platform for brain-wide imaging and reconstruction of individual neurons. *eLife*, 5:e10566.

Edelstein, A., Amodaj, N., Hoover, K., Vale, R., and Stuurman, N. (2010). Computer Control of Microscopes Using μManager. In *Current Protocols in Molecular Biology*. John Wiley & Sons, Inc.

Edelstein, A. D., Tsuchida, M. A., Amodaj, N., Pinkard, H., Vale, R. D., and Stuurman, N. (2014). Advanced methods of microscope control using μManager software. *Journal of Biological Methods*, 1(2):10.

Eggeling, C., Volkmer, A., and Seidel, C. A. M. (2005). Molecular Photobleaching Kinetics of Rhodamine 6G by One- and Two-Photon Induced Confocal Fluorescence Microscopy. *ChemPhysChem*, 6(5):791–804.

Egger, M. D. and Petráń, M. (1967). New Reflected-Light Microscope for Viewing Unstained Brain and Ganglion Cells. *Science*, 157(3786):305–307.

Ehlers, A., Riemann, I., Martin, S., Harzic, R. L., Bartels, A., Janke, C., and König, K. (2007). High (1GHz) repetition rate compact femtosecond laser: A powerful multiphoton tool for nanomedicine and nanobiotechnology. *Journal of Applied Physics*, 102(1):014701.

Emmons, S. W. (2015). The beginning of connectomics: A commentary on White et al. (1986) 'The structure of the nervous system of the nematode Caenorhabditis elegans'. *Phil. Trans. R. Soc. B*, 370(1666):20140309.

Engelbrecht, C. J., Greger, K., Reynaud, E. G., Kržic, U., Colombelli, J., and Stelzer, E. H. K. (2007). Three-dimensional laser microsurgery in light-sheet based microscopy (SPIM). *Optics Express*, 15(10):6420–6430.

Engelbrecht, C. J. and Stelzer, E. H. (2006). Resolution enhancement in a light-sheet-based microscope (SPIM). *Optics Letters*, 31(10):1477–1479.

Ertürk, A., Becker, K., Jährling, N., Mauch, C. P., Hojer, C. D., Egen, J. G., Hellal, F., Bradke, F., Sheng, M., and Dodt, H.-U. (2012a). Three-dimensional imaging of solvent-cleared organs using 3DISCO. *Nature Protocols*, 7(11):1983–1995.

Ertürk, A. and Bradke, F. (2013). High-resolution imaging of entire organs by 3-dimensional imaging of solvent cleared organs (3DISCO). *Experimental Neurology*, 242(0):57 – 64. New imaging techniques.

Ertürk, A., Mauch, C. P., Hellal, F., Förstner, F., Keck, T., Becker, K., Jährling, N., Steffens, H., Richter, M., Hübener, M., Kramer, E., Kirchhoff, F., Dodt, H. U., and Bradke, F. (2012b). Three-dimensional imaging of the unsectioned adult spinal cord to assess axon regeneration and glial responses after injury. *Nature Medicine*, 18(1):166–171.

Escobet-Montalbán, A., Gasparoli, F. M., Nylk, J., Liu, P., Yang, Z., and Dholakia, K. (2018). Three-photon light-sheet fluorescence microscopy. *Optics Letters*, 43(21):5484–5487.

Fahrbach, F. O., Gurchenkov, V., Alessandri, K., Nassoy, P., and Rohrbach, A. (2013a). Light-sheet microscopy in thick media using scanned Bessel beams and two-photon fluorescence excitation. *Opt. Express*, 21(11):13824–13839.

Fahrbach, F. O., Simon, P., and Rohrbach, A. (2010). Microscopy with self-reconstructing beams. *Nat Photon*, 4(11):780–785.

Fahrbach, F. O., Voigt, F. F., Schmid, B., Fritjof Helmchen, and Huisken, J. (2013b). Rapid 3D light-sheet microscopy with a tunable lens. *Opt. Express*, 21(18):21010–21026.

Fehrenbach, J., Weiss, P., and Lorenzo, C. (2012). Variational Algorithms to Remove Stationary Noise: Applications to Microscopy Imaging. *IEEE Transactions on Image Processing*, 21(10):4420–4430.

Feng, G., Mellor, R. H., Bernstein, M., Keller-Peck, C., Nguyen, Q. T., Wallace, M., Nerbonne, J. M., Lichtman, J. W., and Sanes, J. R. (2000). Imaging Neuronal Subsets in Transgenic Mice Expressing Multiple Spectral Variants of GFP. *Neuron*, 28(1):41–51.

Fermann, M. E. and Hartl, I. (2013). Ultrafast fibre lasers. *Nature Photonics*, 7(11):868–874.

Fernández-Suárez, M. and Ting, A. Y. (2008). Fluorescent probes for super-resolution imaging in living cells. *Nature Reviews Molecular Cell Biology*, 9(12):929–943.

Fork, R. L., Greene, B. I., and Shank, C. V. (1981). Generation of optical pulses shorter than 0.1 psec by colliding pulse mode locking. *Applied Physics Letters*, 38(9):671.

Freund, I., Deutsch, M., and Sprecher, A. (1986). Connective tissue polarity. Optical second-harmonic microscopy, crossed-beam summation, and small-angle scattering in rat-tail tendon. *Biophysical Journal*, 50(4):693–712.

Fu, Q., Martin, B. L., Matus, D. Q., and Gao, L. (2016). Imaging multicellular specimens with real-time optimized tiling light-sheet selective plane illumination microscopy. *Nature Communications*, 7:11088.

Fuchs, E., Jaffe, J. S., Long, R. A., and Azam, F. (2002). Thin laser light sheet microscope for microbial oceanography. *Optics Express*, 10(2):145–154.

Fujii, T. G., Nixima, K., and Okanoya, K. (2016). Application of optical clearing methods on the songbird brain. *ORNITHOLOGICAL SCIENCE*, 15(2):163–170.

Gaafar, M. A., Rahimi-Iman, A., Fedorova, K. A., Stolz, W., Rafailov, E. U., and Koch, M. (2016). Mode-locked semiconductor disk lasers. *Advances in Optics and Photonics*, 8(3):370–400.

Gao, L. (2015). Extend the field of view of selective plan illumination microscopy by tiling the excitation light sheet. *Optics Express*, 23(5):6102–6111.

Gao, R., Asano, S. M., Upadhyayula, S., Pisarev, I., Milkie, D. E., Liu, T.-L., Singh, V., Graves, A., Huynh, G. H., Zhao, Y., Bogovic, J., Colonell, J., Ott, C. M., Zugates, C., Tappan, S., Rodriguez, A., Mosaliganti, K. R., Sheu, S.-H., Pasolli, H. A., Pang, S., Xu, C. S., Megason, S. G., Hess, H., Lippincott-Schwartz, J., Hantman, A., Rubin, G. M., Kirchhausen, T., Saalfeld, S., Aso, Y., Boyden, E. S., and Betzig, E. (2019). Cortical column and whole-brain imaging with molecular contrast and nanoscale resolution. *Science*, 363(6424):eaau8302.

Garnache, A., Hoogland, S., Tropper, A. C., Sagnes, I., Saint-Girons, G., and Roberts, J. S. (2002). Sub-500-fs soliton-like pulse in a passively mode-locked broadband surface-emitting laser with 100 mW average power. *Applied Physics Letters*, 80(21):3892–3894.

Giesen, A., Hügel, H., Voss, A., Wittig, K., Brauch, U., and Opower, H. (1994). Scalable concept for diode-pumped high-power solid-state lasers. *Applied Physics B*, 58(5):365–372.

Girkin, J. M. and Wokosin, D. L. (2001). Novel compact sources for multiphoton microscopy. In *Proceedings Volume 4262, Multiphoton Microscopy in the Biomedical Sciences*, volume 4262, pages 186–191.

Girstmair, J., Zakrzewski, A., Lapraz, F., Handberg-Thorsager, M., Tomancak, P., Pitrone, P. G., Simpson, F., and Telford, M. J. (2016). Light sheet microscopy for everyone? Experience of building an OpenSPIM to study flatworm development. *bioRxiv*, page 045187.

Glaser, A. K., Chen, Y., Yin, C., Wei, L., Barner, L. A., Reder, N. P., and Liu, J. T. C. (2018). Multidirectional digital scanned light-sheet microscopy enables uniform fluorescence excitation and contrast-enhanced imaging. *Scientific Reports*, 8(1):13878.

Glaser, A. K., Reder, N. P., Chen, Y., McCarty, E. F., Yin, C., Wei, L., Wang, Y., True, L. D., and Liu, J. T. C. (2017). Light-sheet microscopy for slide-free non-destructive pathology of large clinical specimens. *Nature Biomedical Engineering*, 1(7):0084.

Golgi, C. (1873). Sulla sostanza grigia del cervello. *Gazetta Medica Italiana*, 33:244–246.

Golshani, P., Gonçalves, J. T., Khoshkhoo, S., Mostany, R., Smirnakis, S., and Portera-Cailliau, C. (2009). Internally Mediated Developmental Desynchronization of Neocortical Network Activity. *The Journal of Neuroscience*, 29(35):10890–10899.

Gong, S., Zheng, C., Doughty, M. L., Losos, K., Didkovsky, N., Schambra, U. B., Nowak, N. J., Joyner, A., Leblanc, G., Hatten, M. E., and Heintz, N. (2003). A gene expression atlas of the central nervous system based on bacterial artificial chromosomes. *Nature*, 425(6961):917.

Göppert-Mayer, M. (1931). über Elementarakte mit zwei Quantensprüngen. *Annalen der Physik*, 401(3):273–294.

Gradinaru, V., Treweek, J., Overton, K., and Deisseroth, K. (2018). Hydrogel-Tissue Chemistry: Principles and Applications. *Annual Review of Biophysics*, 47(1):355–376.

Grewe, B. F., Voigt, F. F., van 't Hoff, M., and Helmchen, F. (2011). Fast two-layer two-photon imaging of neuronal cell populations using an electrically tunable lens. *Biomed Opt Express*, 2(7):2035–2046.

Grienberger, C. and Konnerth, A. (2012). Imaging Calcium in Neurons. *Neuron*, 73(5):862–885.

Gualda, E. J., Vale, T., Almada, P., Feijó, J. A., Martins, G. G., and Moreno, N. (2013). OpenSpinMicroscopy: An open-source integrated microscopy platform. *Nature Methods*, 10(7):599–600.

Gürel, K., Wittwer, V. J., Hoffmann, M., Saraceno, C. J., Hakobyan, S., Resan, B., Rohrbacher, A., Weingarten, K., Schilt, S., and Südmeyer, T. (2015). Green-diode-pumped femtosecond Ti:Sapphire laser with up to 450 mW average power. *Optics Express*, 23(23):30043–30048.

Ha, T. and Tinnefeld, P. (2012). Photophysics of Fluorescent Probes for Single-Molecule Biophysics and Super-Resolution Imaging. *Annual Review of Physical Chemistry*, 63(1):595–617.

Hama, H., Hioki, H., Namiki, K., Hoshida, T., Kurokawa, H., Ishidate, F., Kaneko, T., Akagi, T., Saito, T., Saido, T., and Miyawaki, A. (2015a). ScaleS: An optical clearing palette for biological imaging. *Nature Neuroscience*, advance online publication.

Hama, H., Hioki, H., Namiki, K., Hoshida, T., Kurokawa, H., Ishidate, F., Kaneko, T., Akagi, T., Saito, T., Saido, T., and Miyawaki, A. (2015b). Sca*l*eS: An optical clearing palette for biological imaging. *Nature Neuroscience*, 18(10):1518–1529.

Hama, H., Kurokawa, H., Kawano, H., Ando, R., Shimogori, T., Noda, H., Fukami, K., Sakaue-Sawano, A., and Miyawaki, A. (2011). Scale: A chemical approach for fluorescence imaging and reconstruction of transparent mouse brain. *Nat Neurosci*, 14(11):1481–1488.

Haring, R., Paschotta, R., Gini, E., Morier-Genoud, F., Martin, D., Melchior, H., and Keller, U. (2001). Picosecond surface-emitting semiconductor laser with >200 mW average power. *Electronics Letters*, 37(12):766–767.

Hedde, P. N. and Gratton, E. (2016). Selective plane illumination microscopy with a light sheet of uniform thickness formed by an electrically tunable lens. *Microscopy Research and Technique*, pages n/a–n/a.

Hell, S. W. (2007). Far-Field Optical Nanoscopy. *Science*, 316(5828):1153–1158.

Hell, S. W. and Wichmann, J. (1994). Breaking the diffraction resolution limit by stimulated emission: Stimulated-emission-depletion fluorescence microscopy. *Opt. Lett.*, 19(11):780–782.

Helmchen, F. and Denk, W. (2005). Deep tissue two-photon microscopy. *Nat Methods*, 2(12):932–940.

Hildebrand, S., Schueth, A., Herrler, A., Galuske, R., and Roebroeck, A. (2018). Scalable cytoarchitectonic characterization of large intact human neocortex samples. *bioRxiv*, page 274985.

His, W. (1870). Beschreibung eines Mikrotoms. *Archiv für mikroskopische Anatomie*, 6(1):229–232.

His, W. (1880). *Anatomie menschlicher Embryonen*. Vogel.

Hoogland, S., Dhanjal, S., Tropper, A., Roberts, J., Haring, R., Paschotta, R., Morier-Genoud, F., and Keller, U. (2000). Passively mode-locked diode-pumped surface-emitting semiconductor laser. *IEEE Photonics Technology Letters*, 12(9):1135–1137.

Hoogland, S., Garnache, A., Sagnes, I., Roberts, J. S., and Tropper, A. C. (2005). 10-GHz train of sub-500-fs optical soliton-like pulses from a surface-emitting semiconductor laser. *IEEE Photonics Technology Letters*, 17(2):267–269.

Hooke, R. (1665). *Micrographia, or Some Physiological Descriptions of Minute Bodies Made by Magnifying Glasses, with Observations and Inquiries Thereupon.* Printed by Jo. Martyn, and Ja. Allestry, printers to the Royal Society, 1665., London.

Hopt, A. and Neher, E. (2001). Highly Nonlinear Photodamage in Two-Photon Fluorescence Microscopy. *Biophysical Journal*, 80(4):2029 – 2036.

Hopwood, N. (1999). "Giving Body" to Embryos: Modeling, Mechanism, and the Microtome in Late Nineteenth-Century Anatomy. *Isis*, 90(3):462–496.

Hörl, D., Rusak, F. R., Preusser, F., Tillberg, P., Randel, N., Chhetri, R. K., Cardona, A., Keller, P. J., Harz, H., Leonhardt, H., Treier, M., and Preibisch, S. (2018). BigStitcher: Reconstructing high-resolution image datasets of cleared and expanded samples. *bioRxiv*, page 343954.

Horton, N. G., Wang, K., Kobat, D., Clark, C. G., Wise, F. W., Schaffer, C. B., and Xu, C. (2013). In vivo three-photon microscopy of subcortical structures within an intact mouse brain. *Nat Photon*, 7(3):205–209.

Hossfeld, U., Olsson, L., and Markert, M. (2012). Zur Visualisierung menschlicher Embryonen: Das Modell des menschlichen Embryos (Embryo His Br3) der Firma Paul Osterloh (Leipzig). *Rudolstädter naturhistorische Schriften*, 18:13–17.

Hua, L., Zhou, R., Thirumalai, D., and Berne, B. J. (2008). Urea denaturation by stronger dispersion interactions with proteins than water implies a 2-stage unfolding. *Proceedings of the National Academy of Sciences*, 105(44):16928–16933.

Huber, D., Keller, M., and Robert, D. (2001). 3D light scanning macrography. *Journal of Microscopy*, 203(2):208–213.

Huisken, J. (2004). *Multiview Microscopy and Multibeam Manipulation for High Resolution Optical Imaging*. PhD thesis, Albert-Ludwigs-Universität Freiburg im Breisgau.

Huisken, J. (2012). Slicing embryos gently with laser light sheets. *Bioessays*, 34(5):406–411.

Huisken, J. and Stainier, D. Y. R. (2007). Even fluorescence excitation by multidirectional selective plane illumination microscopy (mSPIM). *Opt Lett*, 32(17):2608–2610.

Huisken, J. and Stainier, D. Y. R. (2009). Selective plane illumination microscopy techniques in developmental biology. *Development*, 136(12):1963–1975.

Ji, N., Magee, J. C., and Betzig, E. (2008). High-speed, low-photodamage nonlinear imaging using passive pulse splitters. *Nat Meth*, 5(2):197–202.

Jing, D., Zhang, S., Luo, W., Gao, X., Men, Y., Ma, C., Liu, X., Yi, Y., Bugde, A., Zhou, B. O., Zhao, Z., Yuan, Q., Feng, J. Q., Gao, L., Ge, W.-P., and Zhao, H. (2018). Tissue clearing of both hard and soft tissue organs with the PEGASOS method. *Cell Research*, 28(8):803.

Jones, A. R., Overly, C. C., and Sunkin, S. M. (2009). The Allen Brain Atlas: 5 years and beyond. *Nature Reviews Neuroscience*, 10(11):821–828.

Kalies, S., Kuetemeyer, K., and Heisterkamp, A. (2011). Mechanisms of high-order photobleaching and its relationship to intracellular ablation. *Biomed. Opt. Express*, 2(4):805–816.

Karagiannis, E. D. and Boyden, E. S. (2018). Expansion microscopy: Development and neuroscience applications. *Current Opinion in Neurobiology*, 50:56–63.

Ke, M.-T., Fujimoto, S., and Imai, T. (2013). SeeDB: A simple and morphology-preserving optical clearing agent for neuronal circuit reconstruction. *Nature Neuroscience*, 16(8):1154–1161.

Keller, A., Nuvolone, M., Abakumova, I., Chincisan, A., Reimann, R., Avar, M., Heinzer, D., Hornemann, S., Wagner, J., Kirschenbaum, D., Voigt, F. F., Zhu, C., Regli, L., Helmchen, F., and Aguzzi, A. (2018). Prion pathogenesis is unaltered in a mouse strain with a permeable blood-brain barrier. *PLOS Pathogens*, 14(11):e1007424.

Keller, A., Westenberger, A., Sobrido, M. J., García-Murias, M., Domingo, A., Sears, R. L., Lemos, R. R., Ordoñez-Ugalde, A., Nicolas, G., da Cunha, J. E. G., Rushing, E. J., Hugelshofer, M., Wurnig, M. C., Kaech, A., Reimann, R., Lohmann, K., Dobričić, V., Carracedo, A., Petrović, I., Miyasaki, J. M., Abakumova, I., Mäe, M. A., Raschperger, E., Zatz, M., Zschiedrich, K., Klepper, J., Spiteri, E., Prieto, J. M., Navas, I., Preuss, M., Dering, C., Janković, M., Paucar, M., Svenningsson, P., Saliminejad, K., Khorshid, H. R. K., Novaković, I., Aguzzi, A., Boss, A., Le Ber, I., Defer, G., Hannequin, D., Kostić, V. S., Campion, D., Geschwind, D. H., Coppola, G., Betsholtz, C., Klein, C., and Oliveira, J. R. M. (2013). Mutations in the gene encoding PDGF-B cause brain calcifications in humans and mice. *Nature Genetics*, 45(9):1077–1082.

Keller, P. J. and Dodt, H.-U. (2012). Light sheet microscopy of living or cleared specimens. *Curr Opin Neurobiol*, 22(1):138–143.

Keller, P. J., Schmidt, A. D., Santella, A., Khairy, K., Bao, Z., Wittbrodt, J., and Stelzer, E. H. K. (2010). Fast, high-contrast imaging of animal development with scanned light sheet-based structured-illumination microscopy. *Nature Methods*, 7(8):637–642.

Keller, P. J., Schmidt, A. D., Wittbrodt, J., and Stelzer, E. H. K. (2008). Reconstruction of Zebrafish Early Embryonic Development by Scanned Light Sheet Microscopy. *Science*, 322(5904):1065–1069.

Keller, U. (2007). 2.1 Ultrafast solid-state lasers. In Herziger, G., Weber, H., and Poprawe, R., editors, *2 Short and Ultrashort Pulse Generation*, volume 11 of *Landolt-Börnstein - Group VIII Advanced Materials and Technologies*. Springer-Verlag.

Keller, U., 'tHooft, G. W., Knox, W. H., and Cunningham, J. E. (1991). Femtosecond pulses from a continuously self-starting passively mode-locked Ti:sapphire laser. *Opt. Lett.*, 16(13):1022–1024.

Keller, U. and Tropper, A. C. (2006). Passively modelocked surface-emitting semiconductor lasers. *Physics Reports*, 429(2):67 – 120.

Keller, U., Weingarten, K., Kartner, F., Kopf, D., Braun, B., Jung, I., Fluck, R., Honninger, C., Matuschek, N., and Aus der Au, J. (1996). Semiconductor saturable absorber mirrors (SESAM's) for femtosecond to nanosecond pulse generation in solid-state lasers. *Selected Topics in Quantum Electronics, IEEE Journal of*, 2(3):435–453.

Kim, S.-Y., Cho, J. H., Murray, E., Bakh, N., Choi, H., Ohn, K., Ruelas, L., Hubbert, A., McCue, M., Vassallo, S. L., Keller, P. J., and Chung, K. (2015). Stochastic electrotransport selectively enhances the transport of highly electromobile molecules. *Proceedings of the National Academy of Sciences*, 112(46):E6274–E6283.

Kingslake, R. (2010). *Lens Design Fundamentals*. Academic Press.

Kleinfeld, D., Bharioke, A., Blinder, P., Bock, D. D., Briggman, K. L., Chklovskii, D. B., Denk, W., Helmstaedter, M., Kaufhold, J. P., Lee, W.-C. A., Meyer, H. S., Micheva, K. D., Oberlaender, M., Prohaska, S., Reid, R. C., Smith, S. J., Takemura, S., Tsai, P. S., and Sakmann, B. (2011). Large-scale automated histology in the pursuit of connectomes. *J Neurosci*, 31(45):16125–16138.

Kleinfeld, D., Mitra, P. P., Helmchen, F., and Denk, W. (1998). Fluctuations and stimulus-induced changes in blood flow observed in individual capillaries in layers 2 through 4 of rat neocortex. *Proceedings of the National Academy of Sciences*, 95(26):15741–15746.

Klingberg, A., Hasenberg, A., Ludwig-Portugall, I., Medyukhina, A., Männ, L., Brenzel, A., Engel, D. R., Figge, M. T., Kurts, C., and Gunzer, M. (2017). Fully Automated Evaluation of Total Glomerular Number and Capillary Tuft Size in Nephritic Kidneys Using Lightsheet Microscopy. *Journal of the American Society of Nephrology*, 28(2):452–459.

Klymkowsky, M. W. and Hanken, J. (1991). Chapter 22 Whole-Mount Staining of Xenopus and Other Vertebrates. In Kay, B. K. and Peng, H. B., editors, *Methods in Cell Biology*, volume 36 of *Xenopus Laevis: Practical Uses in Cell and Molecular Biology*, pages 419–441. Academic Press.

Kolesová, H., Čapek, M., Radochová, B., Janáček, J., and Sedmera, D. (2016). Comparison of different tissue clearing methods and 3D imaging techniques for visualization of GFP-expressing mouse embryos and embryonic hearts. *Histochemistry and Cell Biology*, 146(2):141–152.

Krzic, U., Gunther, S., Saunders, T. E., Streichan, S. J., and Hufnagel, L. (2012). Multiview light-sheet microscope for rapid in toto imaging. *Nature Methods*, 9(7):730–733.

Kumar, A., Wu, Y., Christensen, R., Chandris, P., Gandler, W., McCreedy, E., Bokinsky, A., Colón-Ramos, D. A., Bao, Z., McAuliffe, M., Rondeau, G., and Shroff, H. (2014). Dual-view plane illumination microscopy for rapid and spatially isotropic imaging. *Nature Protocols*, 9(11):2555–2573.

Kumar, M., Kishore, S., Nasenbeny, J., McLean, D., and Kozorovitskiy, Y. (2018). Integrated one- and two-photon scanned oblique plane illumination (SOPi) microscopy for rapid volumetric imaging. *arXiv:1804.09844 [physics, q-bio]*.

Kumar, M. and Kozorovitskiy, Y. (2019). Tilt-invariant scanned oblique plane illumination microscopy for large-scale volumetric imaging. *arXiv:1901.00498 [physics]*.

Kumar, S., Wilding, D., Sikkel, M. B., Lyon, A. R., MacLeod, K. T., and Dunsby, C. (2011). High-speed 2D and 3D fluorescence microscopy of cardiac myocytes. *Opt. Express*, 19(15):13839–13847.

Kuramoto, M., Kitajima, N., Guo, H., Furushima, Y., Ikeda, M., and Yokoyama, H. (2007). Two-photon fluorescence bioimaging with an all-semiconductor laser picosecond pulse source. *Optics Letters*, 32(18):2726–2728.

Kusama, Y., Tanushi, Y., Yokoyama, M., Kawakami, R., Hibi, T., Kozawa, Y., Nemoto, T., Sato, S., and Yokoyama, H. (2014). 7-ps optical pulse generation from a 1064-nm gain-switched laser diode and its application for two-photon microscopy. *Optics Express*, 22(5):5746–5753.

Kuznetsov, M. (2010). VECSEL Semiconductor Lasers: A Path to High-Power, Quality Beam and UV to IR Wavelength by Design. In Okhotnikov, O. G., editor, *Semiconductor Disk Lasers*, pages 1–71. Wiley-VCH Verlag GmbH & Co. KGaA.

Lai, H. M., Liu, A. K. L., Ng, H. H. M., Goldfinger, M. H., Chau, T. W., DeFelice, J., Tilley, B. S., Wong, W. M., Wu, W., and Gentleman, S. M. (2018). Next generation histology methods for three-dimensional imaging of fresh and archival human brain tissues. *Nature Communications*, 9(1):1066.

Laikin, M. (2012). *Lens Design*. CRC Press.

Laissue, P. P., Alghamdi, R. A., Tomancak, P., Reynaud, E. G., and Shroff, H. (2017). Assessing phototoxicity in live fluorescence imaging. *Nature Methods*, 14:657–661.

Lamb, W. E., Schleich, W. P., Scully, M. O., and Townes, C. H. (1999). Laser Physics: Quantum Controversy in Action. In Bederson, B., editor, *More Things in Heaven and Earth: A Celebration of Physics at the Millennium*, pages 442–459. Springer New York, New York, NY.

Leeuwenhoek, A. V. (1677). Observations, communicated to the publisher by Mr. Antony van Leewenhoeck, in a dutch letter of the 9th Octob. 1676. here English'd: Concerning little animals by him observed in rain-well-sea- and snow water; as also in water wherein pepper had lain infused. *Philosophical Transactions*, 12(133):821–831.

Lerner, T. N., Shilyansky, C., Davidson, T. J., Evans, K. E., Beier, K. T., Zalocusky, K. A., Crow, A. K., Malenka, R. C., Luo, L., Tomer, R., and Deisseroth, K. (2015). Intact-Brain Analyses Reveal Distinct Information Carried by SNc Dopamine Subcircuits. *Cell*, 162(3):635–647.

Liang, X., Zang, Y., Dong, D., Zhang, L., Fang, M., Yang, X., Arranz, A., Ripoll, J., Hui, H., and Tian, J. (2016). Stripe artifact elimination based on nonsubsampled contourlet transform for light sheet fluorescence microscopy. *Journal of Biomedical Optics*, 21(10):106005–106005.

Liebmann, T., Renier, N., Bettayeb, K., Greengard, P., Tessier-Lavigne, M., and Flajolet, M. (2016). Three-Dimensional Study of Alzheimer's Disease Hallmarks Using the iDISCO Clearing Method. *Cell Reports*, 0(0).

Lin, X., Duan, X., Jacobs, C., Ullmann, J., Chan, C.-Y., Chen, S., Cheng, S.-H., Zhao, W.-N., Poduri, A., Wang, X., Haggarty, S. J., and Shi, P. (2018). High-throughput brain activity mapping and machine learning as a foundation for systems neuropharmacology. *Nature Communications*, 9(1):5142.

Liu, T.-L., Upadhyayula, S., Milkie, D. E., Singh, V., Wang, K., Swinburne, I. A., Mosaliganti, K. R., Collins, Z. M., Hiscock, T. W., Shea, J., Kohrman, A. Q., Medwig, T. N., Dambournet, D., Forster, R., Cunniff, B., Ruan, Y., Yashiro, H., Scholpp, S., Meyerowitz, E. M., Hockemeyer, D., Drubin, D. G., Martin, B. L., Matus, D. Q., Koyama, M., Megason, S. G., Kirchhausen, T., and Betzig, E. (2018). Observing the cell in its native state: Imaging subcellular dynamics in multicellular organisms. *Science*, 360(6386):eaaq1392.

Liu, T.-M., Chu, S.-W., Sun, C.-K., Lin, B.-L., Cheng, P.-C., and Johnson, I. (2001). Multiphoton confocal microscopy using a femtosecond Cr:Forsterite laser. *Scanning*, 23(4):249–254.

Lloyd-Lewis, B., Davis, F. M., Harris, O. B., Hitchcock, J. R., Lourenco, F. C., Pasche, M., and Watson, C. J. (2016). Imaging the mammary gland and mammary tumours in 3D: Optical tissue clearing and immunofluorescence methods. *Breast Cancer Research*, 18(1):127.

Maddaloni, P., Cancio, P., and Natale, P. D. (2009). Optical comb generators for laser frequency measurement. *Measurement Science and Technology*, 20(5):052001.

Madisen, L., Garner, A. R., Shimaoka, D., Chuong, A. S., Klapoetke, N. C., Li, L., van der Bourg, A., Niino, Y., Egolf, L., Monetti, C., Gu, H., Mills, M., Cheng, A., Tasic, B., Nguyen, T. N., Sunkin, S. M., Benucci, A., Nagy, A., Miyawaki, A., Helmchen, F., Empson, R. M., Knöpfel, T., Boyden, E. S., Reid, R. C., Carandini, M., and Zeng, H. (2015). Transgenic Mice for Intersectional Targeting of Neural Sensors and Effectors with High Specificity and Performance. *Neuron*, 85(5):942–958.

Madisen, L., Zwingman, T. A., Sunkin, S. M., Oh, S. W., Zariwala, H. A., Gu, H., Ng, L. L., Palmiter, R. D., Hawrylycz, M. J., Jones, A. R., Lein, E. S., and Zeng, H. (2010). A robust and high-throughput Cre reporting and characterization system for the whole mouse brain. *Nature Neuroscience*, 13(1):133–140.

Mangold, M., Golling, M., Gini, E., Tilma, B. W., and Keller, U. (2015). Sub-300-femtosecond operation from a MIXSEL. *Optics Express*, 23(17):22043–22059.

Mangold, M., Link, S., Klenner, A., Zaugg, C., Golling, M., Tilma, B., and Keller, U. (2014). Amplitude Noise and Timing Jitter Characterization of a High-Power Mode-Locked Integrated External-Cavity Surface Emitting Laser. *IEEE Photonics Journal*, 6(1):1–9.

Mappes, T., Jahr, N., Csáki, A., Vogler, N., Popp, J., and Fritzsche, W. (2012). Die Erfindung des Immersions-Ultramikroskops 1912 – Beginn der Nanotechnologie? *Angewandte Chemie*, 124(45):11370–11375.

Mayer, J., Robert-Moreno, A., Danuser, R., Stein, J. V., Sharpe, J., and Swoger, J. (2014). OPTiSPIM: Integrating optical projection tomography in light sheet microscopy extends specimen characterization to nonfluorescent contrasts. *Optics Letters*, 39(4):1053–1056.

Mayer, J., Robert-Moreno, A., Sharpe, J., and Swoger, J. (2018). Attenuation artifacts in light sheet fluorescence microscopy corrected by OPTiSPIM. *Light: Science & Applications*, 7(1):70.

McConnell, G., Trägårdh, J., Amor, R., Dempster, J., Reid, E., and Amos, W. B. (2016). A novel optical microscope for imaging large embryos and tissue volumes with sub-cellular resolution throughout. *eLife*, 5:e18659.

McDole, K., Guignard, L., Amat, F., Berger, A., Malandain, G., Royer, L. A., Turaga, S. C., Branson, K., and Keller, P. J. (2018). In Toto Imaging and Reconstruction of Post-Implantation Mouse Development at the Single-Cell Level. *Cell*, 175(3):859–876.e33.

McGorty, R., Liu, H., Kamiyama, D., Dong, Z., Guo, S., and Huang, B. (2015). Open-top selective plane illumination microscope for conventionally mounted specimens. *Optics Express*, 23(12):16142–16153.

Mendonca, T., Birkhead, T. R., Cadby, A. J., Forstmeier, W., and Hemmings, N. (2018). A trade-off between thickness and length in the zebra finch sperm mid-piece. *Proceedings of the Royal Society B: Biological Sciences*.

Menegas, W., Bergan, J. F., Ogawa, S. K., Isogai, Y., Venkataraju, K. U., Osten, P., Uchida, N., and Watabe-Uchida, M. (2015). Dopamine neurons projecting to the posterior striatum form an anatomically distinct subclass. *eLife*, 4:e10032.

Mertz, J. and Kim, J. (2010). Scanning light-sheet microscopy in the whole mouse brain with HiLo background rejection. *Journal of Biomedical Optics*, 15(1):016027–016027–7.

Michalzik, R. (2012). *VCSELs: Fundamentals, Technology and Applications of Vertical-Cavity Surface-Emitting Lasers*. Springer.

Mickoleit, M., Schmid, B., Weber, M., Fahrbach, F. O., Hombach, S., Reischauer, S., and Huisken, J. (2014). High-resolution reconstruction of the beating zebrafish heart. *Nature Methods*, 11(9):919–922.

Migliori, B., Datta, M. S., Dupre, C., Apak, M. C., Asano, S., Gao, R., Boyden, E. S., Hermanson, O., Yuste, R., and Tomer, R. (2018). Light sheet theta microscopy for rapid high-resolution imaging of large biological samples. *BMC Biology*, 16(1):57.

Minsky, M. (1988). Memoir on inventing the confocal scanning microscope. *Scanning*, 10(4):128–138.

Mirkhanov, S., Quarterman, A. H., Swift, S., Praveen, B. B., Smyth, C. J. C., and Wilcox, K. G. (2016). Multiphoton imaging with high peak power VECSELs. In *Vertical External Cavity Surface Emitting Lasers (VECSELs) VI*, volume 9734, page 973412. International Society for Optics and Photonics.

Miyawaki, A. and Niino, Y. (2015). Molecular Spies for Bioimaging—Fluorescent Protein-Based Probes. *Molecular Cell*, 58(4):632–643.

Mollenauer, L. F. and Stolen, R. H. (1984). The soliton laser. *Opt. Lett.*, 9(1):13–15.

Müllenbroich, M. C., Silvestri, L., Giovanna, A. P. D., Mazzamuto, G., Costantini, I., Sacconi, L., and Pavone, F. S. (2018a). High-Fidelity Imaging in Brain-Wide Structural Studies Using Light-Sheet Microscopy. *eNeuro*, pages ENEURO.0124–18.2018.

Müllenbroich, M. C., Silvestri, L., Onofri, L., Costantini, I., van't Hoff, M., Sacconi, L., Iannello, G., and Pavone, F. S. (2015). Comprehensive optical and data management infrastructure for high-throughput light-sheet microscopy of whole mouse brains. *Neurophotonics*, 2(4):041404–041404.

Müllenbroich, M. C., Turrini, L., Silvestri, L., Alterini, T., Gheisari, A., Tiso, N., Vanzi, F., Sacconi, L., and Pavone, F. S. (2018b). Bessel Beam Illumination Reduces Random and Systematic Errors in Quantitative Functional Studies Using Light-Sheet Microscopy. *Frontiers in Cellular Neuroscience*, 12.

Müller, W., Kielhorn, M., Schmitt, M., Popp, J., and Heintzmann, R. (2016). Light sheet Raman micro-spectroscopy. *Optica*, 3(4):452–457.

Münch, B., Trtik, P., Marone, F., and Stampanoni, M. (2009). Stripe and ring artifact removal with combined wavelet — Fourier filtering. *Optics Express*, 17(10):8567–8591.

Murakami, T. C., Mano, T., Saikawa, S., Horiguchi, S. A., Shigeta, D., Baba, K., Sekiya, H., Shimizu, Y., Tanaka, K. F., Kiyonari, H., Iino, M., Mochizuki, H., Tainaka, K., and Ueda, H. R. (2018). A three-dimensional single-cell-resolution whole-brain atlas using CUBIC-X expansion microscopy and tissue clearing. *Nature Neuroscience*, page 1.

Murray, E., Cho, J. H., Goodwin, D., Ku, T., Swaney, J., Kim, S.-Y., Choi, H., Park, Y.-G., Park, J.-Y., Hubbert, A., McCue, M., Vassallo, S., Bakh, N., Frosch, M. P., Wedeen, V. J., Seung, H. S., and Chung, K. (2015). Simple, Scalable Proteomic Imaging for High-Dimensional Profiling of Intact Systems. *Cell*, 163(6):1500–1514.

Muyldermans, S. (2013). Nanobodies: Natural Single-Domain Antibodies. *Annual Review of Biochemistry*, 82(1):775–797.

Nicovich, P. R., Walsh, J., Böcking, T., and Gaus, K. (2017). NicoLase—An open-source diode laser combiner, fiber launch, and sequencing controller for fluorescence microscopy. *PLOS ONE*, 12(3):e0173879.

Niedworok, C. J., Schwarz, I., Ledderose, J., Günter Giese, Conzelmann, K.-K., and Schwarz, M. K. (2012). Charting Monosynaptic Connectivity Maps by Two-Color Light-Sheet Fluorescence Microscopy. *Cell Reports*, 2(5):1375 – 1386.

Niu, F., Wu, R., Wu, D., Gou, D., Feng, L., Chen, L., Zhang, Z., and Wang, A. (2019). Photobleaching of ultrashort pulses with different repetition rates in two-photon excitation microscopy. *Laser Physics*, 29(4):046001.

Nojima, S., Susaki, E. A., Yoshida, K., Takemoto, H., Tsujimura, N., Iijima, S., Takachi, K., Nakahara, Y., Tahara, S., Ohshima, K., Kurashige, M., Hori, Y., Wada, N., Ikeda, J.-i., Kumanogoh, A., Morii, E., and Ueda, H. R. (2017). CUBIC pathology: Three-dimensional imaging for pathological diagnosis. *Scientific Reports*, 7(1):9269.

Oh, S. W., Harris, J. A., Ng, L., Winslow, B., Cain, N., Mihalas, S., Wang, Q., Lau, C., Kuan, L., Henry, A. M., Mortrud, M. T., Ouellette, B., Nguyen, T. N., Sorensen, S. A., Slaughterbeck, C. R., Wakeman, W., Li, Y., Feng, D., Ho, A., Nicholas, E., Hirokawa, K. E., Bohn, P., Joines, K. M., Peng, H., Hawrylycz, M. J., Phillips, J. W., Hohmann, J. G., Wohnoutka, P., Gerfen, C. R., Koch, C., Bernard, A., Dang, C., Jones, A. R., and Zeng, H. (2014). A mesoscale connectome of the mouse brain. *Nature*, 508(7495):207–214.

Ohkura, M., Sasaki, T., Kobayashi, C., Ikegaya, Y., and Nakai, J. (2012). An Improved Genetically Encoded Red Fluorescent Ca2+ Indicator for Detecting Optically Evoked Action Potentials. *PLoS ONE*, 7(7):e39933.

Ouzounov, D. G., Wang, T., Wang, M., Feng, D. D., Horton, N. G., Cruz-Hernández, J. C., Cheng, Y.-T., Reimer, J., Tolias, A. S., Nishimura, N., and Xu, C. (2017). In vivo three-photon imaging of activity of GCaMP6-labeled neurons deep in intact mouse brain. *Nature Methods*, 14(4):388–390.

Pan, C., Cai, R., Quacquarelli, F. P., Ghasemigharagoz, A., Lourbopoulos, A., Matryba, P., Plesnila, N., Dichgans, M., Hellal, F., and Ertürk, A. (2016). Shrinkage-mediated imaging of entire organs and organisms using uDISCO. *Nature Methods*, advance online publication.

Park, Y.-G., Sohn, C. H., Chen, R., McCue, M., Yun, D. H., Drummond, G. T., Ku, T., Evans, N. B., Oak, H. C., Trieu, W., Choi, H., Jin, X., Lilascharoen, V., Wang, J., Truttmann, M. C., Qi, H. W., Ploegh, H. L., Golub, T. R., Chen, S.-C., Frosch, M. P., Kulik, H. J., Lim, B. K., and Chung, K. (2019). Protection of tissue physicochemical properties using polyfunctional crosslinkers. *Nature Biotechnology*, 37(1):73–83.

Pende, M., Becker, K., Wanis, M., Saghafi, S., Kaur, R., Hahn, C., Pende, N., Foroughipour, M., Hummel, T., and Dodt, H.-U. (2018). High-resolution ultramicroscopy of the developing and adult nervous system in optically cleared Drosophila melanogaster. *Nature Communications*, 9(1):4731.

Perillo, E. P., McCracken, J. E., Fernée, D. C., Goldak, J. R., Medina, F. A., Miller, D. R., Yeh, H.-C., and Dunn, A. K. (2016). Deep in vivo two-photon microscopy with a low cost custom built mode-locked 1060 nm fiber laser. *Biomedical Optics Express*, 7(2):324–334.

Perin, P., Voigt, F. F., Bethge, P., Helmchen, F., and Pizzala, R. (2019). iDISCO+ for the Study of Neuroimmune Architecture of the Rat Auditory Brainstem. *Frontiers in Neuroanatomy*, 13.

Peter, K. (1906). *Die Methoden Der Rekonstruktion*. G. Fischer.

Picqué, N. and Hänsch, T. W. (2019). Frequency comb spectroscopy. *Nature Photonics*, 13(3):146.

Piksarv, P., Marti, D., Le, T., Unterhuber, A., Forbes, L. H., Andrews, M. R., Stingl, A., Drexler, W., Andersen, P. E., and Dholakia, K. (2017). Integrated single- and two-photon light sheet microscopy using accelerating beams. *Scientific Reports*, 7(1):1435.

Pilz, G.-A., Carta, S., Stäuble, A., Ayaz, A., Jessberger, S., and Helmchen, F. (2016). Functional Imaging of Dentate Granule Cells in the Adult Mouse Hippocampus. *Journal of Neuroscience*, 36(28):7407–7414.

Pitrone, P. G., Schindelin, J., Stuyvenberg, L., Preibisch, S., Weber, M., Eliceiri, K. W., Huisken, J., and Tomancak, P. (2013). OpenSPIM: An open-access light-sheet microscopy platform. *Nat Meth*, 10(7):598–599.

Planchon, T. A., Gao, L., Milkie, D. E., Davidson, M. W., Galbraith, J. A., Galbraith, C. G., and Betzig, E. (2011). Rapid three-dimensional isotropic imaging of living cells using Bessel beam plane illumination. *Nat Meth*, 8(5):417–423.

Podgorski, K. and Ranganathan, G. N. (2016). Brain heating induced by near infrared lasers during multi-photon microscopy. *Journal of Neurophysiology*, page jn.00275.2016.

Power, R. M. and Huisken, J. (2017). A guide to light-sheet fluorescence microscopy for multi-scale imaging. *Nature Methods*, 14(4):360–373.

Power, R. M. and Huisken, J. (2018). Adaptable, illumination patterning light sheet microscopy. *Scientific Reports*, 8(1):9615.

Qi, Y., Yu, T., Xu, J., Wan, P., Ma, Y., Zhu, J., Li, Y., Gong, H., Luo, Q., and Zhu, D. (2019). FDISCO: Advanced solvent-based clearing method for imaging whole organs. *Science Advances*, 5(1):eaau8355.

Ragan, T., Kadiri, L. R., Venkataraju, K. U., Bahlmann, K., Sutin, J., Taranda, J., Arganda-Carreras, I., Kim, Y., Seung, H. S., and Osten, P. (2012). Serial two-photon tomography for automated ex vivo mouse brain imaging. *Nature Methods*, 9(3):255–258.

Ragan, T., Sylvan, J. D., Kim, K. H., Huang, H., Bahlmann, K., Lee, R. T., and So, P. T. C. (2007). High-resolution whole organ imaging using two-photon tissue cytometry. *Journal of Biomedical Optics*, 12(1):014015–014015–9.

Renier, N., Adams, E. L., Kirst, C., Wu, Z., Azevedo, R., Kohl, J., Autry, A. E., Kadiri, L., Umadevi Venkataraju, K., Zhou, Y., Wang, V. X., Tang, C. Y., Olsen, O., Dulac, C., Osten, P., and Tessier-Lavigne, M. (2016). Mapping of Brain Activity by Automated Volume Analysis of Immediate Early Genes. *Cell*, 165(7):1789–1802.

Renier, N., Wu, Z., Simon, D. J., Yang, J., Ariel, P., and Tessier-Lavigne, M. (2014). iDISCO: A Simple, Rapid Method to Immunolabel Large Tissue Samples for Volume Imaging. *Cell*, 159(4):896–910.

Resan, B., Aviles-Espinosa, R., Kurmulis, S., Jacob Licea-Rodriguez, Brunner, F., Rohrbacher, A., David Artigas, Loza-Alvarez, P., and Weingarten, K. J. (2014). Two-photon fluorescence imaging with 30 fs laser system tunable around 1 micron. *Opt. Express*, 22(13):16456–16461.

Reynaud, E. G., Peychl, J., Huisken, J., and Tomancak, P. (2015). Guide to light-sheet microscopy for adventurous biologists. *Nature Methods*, 12(1):30–34.

Richardson, D. S. and Lichtman, J. W. (2015). Clarifying Tissue Clearing. *Cell*, 162(2):246–257.

Ritter, J. G., Spille, J.-H., Kaminski, T., and Kubitscheck, U. (2011). A cylindrical zoom lens unit for adjustable optical sectioning in light sheet microscopy. *Biomedical Optics Express*, 2(1):185–193.

Robertson, A., Knappe, R., and Wallenstein, R. (1997). Kerr-lens mode-locked Cr:LiSAF femtosecond laser pumped by the diffraction-limited output of a 672-nm diode-laser master-oscillator power-amplifier system. *JOSA B*, 14(3):672–675.

Rocha, M. D., Düring, D. N., Bethge, P., Bethge, P., Voigt, F. F., Hildebrand, S., Helmchen, F., Pfeifer, A., Hahnloser, R. H. R., and Gahr, M. (2019). Tissue clearing and light sheet microscopy: Imaging the unsectioned adult zebra finch brain at cellular resolution. *Frontiers in Neuroanatomy*, 13.

Roelofs, A. J., Coxon, F. P., Ebetino, F. H., Lundy, M. W., Henneman, Z. J., Nancollas, G. H., Sun, S., Blazewska, K. M., Bala, J. L. F., Kashemirov, B. A., Khalid, A. B., McKenna, C. E., and Rogers, M. J. (2010). Fluorescent risedronate analogues reveal bisphosphonate uptake by bone marrow monocytes and localization around osteocytes in vivo. *Journal of Bone and Mineral Research*, 25(3):606–616.

Royer, L. A., Lemon, W. C., Chhetri, R. K., and Keller, P. J. (2018). A practical guide to adaptive light-sheet microscopy. *Nature Protocols*, 13(11):2462.

Royer, L. A., Lemon, W. C., Chhetri, R. K., Wan, Y., Coleman, M., Myers, E. W., and Keller, P. J. (2016). Adaptive light-sheet microscopy for long-term, high-resolution imaging in living organisms. *Nature Biotechnology*, advance online publication.

Royer, L. A., Weigert, M., Günther, U., Maghelli, N., Jug, F., Sbalzarini, I. F., and Myers, E. W. (2015). ClearVolume: Open-source live 3D visualization for light-sheet microscopy. *Nature Methods*, 12(6):480–481.

Rühland, S., Wechselberger, A., Spitzweg, C., Huss, R., Nelson, P. J., and Harz, H. (2015). Quantification of in vitro mesenchymal stem cell invasion into tumor spheroids using selective plane illumination microscopy. *Journal of Biomedical Optics*, 20(4):040501.

Russell, E. S. (1916). *Form and Function - A Contribution to the History of Animal Morphology*. Fili-Quarian Classics.

Saghafi, S., Becker, K., Hahn, C., and Dodt, H.-U. (2014). 3D-ultramicroscopy utilizing aspheric optics. *Journal of Biophotonics*, 7(1-2):117–125.

Saghafi, S., Becker, K., Jährling, N., Hahn, C., and Dodt, H.-U. (2015). Recent developments in light sheet ultramicroscopy imaging techniques. volume 9536, pages 95360C–95360C–7.

Saleh, B. E. A. and Teich, M. C. (2007). *Fundamentals of Photonics*. Wiley-Interscience, Hoboken, N.J, 2. edition.

Santi, P. A., Johnson, S. B., Hillenbrand, M., GrandPre, P. Z., Glass, T. J., and Leger, J. R. (2009). Thin-sheet laser imaging microscopy for optical sectioning of thick tissues. *BioTechniques*, 46(4):287–294.

Schacht, P., Johnson, S. B., and Santi, P. A. (2010). Implementation of a continuous scanning procedure and a line scan camera for thin-sheet laser imaging microscopy. *Biomedical Optics Express*, 1(2):598–609.

Scherf, N. and Huisken, J. (2015). The smart and gentle microscope. *Nature Biotechnology*, 33(8):815–818.

Schindelin, J., Arganda-Carreras, I., Frise, E., Kaynig, V., Longair, M., Pietzsch, T., Preibisch, S., Rueden, C., Saalfeld, S., Schmid, B., Tinevez, J.-Y., White, D. J., Hartenstein, V., Eliceiri, K., Tomancak, P., and Cardona, A. (2012). Fiji: An open-source platform for biological-image analysis. *Nature Methods*, 9(7):676–682.

Schneider, J. (2012). *Entwicklung Eines Ultraschnellen Elektro-Optischen Scanners Für STED - Nanoskopie*. PhD thesis, RWTH Aachen.

Schwarz, M. K., Scherbarth, A., Sprengel, R., Engelhardt, J., Theer, P., and Giese, G. (2015). Fluorescent-Protein Stabilization and High-Resolution Imaging of Cleared, Intact Mouse Brains. *PLOS ONE*, 10(5):e0124650.

Sharpe, J., Ahlgren, U., Perry, P., Hill, B., Ross, A., Hecksher-Sørensen, J., Baldock, R., and Davidson, D. (2002). Optical Projection Tomography as a Tool for 3D Microscopy and Gene Expression Studies. *Science*, 296(5567):541–545.

Sheetz, K. E., Hoover, E. E., Carriles, R., Kleinfeld, D., and Squier, J. A. (2008). Advancing multifocal nonlinear microscopy: Development and application of a novel multibeam Yb:KGd(WO4)2 oscillator. *Opt. Express*, 16(22):17574–17584.

Siedentopf, H. and Zsigmondy, R. (1902). Uber Sichtbarmachung und Größenbestimmung ultramikoskopischer Teilchen, mit besonderer Anwendung auf Goldrubingläser. *Annalen der Physik*, 315(1):1–39.

Sigal, Y. M., Zhou, R., and Zhuang, X. (2018). Visualizing and discovering cellular structures with super-resolution microscopy. *Science*, 361(6405):880–887.

Silvestri, L., Bria, A., Sacconi, L., Iannello, G., and Pavone, F. S. (2012). Confocal light sheet microscopy: Micron-scale neuroanatomy of the entire mouse brain. *Opt. Express*, 20(18):20582–20598.

Simon, W. (1965). Photomicrography of Deep Fields. *Review of Scientific Instruments*, 36(11):1654.

Spalteholz, W. (1911). *Über Das Durchsichtigmachen von Menschlichen Und Tierischen Präparaten Und Seine Theoretischen Bedingungen, Nebst Anhang: Über Knochenfärbung*. S. Hirzel. LCCB: 15015140.

Spence, D. E., Kean, P. N., and Sibbett, W. (1991). 60-fsec pulse generation from a self-mode-locked Ti:sapphire laser. *Opt. Lett.*, 16(1):42–44.

Stefaniuk, M., Gualda, E. J., Pawlowska, M., Legutko, D., Matryba, P., Koza, P., Konopka, W., Owczarek, D., Wawrzyniak, M., Loza-Alvarez, P., and Kaczmarek, L. (2016). Light-sheet microscopy imaging of a whole cleared rat brain with Thy1-GFP transgene. *Scientific Reports*, 6.

Steinke, H. and Wolff, W. (2001). A modified Spalteholz technique with preservation of the histology. *Annals of Anatomy - Anatomischer Anzeiger*, 183(1):91–95.

Stelzer, E. H. K., Lindek, S., Albrecht, S., Pick, R., Ritter, G., Salmon, N. J., and Stricker, R. (1995). A new tool for the observation of embryos and other large specimens: Confocal theta fluorescence microscopy. *Journal of Microscopy*, 179(1):1–10.

Stosiek, C., Garaschuk, O., Holthoff, K., and Konnerth, A. (2003). In vivo two-photon calcium imaging of neuronal networks. *Proceedings of the National Academy of Sciences*, 100(12):7319–7324.

Strnad, P., Gunther, S., Reichmann, J., Krzic, U., Balazs, B., de Medeiros, G., Norlin, N., Hiiragi, T., Hufnagel, L., and Ellenberg, J. (2016). Inverted light-sheet microscope for imaging mouse pre-implantation development. *Nature Methods*, 13(2):139–142.

Studier, H., Breunig, H. G., and König, K. (2010). Two-photon imaging with 80 MHz and 1-GHz repetition rate Ti:sapphire oscillators. In *Proceedings Volume 7569, Multiphoton Microscopy in the Biomedical Sciences X*, volume 7569, pages 75691D–75691D–5.

Studier, H., Breunig, H. G., and König, K. (2011). Comparison of broadband and ultrabroadband pulses at MHz and GHz pulse-repetition rates for nonlinear femtosecond-laser scanning microscopy. *Journal of Biophotonics*, 4(1-2):84–91.

Susaki, E. A., Tainaka, K., Perrin, D., Fumiaki Kishino, Tawara, T., Watanabe, T. M., Chihiro Yokoyama, Onoe, H., Eguchi, M., Yamaguchi, S., Abe, T., Kiyonari, H., Shimizu, Y., Atsushi Miyawaki, Yokota, H., and Ueda, H. R. (2014). Whole-Brain Imaging with Single-Cell Resolution Using Chemical Cocktails and Computational Analysis. *Cell*, 157(3):726 – 739.

Susaki, E. A., Tainaka, K., Perrin, D., Yukinaga, H., Kuno, A., and Ueda, H. R. (2015). Advanced CUBIC protocols for whole-brain and whole-body clearing and imaging. *Nature Protocols*, 10(11):1709–1727.

Svoboda, K., Knox, W. H., Tsuda, S., and Denk, W. (1996). Two-photon-excitation scanning microscopy of living neurons with a saturable Bragg reflector mode-locked diode-pumped Cr:LiSrAlFl laser. *Optics Letters*, 21(17):1411–1413.

Swoger, J., Verveer, P., Greger, K., Huisken, J., and Stelzer, E. H. K. (2007). Multi-view image fusion improves resolution in three-dimensional microscopy. *Opt Express*, 15(13):8029–8042.

Tainaka, K., Kubota, S. I., Suyama, T. Q., Susaki, E. A., Perrin, D., Ukai-Tadenuma, M., Ukai, H., and Ueda, H. R. (2014). Whole-Body Imaging with Single-Cell Resolution by Tissue Decolorization. *Cell*, 159(4):911–924.

Tainaka, K., Kuno, A., Kubota, S. I., Murakami, T., and Ueda, H. R. (2016). Chemical Principles in Tissue Clearing and Staining Protocols for Whole-Body Cell Profiling. *Annual Review of Cell and Developmental Biology*, 32(1):713–741.

Tang, S., Krasieva, T. B., Chen, Z., Tempea, G., and Tromberg, B. J. (2006). Effect of pulse duration on two-photon excited fluorescence and second harmonic generation in nonlinear optical microscopy. *Journal of Biomedical Optics*, 11(2):020501.

Tang, S., Liu, J., Krasieva, T. B., Chen, Z., and Tromberg, B. J. (2009). Developing compact multiphoton systems using femtosecond fiber lasers. *Journal of biomedical optics*, 14(3):030508.

Taniguchi, H., He, M., Wu, P., Kim, S., Paik, R., Sugino, K., Kvitsani, D., Fu, Y., Lu, J., Lin, Y., Miyoshi, G., Shima, Y., Fishell, G., Nelson, S. B., and Huang, Z. J. (2011). A Resource of Cre Driver Lines for Genetic Targeting of GABAergic Neurons in Cerebral Cortex. *Neuron*, 71(6):995–1013.

Taylor, M. A., Vanwalleghem, G. C., Favre-Bulle, I. A., and Scott, E. K. (2018). Diffuse light-sheet microscopy for stripe-free calcium imaging of neural populations. *Journal of Biophotonics*, 11(12).

Theer, P. and Denk, W. (2006). On the fundamental imaging-depth limit in two-photon microscopy. *Journal of the Optical Society of America A*, 23(12):3139–3149.

Theer, P., Dragneva, D., and Knop, M. (2016). πSPIM: High NA high resolution isotropic light-sheet imaging in cell culture dishes. *Scientific Reports*, 6:32880.

Tillberg, P. W., Chen, F., Piatkevich, K. D., Zhao, Y., Yu, C.-C. J., English, B. P., Gao, L., Martorell, A., Suk, H.-J., Yoshida, F., DeGennaro, E. M., Roossien, D. H., Gong, G., Seneviratne,

U., Tannenbaum, S. R., Desimone, R., Cai, D., and Boyden, E. S. (2016). Protein-retention expansion microscopy of cells and tissues labeled using standard fluorescent proteins and antibodies. *Nature Biotechnology*, 34(9):987–992.

Tilma, B. W., Mangold, M., Zaugg, C. A., Link, S. M., Waldburger, D., Klenner, A., Mayer, A. S., Gini, E., Golling, M., and Keller, U. (2015). Recent advances in ultrafast semiconductor disk lasers. *Light: Science & Applications*, 4(7):e310.

Tokunaga, M., Imamoto, N., and Sakata-Sogawa, K. (2008). Highly inclined thin illumination enables clear single-molecule imaging in cells. *Nature Methods*, 5(2):159–161.

Tomer, R., Khairy, K., Amat, F., and Keller, P. J. (2012). Quantitative high-speed imaging of entire developing embryos with simultaneous multiview light-sheet microscopy. *Nat Meth*, 9(7):755–763.

Tomer, R., Lovett-Barron, M., Kauvar, I., Andalman, A., Burns, V. M., Sankaran, S., Grosenick, L., Broxton, M., Yang, S., and Deisseroth, K. (2015). SPED Light Sheet Microscopy: Fast Mapping of Biological System Structure and Function. *Cell*, 163(7):1796–1806.

Tomer, R., Ye, L., Hsueh, B., and Deisseroth, K. (2014). Advanced CLARITY for rapid and high-resolution imaging of intact tissues. *Nat. Protocols*, 9(7):1682–1697.

Tong-Sheng, C., Shao-Qun, Z., Wei, Z., and Qing-Ming, L. (2003). A Quantitative Theory Model of a Photobleaching Mechanism. *Chinese Physics Letters*, 20(11):1940.

Treweek, J. B., Chan, K. Y., Flytzanis, N. C., Yang, B., Deverman, B. E., Greenbaum, A., Lignell, A., Xiao, C., Cai, L., Ladinsky, M. S., Bjorkman, P. J., Fowlkes, C. C., and Gradinaru, V. (2015). Whole-body tissue stabilization and selective extractions via tissue-hydrogel hybrids for high-resolution intact circuit mapping and phenotyping. *Nature Protocols*, 10(11):1860–1896.

Truong, T. V., Supatto, W., Koos, D. S., Choi, J. M., and Fraser, S. E. (2011). Deep and fast live imaging with two-photon scanned light-sheet microscopy. *Nat Meth*, 8(9):757–760.

Tsai, P. S. and Kleinfeld, D. (2009). In vivo two-photon laser scanning microscopy with concurrent plasma-mediated ablation: Principles and hardware realization. In Frostig, R., editor, *Methods for In Vivo Optical Imaging*, pages 59–115. CRC Press.

Udem, T., Holzwarth, R., and Hänsch, T. W. (2002). Optical frequency metrology. *Nature*, 416(6877):233–237.

Valdmanis, J. A., Fork, R. L., and Gordon, J. P. (1985). Generation of optical pulses as short as 27 femtoseconds directly from a laser balancing self-phase modulation, group-velocity dispersion, saturable absorption, and saturable gain. *Optics Letters*, 10(3):131–133.

van de Linde, S., Heilemann, M., and Sauer, M. (2012). Live-Cell Super-Resolution Imaging with Synthetic Fluorophores. *Annual Review of Physical Chemistry*, 63(1):519–540.

Vettenburg, T., Dalgarno, H. I. C., Nylk, J., Coll-Lladó, C., Ferrier, D. E. K., Čižmár, T., Gunn-Moore, F. J., and Dholakia, K. (2014). Light-sheet microscopy using an Airy beam. *Nature Methods*, 11(5):541–544.

Vigouroux, R. J., Belle, M., and Chédotal, A. (2017). Neuroscience in the third dimension: Shedding new light on the brain with tissue clearing. *Molecular Brain*, 10:33.

Villaseñor, R., Ozmen, L., Messaddeq, N., Grüninger, F., Loetscher, H., Keller, A., Betsholtz, C., Freskgård, P.-O., and Collin, L. (2016). Trafficking of Endogenous Immunoglobulins by Endothelial Cells at the Blood-Brain Barrier. *Scientific Reports*, 6:25658.

Voie, A. H. (2002). Imaging the intact guinea pig tympanic bulla by orthogonal-plane fluorescence optical sectioning microscopy. *Hearing Research*, 171(1–2):119–128.

Voie, A. H., Burns, D. H., and Spelman, F. A. (1993). Orthogonal-plane fluorescence optical sectioning: Three-dimensional imaging of macroscopic biological specimens. *Journal of Microscopy*, 170(3):229–236.

Voie, A. H. and Spelman, F. A. (1995). Three-dimensional reconstruction of the cochlea from two-dimensional images of optical sections. *Computerized Medical Imaging and Graphics*, 19(5):377–384.

Voigt, F. F. (2014). *Multi-Area Microscopy: A Modular Two-Photon Microscope for Simultaneous Functional in Vivo Imaging of Multiple Cortical Areas.* Msc Thesis, ETH Zurich. Zurich.

Voigt, F. F., Chen, J. L., Krueppel, R., and Helmchen, F. (2015). A modular two-photon microscope for simultaneous imaging of distant cortical areas in vivo. In *Proceedings Volume 9329, Multiphoton Microscopy in the Biomedical Sciences XV*, volume 9329, pages 93292C–93292C–7.

Waldburger, D., Link, S. M., Mangold, M., Alfieri, C. G. E., Gini, E., Golling, M., Tilma, B. W., and Keller, U. (2016). High-power 100 fs semiconductor disk lasers. *Optica*, 3(8):844–852.

Waldeyer, W. (1863). Untersuchungen über den Ursprung und den Verlauf des Axsencylinders bei Wirbellosen und Wirbelthieren sowie über dessen Endverhalten in der quergestreiften Muskelfaser. *Henle Pfeifer's Z. Rat. Med*, 20:193–256.

Wang, C., Liu, R., Milkie, D. E., Sun, W., Tan, Z., Kerlin, A., Chen, T.-W., Kim, D. S., and Ji, N. (2014a). Multiplexed aberration measurement for deep tissue imaging *in vivo*. *Nature Methods*, 11(10):1037–1040.

Wang, H., Kong, L., Forrest, A., Bajek, D., Haggett, S. E., Wang, X., Cui, B., Pan, J., Ding, Y., and Cataluna, M. A. (2014b). Ultrashort pulse generation by semiconductor mode-locked lasers at 760 nm. *Optics Express*, 22(21):25940–25946.

Wang, H., Zhao, Y., Ezcurra, M., Benedetto, A., Gilliat, A. F., Hellberg, J., Ren, Z., Galimov, E. R., Athigapanich, T., Girstmair, J., Telford, M. J., Dolphin, C. T., Zhang, Z., and Gems, D. (2018a). A parthenogenetic quasi-program causes teratoma-like tumors during aging in wild-type C. elegans. *npj Aging and Mechanisms of Disease*, 4(1):6.

Wang, X., Allen, W. E., Wright, M. A., Sylwestrak, E. L., Samusik, N., Vesuna, S., Evans, K., Liu, C., Ramakrishnan, C., Liu, J., Nolan, G. P., Bava, F.-A., and Deisseroth, K. (2018b). Three-dimensional intact-tissue sequencing of single-cell transcriptional states. *Science*, 361(6400):eaat5691.

Wassie, A. T., Zhao, Y., and Boyden, E. S. (2019). Expansion microscopy: Principles and uses in biological research. *Nature Methods*, 16(1):33.

Weber, M. and Huisken, J. (2011). Light sheet microscopy for real-time developmental biology. *Curr Opin Genet Dev*, 21(5):566–572.

Weber, M., Scherf, N., Meyer, A. M., Panáková, D., Kohl, P., and Huisken, J. (2017). Cell-accurate optical mapping across the entire developing heart. *eLife*, 6:e28307.

White, J. G., Southgate, E., Thomson, J. N., and Brenner, S. (1986). The Structure of the Nervous System of the Nematode Caenorhabditis elegans. *Philosophical Transactions of the Royal Society of London. Series B, Biological Sciences*, 314(1165):1–340.

Wilcox, K. G., Quarterman, A. H., Beere, H., Ritchie, D. A., and Tropper, A. C. (2010). High Peak Power Femtosecond Pulse Passively Mode-Locked Vertical-External-Cavity Surface-Emitting Laser. *IEEE Photonics Technology Letters*, 22(14):1021–1023.

Wilcox, K. G., Tropper, A. C., Beere, H. E., Ritchie, D. A., Kunert, B., Heinen, B., and Stolz, W. (2013). 4.35 kW peak power femtosecond pulse mode-locked VECSEL for supercontinuum generation. *Optics Express*, 21(2):1599–1605.

Willig, K. I., Harke, B., Medda, R., and Hell, S. W. (2007). STED microscopy with continuous wave beams. *Nature Methods*, 4(11):915–918.

Wilt, B. A., Burns, L. D., Wei Ho, E. T., Ghosh, K. K., Mukamel, E. A., and Schnitzer, M. J. (2009). Advances in light microscopy for neuroscience. *Annu Rev Neurosci*, 32:435–506.

Winnubst, J., Bas, E., Ferreira, T. A., Wu, Z., Economo, M. N., Edson, P., Arthur, B. J., Bruns, C., Rokicki, K., Schauder, D., Olbris, D. J., Murphy, S. D., Ackerman, D. G., Arshadi, C., Baldwin, P., Blake, R., Elsayed, A., Hasan, M., Ramirez, D., Dos Santos, B., Weldon, M., Zafar, A., Dudmann, J. T., Gerfen, C. R., Hantman, A. W., Korff, W., Sternson, S. M., Spruston, N., Svoboda, K., and Chandrashekar, J. (2019). Reconstruction of 1,000 Projection Neurons Reveals New Cell Types and Organization of Long-Range Connectivity in the Mouse Brain. *Cell*.

Wissozky, N. (1877). Ueber das Eosin als Reagens auf Hämoglobin und die Bildung von Blutgefässen und Blutkörperchen bei Säugethier- und Hühnerembryonen. *Archiv für mikroskopische Anatomie*, 13(1):479–496.

Wohland, T., Shi, X., Sankaran, J., and Stelzer, E. H. K. (2010). Single Plane Illumination Fluorescence Correlation Spectroscopy (SPIM-FCS) probes inhomogeneous three-dimensional environments. *Optics Express*, 18(10):10627–10641.

Wong, M. D., Dazai, J., Walls, J. R., Gale, N. W., and Henkelman, R. M. (2013). Design and Implementation of a Custom Built Optical Projection Tomography System. *PLoS ONE*, 8(9):e73491.

Wu, Y., Ghitani, A., Christensen, R., Santella, A., Du, Z., Rondeau, G., Bao, Z., Colón-Ramos, D., and Shroff, H. (2011). Inverted selective plane illumination microscopy (iSPIM) enables coupled cell identity lineaging and neurodevelopmental imaging in Caenorhabditis elegans. *Proceedings of the National Academy of Sciences*, 108(43):17708–17713.

Wu, Y., Wawrzusin, P., Senseney, J., Fischer, R. S., Christensen, R., Santella, A., York, A. G., Winter, P. W., Waterman, C. M., Bao, Z., Colón-Ramos, D. A., McAuliffe, M., and Shroff, H. (2013). Spatially isotropic four-dimensional imaging with dual-view plane illumination microscopy. *Nature Biotechnology*, 31(11):1032–1038.

Xu, C. and Webb, W. W. (1996). Measurement of two-photon excitation cross sections of molecular fluorophoreswith data from 690 to 1050 nm. *Journal of the Optical Society of America B*, 13(3):481–491.

Xu, C. and Wise, F. W. (2013). Recent advances in fibre lasers for nonlinear microscopy. *Nat Photon*, 7(11):875–882.

Yang, B., Treweek, J. B., Kulkarni, R. P., Deverman, B. E., Chen, C.-K., Lubeck, E., Shah, S., Cai, L., and Gradinaru, V. (2014). Single-Cell Phenotyping within Transparent Intact Tissue through Whole-Body Clearing. *Cell*, 158(4):945–958.

Yang, W. and Yuste, R. (2019). Brain maps at the nanoscale. *Nature Biotechnology*, page 1.

Yang, Z., Haslehurst, P., Scott, S., Emptage, N., and Dholakia, K. (2016). A compact light-sheet microscope for the study of the mammalian central nervous system. *Scientific Reports*, 6:26317.

Yokoyama, H., Guo, H., Yoda, T., Takashima, K., Sato, K.-i., Taniguchi, H., and Ito, H. (2006). Two-photon bioimaging with picosecond optical pulses from a semiconductor laser. *Optics Express*, 14(8):3467–3471.

Young, M. D., Backus, S., Durfee, C., and Squier, J. (2013). Multiphoton imaging with a direct-diode pumped femtosecond Ti:sapphire laser. *Journal of Microscopy*, 249(2):83–86.

Zarb, Y., Weber-Stadlbauer, U., Kirschenbaum, D., Kindler, D. R., Richetto, J., Keller, D., Rademakers, R., Dickson, D. W., Pasch, A., Byzova, T., Nahar, K., Voigt, F. F., Helmchen, F., Boss, A., Aguzzi, A., Klohs, J., and Keller, A. (2019). Ossified blood vessels in primary familial brain calcification elicit a neurotoxic astrocyte response. *Brain*.

Zaugg, C. A., Hoffmann, M., Pallmann, W. P., Wittwer, V. J., Sieber, O. D., Mangold, M., Golling, M., Weingarten, K. J., Tilma, B. W., Südmeyer, T., and Keller, U. (2012). Low repetition rate SESAM modelocked VECSEL using an extendable active multipass-cavity approach. *Opt. Express*, 20(25):27915–27921.

Zaugg, C. A., Klenner, A., Mangold, M., Mayer, A. S., Link, S. M., Emaury, F., Golling, M., Gini, E., Saraceno, C. J., Tilma, B. W., and Ursula Keller (2014). Gigahertz self-referenceable frequency comb from a semiconductor disk laser. *Opt. Express*, 22(13):16445–16455.

Zeilhofer, H. U., Studler, B., Arabadzisz, D., Schweizer, C., Ahmadi, S., Layh, B., Bösl, M. R., and Fritschy, J.-M. (2005). Glycinergic neurons expressing enhanced green fluorescent protein in bacterial artificial chromosome transgenic mice. *Journal of Comparative Neurology*, 482(2):123–141.

Zipfel, W. R., Williams, R. M., and Webb, W. W. (2003). Nonlinear magic: Multiphoton microscopy in the biosciences. *Nat Biotech*, 21(11):1369–1377.

Acknowledgments

The work presented in this thesis has been carried out in the Laboratory of Neural Circuit Dynamics at the Brain Research Institute, University of Zurich, under the supervision of Fritjof Helmchen. I deeply enjoyed the freedom and unwavering support provided by him to allow me to pursue a wide range of projects and collaborations. In addition, he was a wise and encouraging mentor in dire situations.

Beyond Fritjof, I would like to thank Bruno Weber and Stephan Neuhauss for co-supervising this thesis.

The SDL imaging project presented in this thesis would have been impossible without Florian Emaury, who since 2014 – the time of my semester thesis in the Ultrafast Laser Physics Laboratory at ETH – took up a deep interest in multiphoton imaging and brought semiconductor disk lasers to Fritjof's laboratory. Mario Mangold, Dominik Waldburger, and Sandro Link provided lots of additional support and know-how. In addition, Ursula Keller shall be thanked for – in the spirit of "Just do it!" – supporting an "undoubtedly pretty applied" project.

Daniel Kirschenbaum and Adriano Aguzzi provided the initial motivation to get me back into light-sheet microscopy and shared immense amounts of know-how on tissue clearing. Ladan Egolf took up light-sheet imaging as a pet project and established the CLARITY clearing pipeline in the Helmchen lab together with Dubravka Göckeritz-Dujmovic. Together with Philipp Bethge, Stew Berry, Julia Kaiser, Alexander van der Bourg, and Balazs Laurenczy, Ladan also provided welcome respites from the litte insanities of PhD life. And – of course, I'm legally required to thank Alex for his LaTeX thesis template. Together with Stefano Carta he also helped to carry out in vivo experiments. Martin Wieckhorst and Hansjörg Kasper helped with lots of custom electronics for the mesoSPIM. Stefan Giger machined countless microscope parts with great skill and care (and calm when version numbers got mixed up). Frank David and Pietro Morciano provided IT support, arranged for many terabytes of storage, and came to understand that the phrase "Another workstation, please – this time with (even) more RAM, if possible..." mostly translates into "lots of work" and "weird mainboards, weird problems".

In early June 2017, the mesoSPIM turned from a typical one-off laboratory setup into something bigger when Christian Lüscher and Anthony Holtmaat decided – seemingly in a split second – that they wanted to have one in Geneva which provided the push to start the mesoSPIM initative. Over the course of the following year, Gilles Reymond shared his VR tools and Stéphane Pagès and Laura Batti provided immense support in bringing the mesoSPIM to the Wyss Center and organized a meeting that introduced the system to a wider audience – Thanks for all your help!

When setting up the mesoSPIM in Geneva, Evgenia Platonova helped enormously, went on to build a whole mesoSPIM and provided extensive support in image processing – thanks for the amazing color projection and so much more!

Paola Perin provided the incentive to start imaging iDISCO samples with the mesoSPIM which opened a whole new range of applications and turned out to be much easier than I thought – I am indepted to you for that.

Martina Schaettin, Thomas Topilko and Nicolas Renier generously provided some of the most beautiful cleared samples I have ever seen – thanks for all that!

After some short discussions at SfN 2018, a box with amazing human cortex samples arrived from Sven Hildebrand, Anna Schueth and Alard Roebroeck – thanks for doing this on such short notice!

Finally, I would like to thank my family – Evi, Wolfgang, Thomas, Christina, Serena and Lorenzo for all their support. And – beyond compare, Rahel for so many wonderful moments.

Fabian Friedrich Voigt

Brain Research Institute
Helmchen Group
University of Zurich
Winterthurer Str. 190
CH-8057 Zurich

Email: voigt@hifo.uzh.ch
Orcid-ID: orcid.org/0000-0002-7108-2176
Code: github.com/ffvoigt

Personal

Born on April 20, 1987 in Potsdam, Germany (German Citizen)

Education

PhD student in the group of Fritjof Helmchen, University of Zurich, Apr 2015 – May 2019

MSc in Interdisciplinary Sciences with Major in Physics and Neuroscience
(with distinction, grade: 5.97), ETH Zurich, February 2015

BSc in Interdisciplinary Sciences (grade: 5.31), ETH Zurich, March 2012

Abitur (*Secondary Education*), Hermann-von-Helmholtzgymnasium Potsdam, Germany
(with distinction, grade: 1.0), 1999 – 2006

Teaching

EMBO Practical Course: Two-photon imaging of brain dynamics, September 3-9, 2017

PHY103: Physical colloquium for medical students, Fall semester 2016

EMBO Practical Course: Two-photon imaging of brain circuit function, September 1-7, 2013

Additional Training

Labortierkurs Modul 1 (Training in Animal Experimentation) FELASA-accredited. June 2012.

Summer School on "Opto-mechanical Design in Astronomy" of the Leibniz-Institute for Astrophysics Potsdam, June 20-23, 2011

Summer Schools by the German National Academic Foundation on the Physics of the Cytoskeleton (Olang, 2009) and Immunology (Nice, 2010)

Awards and Scholarships

Scholarship by the German National Academic Foundation (Studienstiftung des deutschen Volkes) 2007 – 2014

ETH Medal 2015 (Awarded annually for the best Msc Thesis in each ETH department)

Willy-Studer-Prize 2015 (Awarded annually to the top student in each degree course at ETH Zürich)

HIFO-Talk 2016

Publications

Preprints

Fabian F. Voigt, Daniel Kirschenbaum, Evgenia Platonova, Stéphane Pagès, Robert A. A. Campbell, Rahel Kastli Martina Schaettin, Ladan Egolf, Alexander van der Bourg, Philipp Bethge, Karen Haenraets, Noémie Frézel, Thomas Topilko, Paola Perin, Daniel Hillier, Sven Hildebrand, Anna Schueth, Alard Roebroeck, Botond Roska, Esther Stoeckli, Roberto Pizzala, Nicolas Renier, Hanns Ulrich Zeilhofer, Theofanis Karayannis, Urs Ziegler, Laura Batti, Anthony Holtmaat, Christian Lüscher, Adriano Aguzzi, Fritjof Helmchen: "The mesoSPIM initiative: open-source light-sheet microscopes for imaging in cleared tissue", bioRxiv, biorxiv.org/content/10.1101/577122v1

Wolfgang Omlor, Pia Sipilae, Anna-Sophia Wahl, Henry Luetcke, Balazs Laurenczy, I-Wen Chen, Lazar T. Sumanovski, Marcel van 't Hoff, Philipp Bethge, *Fabian F. Voigt*, Martin E. Schwab, Fritjof Helmchen: "Context-dependent limb movement encoding in neuronal populations of motor cortex", bioRxiv, biorxiv.org/content/10.1101/588129v1

Journal Articles

Yvette Zarb, Ulrike Weber-Stadlbauer, Daniel Kirschenbaum, Diana Rita Kindler, Juliet Richetto, Daniel Keller, Rosa Rademakers, Dennis W. Dickinson, Andreas Pasch, Tatiana Byzova, Khayrun Nahar, *Fabian F. Voigt*, Fritjof Helmchen, Andreas Boss, Adriano Aguzzi, Jan Klohs, Annika Keller: "Ossified blood vessels in primary familial brain calcification elicit a neurotoxic astrocyte response", Brain, early acess (2019), doi: 10.1093/brain/awz032

Mariana Diales Rocha, Daniel Normen Düring, Philipp Bethge, *Fabian F. Voigt*, Staffan Hildebrand, Fritjof Helmchen, Alexander Pfeifer, Richard Hans Robert Hahnloser, Manfred Gahr: Tissue clearing and light sheet microscopy: "Imaging the unsectioned adult zebra finch brain at micrometer resolution", Frontiers in Neuroanatomy (2019), doi: 10.3389/fnana.2019.00013

Paola Perin, *Fabian Voigt*, Philipp Bethge, Fritjof Helmchen, Roberto Pizzala: "iDISCO for the study of neuroimmune architecture of the rat auditory brainstem", Frontiers in Neuroanatomy, (2019), doi: 10.3389/fnana.2019.00015

Annika Keller, Mario Nuvolone, Irina Abakumova, Josephin Wagner, Daniel Kirschenbaum, *Fabian F. Voigt*, Caihong Zhu, Luca Regli, Fritjof Helmchen, and Adriano Aguzzi: "Prion pathogenesis is unaltered in a mouse strain with a permeable blood-brain barrier", PLoS Pathogens 14(11): e1007424 (2018), doi: 10.1371/journal.ppat.1007424

Diederik P. Moeys, Federico Corradi, Chenghan Li, Simeon Bamford, Luca Longinotti, Christian Brandli, *Fabian F. Voigt*, Stewart Berry, Gemma Taverni, Fritjof Helmchen, and Tobi Delbruck: "A Sensitive Dynamic and Active Pixel Vision Sensor for Color or Neuronal Imaging Applications" , IEEE Transactions on Biomedical Circuits and Systems, Vol. 12, Issue 1, (2018), pp. 123-136, doi:10.1109/TBCAS.2017.2759783

Philipp Bethge*, Stefano Carta*, Dayra A. Lorenzo, Ladan Egolf, Despoina Goniotaki, Linda Madisen, *Fabian F. Voigt*, Jerry Chen, Bernard Schneider, Masamichi Ohkura, Junichi Nakai, Hongkui Zeng, Adriano Aguzzi, and Fritjof Helmchen: "An R-CaMP1.07 reporter mouse for cell-type-specific and inducible expression of a sensitive red fluorescent calcium indicator", PLOS One, 12(6): e0179460 (2017). doi:10.1371/journal.pone.0179460

*Fabian F. Voigt**, Florian Emaury*, Philipp Bethge, Dominik Waldburger, Sandro M. Link, Stefano Carta, Alexander van der Bourg, and Fritjof Helmchen, and Ursula Keller: "Multiphoton in vivo imaging with

a femtosecond semiconductor disk laser"; Biomedical Optics Express, Vol. 8, Issue 7, pp. 3213-3231 (2017); doi:10.1364/BOE.8.003213

Jerry L. Chen*, *Fabian F. Voigt**, Mitra Javadzadeh, Roland Krueppel, and Fritjof Helmchen: "Long-Range Population Dynamics of Anatomically Defined Neocortical Networks", eLife, May 24th, 2016, doi: 10.7554/eLife.14679

Florian O. Fahrbach, *Fabian F. Voigt*, Benjamin Schmid, Fritjof Helmchen, and Jan Huisken: "Rapid 3D light-sheet microscopy with a tunable lens", Optics Express, Vol. 21, Issue 18, pp. 21010-21026 (2013); doi:10.1364/OE.21.021010

Jerry L Chen*, Oliver A Pfäffli*, *Fabian F. Voigt*, David J Margolis, and Fritjof Helmchen: "Online correction of licking-induced brain motion during two-photon imaging with a tunable lens", Journal of Physiology, Vol. 591, Issue 19, pp. 4689-4698 (2013); doi:10.1113/jphysiol.2013.259804

Benjamin F. Grewe*, *Fabian F. Voigt**, Marcel van 't Hoff and Fritjof Helmchen: "Fast two-layer two-photon imaging of neuronal cell populations using an electrically tunable lens."; Biomedical Optics Express, Vol. 2, Issue 7, pp. 2035-2046 (2011); doi:10.1364/BOE.2.002035

Christoph J. Engelbrecht*, *Fabian Voigt** and Fritjof Helmchen: "Miniaturized selective plane illumination microscopy (miniSPIM) for high-contrast in vivo fluorescence imaging"; Optics Letters, Vol. 35, Issue 9, pp. 1413-1415 (2010); doi:10.1364/OL.35.001413.

(*: equal contributions)

Conference Proceedings

Gemma Taverni, Diederik Paul Moeys, *Fabian F. Voigt*, Chenghan Li, David San Segundo Bello, Vasyl Motsnyi, Stewart Berry, Pia Sipilä, Fritjof Helmchen, and Tobi Delbruck: "In-vivo imaging of neural activity with dynamic vision sensors", IEEE (Conference: 2017 Biomedical Circuits and Systems Conference – BioCAS), doi: 10.1109/BIOCAS.2017.8325076

Fabian F. Voigt, Jerry L. Chen, Roland Krüppel and Fritjof Helmchen: "A modular two-photon microscope for simultaneous imaging of distant cortical areas in vivo" SPIE Proceedings (Conference: Multiphoton Microscopy in the Biomedical Sciences XV), Paper 9329-81

Other Publications

Fabian F. Voigt: "Focusing in microscopy using Optotune's focus-tunable lens EL-10-30", application note (9/2011), available on www.optotune.ch

David Leuenberger and Fabian F. Voigt: "Focus-Tunable Lenses Enable 3-D Microscopy", Biophotonics Magazine (4/2015), available on www.photonics.com

Talks

Informal seminar, Schnitzer Group, Stanford University, November 12th, 2018

10th Light Sheet Fluorescence Microscopy Conference, Dresden, August 12th, 2018

European Light Microscopy Initiative Meeting, Dublin, June 5th, 2018

Informal seminar, Hillman Group, Zuckerman Institute, Columbia University, April 17th, 2018

Neural Circuits Meeting, Cold Spring Harbor, April 13th, 2018

Wyss Center Workshop on Lightsheet Microscopy, Geneva, March 19th, 2018 (invited)

Frontiers in Neurophotonics Symposium 2017, Bordeaux, October 15th, 2017

INI-HIFO Symposium, September 28th, 2017

ZNZ PhD Retreat, May 19th, 2017

HIFOday, May 11th, 2017

Centre of Microscopy and Image Analysis, University of Zurich, June 15th, 2017 (invited)

HIFOday, May 4th, 2016

Focus on Microscopy, Göttingen, April 1st, 2015

Informal seminar, Schnitzer Group, Stanford University, February 13th, 2015

Frontiers in Neurophotonics Symposium 2013, Bordeaux, October 4th, 13

Informal seminar, Hillman Group, Columbia University, October 23rd, 2012

Informal seminar, Schnitzer Group, Stanford University, November 18th, 2011

ETH Microscopy seminar / Life in Focus Joint Graduate Student & Postdoc Exchange between Zurich and Paris, October 6th, 2011

CIMST annual meeting, Zurich, September 5th, 2011

Poster presentations

Annual meeting of the Society of Neuroscience (Dynamic Poster), San Diego, 2018

Swiss Society for Neuroscience Meeting, Zurich, 2018

HIFO Evaluation, Zurich, 2018

Frontiers in Neurophotonics Symposium, Bordeaux, 2017

Neuroscience Center Zurich Annual Symposium 2017

Focus on Microscopy, Bordeaux, 2017

Neuroscience Center Zurich Annual Symposium 2015

Photonics West (BiOS), San Francisco, 2015 (Poster 9329-81)

Annual meeting of the Society of Neuroscience, Washington DC, 2014 (Poster 850.12)

Optical imaging of brain structure and function on multiple spatial scales, CNRS Jaques Monod conference, Roscoff, 2014

Annual meeting of the Society of Neuroscience, New Orleans, 2012 (Poster 927.11)

Annual meeting of the Society of Neuroscience, Washington DC, 2011 (Poster 107.6)

Focus on Microscopy, Konstanz, 2011

Imaging brain circuits in health and disease, CNRS Jaques Monod Conference, Roscoff, 2010

7th FENS Forum of European Neuroscience, Amsterdam, 2010